2015

Flow Structure on Unsteady Maneuvering Wings

Matthew Bross
Lehigh University

FLOW STRUCTURE ON UNSTEADY MANEUVERING WINGS

by

Matthew R. Bross

Presented to the Graduate and Research Committee

of Lehigh University

in Candidacy for the Degree of

Doctor of Philosophy

in

Mechanical Engineering

Lehigh University

May, 2015

DISSERTATION SIGNATURE SHEET

Approved and recommended for acceptance as a dissertation in partial fulfillment of the requirements for the degree of Doctor of Philosophy.

_____

Date

_____

Professor Donald Rockwell

Dissertation Director

_____

Accepted Date

Committee Members:

_____

Professor D. O. Rockwell

_____

Professor A. Oztekin

_____

Professor Y. Liu

_____

Professor H.D. Ou-Yang

ACKNOWLEDGMENTS

I would like to acknowledge my sincere gratitude to my doctoral research advisor, Dr. Donald Rockwell, for his extensive wisdom, guidance, and tutelage throughout the supervision of this study. I have benefited both professionally and personally from working with one of the predominant researchers in the area of fluid mechanics.

I would also like to thank the members of my doctoral committee, Dr. Alparslan Oztekin, Dr. Yaling Liu, Dr. Daniel Ou-Yang, for their evaluation, suggestions, and time provided toward this work.

I would also like to thank all of the members of the machine shop staff including, Mr. Richard Towne, Mr. James Bunderla, Mr. Eli Towne, and Mr. Bill Maroun. Their extraordinary craftsmanship, advice, and support were crucial in the completion of this project.

In addition, I am also very thankful to Mrs. JoAnn Casciano, Mrs. Jennifer R. Smith and Mrs. Barbara McGuire for their kindness and administrative assistance. Many thanks to my colleagues and friends, Mr. Naazer Ashraf for his support in all things technical, Dr. Cem Alper Ozen, Dr. Egemen Tinar, and Dr. Turgut Yilmaz for their valuable contributions, moral support and friendship. In addition, I would like to specially thank Dr. Ahmet Burak Tuna, Dr. Maxwell Wolfinger, and Mr. Daniel Tudball Smith for many insightful conversations, laughs, and support during our graduate years at Lehigh.

All of this would not be possible however without the support of my loving parents, family, and friends. I would like to thank them for their endless moral support and motivation throughout my doctoral studies.

TABLE OF CONTENTS

Page

TITLE……i

CERTIFICATE OF APPROVAL……ii

ACKNOWLEDGEMENTS……iii

TABLE OF CONTENTS……..v

LIST OF FIGURES……...x

NOMENCLATURE……..xvi

ABSTRACT……1

CHAPTER 1……...3

INTRODUCTION……3

1.1 *MOTIVATION*……3

1.2 *FLOW STRUCTURE AND LOADING ON PITCHING WINGS*……...…3

1.3 *FLOW STRUCTURE AND LOADING ON ROTATING WINGS*……..8

1.4 *UNRESOLVED ISSUES*……...16

1.5 *RESEARCH OBJECTIVES*……..17

CHAPTER 2…… 30

EXPERIMENTAL SYSTEMS AND TECHNIQUES…… 30

2.1 WATER CHANNEL SYSTEM……..30

2.2 KINEMATICS AND MOTION CONTROL……..31

2.2.1 Kinematics and Wing Planforms……..31

2.2.2 Pure Rotation in Presence of Freestream……..31

2.2.3 Combined Pitch-Up and Rotation Apparatus……...32

2.2.4 Motion Control Components……..……..33

2.3 QUANTITATIVE IMAGING TECHNIQUES……..……...…….34

2.3.1 Stereo Particle Image Velocimetry……...34

2.3.2 SPIV system of Components……....35

2.3.3 Processing and Post-Processing of Vector Field…….....36

2.3.4 Volume reconstruction……..……38

2.4 ERROR ANALYSIS……..……..…38

2.4.1 Random Error……..……..…38

2.4.2 Bias Error……..……...…40

2.4.3 Out of Plane Velocity Error……..……...…41

2.4.4 Phase Averaging Error Reduction……..……..…42

CHAPTER 3…….58

FLOW STRUCTURE ON A ROTATING WING: EFFECT OF STEADY INCIDENT FLOW…….…58

3.1 BACKGROUND…….….58

3.2 EXPERIMENTAL SYSTEMS AND TECHNIQUES…….58

3.3 SECTIONAL FLOW STRUCTURE REPRESENTATIONS: ADVANCE RATIO VARIATION…….……..62

3.3.1 Spanwise Vorticity……...…….……62

3.3.2 Spanwise Velocity…….……...65

3.3.3 Streamlines…….…….....66

3.4 THREE DIMENSIONAL FLOW STRUCTURE: EXTREME VALUES OF ADVANCE RATIO…….…….....69

3.4.1 Spanwise Vorticity…….…….....69

3.4.2 Spanwise Velocity…….…….....70

3.4.3 Q-Criterion…….…….....70

3.5 CONCLUSIONS …….…….....72

CHAPTER 4…….……86

FLOW STRUCTURE ON A SIMULTANEOUSLY PITCHING AND ROTATING WING……..……..……..…86

4.*1 BACKGROUND*…….……..……86

4.2 EXPERIMENTAL SYSTEMS AND TECHNIQUES….……..……..…86

4.3 FLOW STRUCTURE: EVOLUTION OF SECTIONAL SPANWISE VORTICITY….……...……..……..…91

4.4 FLOW STRUCTURE: EVOLUTION OF SECTIONAL SPANWISE VORTICITY….……...……..……..…92

4.4.1 Iso-Surfaces of Q-Criterion……...……..……..…92

4.4.2 Three-Dimensional Patterns of Spanwise Vorticity…..……..….94

4.4.2 Helicity and Three-Dimensional Streamline Patterns…..……94

4.5 FLOW STRUCTURE: SECTIONAL REPRESENTATIONS…..……97

4.5.1 Sectional Patterns of Spanwise Vorticity…….……97

4.5.2 Sectional Downwash……...…….……98

4.5.3 Sectional Spanwise-Oriented Velocity……..…….....100

4.5.4 Sectional Spanwise-Oriented Vorticity Flux…….....101

4.6 FLOW STRUCTURE: EFFECT OF PITCH-RATE…….....103

4.6.1 Vortical Structures at Leading-Edge and From Trailing-Edge.....103

4.6.2 Relaxation of Vortical Structures.....106

4.7 CONCLUSIONS.....108

4.7.1 Effects of rotation on the flow structure induced by pitch-up motion of a wing.....108

4.7.2 Effects of rotation on the flow structure induced by pitch-up motion of a wing: relaxation after cessation of pitch-up.....109

4.7.3 Effects of rotation on the flow structure induced by pitch-up motion of a wing: comparison with the flow structure arising from pure rotation.....110

CHAPTER 5……...125

THREE-DIMENSIONAL FLOW STRUCTURE ALONG SIMULTANEOUSLY PITCHING AND ROTATING WINGS: EFFECT OF PITCH RATE……...125

5.*1 BACKGROUND*…….……...125

5.2 EXPERIMENTAL SYSTEMS AND TECHNIQUES……...125

5.3 THREE DIMENSIONAL REPRESENTATIONS OF FLOW STRUCTURE: COMBINED ROTATION AND PITCH-UP…….....128

5.3.1 Cessation of Pitch-Up Maneuver and Relaxation of the Vortex System…….....128

5.4 THREE-DIMENSIONAL DEVELOPMENT OF FLOW STRUCTURE……131

5.4.1 Vortex structure as a function of pitch rate: comparison at given angles of attack. ……..131

5.4.2 Vortex structure and helical density as a function of pitch rate: comparison at given angles of attack. ……..…..132

5.4.3 Vortex structure as a function of pitch rate: comparison at given angles of rotation. ……..…….133

5.4.4 Vortex structure and helical density as a function of pitch rate: comparison at given angles of rotation. ……..……134

5.5 TEMPORAL DEVELOPMENT OF INTERIOR STRUCTURE OF THE THREE-DIMENSIONAL VORTEX SYSTEM……..135

5.6. CONCLUDING REMARKS ……137

5.6.1 Relaxation of the flow structure during pure rotation after simultaneous rotation and pitch-up motion of wing……137

5.6.2 Flow structure at: given angle of attack for variable angle of rotation; and at given rotation angle for variable angle of attack for wings undergoing combined rotation and pitch-up……138

5.6.3 Temporal development of interior structure of vortex system……139

CHAPTER 6…….…….……149

CONCLUSIONS AND RECOMMENDATIONS……..……..……149

6.1 CONCLUSIONS…….....149

6.1.1 *Flow structure on a rotating wing: effect of incident flow*.....149

6.1.2 *Flow structure on combined pitching and rotating wings*.....150

6.1.3 *Effect of pitch rate on development of three dimensional flow structure on combined pitching and rotating wings*.....151

6.1 RECOMMENDATIONS…….....152

WORKS CITED…….……...…154

APPENDIX A…….……...…….158

SUPPLEMENT TO CHAPTER 2: ERROR ANALYSIS

PHASE AVERAGING EFFECT ON FLOW STRUCTURE……..…...158

RANDOM AND BIAS ERROR EFFECT ON VOLUME RECONSTRUCTION..159

APPENDIX B…….……...……..165

SUPPLEMENT TO CHAPTER 3: FLOW STRUCTURE ON A ROTATING WING: EFFECT OF STEADY INCIDENT FLOW

RECOVERY FROM THREE-DIMENSIONAL STALL ON A ROTATING WING

……..…….....165

VARIATION OF EFFECTIVE ANGLE OF ATTACK …….……..…165

APPENDIX C…….……...…….170

SUPPLEMENT TO CHAPTER 3: THREE-DIMENSIONAL FLOW STRUCTURE ALONG SIMULTANEOUSLY PITCHING AND ROTATING WINGS

MULTIPLE REVOLUTIONS PRIOR TO PITCH-UP….....170

DELAYED OR ADVANCED ROTATION BEFORE PITCH-UP MOTION

…….…..…...170

VITA……...…….……...…176

LIST OF FIGURES

Page

Figure 1.1: Evolution of dynamic stall vortex for rapidly pitching NACA 0015 airfoil (Visbal & Shang, 1989). ……...19

Figure 1.2: Maximum C_L/C_D vs. pitch rate K for different pitch axis locations x/C on a rapidly pitching flat plate (Eldredge et al., 2010). ……....19

Figure 1.3: Rapidly pitching rectangular and elliptical plates (Yilmaz & Rockwell, 2012). …….....20

Figure 1.4: Comparison of computed (Visbal 2012) and experimental (Yilmaz & Rockwell 2012) three-dimensional flow structure for rapidly pitching plate at $K = 0.098$. Iso-surface of Q-criterion for (a,e) experimental, (b,f) computed hi-resolution, and (c,d) filtered computational data.…….....21

Figure 1.5: Comparison of lift and drag values for rapidly pitching plate. Time averaged steady state values and other literature data (Grey lines). Maximum Instantaneous transient values occur during the creation of the LEV (black lines) (Zhang & Schluter, 2012)……..22

Figure 1.6: Rotational accelerations in the flow for a hovering wing during downstroke. These accelerations include, angular, centripetal, and Coriolis. (Lentink & Dickson, 2009a). …….....23

Figure 1.7: Smoke visualization of *Manduca sexta* (Hawkmoth) (A) and mechanical (B) flapping wings (Ellington et al., 1996). ……23

Figure 1.8: Force measurements for a flapping wing (Dickinson et al. (1999))……...24

Figure 1.9: Qualitative bubble visualization on a rotating *D. melanogaster* wing (Lentink & Dickson, 2009b). ……...24

Figure 1.10: Vortex structure over *D. melanogaster* wings with different values of aspect ratio *AR*. Vortex structures are visualized with surfaces of Q-criterion and colored with spanwise vorticity. Instantaneous images show the wing at 270° of rotation (Harbig et al., 2013). …….....25

Figure 1.11: Vortex structure over a *D. melanogaster* wing of $AR = 2.91$ during the downstroke portion of rotation at $\phi = 45°$. Flow structure at span based Reynolds numbers $Re_r = 613$ and 7667 and advance ratios $J = 0$, 0.25 and 0.5 are visualized with surfaces of Q-criterion (Harbig et al., 2014). ……..….....26

Figure 1.12: Top (plan) views of $AR = 2$ and 4 for matching chords of travel s/C. Flow structure is visualized with iso-surfaces of Q-criterion colored with helical density (Carr et al., 2013a). ……..…….....27

Figure 1.13: Surface pressure distribution on the suction side of the wing and corresponding near-body flow structures during the forward stroke of wing undergoing rotation and translation kinematics (Garmann & Visbal, 2013). ……..……28

Figure 1.14: Lift and drag polars for unidirectional rotating wing at Re = 1400. Triangles represent angles of attack, varying from 0° to 90°, for Rossby (R_o) numbers varying from 2.9 to ∞ (Lentink & Dickinson, 2009b). ……..….....29

Figure 2.1: Water channel system. ……..….....45

Figure 2.2: Water channel calibration. ……..….....45

Figure 2.3: Typical kinematics of wing motion for purely rotating and combined pitch-up and rotation. ……..….....46

Figure 2.4: Apparatus for pure rotation of wing (Ozen (2013)). ……..….....46

Figure 2.5: Apparatus for combined pitch-up and rotation of wing. ……..….....47

Figure 2.6: Motion control and SPIV setup for pure rotation of wing with incident freestream. ……..….....48

Figure 2.7: Motion control and SPIV setup for combined pitch up and rotation. ……..….....49

Figure 2.8: Scheimpflug condition (Prasad & Jenson (1995))…….50

Figure 2.9: SPIV arrangement for pure rotation with incident freestream.....51

Figure 2.10: SPIV arrangement for combined pitching and rotating apparatus. 51

Figure 2.11: Vector conditioning process in Insight 3G. 52

Figure 2.12: Illustration of concept of phase averaging. 53

Figure 2.13: Volume reconstruction technique. 54

Figure 2.14: Particle image location and associated error in image diameter subscript c_τ d_τ. (Adrain & Westerweel (2009)). 55

Figure 2.15: Error reduction as function of d_τ/d_r. (Prasad et al. 1997). 55

Figure 2.16: Bias error estimation for subpixel displacement. (Adrian & Westerweel 2009). 56

Figure 2.17: Error ratio as function of stereo half angle α . (Lawson & Wu (1997)). 56

Figure 2.18: RMS vorticity and velocity for instantaneous to 208 phased averaged images. 57

Figure 2.19: RMS vorticity and velocity for groups of six phased averaged images.

.....57

Figure 3.1: (a) Schematic of rotating wing and related parameters as well as orientation of the laser sheet. (b) Side view of wing as viewed during experiment. (c) Laboratory fixed reference frame where *U'* = -*U*. 76

Figure 3.2: Schematic of water channel test section and orientation of stereo PIV. Also indicated is side view of wing as seen by camera A. 77

Figure 3.3a: Comparison of patterns of spanwise vorticity $\omega_z C/V_{eff}$ at the midspan of the wing for α_{eff} = 45°. Patterns are shown at four different values of advance ratio *J* as a function of ϕ during the early stages of rotation (ϕ = 0°, 9°, 13.5°, 18°).....78

Figure 3.3b: Comparison of patterns of spanwise vorticity $\omega_z C/V_{eff}$ at the midspan of the wing for α_{eff} = 45°. Patterns are shown at four different values of advance ratio *J* as a function of ϕ during the intermediate and final stages of rotation (ϕ = 36°, 45°, 90°, 270°).....79

Figure 3.4: Comparison of patterns of spanwise velocity w/V_{eff} at the midspan of the wing for α_{eff} = 45°. Superposed are spanwise vorticity, $\omega_z C/V_{eff}$ contour lines. Patterns are shown at four different values of advance ratio *J* as a function of ϕ during the intermediate and final stages of rotation (ϕ = 36°, 45°, 90°, 270°).....80

Figure 3.5a: Streamline topology in wing fixed reference frame at the midspan of the wing for α_{eff} = 45°. Patterns are shown at four different values of advance ratio *J* as a function of ϕ during the early stages of rotation (ϕ = 0° to 18°).....81

Figure 3.5b: Streamline topology wing fixed reference frame at the midspan of the wing for α_{eff} = 45°. Patterns are shown at four different values of advance ratio *J* as a function of ϕ during the intermediate and final stages of rotation (ϕ = 36° to 270°).....82

Figure 3.6: Sectional cuts of spanwise vorticity $\omega_z C/V_{eff}$ on chordwise oriented planes for values of advance ratio *J* = 0 and 0.537 at rotation angle ϕ = 36°.....83

Figure 3.7: Iso-Surface of spanwise velocity for *J* = 0 and 0.537 at rotation angle ϕ = 36°. For both values of *J*, iso-surface volumes correspond to levels of w/V_{eff} = 0.4. 84

Figure 3.8: Surfaces of iso-*Q* corresponding to a level of *Q* = 5, for advance ratios *J* = 0 and 0.537 at a rotation angle, ϕ = 36°.....85

Figure 4.1: Schematic of rotating-pitching wing and related parameters….....113

Figure 4.2: Schematic of rotating-pitching wing apparatus and PIV arrangement. 114

Figure 4.3: Sectional images of spanwise vorticity $\omega_z C/U$ and $\omega_z C/V_{rg}$ at midspan of wing for: pure pitch-up; pitch-up and rotation; and pure rotation at convective times, $\tau = tU/C$ or tV_{rg}/C = 2, 2.4, 3.2, 4, and 5.6. Images for pure pitch-up were determined from data set of Yilmaz (2011). 115

Figure 4.4: Iso-surfaces of Q-criterion for pure pitch-up, pitch-up and rotation, and pure rotation of wing. Image for pure pitch-up was constructed from data set of Yilmaz (2011). 116

Figure 4.5: Sectional images of spanwise oriented vorticity, $\omega_z C/U$ and $\omega_z C/V_{rg}$ along span of wing undergoing pitch-up, pitch-up and rotation, and rotation. Image for pure pitch-up was constructed from data set of Yilmaz (2011).....117

Figure 4.6: Streamlines and colored helical density h on iso-Q surfaces for flat plate undergoing pitch-up, pitch-up and rotation, and rotation. For pure pitch-up, h-Q and streamlines images were constructed from data set of Yilmaz (2011). 118

Figure 4.7: Sectional images of spanwise-oriented vorticity, $\omega_z C/U$ and $\omega_z C/V_{rg}$ along span of wing undergoing pitch-up, pitch-up and rotation, and rotation. For pure pitch-up, images in Figures 7-10 were determined from data set of Yilmaz (2011). 119

Figure 4.8: Sectional (color) contours of v-component of velocity superposed on sectional (black line) contours of spanwise-oriented vorticity, $\omega_z C/U$ and $\omega_z C/V_{rg}$ along span of wing undergoing pitch-up, pitch-up and rotation, and rotation. ….....120

Figure 4.9: Sectional (color) contours of w (spanwise) component of velocity superposed on sectional (black line) contours of spanwise-oriented vorticity, $\omega_z C/U$ and $\omega_z C/V_{rg}$ along span of wing undergoing pitch-up, pitch-up and rotation, and rotation.

…….121

Figure 4.10: Sectional (color) contours of spanwise vorticity flux, $\omega_z Cw/(U)^2$ and $\omega_z Cw/(V_{rg})^2$ superposed on sectional (black line) contours of spanwise-oriented vorticity, $\omega_z C/U$ and $\omega_z C/V_{rg}$ along span of wing undergoing pitch-up, pitch-up and rotation, and rotation.……122

Figure 4.11: Sectional images of spanwise-oriented vorticity $\omega_z C/V_{rg}$ for: simultaneous pitch-up and rotation of wing (left column); and pure rotation of wing (right column) at different pitch rates K ……123

Figure 4.12: Sectional images of spanwise-oriented vorticity, $\omega_z C/V_{rg}$ at midspan of wing for simultaneous pitch-up and rotation: at end of pitch-up motion (left column); and subsequent relaxation after end of pitch-up motion (right column). ……..124

Figure 5.1: Schematic of rotating-pitching wing and corresponding parameters..……141

Figure 5.2: Iso-surfaces of *Q*-criterion at cessation of pitch-up maneuver (left column) and relaxation of flow structure after 3τ rotational relaxation for reduced pitch rates K = 0.1, 0.2, and 0.4 (right column)……142

Figure 5.3a: Iso-surfaces of *Q*-criterion for values of reduced pitch rate (columns of images) K = 0.1, 0.2 and 0.4 at angles of attack, α = 15°, 30°, and 45° (rows of images). ……..……143

Figure 5.3b: Iso-surfaces of *Q*-criterion (compare Figure 3a) colored with helical density *h* for values of reduced pitch rate (columns of images) K = 0.1, 0.2 and 0.4 at angles of attack, α = 15°, 30°, and 45° (rows of images). ……..…144

Figure 5.4a: Iso-surfaces of *Q*-criterion for values of reduced pitch rate (columns of images) K = 0.1, 0.2 and 0.4 at angles of rotation, ϕ = 10°, 30°, and 50° (rows of images). ……..……145

Figure 5.4b: Iso- surfaces of *Q*-criterion (see Figure 4a) colored with helical density *h* for values of reduced pitch rate (columns of images) K = 0.1, 0.2 and 0.4 at angles of rotation, ϕ = 10°, 30°, and 50° (rows of images). ……...146

Figure 5.5a: Iso-surfaces of *Q*-criterion (left column) and iso-*Q* colored with *h* (right column), for reduced pitch rate K = 0.1 at angles of rotation, ϕ = 10°, 20°, 30°, and 40° (rows of images)..……..…….147

Figure 5.5b: Iso-surfaces of *Q*-criterion (left column) and iso-*Q* colored with *h* (right column), for reduced pitch rate K = 0.4 at angles of rotation, ϕ = 10°, 20°, 25°, and 30° (rows of images)……..……148

Figure A.1: Effect of phase averaging on spanwise vorticity contours at the midplane. An instantaneous image and phase averaged images constructed from 3, 6, and 200 instantaneous images are shown. The convergence of 3 components of velocity and vorticity is shown at 3 locations indicated on the images: 1 chord to the left of the wing (pt. 1), within the leading edge vortex (pt. 2), and 1 chord to the right of the wing (pt. 3). ……161

Figure A.2: Effect of phase averaging on spanwise vorticity contour lines at the midplane. Sets of six averages are compared, superposition of all sets (36 total) are proved. Variation of 3 components of velocity and vorticity shown at 3 locations, 1 chord to the left of the wing (pt. 1), within the leading edge vortex (pt. 2), and 1 chord to the right of the wing (pt. 3). ……162

Figure A.3: Effect of random perturbation of the order of 5% of V_{rg} to all velocity components on reconstructed volume image. Attenuation of random error with phase averaging is shown. ……..…163

Figure A.4: Effect of bias perturbation of the order of 5% of V_{rg} to all velocity components on reconstructed volume image for each phase average…….164

Figure B.1: Sectional cuts of spanwise vorticity $\omega_z C/V_{eff}$ on chordwise-oriented planes. ……..167

Figure B.2: Sectional cut of spanwise vorticity $\omega_z C/V_{eff}$ at the midplane location for α_{eff} = 30°, 45°, and 60° at rotation angles ϕ = 0°, 9°, and 18°. Advance ratio J = 0.171 for all cases…….……168

Figure B.3: Sectional cut of spanwise vorticity $\omega_z C/V_{eff}$ at the midplane location for α_{eff} = 30°, 45°, and 60° at rotation angles ϕ = 36°, 90°, and 270°; advance ratio J = 0.171 for all cases. ……..169

Figure C.1: Sectional slices at the midplane for simultaneous pitch-up and rotation of a wing (left image) and simultaneous pitch-up and rotation of a wing where the pitching motion starts after 5 full revolutions at zero angle of attack for pitch rates K = 0.1, 0.2 and 0.4…….172

Figure C.2: Three dimensional iso-Q surfaces of pitch-up and rotation of a wing (left image) and simultaneous pitch-up and rotation where the pitching motion starts after 5 full revolutions at zero angle of attack…….173

Figure C.3: Sectional slices taken at the midplane for simultaneous pitch-up and rotation of a wing for pitch rates K = 0.1, 0.2 and 0.4. Columns (*a*-*h*) represent the wing starting pitch-up at various times before the rotation starts. Column (*i*) represents the simultaneous starts of rotation and pitch-up motions……..174

Figure C.4: Sectional slices taken at the midplane for simultaneous pitch-up and rotation of a wing for pitch rates K = 0.1, 0.2 and 0.4. Columns (*j*-*m*) represent the wing rotating at various times before the pitching begins. Column (*i*) represents the simultaneous starts of rotation and pitch-up motions……..175

NOMENCLATURE

a	Free parameter defining degree of smoothing
AR	Aspect ratio
b	Span length
C	Chord length
c_τ	centroid consant
C_L	Lift Coefficient
C_D	Drag Coefficient
d_τ	particle image diameter
d_r	pixel pitch
d_p	particle diameter
$f^\#$	f-number of camera lens
$G(t)$	Smoothing function
h	Helical density
J	Advance ratio $J = U/V_{tip}$
K	Dimensionless angular pitch rate
M_O	image magnification
Q	Q-criterion
r	Spanwise position/radial distance from the center of rotation
r_g	Radial distance to the radius of gyration of the wing
r_o	Radial distance to the root of the wing
r_{tip}	Radial distance to the tip of the wing
Re	Reynolds number
Re_s	Reynolds number based on span of wing
Re_{rg}	Reynolds number based chord and on the velocity at the radius of gyration
Re_{tip}	Reynolds number based chord and on the velocity at the tip
R_o	Rossby number
S	number of chord lengths tip of wing travels
$\boldsymbol{S}$	Asymmetric component of the velocity gradient tensor
t	Plate/wing thickness
	Time
t^*	convective time
u	Horizontal (streamwise) component of the velocity
U	Free-stream velocity
U_∞	Free-stream velocity
v	Vertical component of the velocity
$\boldsymbol{V}$	Three-dimensional velocity field

V	Velocity magnitude
V_{rg}	Velocity at the radius of gyration of wing/plate
V_{tip}	Velocity at the tip of the plate/wing
V_{eff}	Effective velocity of the plate/wing
w	Spanwise (transverse) component of the velocity
x	Coordinate in the streamwise direction
y	Coordinate in the vertical direction
z	Coordinate in the transverse direction

Greek Symbols

α	geometric angle of attack
	Stereo half angle
$\dot{\alpha}$	Angular pitch rate
α_{eff}	Effective angle of attack
α_o	geometric angle of attack
$\dot{\alpha}_o$	Angular pitch rate
ϕ	Instantaneous azimuthal rotation angle
$\dot{\phi}$	Angular rotation rate
$\sigma_{\Delta X}$	RMS random in-plane displacement error
$\sigma_{\Delta V}$	RMS random in-plane velocity error
$\sigma_{\Delta Z}$	RMS random out of plane displacement error
δ_Z	depth of field
θ	Lens angle in SPIV arrangement
	Stereo half angle
$\boldsymbol{\Omega}$	Symmetric component of the velocity gradient tensor
Ω	Dimensionless angular rotation rate
Γ	Circulation from spanwise vorticity componant
τ	Convective/non-dimensional time
υ	Kinematic viscosity
$\boldsymbol{\omega}$	Three-dimensional vorticity field
ω_x	Streamwise component of the vorticity
ω_y	Vertical component of the vorticity
ω_z	Spanwise component of the vorticity

Operators

Δ	Difference

Δ	Del operator

Acronyms

LEV	Leading-Edge Vortex
TV	Tip vortex
MAV	Micro-Air Vehicle
PIV	Particle Image Velocimetry
SPIV	Stereoscopic Particle Image Velocimetry
CCD	Charge-Coupled Device
FFT	Fast-Fourier Transform

ABSTRACT

The flow structure along a rotating wing in steady incident flow is compared to the structure on a rotating wing in quiescent fluid, in order to clarify the effect of advance ratio J (ratio of free-stream velocity to tip velocity of wing, U/V_{tip}). Stereoscopic particle image velocimetry leads to patterns of vorticity, velocity, and Q-criterion (constant values of the second invariant of the velocity gradient tensor), as well as streamlines, which allow identification of critical points of the flow. Prior to the onset of motion, the wing is at high angle of attack, and the steady incident flow yields a fully stalled state along the wing. After the onset of wing motion, the effective angle of attack is held constant over the range of J, and the wing rotates from rest to a large angle that corresponds to attainment of the asymptotic state of the flow structure. After the onset of rotation, the stalled region quickly gives rise to a stable leading edge vortex. Throughout the rotation maneuver, the development of the flow structure in the leading edge region is relatively insensitive to the value of J. In the trailing-edge region, however, the structure of the shed vorticity layer is strongly dependent on the value of J. Further insight into the effects of J is provided by three-dimensional patterns of spanwise-oriented vorticity, spanwise velocity, and Q-criterion.

In addition, the three-dimensional flow structures on a wing subjected to simultaneous pitch-up and rotational motion are characterized. The features associated with these simultaneous motions include: stabilization of the large-scale vortex generated at the leading-edge, which, for pure pitch-up motion, rapidly departs from the leading-edge region; preservation of the coherent vortex system involving both the tip vortex and the leading-edge vortex, which severely degrades for pure rotational motion; and rapid

relaxation of the flow structure upon termination of the pitch-up component of motion, whereby the relaxed flow converges to a similar state irrespective of the pitch rate. Three-dimensional surfaces of iso-*Q* and helicity are employed in conjunction with sectional representations of spanwise vorticity, velocity, and vorticity flux to interpret the flow physics.

To complement the foregoing investigation of the simultaneous rotating and pitching wing, the temporal development flow over a combined pitching and rotating wing is characterized. In addition, the effect of pitch rate is explored. Imaging is performed for a range of pitch rates, with emphasis on the three-dimensional structure during start-up and relaxation. Surfaces of transparent iso-*Q* and helicity are employed to interpret the flow physics. The onset and development of the components of the vortex system, i.e., the leading-edge, tip, and trailing-edge vortices, are strongly influenced by the value of pitch rate relative to the rotation rate. Comparisons at the same angle of attack indicate that the formation of vortical structures is delayed with increasing pitch rate. However, comparisons at the same rotation angle for different values of pitch rate reveal similar flow structures, thereby indicating predominance of rotation effects. Extreme values of pitch rate can lead to radically different sequences of development of the components of the three-dimensional vortex system. Nevertheless, consistently positive vorticity flux is maintained through these components, and the coherence of the vortex system is maintained.

CHAPTER 1

INTRODUCTION

1.1 MOTIVATION

Large amplitude, unsteady motion of wings has been of great interest in recent years. This type of maneuver, involving rotation, pitch-up, and plunging, is common in biological flyers, and is in stark contrast to the generally two-dimensional steady flow over conventional aircraft wings. The development of small (micro) unmanned aero vehicles (MAV) for civilian and military applications has spurred research on the flow physics of bio-inspired flight. Overviews of flapping flight are provided by Lehmann & Dickinson (1998), Sane et al. (2003), and Shyy et al. (2010). Of specific interest herein are investigations related to the flow structure and loading due to pure pitch-up, combined pitch-up and rotation, and pure rotation of a wing, with emphasis on finite span wings having low aspect ratio.

1.2 FLOW STRUCTURE AND LOADING ON PITCHING WINGS

The unsteady flow separation on an airfoil or other lifting surface executing time-dependent motion, such as large-amplitude pitching motion, induces a large-scale vortical structure associated with dynamic stall. The overviews of McCroskey (1982) and Ekaterinaris & Platzer (1998) indicate that dynamic stall was initially identified in helicopter and turbomachinery applications. However, the flow structure arising from large amplitude, non-periodic pitch-up motion of a wing with finite aspect ratio has received limited attention.

The seminal computational study of Visbal & Shang (1989) examined an airfoil

undergoing large amplitude pitch-up motion. They investigated the two-dimensional, low Reynolds number (Re = 104) flow past a NACA 0015 airfoil pitched at constant rate to 60° angle of attack. Their parametric study revealed the effects of pitch rate and location of the pivot axis on the flow structure and aerodynamic loading on a rapidly pitching airfoil. Visbal & Shang (1989) identified the formation and development of the dynamic stall vortex, which is shown in Figure 1.1. They also established a strong connection between the maximum lift created by the airfoil and both the pitch rate and location of the pitch axis.

Shih et al. (1992) experimentally characterized the flow past a two dimensional NACA 0012 airfoil pitching to a maximum angle of attack α = 30° at a low Reynolds number Re = 5000. They employed particle image velocimetry to visualize the formation and growth of leading- and trailing-edge vortex structures during the pitch-up maneuver. Shih et al. (1992) concluded that leading-edge flow separation occurs when α = 20°, resulting in a local accumulation of vorticity, which develops into a leading-edge vortex having a scale of one-half the wing chord. Shih at al. (1992) conclude that the large-scale vortex structure originates completely from the leading-edge during the early part of the pitch-up maneuver.

Eldredge & Wang (2010) computationally investigated the effects of reduced pitch rate ($K = \dot{\alpha}_0 c/(2U_\infty)$ = 0.05 and 0.1) and pitch axis location (X/C = 0, 0.25, and 0.5) on the flow structure and loading of a two-dimensional flat plate undergoing a linear pitch-up maneuver. The flat plate pitched to a maximum angle of attack α = 45° in a uniform flow; the Reynolds number based on the plate chord was Re = 1000. Their results suggest a dependence of the maximum lift and drag coefficients on the values of K

and *X/C* (see Figure 1.2). Furthermore, both an additional delay in the development of the leading-edge vortex and an increase in its overall scale were evident for increasing *K* at a given value of *X/C*.

Garmann & Visbal (2011) performed a three-dimensional simulation of the flow structure along a rapidly pitching plate. They studied the effect of Reynolds number (*Re* = 5000 to 40 000), spanwise extent (span/chord = *b/C* = 0.1, 0.2, 0.4, and 0.8), and initial acceleration on the flow structure and aerodynamic loading on the plate during the pitch-up maneuver. They observed that force magnitudes and contour patterns of constant spanwise vorticity appeared to be insensitive to the variation of spanwise extent of the wing. The development of the dynamic stall vortex also appeared to be independent of a change in initial acceleration. Moreover, volume representations of iso-*Q* surfaces indicated that the aerodynamic loading and flow structure were relatively insensitive to changes of the Reynolds number. The only distinction was a loss in flow structure coherence with increasing Reynolds number.

Granlund et al. (2011) performed an experimental investigation involving pitching of low aspect ratio (*AR* = 2), rectangular and elliptical flat plates at a low Reynolds number (10 000). Force measurement and dye visualization were determined for both planforms as each plate pitched from 0° to 90°. Reduced pitch rates of *K* = 0.03 and 0.2 and pivot point locations of *x/C* = 0, 0.5, and 1 were investigated. Their results indicate that planform differences do not contribute in a major way to the flow structure and loading. However, an increase in lift coefficients can be attributed to an increase in pitch rate *K*. Furthermore, the growth and subsequent shedding of the leading-edge vortex appeared to correlate with peaks of the lift coefficients.

Yilmaz et al. (2010) also addressed three-dimensional effects via flow visualization (dye injection). They explored the flow patterns due to unsteady motion of a rapidly pitching or plunging low aspect ratio (AR = 2) flat plate. Yilmaz et al. (2010) explored alterations of the flow structure for the pitch-up and return motion due to variations of the reduced pitch rate (K = 0.1, 0.2, 0.35) and the pitch pivot axis (x/C = 0, 0.25, 0.5, 0.75, and 1); in all cases, the Reynolds number was Re = 10 000. Flow visualization revealed a delay in formation of the leading-edge vortex due to a change in pitch rate, for a given pitch axis location. Yilmaz et al. (2010) also qualitatively identified the highly three-dimensional nature of the flow structure on finite wings undergoing pitch-up maneuvers.

Yilmaz & Rockwell (2012) employed quantitative flow visualization, in the form of stereo particle image velocimetry, to construct the three-dimensional flow patterns on a finite span wing due to pure pitch-up motion. Their investigation addressed the flow structure along low aspect-ratio rectangular and elliptical wings (AR = 2) undergoing pitch-up motion to high angle of attack (α = 45°); the value of Reynolds number was Re = 10 000 based on wing chord. The time evolution of volumetric vortex structures was characterized for fixed values of reduced pitch rate (K = 0.098) and pitch axis location (x/C = 0.25). The high resolution volume representations provided in Figure 1.3 indicated that evolution of the flow structure was distinctly different for the elliptical and rectangular plates, but, after sufficient relaxation time, comparable three-dimensional structures existed. These experimental results are compared with the computations of Visbal (2012) in Figure 1.4. The high resolution of the computational data provides small scale flow structure detail, however, when the computational data is filtered to

match PIV data, the experimental and computational results are in good agreement.

More recently, Hartloper et al. (2013) used a three-dimensional particle tracking velocimetry (3D-PTV) visualization technique, as well as force measurements, to characterize the flow structure and loading along a nominally two-dimensional (infinite aspect ratio) plate and a low aspect ratio (AR = 4) rectangular plate, at reduced pitch rates K = 0.26 and 1.57. The plates were subjected to half-cosine pitching motion and reached a maximum angle of attack of 45°. For a plate that spanned the entire width of the test section, the growth of the leading-edge vortex appeared independent of pitch angle α, whereas, for the low aspect-ratio plate, the growth of the leading-edge vortex correlated with the convective time scale, $t^* = tU_\infty/c$. They also concluded that the leading-edge and tip vortices grow independently of each other. However, the tip vortex influences the dynamics of the leading-edge vortex, resulting in an arch-shaped vortex structure near the midplane of the wing, as first computed by Visbal (2011), and experimentally examined by Yilmaz & Rockwell (2012).

The influence of the leading-edge vortex on the lift generated by a rapidly pitching wing was also examined by Zhang & Schlüter (2012). They computed the lift generated by a rapidly pitching AR = 2 flat plate, at chord based Reynolds numbers from Re = 440 to 21 000. Figure 1.5 provides the lift and drag polar plots for time averaged, steady state values as well as the transient maximum values, obtained during the formation of the leading-edge vortex. For $Re < 2000$, viscous effects result in a decrease of aerodynamic efficiency (C_L/C_D). However, for higher Reynolds numbers ($Re > 2000$), the lift to drag ratio based on the maximum instantaneous values during generation of the leading-edge vortex appears to be insensitive to Reynolds number. This observation may

explain why a vast range of biological flyers operating over a range of Reynolds numbers employ a leading-edge vortex for lift generation.

1.3 FLOW STRUCTURE AND LOADING ON ROTATING WINGS

Angular, centripetal and Coriolis accelerations influence spanwise flow and vortex structures on a flapping wing undergoing rotational motion. Lentink & Dickinson (2009a) provide a conceptual framework for the influence of a leading-edge vortex on aerodynamic performance of flapping wings, as well as related scaling phenomena. Figure 1.6 displays the associated rotational accelerations, angular, centripetal, and Coriolis in the flow over a *Drosophila melanogaster* wing. Of specific interest herein are investigations related to pure rotation, at fixed angle of attack, and combined pitching and rotating wings.

Ellington et al. (1996) visualized the leading-edge vortex on a *Manduca sexta* (Hawk moth) and mechanical flapping model (see Figure 1.7). They concluded that flow along the span of wing on the order of the wing tip velocity is essential for the stability of the leading-edge vortex. Dickinson et al. (1999) explored the aerodynamic forces on a dynamically scaled *D. melanogaster* (fruit fly) flapping wing for a range of angles of attack. The resulting lift and drag coefficients are provided in Figure 1.8 as functions of time and angle of attack. The top two images (A and B) show that C_L and C_D experience a peak during the transient (acceleration) portion of the wing motion, before leveling off once the wing reaches a constant steady velocity. The bottom left graph (C) indicates that the wing experiences more lift than drag for angles of attack between 9° and 45°, however, after 45°, the drag rapidly increases. This is attributed to the contribution of the

normal force to drag as the angle of attack exceeds 45°. Perhaps the most interesting result is the polar representation (D) of the steady force coefficients compared with two-dimensional experimental measurements at a similar Reynolds number (Dickinson & Götze, 1993). At low angle of attack, the three-dimensional results are very similar to the performance of a two-dimensional wing. However, at higher angle of attack, the three-dimensional steady flow produced a larger lift to drag ratio than the 2-D steady measurements. In essence, their results indicate that three-dimensional mechanisms positively contribute to aerodynamic performance for bio-inspired wings at high angles of attack.

Lentink & Dickinson (2009b), Dickson & Dickinson (2004), and Poelma et al. (2006) also examined models of dynamically scaled *D. melanogaster* wings. These investigations explored Reynolds number effects, aerodynamic loading, and wing kinematics. Lentink & Dickinson (2009b) considered a rotating wing model that represented a *D. melanogaster*, with fixed angles of attack α = 36° and 45° for *Re* = 110 and 1400. The existence of a stable leading-edge vortex with strong axial flow is demonstrated in Figure 1.9. They attributed the vortex stability to Coriolis and centripetal fluid accelerations. Dickson & Dickinson (2004) classified the effect of flight parameters on the loading of a dynamically scaled AR = b/C, $\approx$ 4, where b and C are the span and mean chord of the wing respectively, *D. melanogaster* wing rotating at constant angle of attack with a *Re* = 140; the flow structure was not addressed. Dickson & Dickinson (2004) showed that the amplitudes of the lift and drag coefficients were not only dependent on the angle of attack, but also the tip velocity ratio, which is the ratio of the chordwise components of flow velocity at the wing tip due to translation and revolution

(i.e. infinite tip velocity ratio represents a translating wing). In addition, Poelma et al. (2006) characterized the three-dimensional structure on the model *D. melanogaster* wing. Volumetric representations of vortices indicated that, after the initial stage of rotation, strong spanwise flow exists through the stable leading-edge vortex.

Harbig et al. (2013) and Harbig et al. (2014) computationally examined the flow over a rotating *D. melanogaster* wing. Parameters such as aspect ratio (*AR*), Reynolds number, and advance ratio (*J)* were addressed in relation to the leading-edge vortex stability and aerodynamic performance. Harbig et al. (2013) conclude that effects due to Reynolds number and aspect ratio (*AR*) are coupled, and an alternative Reynolds number scaling based on the span of the wing, as opposed to the chord, is more appropriate. Furthermore, the lower *AR* ratio wing (*AR* = 2.91) outperformed (higher lift coefficients) a larger *AR* (*AR* = 7.28) wing, due to the *LEV* break down near the tip for the larger *AR*. Figure 1.10 displays the flow structure on different *AR* wings at two span based Reynolds numbers. Harbig et al. (2014) extended these results by computing the flow structure and loading on a flapping wing in a forward flight configuration. They demonstrated that the added relative velocity incident on the wing during the downstroke at non-zero advance ratios *J* increases the growth rate of the leading-edge vortex. They calculated that the aerodynamic performance improves with increasing *J*. This trend was observed for both values of Reynolds number (Re_r = 613 and Re_r = 7667) based on span. The flow structure for both Re_r = 613 and 7667 is provided in Figure 1.11. At the larger Reynolds number, the leading-edge vortex closely resembles that at lower Re_r, except that the flow pattern at higher Re_r experiences vortex breakdown starting in the tip region of the wing. Harbig et al. (2014) suggest that MAV designers should use low *AR* wings to avoid

vortex shedding over a large range of flight speeds. Other investigations related to the effect of advance ratio on flapping wings include Dickson & Dickinson (2004), Bross et al. (2013), Nagai et al. (2009), and Gopalakrishnan & Tafti (2010).

The extensive work on rotating wings also includes investigations involving simple geometric planforms. These investigations mainly involve variations of aspect ratio and Reynolds number, at fixed angle of attack. Ansari et al. (2009) and Ansari et al. (2011) demonstrated the effect of Reynolds number on the structure of the leading-edge vortex on a low aspect ratio (AR = 2.5) rectangular wing, which underwent rotation at a fixed angle of attack α = 45° in quiescent fluid. Flow visualization at different sectional cuts along the wing revealed how different Reynolds numbers (Re = 500 and 15 000) create a similar structure of the leading-edge vortex during the start-up of wing rotation. A slight loss of coherence of the vortex structure and the onset of more pronounced Helmholtz instabilities appeared at the larger Reynolds number.

Ozen & Rockwell (2011) used quantitative imaging to determine the structure and retention of the leading-edge vortex on an aspect ratio AR = 1 rectangular wing rotating at fixed angle of attack. Their experiments led to the observation that, for a given angle of attack, the scale and form of the vortex was relatively insensitive to Reynolds number, in the range Re = 5400 to 21 600. In addition, they indicated that the presence of strong spanwise (axial) flow and downwash corresponds to the stable leading-edge vortex on the leeward side of the wing. Garmann et al. (2013) computed the vortex structure and aerodynamic loading on a rotating rectangular flat plate of aspect ratio AR = 1, for a range of Reynolds numbers between 200 and 60 000. These numerical simulations were shown to be in good agreement with the experimental results of Ozen & Rockwell (2011)

for cases where values of parameters were matched. Namely, an attached leading-edge vortex persisted to large angle of rotation.

Kim & Gharib (2010) examined the three-dimensional flow structure and loading on a rotating flat plate for Reynolds numbers between 60 and 8800. They demonstrated a conical, stable structure of the leading-edge vortex, along with an established spanwise flow, along a plate of aspect ratio $AR = 2$. Moreover, they observed a decrease in the impulse and lift forces acting on the wing with a decrease in Reynolds number. Ozen & Rockwell (2012) also addressed the three-dimensional flow structure on a wing of aspect ratio $AR = 2$ during the early and late stages of rotation. They employed stereo particle image velocimetry (SPIV) to characterize the relationship between volumetric representations of the structure of the leading-edge vortex and sectional concentrations of both chordwise and spanwise oriented vorticity, as well as spanwise flow. In turn, these features were related to the coherence of the tip and root vortices.

Cheng et al. (2013) quantified the flow patterns along wings revolving at high angle of attack in quiescent fluid using a volume PIV approach. From flow field data on an $AR = 7$ (two times the wing span/mean chord length) wing at a 45° angle attack, rotating at $Re = 220$, they calculated terms in the vorticity transport equation in order to identify the underlying vortex dynamics associated with a stable leading-edge vortex. They identified that convection in the radial and vertical directions is more important than convection in the spanwise direction, in determining the stability of the leading-edge at this very low Reynolds number. Other investigations employing full volumetric visualization (Tomographic-PIV) include Percin et al. (2014). They visualized the flow structure and measured the loading in the tip region of an $AR = 2$ rectangular plate at 30°,

45°, and 60° angles of attack and *Re* = 20 000. Their three dimensional results show the temporal growth of coherent leading-edge and tip vortices, with strong spanwise flow observed through the core of the leading edge vortex. Furthermore, the force generated on the wing for all angles of attack was mostly normal to the wing surface throughout the rotation. The highest lift occurred for 45° angle of attack and the highest drag occurred at 60°, a result similarly observed by Dickinson et al. (1999).

Carr et al. (2013a) highlighted the differences in the tip vortex behavior for rotating rectangular plates at a fixed angle of attack and Reynolds number *Re* = 5000. Quantitative flow visualization revealed that the leading-edge vortex was less coherent near the tip of a wing having an aspect ratio *AR* = 4, compared to *AR* = 2 (Figure 1.12). The tip vortex enhanced the coherence of the leading-edge vortex in this region on the *AR* = 2 wing, relative to the *AR* = 4 wing. Additionally, Carr et al. (2013b) measured an increase in lift coefficient as aspect ratio is decreased. Wojcik & Buchholz (2014) compared sectional cuts of the flow structure along the span of a rotating *AR* = 2 and 4 rectangular plate at various Reynolds numbers, angles of attack, and phases of rotation. They observed an increase in the strength of the leading-edge vortex as the Reynolds number changed from *Re* = 4000 to 16 000. However, similar trends in vortex development were observed for both aspect ratios over the range of Reynolds number.

More recently, Garmann & Visbal (2014) computed the flow structure along, and aerodynamic performance of, revolving wings of *AR* = 1, 2, 4and 4 at a root Reynolds number of *Re* = 1000. Three-dimensional visualizations showed the presence of a stable, coherent vortex structure shortly after the onset of motion for all aspect ratios. The scale, and eventual breakdown, of the leading-edge vortex was sensitive to distance from the

axis of rotation, i.e. aspect ratio. Garmann & Visbal (2014) also computed coefficients of lift and drag throughout the motion. For AR = 2 and 4, C_D and C_L initially increase, eventually reaching a plateau at larger rotation angles. The AR = 1 wing exhibited the same trend in performance but does not reach the higher plateau peak values of C_D and C_L attained for larger aspect ratio wings. In addition, analysis of the centrifugal, Coriolis, and pressure gradient forces, evaluated for all aspect ratios at 25% span, showed that pressure gradient and centrifugal terms were mainly responsible for the large regions of outboard flow on the suction side of the wing. They also noted that the normal (with respect to wing surface) component of the Coriolis force shows a moderate contribution in the core and at the base of the leading-edge vortex (LEV), suggesting that the Coriolis force hinders attachment of the leading-edge vortex.

Garmann & Visbal (2013) provide high fidelity computational results for revolving and rectilinear translating AR = 2 rectangular plates, both at Re = 3000. Provided in Figure 1.13 is the resulting flow structure and surface pressure distribution on the plates during the upstroke for both rotating and translating kinematics. The rotating wing exhibits a conical shaped leading-edge vortex that remains attached across the span of the wing, and the surface pressure distribution suggests that this attached vortex provides constant suction throughout the maneuver. The translating wing is characterized by the formation of tip vortices that evolve into a large arch vortex extending across the span of the plate. Initially, the tip vortices provide suction, however at the late stage of development, the arch vortex detaches from the surface, creating a loss in surface pressure. Garmann & and Visbal (2013) calculated a 32% reduction in cycle-averaged

lift for the translating plate in comparison to the rotating wing, due to the difference in the lift generating vortex structure for each case.

Wolfinger & Rockwell (2014) experimentally investigated the effect of increasing Rossby number on the flow structure on a rotating wing of AR = 1.13 at Re = 1400. The Rossby number defined by $R_o = r_g/C$, where r_g and C are the radius of gyration and chord of the wing. By increasing r_g, and hence Rossby number, a rotating wing begins to resemble a translating wing respectively due to the large rotational radius. Wolfinger & Rockwell (2014) vary the Rossby number from 1.2 to 5.1 and demonstrate, through three-dimensional representations, that the root, leading-edge, and tip vortex structures decrease in coherence with increasing R_o. These results give further insight into the findings of Garmann & Visbal (2013) and Lentink & Dickinson (1998b) (see Figure 1.14) that show a decrease in aerodynamic performance for increasing Rossby number. This indicates an enhancement of lift forces generated from a rotating wing as opposed to a translating wing.

Biological flyers that inspire the design of micro air vehicles typically employ a combination of pitching, plunging, and rotational motions in order to optimize the aerodynamic performance. The present investigation focuses on the detailed flow structure along a low aspect ratio wing undergoing a prevalent combination of motions, i.e., combined pitch-up and rotation, in comparison with simple pitch-up and pure rotation. Additionally the effect of advance ratio J on the development of the flow structure along, and in the wake of, a rotating wing, maintained at a constant value of effective angle of attack, is explored. Quantitative imaging is employed to characterize the detailed three-dimensional flow structure. These maneuvers were chosen to represent

generic unsteady motions, and are broadly applicable to a range of applications, including a rotating helicopter blade or propeller. Within the category of bio-inspired phenomena, the combination of pitch-up and rotation is most akin to a perching type maneuver of a biological flyer. Of particular interest is the effect of rotation on the evolution of the flow structure induced by pitch-up motion.

1.4 UNRESOLVED ISSUES

Taking into account the previous related investigations, as summarized in the foregoing, the major unresolved issues relevant to the present investigation are as follows:

Quantitative three-dimensional flow structure on rotating wings with non-zero advance ratio. In contrast to the case of a wing rotating in quiescent fluid, very little attention has been devoted to the flow structure along a low aspect ratio wing rotating in an incident steady flow, whereby the direction of flow is along the axis of rotation. This configuration corresponds to a 90° stroke plane; it is representative of fast forward and climbing flight (Lentink & Dickinson 2009a). A deeper understanding of the complex three-dimensional flow can be determined with particle image velocimetry

Flow Structure on a combined pitching and rotating wing. Previous studies on low aspect ratio flight have focused on purely pitching, purely rotation, and flapping wings. Despite several studies that address flapping flight, little has been done to visualize the flow structure on a simplified rotating and pitching wing, where the onset of the pitch-up maneuver coincides with the start of rotation. This maneuver is most akin to the perching motion of birds or insects. Quantitative flow visualization of the three-dimensional flow

structure on a wing undergoing combined pitch-up and rotation will lead to a better understanding of the differences in flow structure on a purely rotating wing and a purely pitching wing.

Effect of pitch rate on flow structure for combined pitching and rotating wing. The effect of pitch rate relative to rotation rate on the development of the tip, root, and leading-edge components of the three-dimensional vortex system on a combined pitch-up and rotation maneuver has not been addressed.

Temporal development of flow on combined pitching and rotating wings. The development of leading-edge, root, tip, and wake structures, from their origin to their fully evolved forms, has received little attention for the combined pitching and rotating wing. Visualization is needed for the transient development of the three-dimensional vortex structures during the early stage of motion to the fully evolved state.

1.5 RESEARCH OBJECTIVES

The aforementioned unresolved issues will be addressed by characterizing the three-dimensional flow field generated by low aspect ratio purely rotating wing in hover and forward flight configurations, as well as combined pitching and rotating wings in quiescent flow. Three-dimensional representations of iso-Q, helicity, and streamlines are employed in conjunction with sectional representations of spanwise vorticity, velocity, and vorticity flux to interpret the flow physics.

More specifically, the research objectives in the present investigation are as follows:

(1) Design and construct an experimental apparatus capable of maneuvers of simplified wings, including pure rotation, pure pitch-up, and combined pitch up and rotation. Implement this experimental apparatus with a quantitative flow visualization system (SPIV) for flow structure identification.

(2) Characterize three-dimensional flow structures on a purely rotating wing for a range of advance ratios. Examine the effect of forward flight velocities on the root, tip, and leading-edge vortices.

(3) Identify the three-dimensional flow structures on a combined pitching and rotating wing. Compare the vortex structure for combined motion with the structure along purely pitching and purely rotating wings.

(4) Explore the effect of variation of non-dimensional pitch rate relative to rotation rate for the combined pitch-up and rotation maneuver.

(5) Identify the three-dimensional temporal development of the root, tip, and leading-edge vortex structures for the combined pitch-up and rotation maneuver.

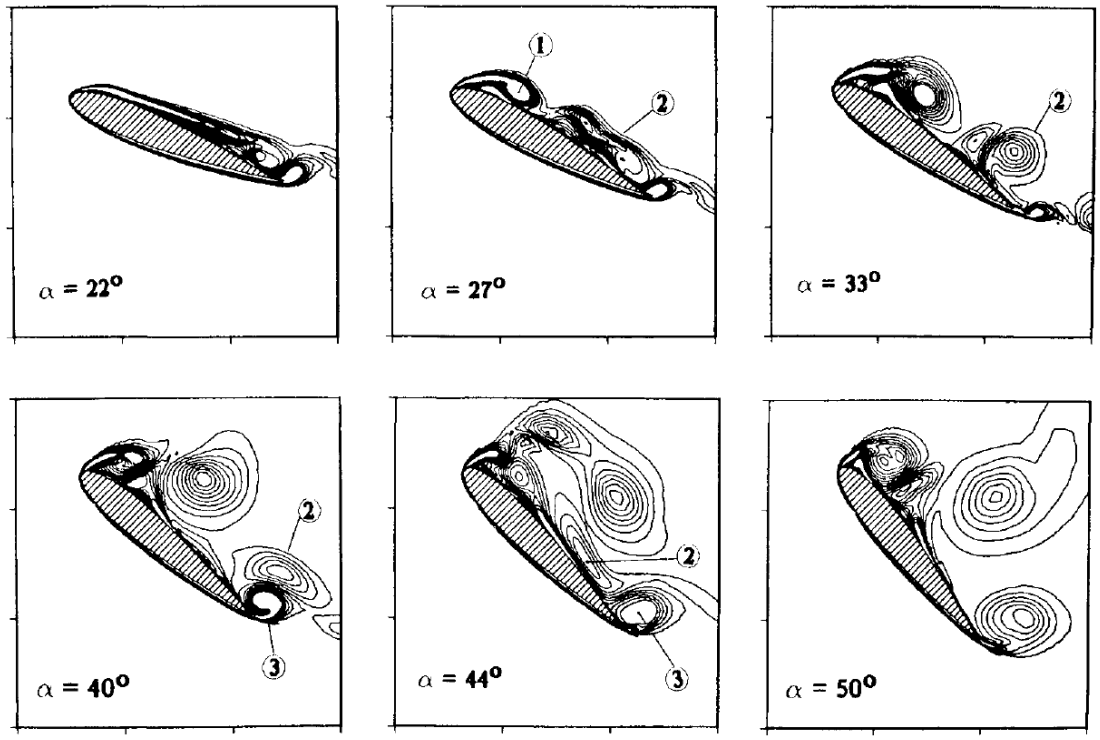

Figure 1.1: Evolution of dynamic stall vortex for rapidly pitching NACA 0015 airfoil (Visbal & Shang, 1989).

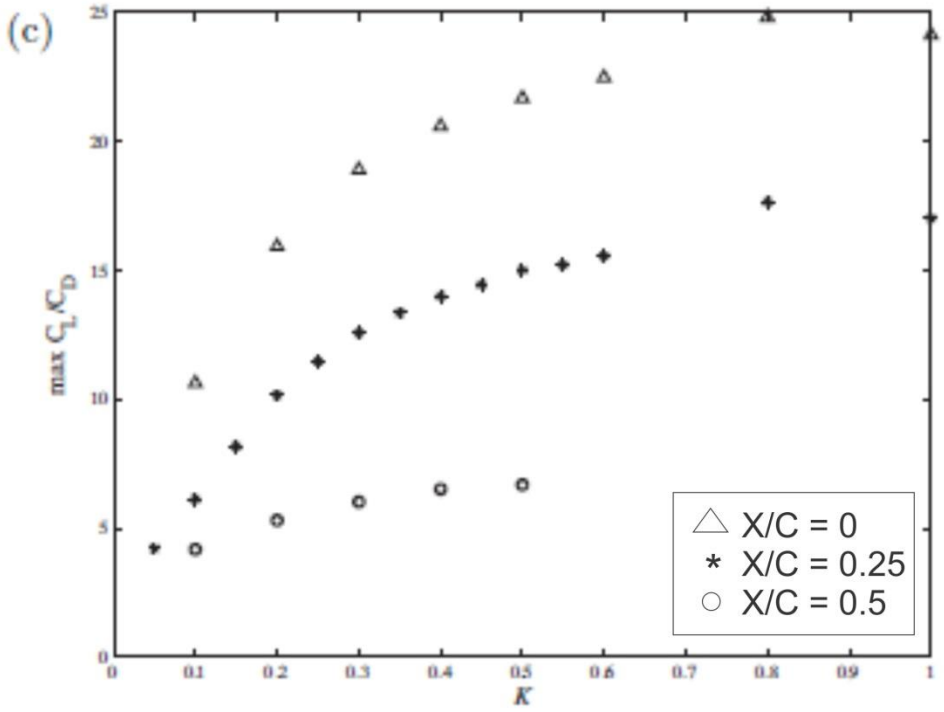

Figure 1.2: Maximum C_L/C_D vs. pitch rate K for different pitch axis locations x/C on a rapidly pitching flat plate (Eldredge et al., 2010).

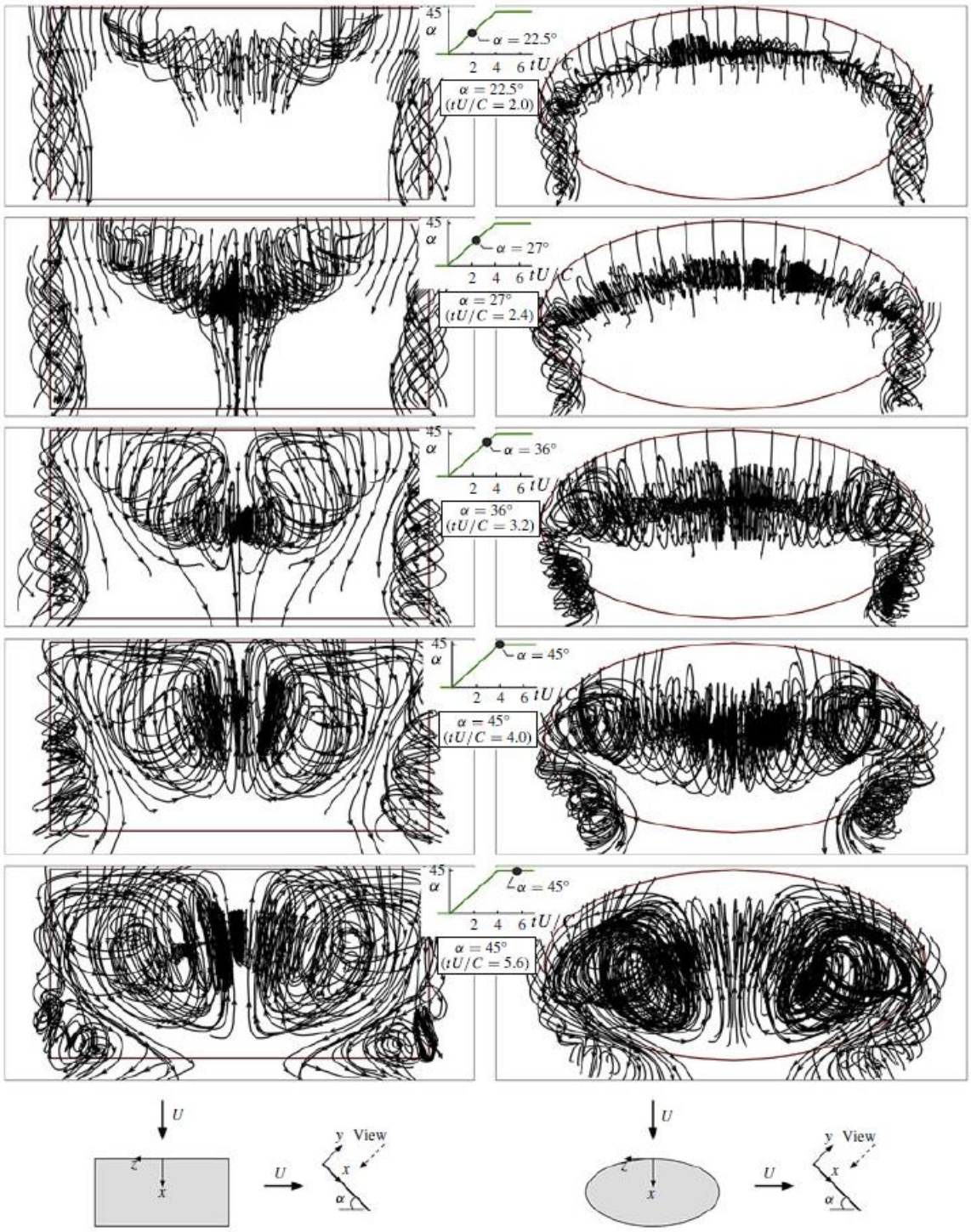

Figure 1.3: Rapidly pitching rectangular and elliptical plates (Yilmaz & Rockwell, 2012).

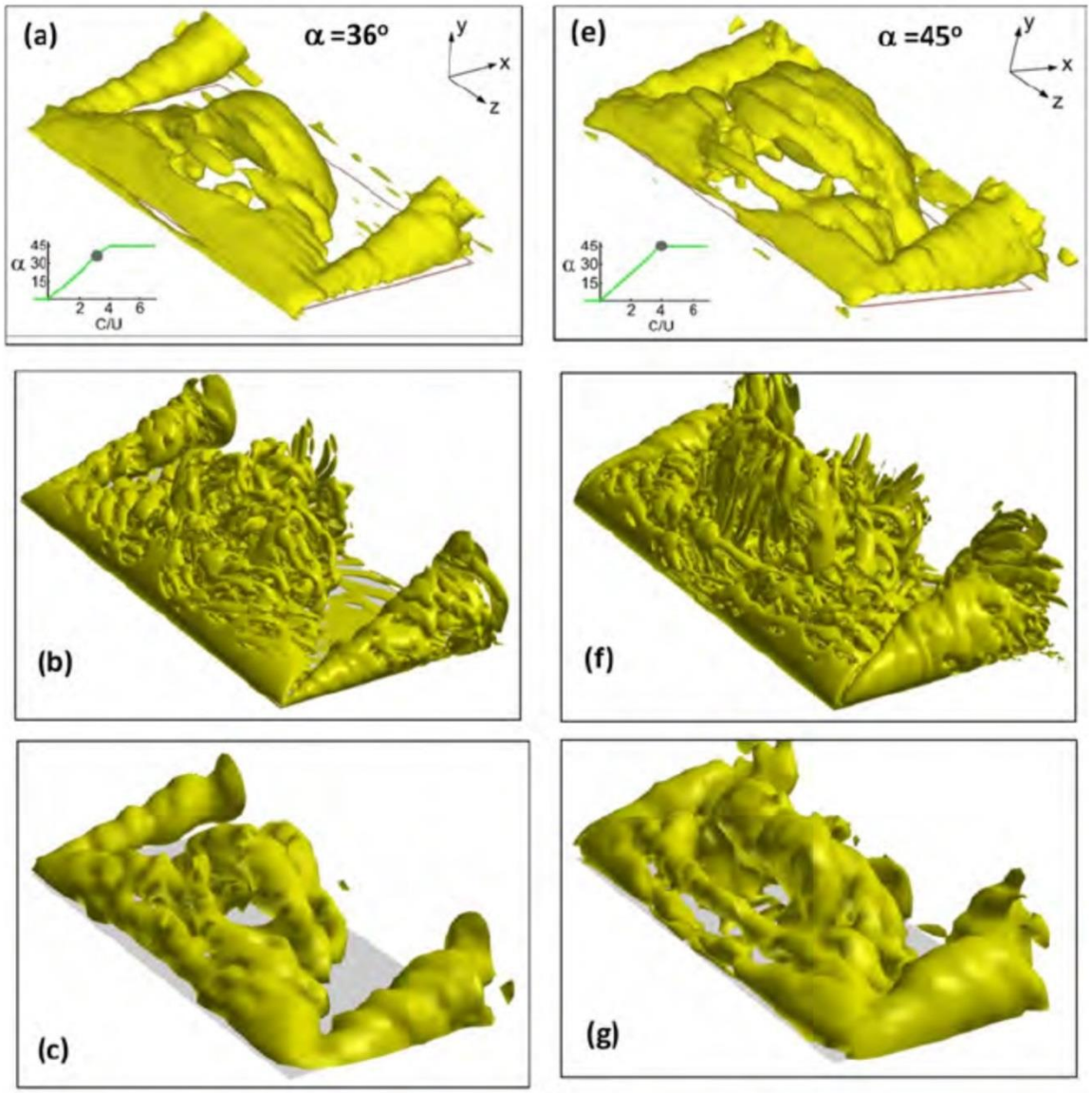

Figure 1.4: Comparison of computed (Visbal 2012) and experimental (Yilmaz & Rockwell 2012) three-dimensional flow structure for rapidly pitching plate at $K = 0.098$. Iso-surface of Q-criterion for (a,e) experimental, (b,f) computed hi-resolution, and (c,d) filtered computational data.

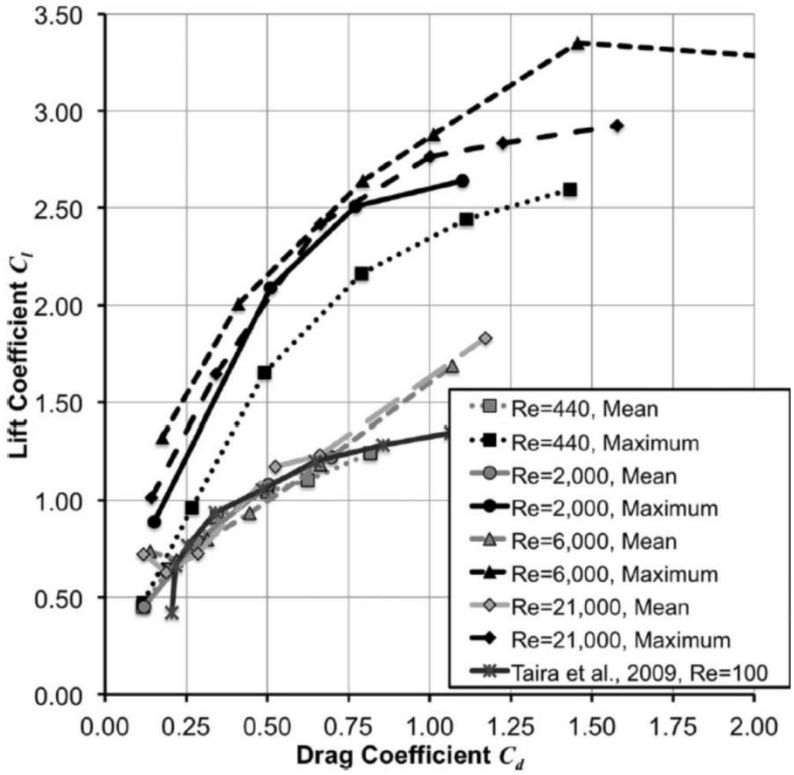

Figure 1.5: Comparison of lift and drag values for rapidly pitching plate. Time averaged steady state values and other literature data (Grey lines). Maximum Instantaneous transient values occur during the creation of the LEV (black lines) (Zhang & Schluter, 2012).

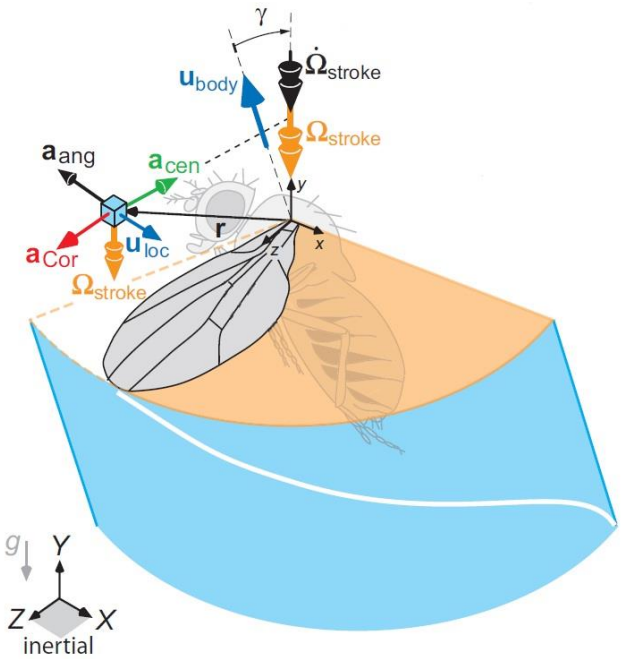

Figure 1.6: Rotational accelerations in the flow for a hovering wing during downstroke. These accelerations include, angular, centripetal, and Coriolis. (Lentink & Dickson, 2009a).

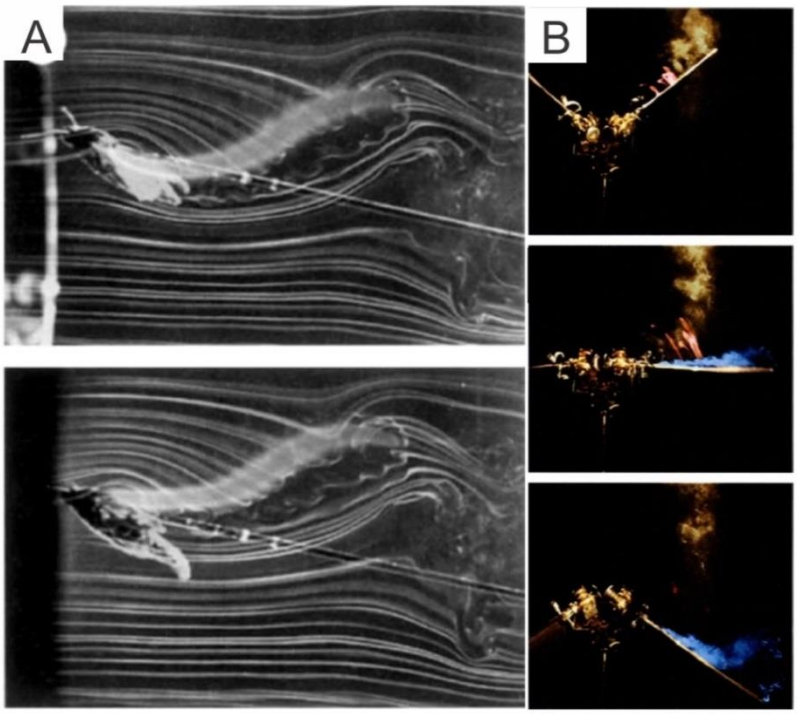

Figure 1.7: Smoke visualization of *Manduca sexta* (Hawkmoth) (A) and mechanical (B) flapping wings (Ellington et al., 1996).

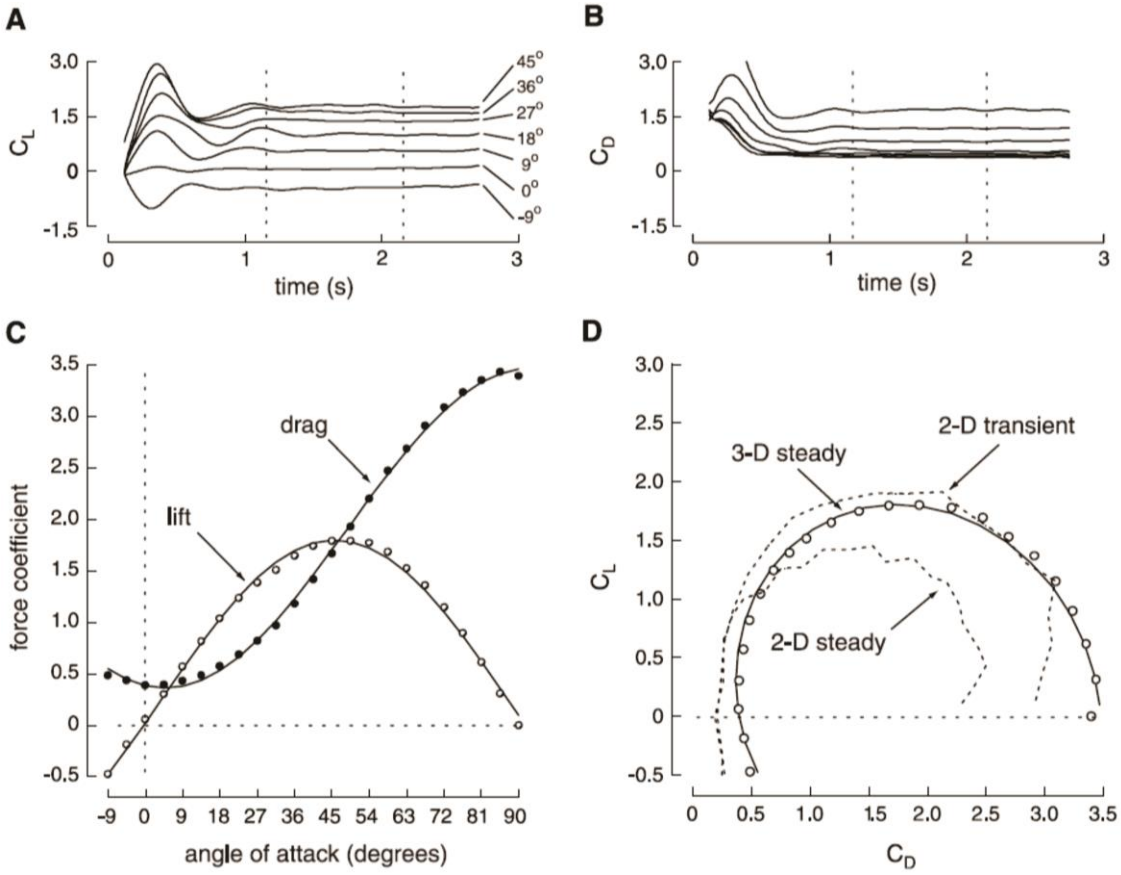

Figure 1.8: Force measurements for a flapping wing (Dickinson et al. (1999)).

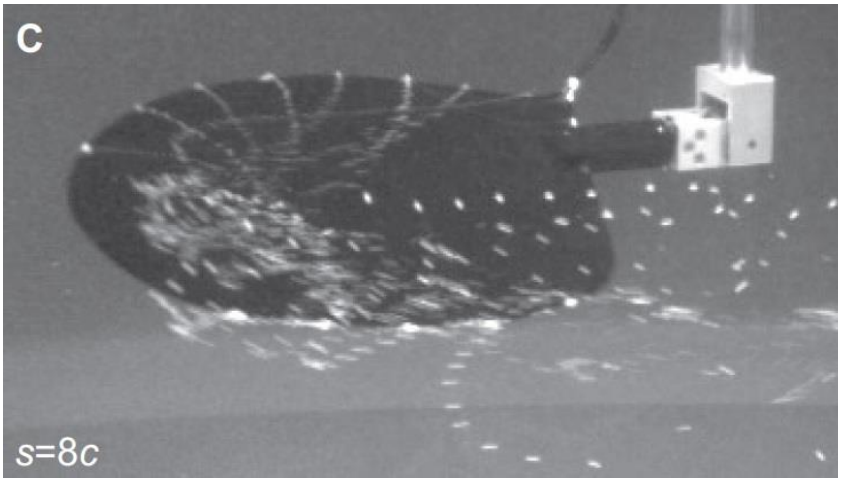

Figure 1.9: Qualitative bubble visualization on a rotating *D. melanogaster* wing (Lentink & Dickson, 2009b).

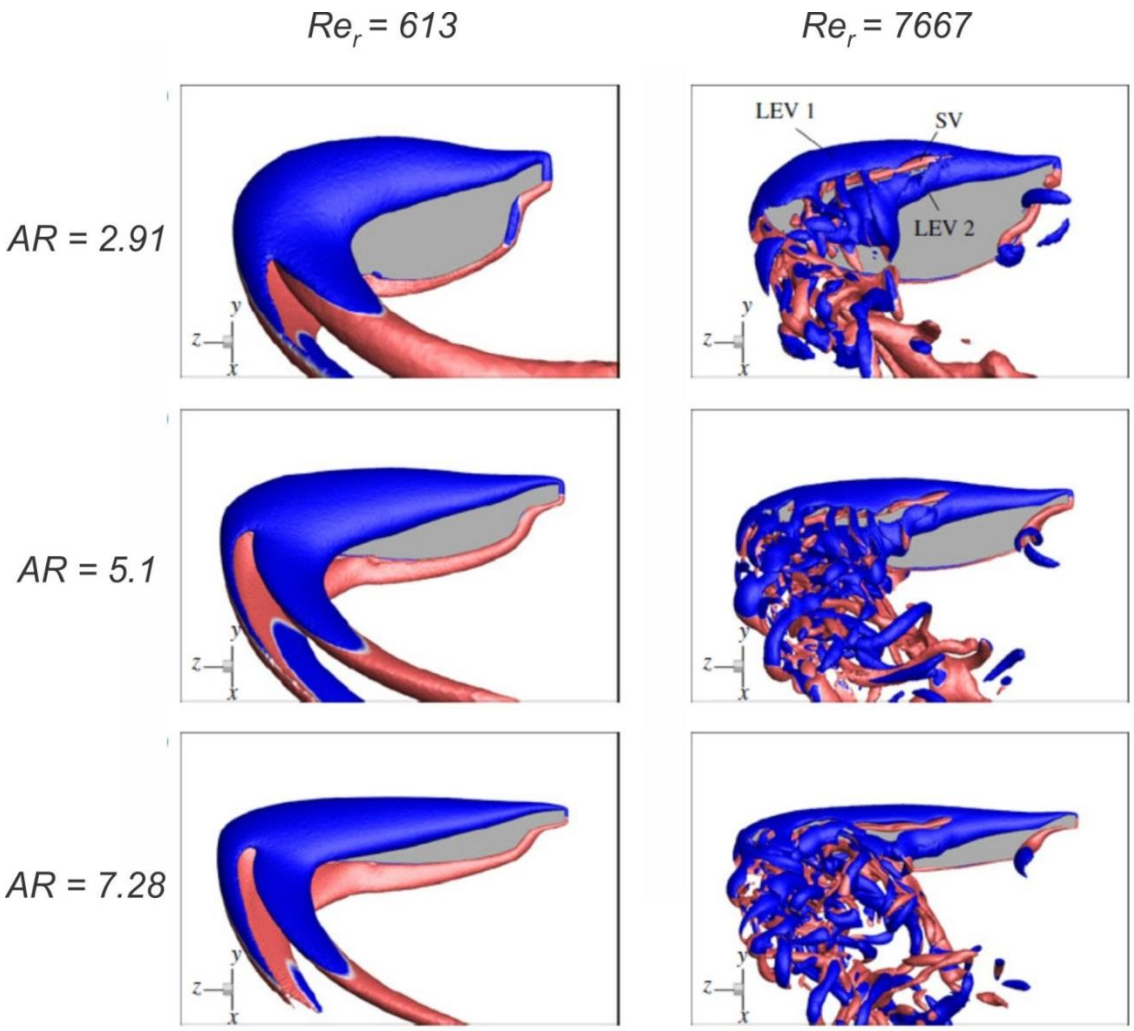

Figure 1.10: Vortex structure over *D. melanogaster* wings with different values of aspect ratio *AR*. Vortex structures are visualized with surfaces of Q-criterion and colored with spanwise vorticity. Instantaneous images show the wing at 270° of rotation (Harbig et al., 2013).

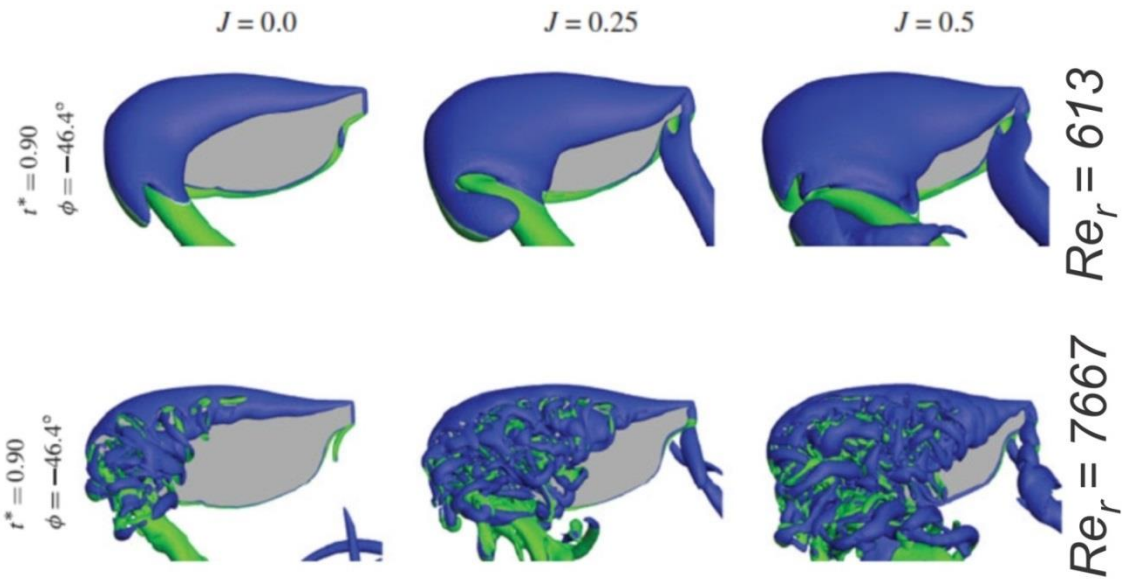

Figure 1.11: Vortex structure over a *D. melanogaster* wing of *AR* = 2.91 during the downstroke portion of rotation at Φ = 45°. Flow structure at span based Reynolds numbers Re_r = 613 and 7667 and advance ratios *J* = 0, 0.25 and 0.5 are visualized with surfaces of *Q*-criterion (Harbig et al., 2014).

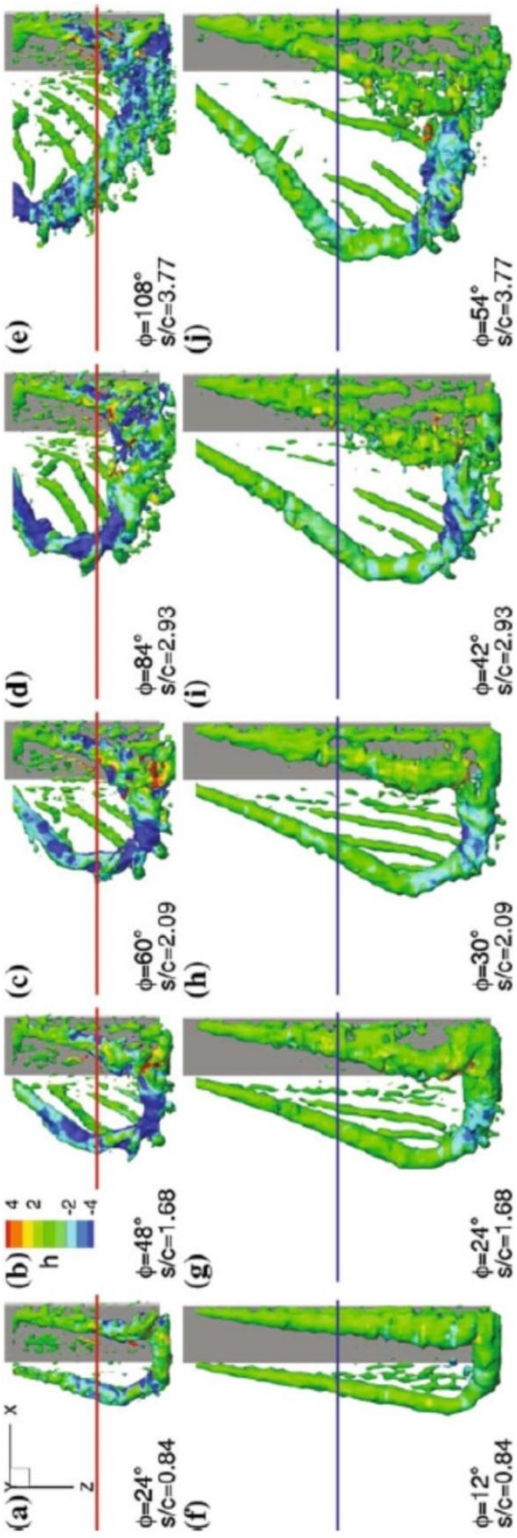

Figure 1.12: Top (plan) views of *AR* = 2 and 4 for matching chords of travel *s/C*. Flow structure is visualized with iso-surfaces of *Q*-criterion colored with helical density (Carr et al., 2013a).

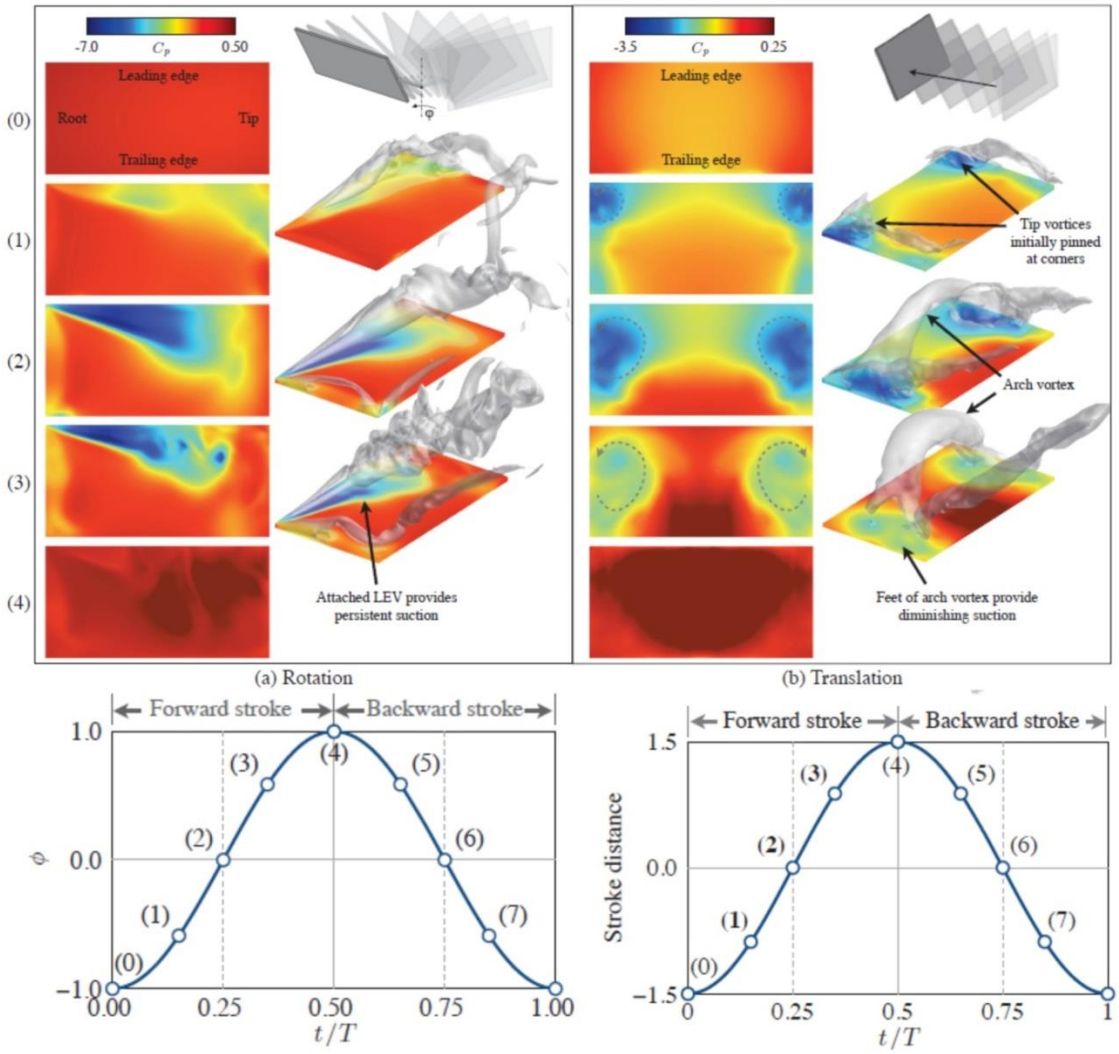

Figure 1.13: Surface pressure distribution on the suction side of the wing and corresponding near-body flow structures during the forward stroke of wing undergoing rotation and translation kinematics (Garmann & Visbal, 2013).

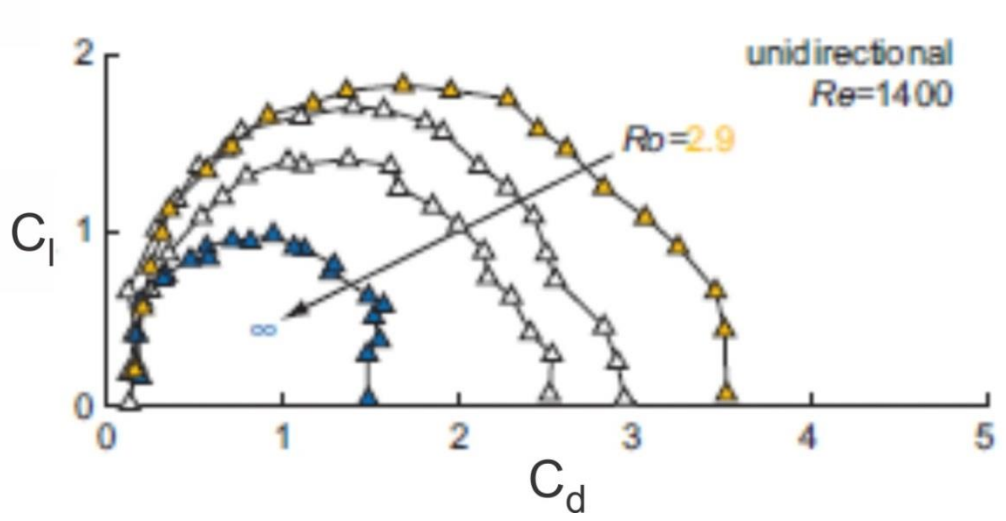

Figure 1.14: Lift and drag polars for unidirectional rotating wing at Re = 1400. Triangles represent angles of attack, varying from 0° to 90°, for Rossby (R_o) numbers varying from 2.9 to ∞ (Lentink & Dickinson, 2009b).

CHAPTER 2

EXPERIMENTAL SYSTEMS AND TECHNIQUES

In this chapter, the experimental system and visualization techniques used in this research are described in detail. The water channel where experiments were performed is discussed in section 2.1. The kinematics of motion and motion control mechanisms are described in section 2.2. This section includes descriptions of both the apparatus for the purely rotating wing and the apparatus for the wing undergoing combined pitch-up and rotation. Additionally, the quantitative flow visualization technique, known as particle image velocimetry (PIV), is discussed in 2.3. Finally, an error analysis of the PIV techniques used in this dissertation is included in section 2.4.

2.1 WATER CHANNEL SYSTEM

Experiments were performed in a custom designed, large-scale, free surface, low turbulence water channel in the Fluid Mechanics Laboratory at Lehigh University. A schematic of the water channel was shown in Figure 2.1. The main test section has overall length of 4877 mm, a width of 927 mm, and a depth of 610 mm. An arrangement of honeycombs and screens downstream of the reservoir and upstream of a 2:1 contraction maintains the turbulence intensity below 0.5%. The walls of the test section are comprised of optically transparent Plexiglas, allowing for quantitative imaging techniques. Using the pump control unit, linear variation of the free-stream velocity in the test section was achieved by variation of the axial flow pump RPM. Using PIV experiments, a calibration curve of flow speed vs. pump RPM was made. Figure 2.2 shows a calibration of channel flow speed vs. pump RPM, at a water temperature of 23 C.

2.2 KINEMATICS AND MOTION CONTROL

2.2.1 Kinematics and Wing Planforms

The experiments discussed herein involve linear position ramp motions for a rotating and pitching wing. The details of the prescribed kinematics in terms of rotation rate or pitch rate can be found within Chapters 3, 4 and 5. Figure 2.3 displays a typical ramp motion for pure rotation (Φ) and combined pitch-up and rotation (Φ and α). Indicated in this diagram are slight smoothing of the ramp at the initiation and cessation of each maneuver. The smoothing, prescribed by Eldredge *et. al.* (2009), limited the effects of transient vibrations in the experimental apparatuses during the acceleration period. For most experiments, this type of smoothing was employed; however, for the pitching motions in Chapter 5, simple linear acceleration was used due to the rapid ramp rate.

A rectangular wing model of transparent acrylic was used in each of the experiments. The ratio of the span (b) to the chord (C) of the wing, i.e., aspect ratio $AR = b/C$, for each wing was $AR = 2$. The specific dimensions of each wing can be found in chapters 3, 4, and 5.

2.2.2 Pure Rotation in Presence of Freestream

In order to provide the different types of motion described in the previous section, an in-house control mechanism was designed. For experiments pertaining to pure rotation with an incident freestream, the apparatus shown in Figure 2.4 was used. This motion system was designed and constructed by Cem Ozen; a description can be found in his doctoral dissertation (Ozen, 2013). This apparatus used a system of pulleys, belts,

and computer controlled stepper motors to provide rotational motion to a wing at a fixed angle of attack.

The wing in Figure 2.4 was held in position by a horizontal support rod with a rounded tip. The horizontal support rod was also the axis of rotation for the wing, and it was oriented parallel to the freestream direction. The rod was vertically located at the mid-depth location of the water channel. In this orientation, the wing was exposed to the unobstructed incident freestream throughout 360° of rotation. Before each experiment, the angle of attack of the wing was manually adjusted via set screws at the union of the wing root and the horizontal support. Motion was transferred from the high resolution stepper motor to the horizontal support rod via a system of belts and pulleys. To eliminate effects due to vibration in the mechanical system, a solid brass damper was attached to the end of the stepper motor. The entire rotating wing assembly was attached to a linear traverse, allowing for cross-stream positioning of the wing.

2.2.3 Combined Pitch-Up and Rotation Apparatus

In order to explore more complicated motions, specifically combinations of pitching and rotation, a second original apparatus was designed and constructed in-house. In Figure 2.5 a schematic of the combined rotation and pitching system was displayed.

The rectangular wing model, shown in Figure 2.5, was connected to a brass rod that passes through a bronze, cylindrical housing. The bronze housing was constructed from bearing bronze, which contains embedded graphite, therefore the housing acts as a bushing for the brass rod. Inside the bronze housing, a small stainless steel sprocket attaches to the pitching rod. A stainless steel chain connects this sprocket to a matching

sprocket at the top of the apparatus; the chain was contained within a hollow brass pipe. The top sprocket connects to a rod, which was supported by a bearing pillow block. On the other side of the pillow block, a set of pulleys and belts connects the pitching system to a high-resolution stepper motor. By rotating the motor, the pulleys and belt rotate the sprocket and chain system, which changes the angle of attack of the wing. To achieve simultaneous rotation and pitching, the entire pitching system was mounted on a rotation stage. This rotation stage was driven by another stepper motor, allowing for 360° of rotation of the wing while it was simultaneously pitched by the aforementioned drive system.

Each stepper motor was driven by micro stepper drivers, which were controlled through LabView software. Encoders attached to the stepper motors record the motor position. When the encoder recorded the stepper motor position ±2 steps from the prescribed motion profile, an error message was displayed. Additionally, the mechanical lag in the components for this apparatus was estimated to be 1° and 2° respectively for the pitching and rotation motions.

2.2.4 Motion Control Components

Figures 2.6 and 2.7 indicate the motion control components, as well as the orientation of each experimental apparatus in the water channel. Also displayed are the quantitative imaging components, which are described in section 2.3. For both experimental rigs, the control system includes National Instruments P70530 micro-stepper drives, a National Instruments PCI-7344 4-card, and a UMI-7764 indexer box. The motion for each experiment was created individually and exported to LabVIEW

Motion Assistant. This software generates the discrete motion profiles, which were then sent to the indexer. The indexer converts the profiles to electric signals, which were sent to the micro-stepper driver and subsequently the stepper motors. The encoders on the stepper motor record the position of the stepper motor and compare the actual position of the stepper motor to the prescribed motion profile.

2.3 QUANTITATIVE IMAGING TECHNIQUES

2.3.1 Stereo Particle Image Velocimetry

Particle image velocimetry (PIV) was a quantitative flow visualization technique used to determine the vector velocity field of a particular flow by measuring the displacement of fine particles, in order to track the motion of the fluid. An extensive overview of this measurement technique was compiled in Adrian & Westerweel (2010). The technique involves illumination of a plane of interest with two short bursts of laser light. The particles illuminated in each laser pulse were captured by a CCD camera system which stores each image in separate frames. The image pairs were then analyzed using software that divides each image into a grid of points, which are referred to as interrogation points. A correlation algorithm then determines the effective displacement of particles within a defined window around each interrogation point. The computer program divides the effective displacement by the time delay between laser pulses and determines a two dimensional (in-plane) velocity vector at each interrogation point. Stereoscopic particle image velocimetry (SPIV) was a technique involving a combination of two overlapping velocity vector fields, thereby resolving the out of plane velocity

component. This technique provides an instantaneous three-dimensional velocity fields on a two-dimensional plane.

In order to determine the velocity field using the SPIV method, calibration of a known grid must be performed. The calibration process involves placing a target in the field of view with a 10 mm *x-y* grid pattern. Additionally, 50% of the grid points are allocated on a second milled surface, which was 1 mm deep. The target was carefully aligned with the laser sheet so that both planes are evenly illuminated. Once the target was in place, the dots imaged by each camera must be brought into focus. For the camera perpendicular to the laser plane, the focus ring was adjusted so that all of the dots were focused across the field of view. For the offset camera, distortions across the field of view must be accounted for. Aligning the object, lens, and image planes so that they intersect at a point (Figure 2.8) accounts for these distortions, and this geometric configuration was known as the Scheimpflug condition. When this condition was met, the image seen by the offset camera will be focused across the image plane; however, the magnification of the image particles will vary across this plane. Using special cameras that allow adjustment of the image and lens plane, this condition can be satisfied. After obtaining focused images from each camera, a calibration algorithm in Insight 3G, which was a commercial computer program developed for PIV, determines the mapping functions required to map each camera view onto one combined grid.

2.3.2 SPIV system of Components

Quantitative imaging via angular displacement stereo particle image velocimetry (SPIV) was used to determine the three-dimensional velocity field. Figures 2.6 and 2.7

display schematics of the SPIV arrangement for each experimental appartatus. In order to employ SPIV, the water was seeded with 12 μm hollow metallic coated plastic spheres, providing 15-20 particle images in the interrogation window; the window size was 32 x 32 pixels. A 1 mm thick laser sheet was produced by a dual-pulsed Litron Nano-L Nd-YAG laser, which operated between 30-40 mJ with a frequency 14.29 Hz. The laser plane was oriented in the streamwise direction of the water channel. This was achieved through a series of cylindrical and spherical lenses and a prism, which were located at the laser head exit.

Images were acquired with TSI PowerView 2 megapixel cameras having CCD arrays of 1600 by 1200 pixels. Figures 2.9 and 2.10 provide a plan view of the SPIV arrangement for each apparatus. The angular displacement camera arrangement has one camera viewing the side of the laser plane straight on, while the other camera was displaced at an offset angle of θ = 45°. The offset camera also views the laser sheet through a liquid prism, located on the exterior of the vertical side of the water channel, in order to reduce the refractive distortions between air and water. Images were acquired at 14.29 Hz in order to match the laser repetition rate. The chordwise magnifications and total number of vectors in the field of view depend on the particular experiment. These values are indicated in each respective chapter detailing experimental results. TSI Insight 3G software was used to acquire and process the images. Further details of the vector processing and volume reconstruction can be found in the next section.

2.3.3 Processing and Post-Processing of Vector Field

A detailed pipeline of the vector processing procedure was shown in Figure 2.11. At the top of Figure 2.11, pairs of images from Camera 1 and Camera 2 are shown**.** Each camera acquires two images, corresponding to each laser pulse. These images are known as Frame A and Frame B, and the time delay between them was set to satisfy particle displacement guidelines specified in Adrian and Westerweel (2011). Each image passes through a frame to frame correlation function to determine the most probable displacement of particles within each interrogation spot. In Figure 2.11 a magnified view of one interrogation window shows the particles in Frames A and B at one interrogation point location. The most probable correlation was determined for each interrogation window, and a vector was drawn at each grid location. In these investigations, interrogation windows were 32x32 pixels. The resulting vector field for each camera displays a two-dimensional velocity field. The two-dimensional vectors created in each image plane were mapped to the combined object plane using the calibration information, in order to obtain the three-dimensional velocity data.

Post-processing of the vector data involves vector validation and smoothing of the vectors in the field of view. Vectors were validated by determining the difference between the vectors and a local median of neighborhood vectors and removing vectors outside the specified tolerance. For the experiments performed herein, the neighborhood size was set to 3x3 grid points and a velocity tolerance of 2 pixels was specified. The deleted vectors were then replaced by a vector replacement procedure. The holes were filled with the local mean value of the neighborhood vectors. The algorithm first fills the holes with the most valid neighbors and continues in a recursive manner until all the holes were filled. Finally, smoothing between the vector locations was performed using a

Gaussian–weighted mean of neighborhood vectors. This process removes any noise associated with the grid spacing of velocity vectors.

The experiments presented herein involve flow structures that are of short duration, and therefore time-averaging was not possible. However, phase-averaging was possible by using the motion profile of the wing as a reference. Referring to Figure 2.12, image acquisition occurs when the wing chord and the laser sheet are parallel. The initial position of the wing was set at a desired rotation angle Φ. After the first run, the initial position of the wing was reset, and the experiment was performed again. The velocity fields generated from successive runs can then be averaged together to create a phase averaged velocity field. The number of averages needed, and the effect that averaging has on the velocity field, will be addressed in more detail in the error analysis section.

2.3.4 Volume reconstruction

Experiments were often performed at one spanwise location along the wing. Single plane imaging was useful for establishing trends and rapidly performing multiple experiments with a variety of parameters. However, flows over unsteady maneuvering wings are highly three-dimensional. Therefore, imaging of the entire flow structure across the span of the wing was necessary. To achieve this, the entire wing apparatus was translated in the z-direction so that the wing intersects the laser plane at different locations along the span of the wing. In Figure 2.13, three laser sheet positions are shown, representing different wing locations with respect to the laser sheet location. The optimal spacing $\Delta r/b$ between the planes was set to be small enough to resolve all of the

structures across the span as well as in the wake of the wing. An example of a fully re-constructed structure with 50 planes was shown at the bottom of Figure 13.

2.4 ERROR ANALYSIS

2.4.1 Random Error

Errors associated with particle image velocimetry involve bias error, random error, and non-repeatability of the flow. Manifestation of these types of errors in velocity data obtained from the SPIV arrangement used for this research, as well as strategies for the minimization of errors, are discussed herein. The detailed overview of particle velocimetry techniques provided by Adrian and Westerweel (2009) serves as the main reference for the following discussion.

Instantaneous velocities obtained from PIV can be influenced by random errors that effect the magnitude and direction of velocity vectors on the grid. One source of this error comes from random fluctuations in the light sheet intensity. These fluctuations effect the correlation algorithm and calculation of velocity vectors on the grid. Another source of random error arises from inaccurate location of the centroid location of particles in the PIV image. By not locating the center of the particle, the displacement calculated by the correlation will be slightly inaccurate. Provided in Figure 2.14 is a particle with image diameter d_τ at two instants of time. The error in locating the center of the particle is then approximated by $c_\tau\, d_\tau$.

Adrian & Westerweel (2009) indicate that the constant c_τ depends on the ability of the procedure to determine the displacement of the particle. That is, the choice of

interrogation method, peak location technique, and irregularity of particle images (Prasad et al. 1992) determines c_τ. For experimental parameters similar to the present SPIV arrangement, Adrian and Westerweel estimate c_τ to be between 0.05 and 0.07. The RMS random error can then be calculated from:

$$\sigma_{\Delta X} = c_\tau \, d_\tau.$$

Where, d_τ = particle image diameter = $M_o[1.5\delta_z\lambda + {d_p}^2]^{1/2}$, δ_Z = depth of field = $4(1+\frac{1}{M_0})^2 {f^\#}^2 \lambda$, d_r = pixel pitch (our cameras 7.4 μm/pixel), d_p = particle diameter (~11-12 μm), and c_τ = centroid constant. To calculate the RMS random displacement error with the above equations, the diameter d_τ of the particle in the image plane must be determined. This involves knowledge of the image magnification M_O, depth of field δ_Z, laser light wavelength symbol, physical particle diameter d_p, the f-number or $f^\#$ of the camera, and centroid constant c_τ.

The RMS velocity error is given by $\sigma_{\Delta V} = \sigma_{\Delta X} / (M_O \Delta t)$, where Δt represents the time delay between image captures and M_o is the magnification or pixel size. The RMS velocity error can then be compared to a characteristic velocity of the flow, e.g., the tangential velocity V_{rg} of the wing at the radius of gyration. The details for each specific error calculation are found in subsequent chapters. In general, however, the RMS random

velocity error for in-plane velocity components was estimated to be 4-5% of V_{rg} or freestream velocity *U*.

2.4.2 Bias Error

Bias error in PIV data represents a fixed shift in velocity measurements due to the spatial separation of sampling of velocity. In other words, the grid spacing of interrogation windows can bias a velocity vector direction and magnitude. Bias error becomes important when the pixel size is much larger than the particle image diameter. Therefore the ratio of particle image diameter to pixel pitch of the camera d_τ/d_r is an important parameter when considering bias error. Figure 2.15 provides a plot of the random and bias error vs. d_τ/d_r for c_τ = 0.05 and 0.07. This figure provided by Adrian & Westerweel (1992) indicates that the random and bias errors are minimized when d_τ/d_r = 2.

Estimation of the bias error in terms a percentage of a characteristic velocity is given in Figure 2.16. It shows the bias displacement error symbol as a function of fractional particle displacement $\Delta X/d_r$ for three cases of d_τ/d_r and three methods of subpixel correlation functions. For example, for experiments presented in this dissertation, d_τ/d_r was approximately 1.6. Consulting Figure 2.16 and the Gaussian fit line, the subpixel displacement bias error is approximately 5% of V_{rg}.

2.4.3 Out of Plane Velocity Error

The error in velocity vectors discussed in sections 2.4.1 and 2.4.2, pertain to in-plane displacement measurements. Errors in the out of plane displacements, arising from a SPIV arrangement, must also be accounted for. Exploring the influence of camera arrangement on the out of plane random displacement error, Lawson and Wu (1997) proposed the following ratio of out of plane and in-plane RMS displacement errors, $\sigma_{\Delta Z}/\sigma_{\Delta X} = \tan(\alpha)^{-1}$. In this equation, α is the stereo half angle, or the physical angular separation of the stereo cameras, which is 22.5° for our SPIV setup. Figure 2.17 shows a plot of error ratio as a function of stereo half angle. For $\alpha = 22.5°$, the error ratio ($\sigma_{\Delta Z}/\sigma_{\Delta X}$) is approximately 2.7. Since in-plane error ($\sigma_{\Delta X}$) is calculated in section 2.4.2, the out of plane random displacement error ($\sigma_{\Delta Z}$) can be calculated relative to the determined in-plane error.

2.4.4 Phase Averaging Error Reduction

The error analysis mentioned in the previous section calculates bias and random errors based on theoretical analysis of PIV techniques and geometry for instantaneous results. Another way to reduce error is to employ phase-averaging. Phase averaging successively reduces the magnitude of random error in the velocity grid. However, bias error will not be minimized with phase averaging. Additionally, when looking at the grid of instantaneous velocities, the error due to small non-repeatability of the flow structure is also present. This uncertainty is not distinguishable from the random error in PIV data. However, phase averaging decreases both the error due to the non-repeatability of flow and the random error.

To measure the reduction of error with phase averaging, an experiment was performed where 208 instantaneous SPIV images were acquired on a rotating wing at 45° angle of attack. The images, captured at the midspan and at 120° of rotation after the onset of motion, visualize a fully evolved leading-edge vortex. The images were then phased averaged successively, such that the final velocity grid was the average of 208 realizations. Assuming that the error at 208 phase-averages is sufficiently minimized, an error map for each average can be created by subtracting each averaged velocity field with the 208 averaged grid. The RMS of the error map can then be calculated, which provides the reduction of random error in the image as the number of averages increases. Therefore, RMS velocity was calculated by taking the RMS of ((Velocity(i)-Velocity(208)) for i = 1 to 208, where i is the number of averages. Figure 2.18 provides the RMS calculation for each component of velocity and spanwise vorticity; each of these parameters is plotted (on the vertical axis of the plot) against the number of averages, on the horizontal axis. The velocities are normalized with V_{rg}. Looking at six averages, the RMS error is approximately 5%to 6% of normalized subscript? V_{rg} (V_{rg} = 1). Additionally, the RMS vorticity is plotted in Figure 2.18; it is scaled with a characteristic non-dimensional value of vorticity 10, which was often near the peak vorticity value measured in the present experiments. Therefore, the RMS values for vorticity are a percentage of this characteristic vorticity, and, at six averages, the RMS error is approximately 5%.

For most of the volumetric images presented in subsequent sections, the number of phase averages was six. It is then worth exploring the RMS error among groups of six averages from the data set of 208 instantaneous images. Each set of six averages contains

non-successive instantaneous images. Using the same RMS error calculation as for Figure 2.18, each group of six averages was compared to the averaged field of 208 images. The results for *x*, *y*, and *z* components of velocity and spanwise vorticity are provide in Figure 2.19. Each location on the horizontal axis represents a grouping of six averaged instantaneous images (32 groups in total), and the vertical axis represents the RMS error. Figure 2.19 indicates that there is some variation in the RMS magnitude for groups of six averages; this variation is, however, between 1 and 2%.

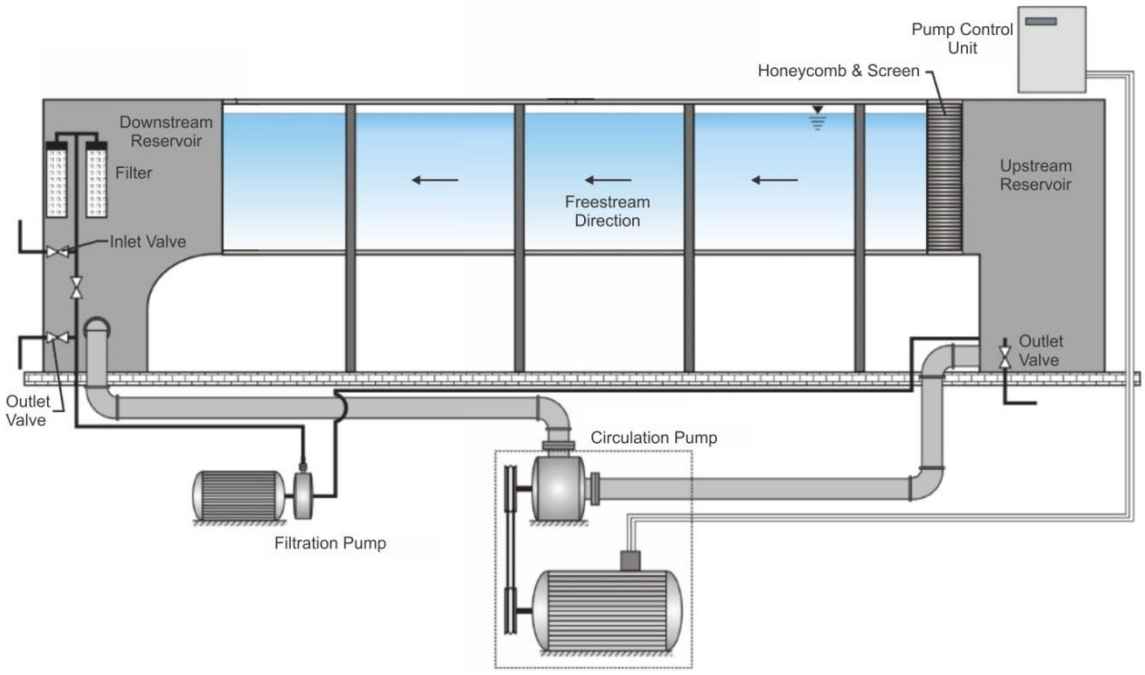

Figure 2.1: Water channel system.

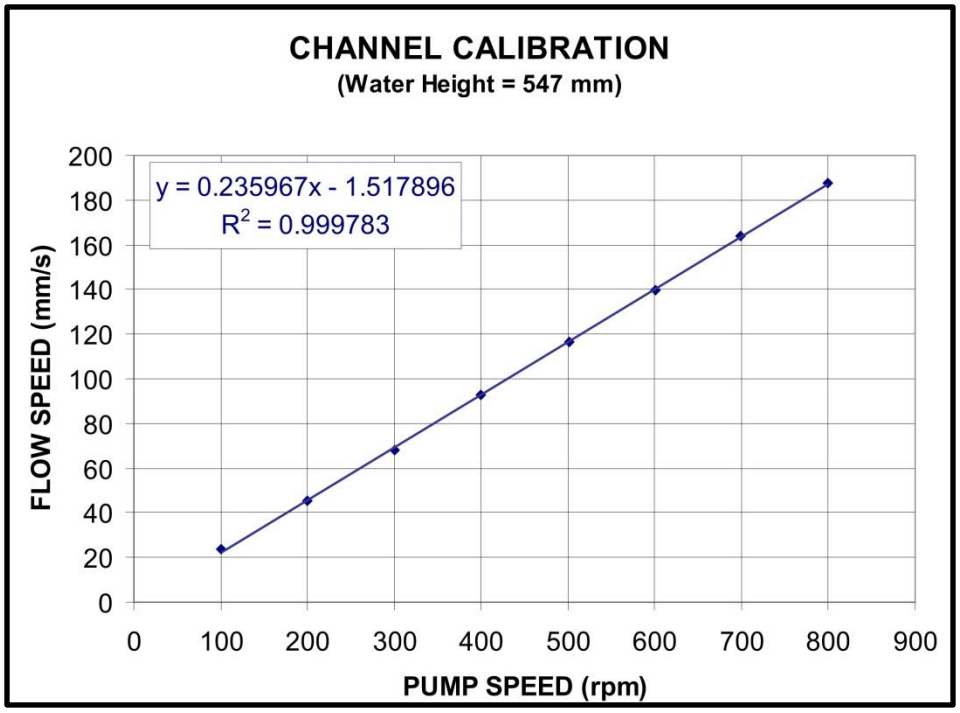

Figure 2.2: Water channel calibration.

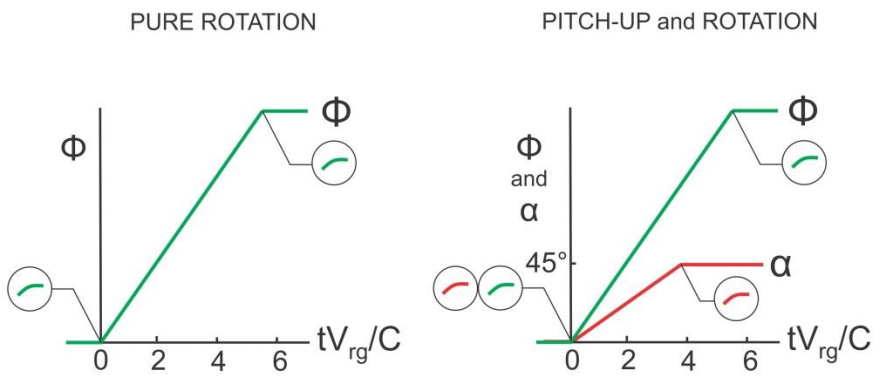

Figure 2.3: Typical kinematics of wing motion for purely rotating and combined pitch-up and rotation.

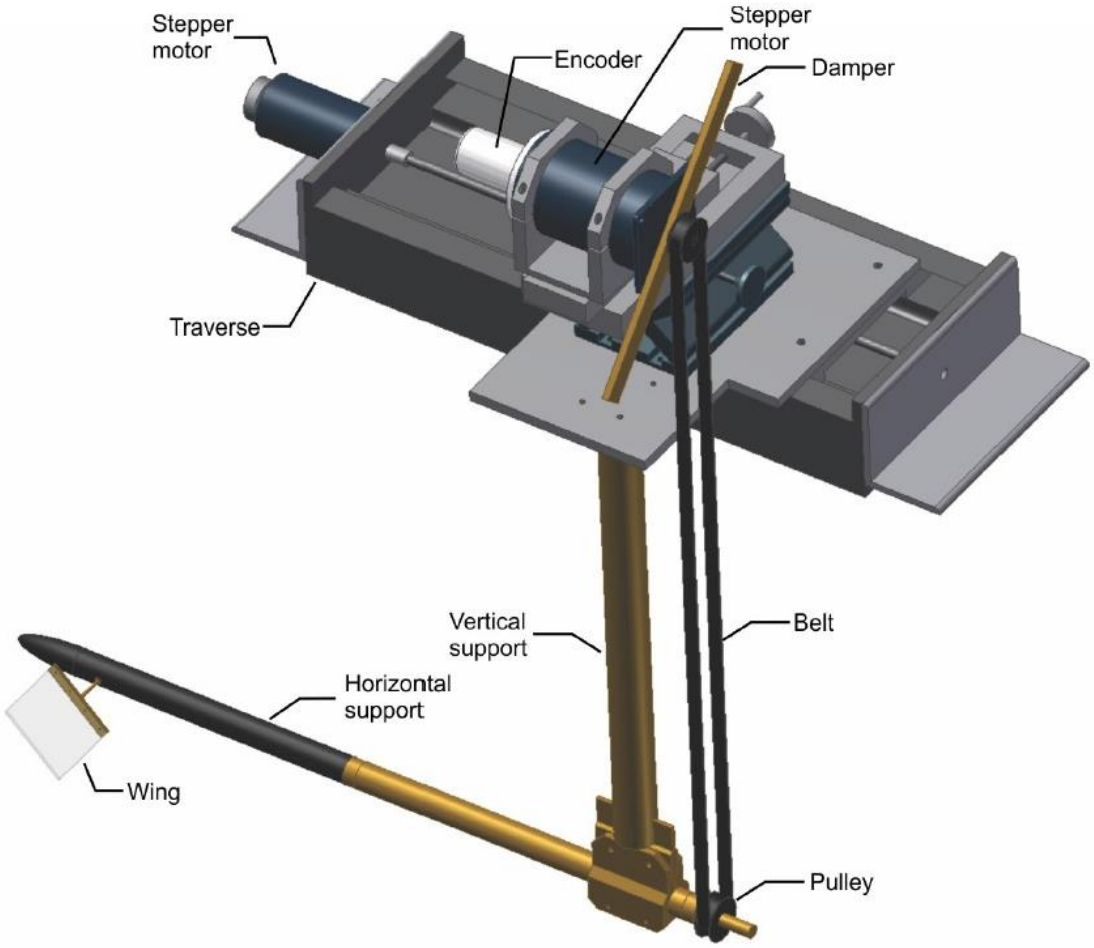

Figure 2.4: Apparatus for pure rotation of wing (Ozen (2013))

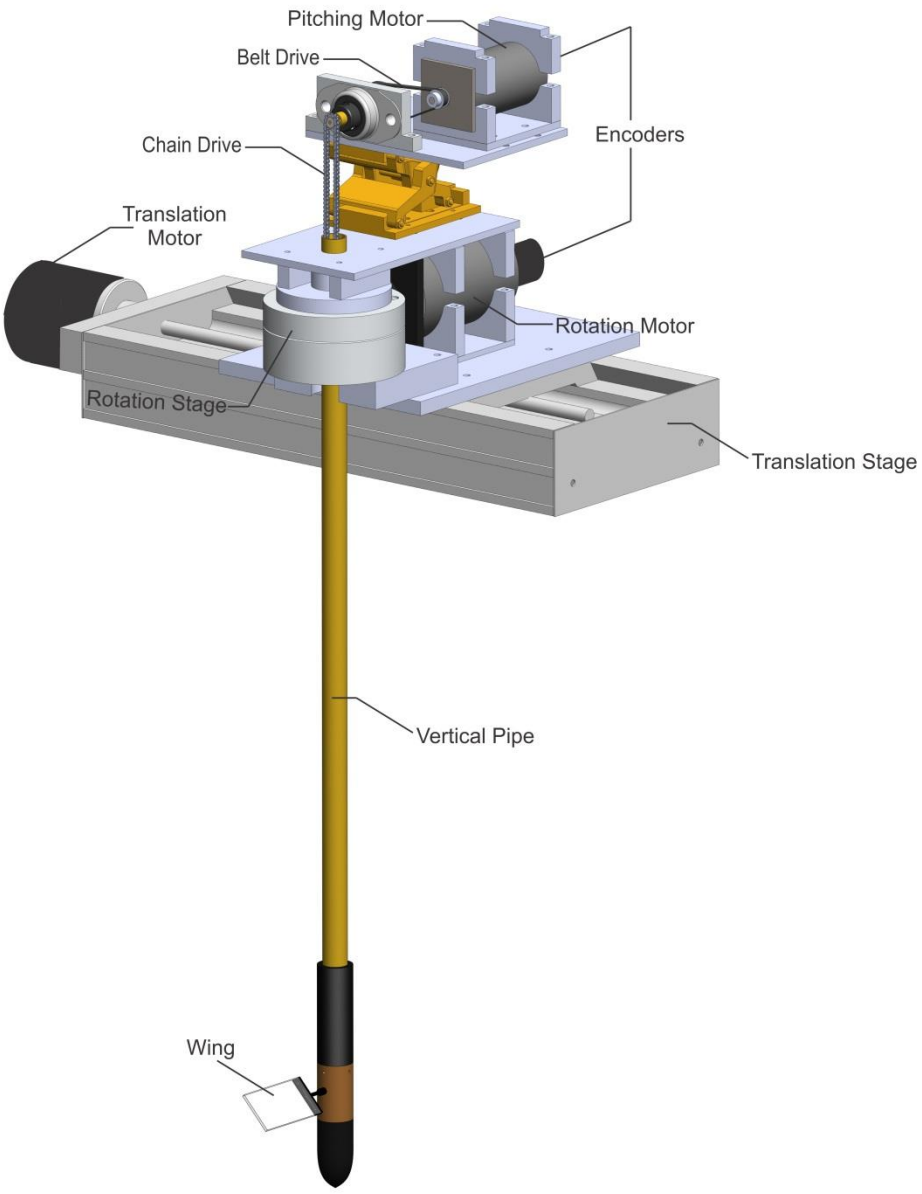

Figure 2.5: Apparatus for combined pitch-up and rotation of wing.

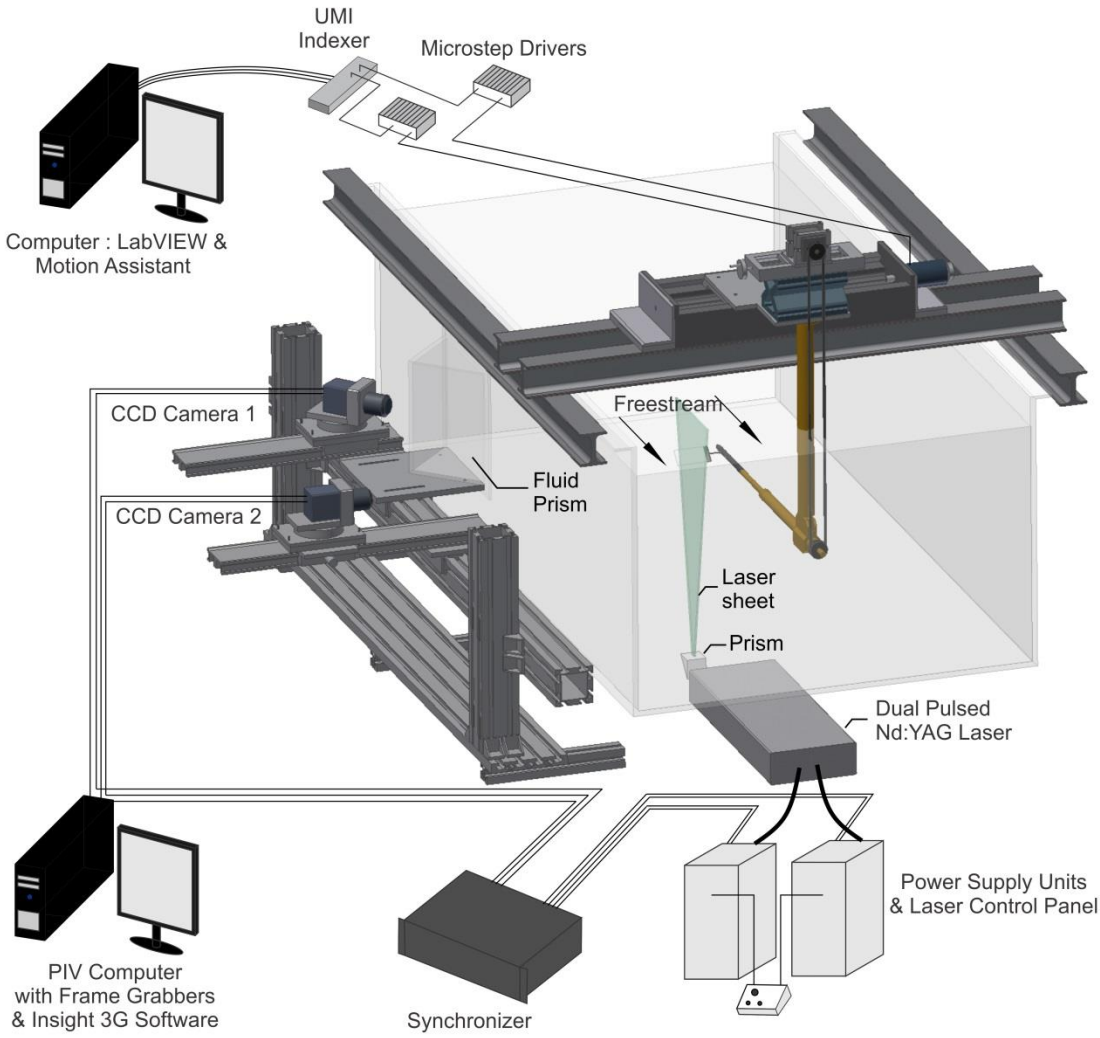

Figure 2.6: Motion control and SPIV setup for pure rotation of wing with incident freestream.

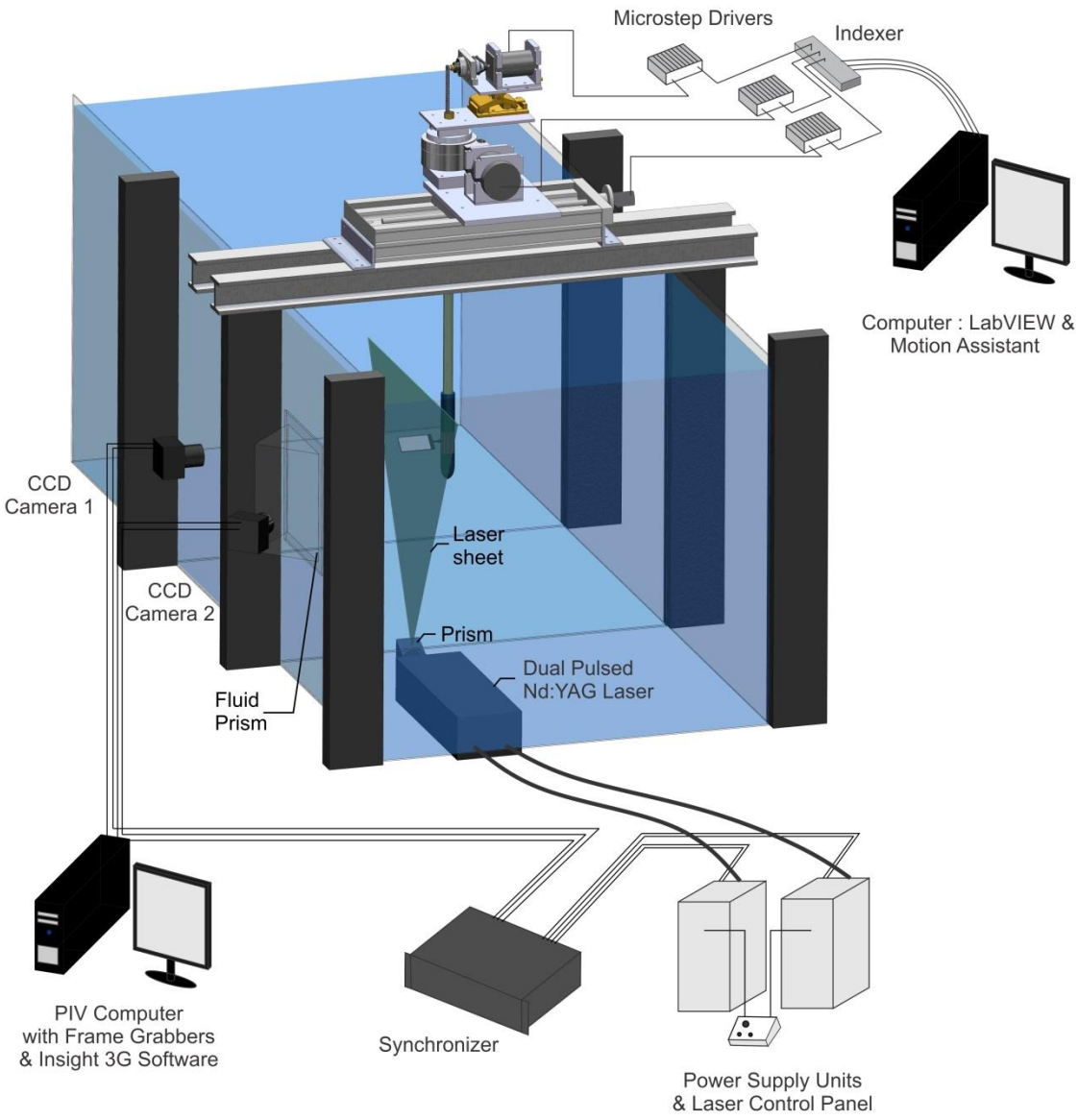

Figure 2.7: Motion control and SPIV setup for combined pitch up and rotation.

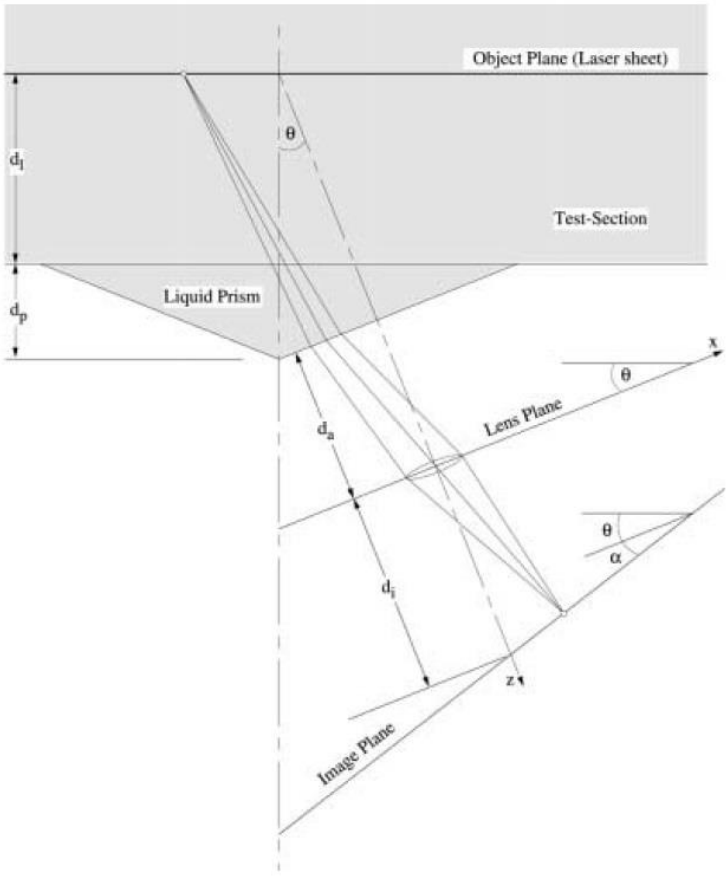

Figure 2.8: Scheimpflug condition (Prasad & Jenson (1995))

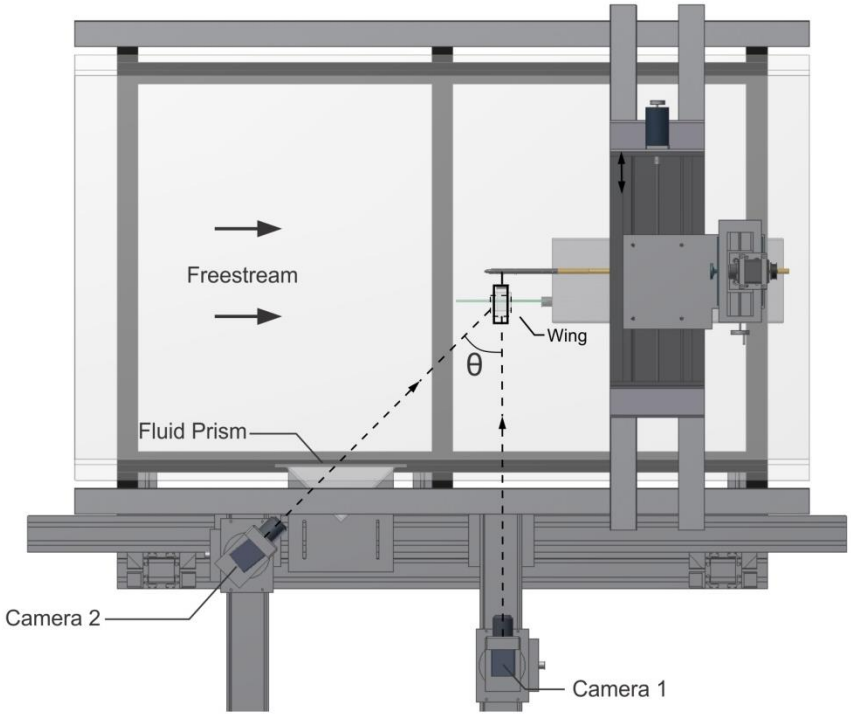

Figure 2.9: SPIV arrangement for pure rotation with incident freestream.

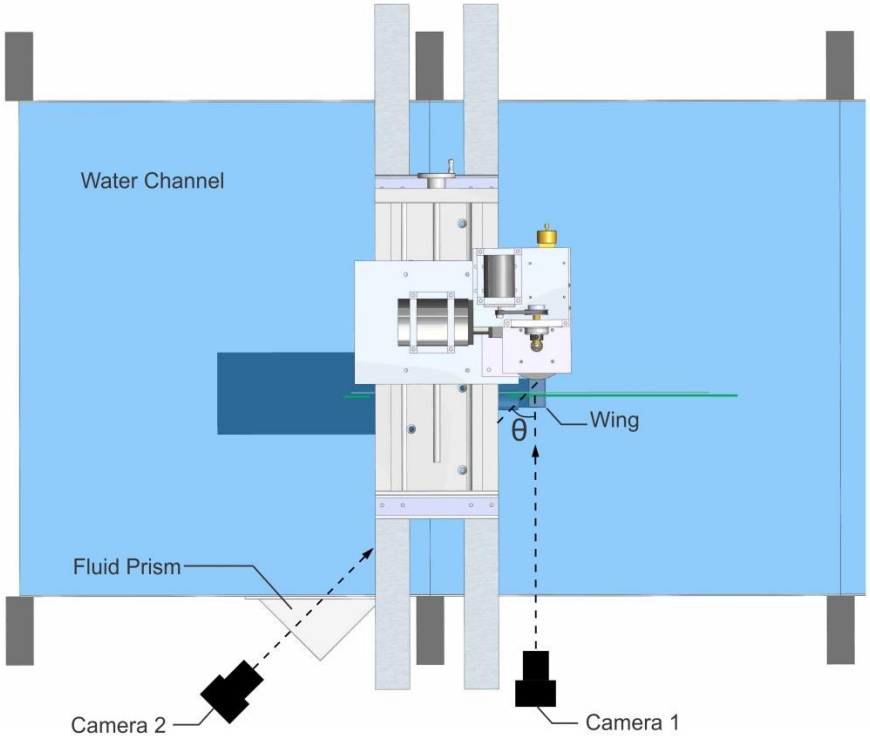

Figure 2.10: SPIV arrangement for combined pitching and rotating apparatus.

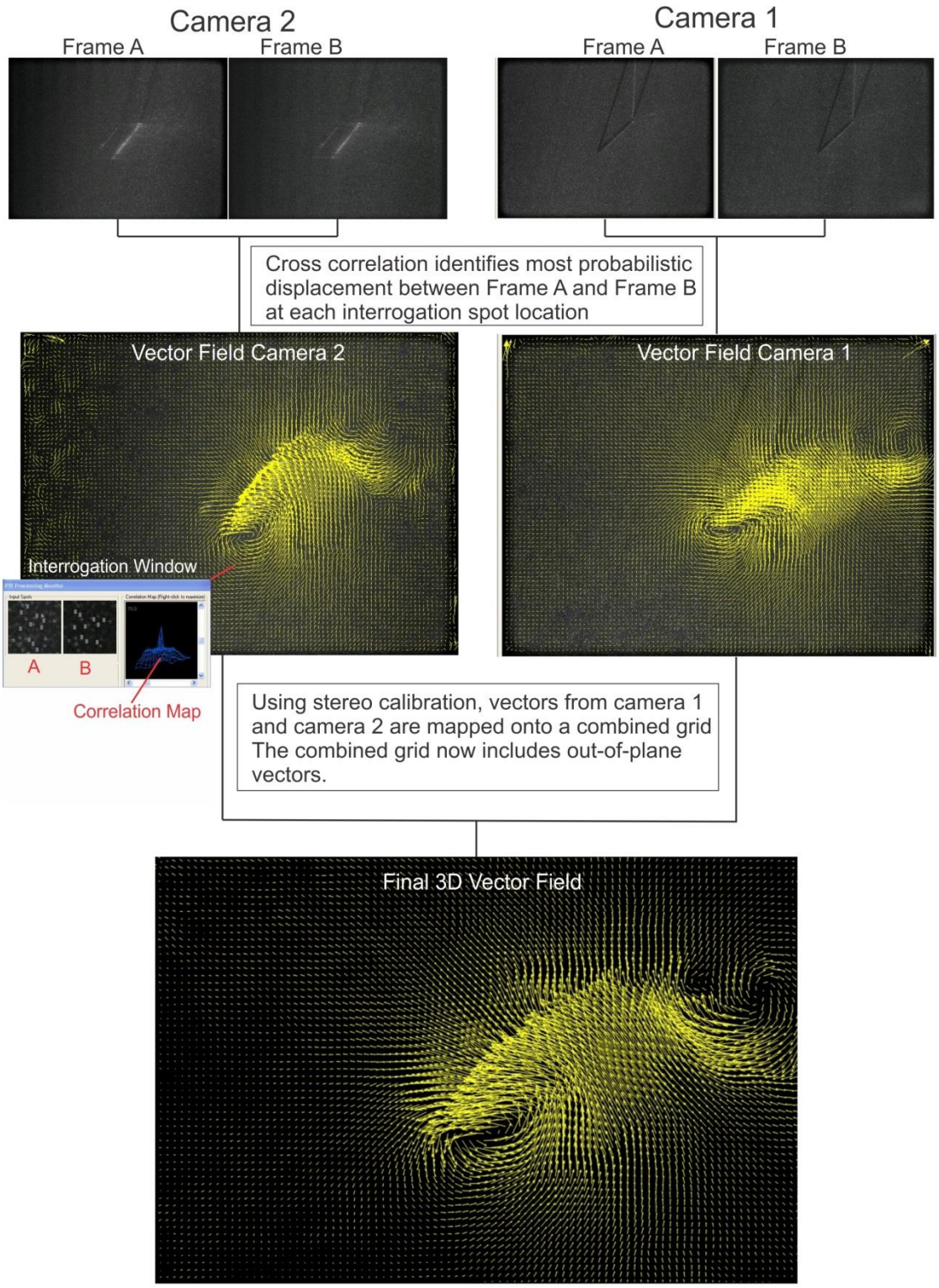

Figure 2.11: Vector conditioning process in Insight 3G.

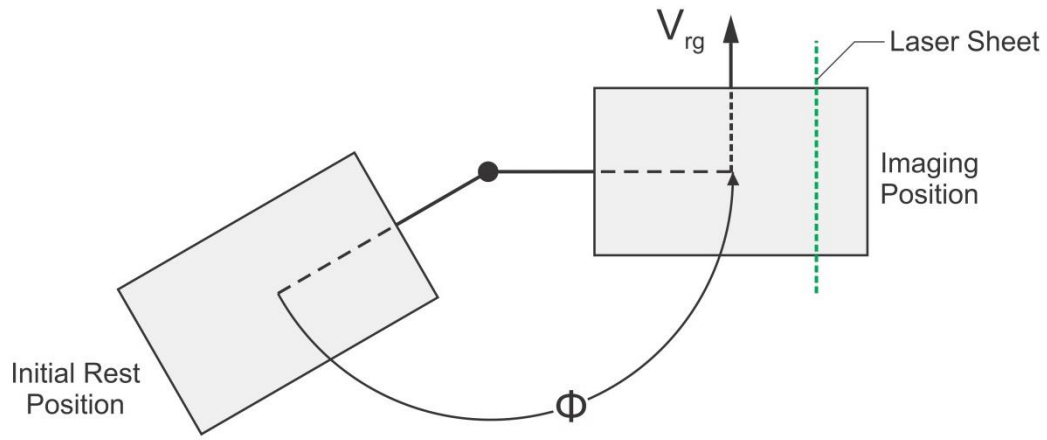

Figure 2.12: Illustration of phase averaging concept.

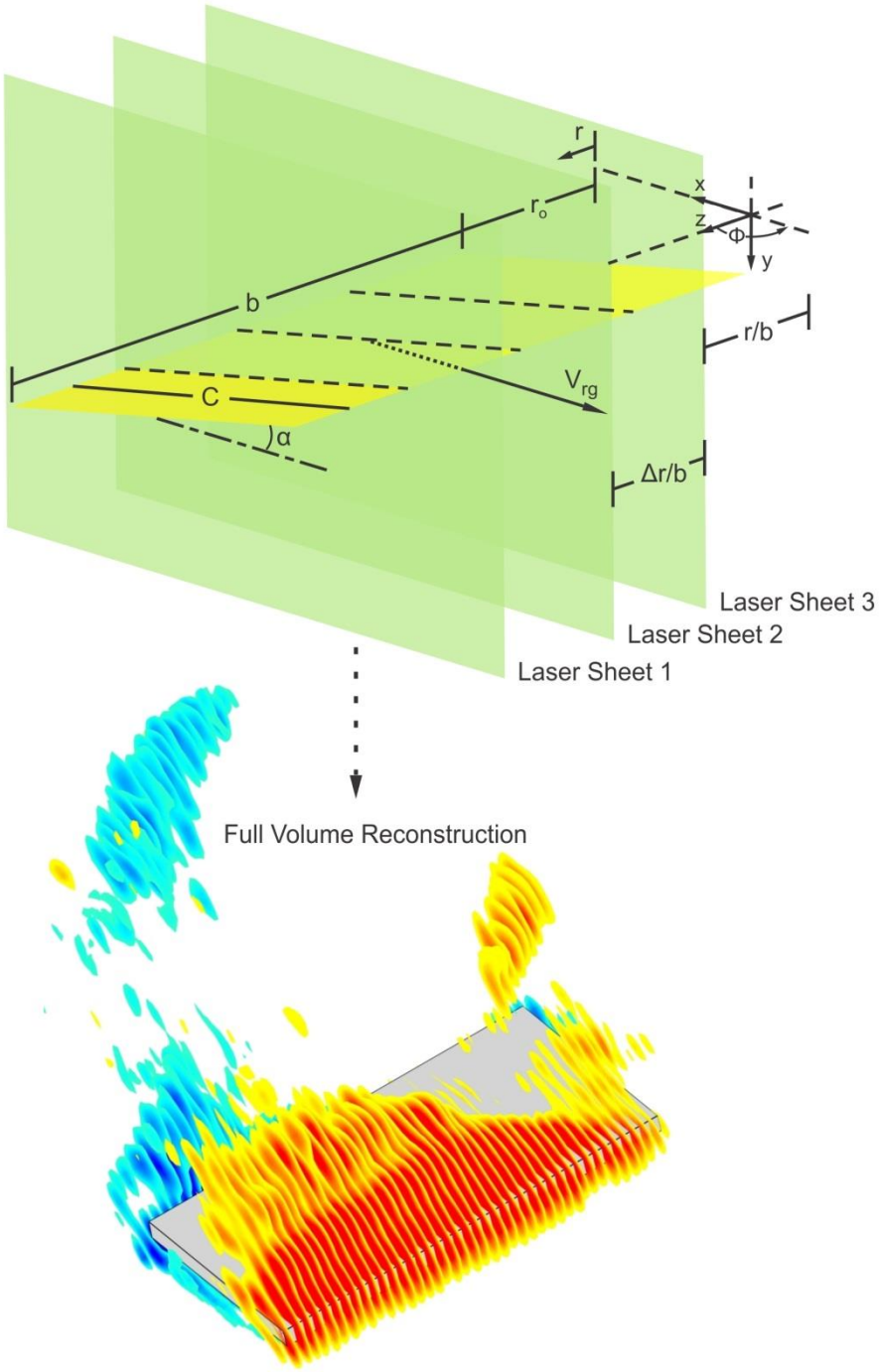

Figure 2.13: Volume reconstruction technique.

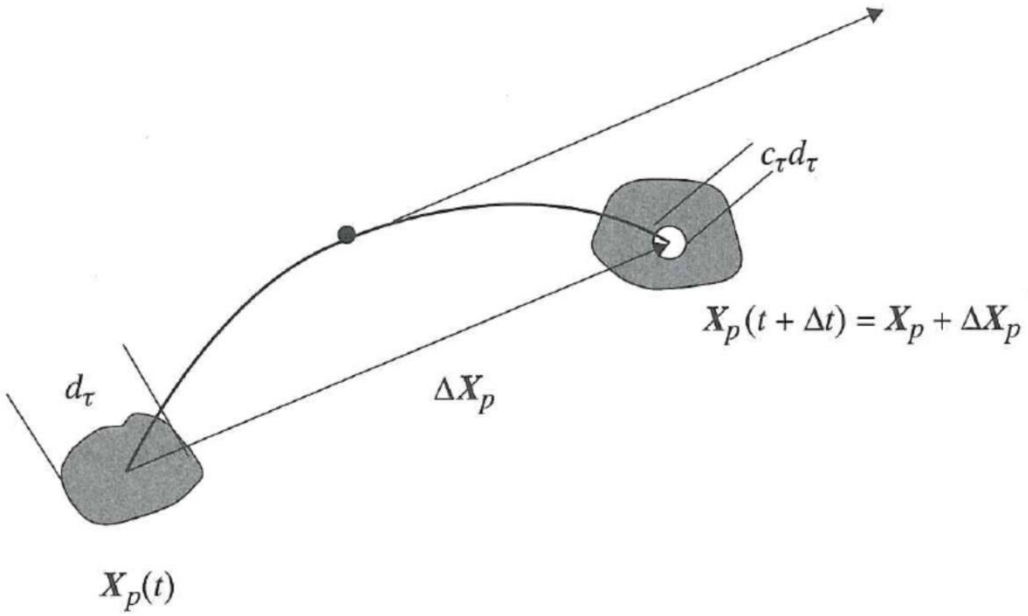

Figure 2.14: Particle image location and associated error in image diameter subscript c_τ d_τ. (Adrain & Westerweel (2009))

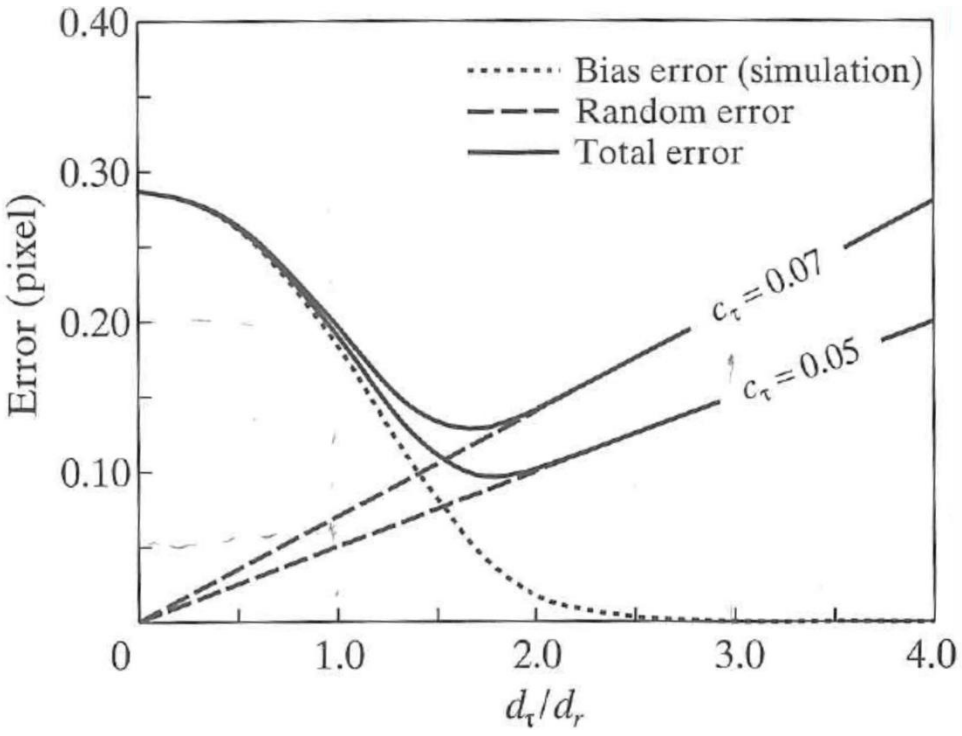

Figure 2.15: Error reduction as function of d_τ/d_r. (Prasad et al. 1992).

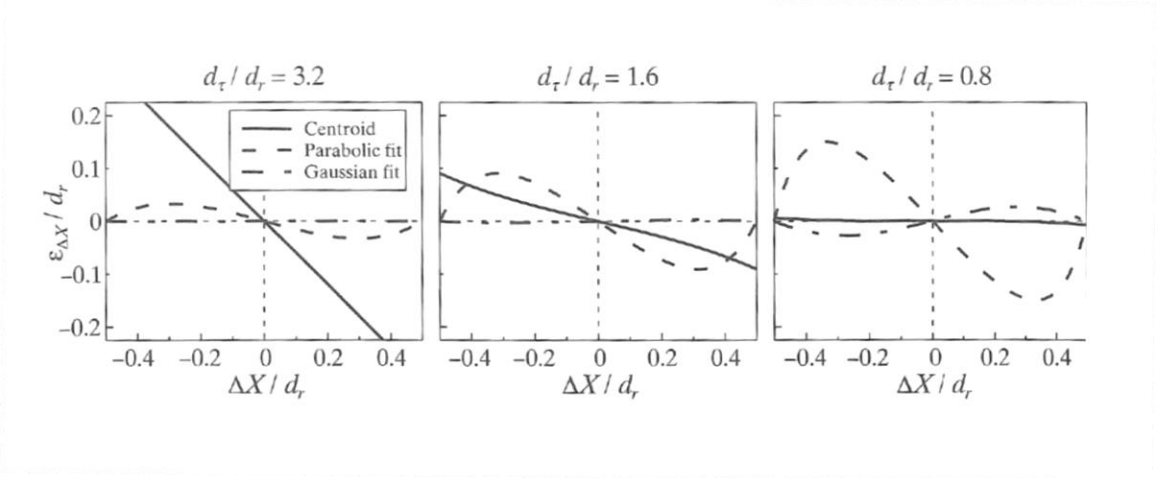

Figure 2.16: Bias error estimation for subpixel displacement. (Adrian & Westerweel 2009).

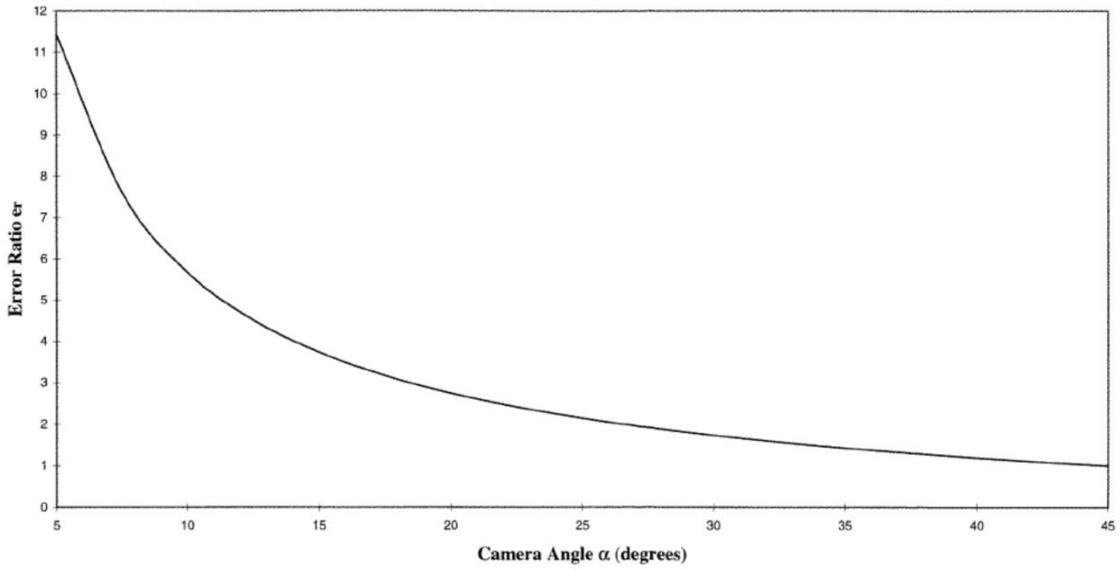

Figure 2.17: Error ratio as function of stereo half angle α . (Lawson & Wu (1997)).

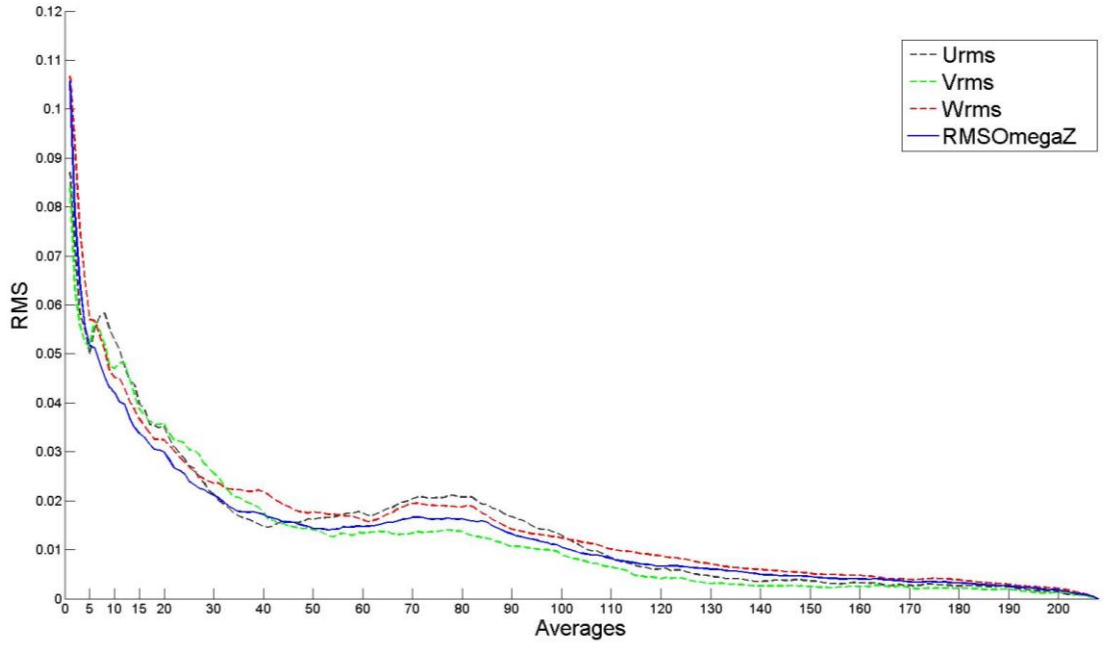

Figure 2.18: RMS vorticity and velocity for instantaneous to 208 phased averaged images.

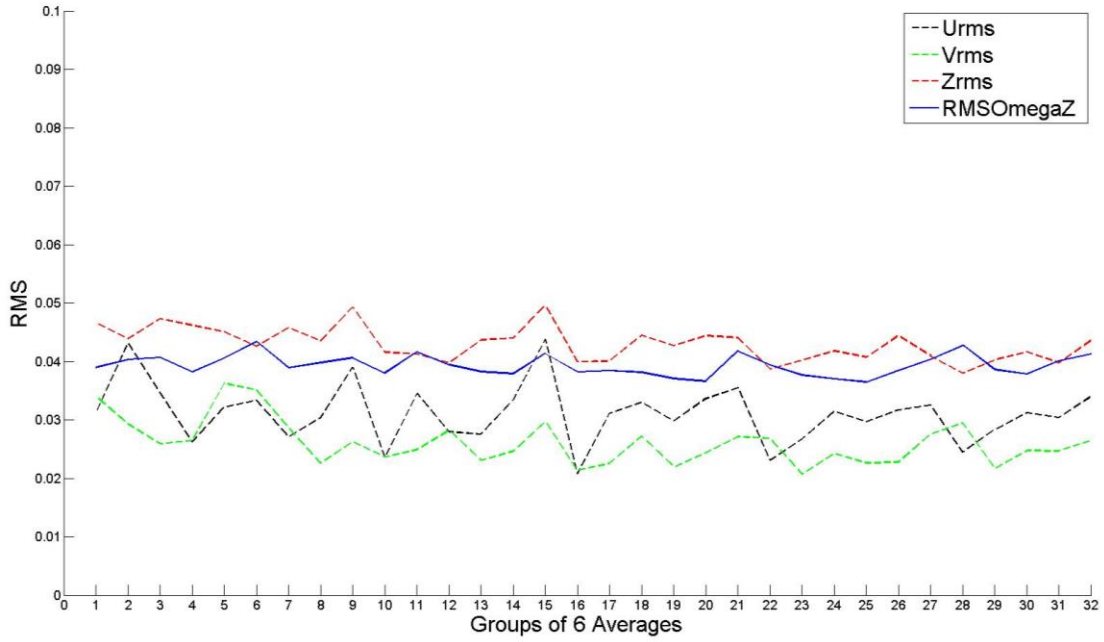

Figure 2.19: RMS vorticity and velocity for groups of six phased averaged images.

CHAPTER 3

FLOW STRUCTURE ON A ROTATING WING: EFFECT OF STEADY INCIDENT FLOW

3.1 BACKGROUND

In recent years, there has been major interest in the flow structure and loading on wings undergoing various unsteady maneuvers. The motivation for understanding biologically inspired flight at low Reynolds number comes from interest in small unmanned air vehicles. Flapping wings of insects and birds are characterized by large amplitude motions including rotation, pitching, and plunging. In contrast, to the case of a wing rotating in quiescent fluid, very little attention has been devoted to the flow structure along a low aspect ratio wing rotating in an incident steady flow, whereby the direction of flow is along the axis of rotation. This configuration corresponds to a 90° stroke plane; it is representative of fast forward and climbing flight (Lentink & Dickinson, 2009a). The advance ratios investigated herein were determined by using incident mean flow velocities consistent with the forward flight velocities used by Dickson & Dickinson (2004) and Harbig et al. (2014). This investigation employs quantitative imaging to characterize the effect of advance ratio J on the development of the flow structure along, and in the wake of, a rotating wing maintained at a constant value of effective angle of attack.

3.2 EXPERIMENTAL SYSTEM AND TECHNIQUES

Experiments were performed in a free-surface water channel with an overall test section length of 4,877 mm, a width of 927 mm, and a depth of 610 mm. Figure 3.1 shows isometric and side views of the rotating wing system. A clear acrylic flat plate

with sharp (rectangular) edges was used as the wing model. The lighter gray (yellow-colored) wing has an aspect ratio $AR = b/C = 2$, a chord C = 38.1 mm, a span b = 78.1 mm and a thickness t = 2.8 mm. The root of the wing was connected to a rotating centerbody of diameter 12.7 mm with a rod, which had a diameter of 3.17 mm at the wing root. The distance between the surface of the rotating body and the root of the wing was maintained at 25.4 mm while the distance from the center of rotation to the root of the wing was, r_o = 31.8 mm. The darker gray (green) plane represents the laser sheet that intersects the wing; it is oriented in the chordwise direction.

The freestream velocity had values of U = 0, 50, 100, and 150 mm/s, corresponding to four values of advance ratio $J = U/V_{tip}$ = 0, 0.179, 0.358, and 0.537. The wing was rotated about the x-axis at two different angular velocities Ω, corresponding to values of tip velocity V_{tip} = 618 mm/s in absence of the freestream U ($J = U/V_{tip} = 0$) and V_{tip} = 279 mm/s in presence of the freestream. The Reynolds number based on the effective tip velocity $V_{eff\,(tip)} = \left[V_{tip}^2 + U^2\right]^{1/2}$ is Re = 23,430 for J = 0 and Re = 10,766, 11,257, and 12,030 for J = 0.179, 0.358, and 0.537 respectively. Patterns of vorticity at extreme values of Reynolds number for matched parameters (not shown herein) indicated that the distinctions were insignificant. The effective angle of attack was maintained at α_{eff} = 45° at the midspan for each advance ratio $J = U/V_{tip}$ by varying the geometrical angle of attack α_{gem} in accord with variations of U. The side view of the wing in Figure 3.1b shows the appropriate vector diagram as viewed during the experiment, including vectors of the tangential velocity of the wing V_{rg} at the radius of

gyration and the velocity of the incident flow U. Figure 3.1c shows the wing in the laboratory fixed reference frame, where $U' = -U$. Also displayed are the effective velocity V_{eff} and the effective angle of attack α_{eff} at the radius of gyration. The magnitude of V_{eff} indicated in Figure 3.1c, and in subsequent figures and text, is calculated at the radius of gyration according to $V_{eff\,(tip)} = \left[V_{tip}^2 + U^2\right]^{1/2}$. Therefore, in the absence of the freestream ($J = 0$) $V_{eff\,(rg)} = V_{rg}$. The effective angle of attack is given by,

$$\alpha_{eff} = \left(90^\circ - \alpha_{gem}\right) + \text{atan}\left(U'/V_{rg}\right)$$

Quantitative imaging via angular displacement stereo particle image velocimetry (SPIV) was used to determine the three-dimensional velocity field. Figure 3.2 illustrates the water channel test section and SPIV arrangement. Using a two-plane calibration target, the mapping functions linking the camera to the object plane were created. Careful manual alignment of the calibration target and the laser plane were further refined using an automapping algorithm in commercially available software. The water was seeded with 12μm hollow metallic coated plastic spheres, providing 15-20 particle images in the interrogation window size of 32 x 32 pixels^2. A 1 mm thick laser sheet was produced by a dual-pulsed Nd-YAD operating at 14.29 Hz. Images were acquired with a camera system having a CCD array of 1600 by 1200 pixels^2. Image pairs were acquired at an effective chordwise magnification of 8.5 pixels/mm. The acquired images are evaluated using a cross-correlation technique with 50% overlap, yielding 5,335 and 5,390 vectors in the field of view for experiments with and without a freestream respectively.

An estimation of the in- and out-of-plane uncertainties followed procedures outlined in Adrian & Westerweel (2010). The RMS random error estimation of in-plane

velocity vectors was between 2-5% of the maximum velocity. The out-of-plane displacement is often expressed in terms of the error ratio, i.e. the ratio of random RMS error in the *z*-direction to the random RMS error in x-direction (assuming errors in x and y directions are equivalent). Using the theoretical relationship, $\sigma_{\Delta z}/\sigma_{\Delta x} \cong (\tan\theta)^{-1}$ (Lawson & Wu 1997), where θ is the stereo half angle, the error ratio is equivalent to 2.41. The estimated random RMS in-plane error is $\sigma_{\Delta x}$ = 7.08μ*m*, therefore the estimated out-of-plane random RMS error is $\sigma_{\Delta z}$ = 17.06μ*m*. An assessment of the uncertainty in the three-dimensional reconstruction techniques can be found in Yilmaz & Rockwell (2012).

Image acquisition at the mid-span of the wing was repeated ten times and ten instantaneous images were phase averaged to produce final images. Three-dimensional images of stacked slices of spanwise vorticity $\omega_z C/V_{eff}$ and iso-surfaces of spanwise velocity w/V_{eff} as well as the parameter *Q* (defined subsequently) involved acquisition of three instantaneous images at each location of the laser sheet along the span of the wing; these images were then phase averaged prior to construction of a three-dimensional image. In order to change the position of the laser sheet along the span of the wing, a traverse system translates the entire rotating wing assembly to successive spanwise locations. Image acquisition was performed on 39 planes for J = 0 and on 38 planes for J = 0.537, with a spacing of $\Delta r/b$ = 0.032. The spatial separation of the velocity data on the PIV imaging planes is 1.87 mm, which corresponds to a non-dimensional distance of $\Delta x/b = \Delta y/b$ = 0.024. The total number of velocity vectors in the volume is 208,065 for J = 0 and 204,820 for J = 0.537. Three-dimensional representations of the flow structure

were slightly smoothed with a single pass of a moving average algorithm (Kim & Gharib 2010). In essence, this algorithm shifts the value of a variable at a particular point in the grid by the average of the six surrounding points, e.g. $w_{new} = \left(w_{old} + w_{6avg}\right)/2$, where w_{6avg} is the average of the six neighboring points.

The first group of experiments involves investigation of the flow structure at the midspan of the wing for sequential values of rotation angle ϕ. The wing starts from rest and rotates at a constant rate to an angle of rotation of ϕ = 320°. For the experiments in absence of the freestream (J = 0) the wing reaches a constant angular velocity at ϕ = 27°. Similarly, for experiments in the presence of the freestream (J > 0) the wing reaches a constant angular velocity at ϕ = 23°. Slight smoothing, corresponding to a value of the parameter a = 700 of Eldredge et al. (2009) was used at the beginning and end of the linear ramp-up motion to avoid possible vibration and transient effects. Imaging is performed at ϕ = 0°, 9°, 13.5°, 18°, 36°, 45°, 90° and 270°, with the wing maintained at an effective angle of attack of α_{eff} = 45°. In the second group of experiments, three-dimensional volume images are constructed at ϕ = 36° for the same effective angle of attack as in the foregoing, α_{eff} = 45°. The distance s that the wing has travelled at a specific rotation angle can be expressed in terms of chord lengths C at the tip, i.e., $S = s/C = \Phi r_{tip}/C$.

3.3 SECTIONAL FLOW STRUCTURE REPRESENTATIONS: ADVANCE RATIO VARIATION

3.3.1 Spanwise Vorticity

Figures 3.3a and 3.3b show patterns of normalized spanwise vorticity $\omega_z C/V_{eff}$ on a plane corresponding to the mid-span of the wing. The spatial domain of the *x* and *y* directions in Fig. 3a and subsequent plots are normalized with the chord length *C*, *i.e.* x/C and y/C. In these images, it is evident that the angle of inclination of the plate varies with advance ratio *J*. These changes of geometric angle of attack α_{gem} are necessary to maintain the same effective angle of attack, α_{eff} = 45° when changing the advance ratio *J*.

In figure 3.3a, the initial stage of rotation is represented by the rotation angles ϕ = 0°, 9°, 13.5°, 18°. At each value of ϕ, the vorticity patterns are shown for four different values of advance ratio, $J = U/V_{tip}$ = 0, 0.179, 0.358, and 0.537. The first row of images, designated as ϕ = 0°, shows the flow structure prior to onset of the plate motion. The freestream was initiated approximately 300 seconds prior to the onset of wing rotation, which corresponds to a convective time $\tau = tV_{rg}/C = 1.42\times10^{6}$. This long convective time scale ensured attainment of a steady state, fully-stalled flow prior to the onset of wing motion, as represented by the time-averaged images in the top row of figure 3.3a. These images clearly indicate that the magnitude of $\omega_z C/V_{eff}$ within the separated vorticity layer increases with advance ratio *J*, which corresponds to increasing free stream velocity *U*. (Note that, for the limiting case of the plate at rest at ϕ = 0°, V_{tip} = 0; the values of *J* should therefore be interpreted as the values that would exist if the plate were rotating.)

At successively larger values of rotation angle ϕ = 9°, 13.5°, 18° in figure 3.3a, the images show the formation of a leading edge vortex at the top of the plate. It is not

shed from the edge of the plate, despite the presence of the free stream velocity U and thereby finite J. Moreover, this concentration of $\omega_z C/V_{eff}$ has a remarkably similar evolution over the entire range of ϕ and J.

The pre-existing layer of distributed vorticity from the leading (top) edge, which is connected to the vorticity concentration at the leading-edge, is displaced from the leading edge to the trailing edge, and the magnitude of this displacement increases with rotation angle. This displacement is likely due to the induced velocity from the growing leading-edge vortex. Concerning the vorticity shed from the trailing-edge, it has the form of a vorticity concentration at zero advance ratio, i.e., $J = 0$. However, as J increases, the trailing vorticity transforms from a concentration to a distributed layer, which extends a substantial distance from the trailing-edge.

Figure 3.3b shows the intermediate and final stages of the vortex structure. At rotation angles of $\phi = 36°$ and 45° and all values of advance ratio J, the scale of the leading-edge-vortex has grown substantially relative to its scale at the lower rotation angles indicated in figure 3.3a. Despite this, the leading-edge-vortex remains attached, i.e. the center of the vorticity concentration remains close to the surface of the wing. At these rotation angles of $\phi = 36°$ and 45°, small scale shedding of vorticity from the trailing edge is apparent for $J = 0$, 0.179, and 0.358, but at $J = 0.537$, the trailing vorticity tends to the form of a continuous, distributed layer of vorticity. In the final phase of development, represented at rotation angles of $\phi = 90°$, the leading-edge vortex undergoes a transformation at advance ratios of $J = 0.358$ and 0.537 where it loses its highly organized character. At $\phi = 90°$, $J = 0.537$, a strong concentration of secondary vorticity, which is induced by the leading-edge vortex, occurs between the leading-edge

vortex and the plate. Moreover, concentrations of both positive and negative vorticity, are distinguishable aft of this region. These unusual elements of the vorticity pattern are apparently associated with transformation to the corresponding pattern at ϕ = 270°. An ordered structure of the leading-edge vortex is recovered at a rotation angle of ϕ = 270° for all values of *J*. Moreover, the phase averaged patterns of vorticity closely resemble instantaneous patterns, except at the largest rotation angle of ϕ = 270°. The phase averaged vorticity at ϕ = 270° shows a distributed extension of the vortex structure. It is a result of both the leading-edge vortex growing in scale with rotation angle and the onset of disorder, i.e. the onset of shedding of the leading-edge vortex.

3.3.2 Spanwise Velocity

Figure 3.4 depicts patterns of spanwise velocity w/V_{eff} for the intermediate (ϕ = 36° and 45°) and final (ϕ = 90° and 270°) stages of rotation. Superposed on these velocity contours are contour lines of constant spanwise vorticity $\omega_z C/V_{eff}$ for rotation angles of ϕ = 36°, 45°, 90°, and 270°. The range of dimensionless vorticity contour level and the incremental value are $\omega_z C/V_{eff}$ = -10 to 18 and $\Delta\left(\frac{\omega_z C}{V_{eff}}\right) = 2$. For rotation angles of ϕ = 36° and 45°, the regions of highest spanwise velocity w/V_{eff} correspond to the locations of largest spanwise vorticity for all values of advance ratio *J*. At ϕ = 90°, the cluster of high w/V_{eff} has moved towards the trailing edge and into the wake for *J* = 0 and 0.179. This cluster takes the form of an extended layer, rather than a region of highly concentrated velocity. This transformation does not, however, occur at larger values of *J* = 0.358 and 0.537 where the leading-edge vortex exhibits some disorganization. A

concentration of large w/V_{eff} remains at the leading-edge at J = 0.358 and at J = 0.537 in addition to a large scale region of w/V_{eff} extending all the way from the leading-edge into the wake. The wide region of large amplitude positive spanwise velocity w/V_{eff} that extends over the entire chord of the wing from the leading-to the trailing-edge for at ϕ = 90° for J = 0.358 and 0.537 is associated with deflection of the leading-edge vorticity layer away from the surface of the wing and, simultaneously, generation of a secondary concentration of vorticity between the layer from the leading-edge and the wing surface. At ϕ = 270°, the patterns of spanwise velocity are generally similar for all values of advance ratio J, namely the regions of largest extent occur in the vicinity of the trailing-edge and into the wake. The origin of the low level blue contours in the vicinity of the leading edge vortex, which also have been observed in the independent experiments of Ozen & Rockwell (2012) and Carr et al. (2013a) represent a minor counter spanwise flow, the origin of which has not been resolved.

3.3.3 Streamlines

Streamline patterns are shown in Figures 3.5a and 3.5b. These streamlines are shown in the reference frame of the wing; they are obtained by subtracting the tangential velocity of the wing. The first row of images in figure 3.5a corresponds to the plate at rest, prior to the onset of motion, these images are at angle ϕ = 0°. For values of J = 0.179, 0.358 and 0.537, the flow is massively separated in the wake of the plate. Upstream-oriented streamlines in the near-wake merge into downstream-oriented, negative bifurcation lines *BL-*; they are coincident with the separation lines from the

edges of plate. A well-defined half-saddle point *S*, i.e., stagnation point, occurs on the windward (upstream) side of the plate.

At sufficiently large angle ϕ following startup, a well-defined half-saddle point *S* can be identified on the windward side of the wing. It is distinctly defined at ϕ = 13.5° for values of *J* = 0 .179, 0.358 and 0.537. At *J* = 0, however, the half-saddle point *S* is not clearly apparent until ϕ = 45°. The location of *S* remains close to the leading (top) edge of the plate, that is, within 0.06*C-0.1C* from the leading-edge over the entire range of *J* and ϕ.

At the trailing-edge of the plate, the patterns of streamlines show varying degrees of distortion and deflection depending upon the value of rotation angle ϕ and advance ratio *J*. For *J* = 0, at the smallest three rotation angles ϕ = 9°, 13.5°, and 18° the streamlines are not parallel to the windward and leeward sides of the plate as they approach the trailing edge and, moreover, the streamline from the tip of the trailing edge is ill defined. At ϕ = 36° through 270°, this streamline is inclined at a relatively large angle, in the range from 17° to 22°, with respect to the chord line of the plate. For *J* = 0.179, the streamlines from the windward side of the plate are substantially distorted in the vicinity of the trailing-edge for low rotation angles of 13.5° and 18°. At larger angles of rotation angle ϕ = 36° to 270°, the angle of inclination $\Delta\alpha_s$ of the streamline from the tip of the trailing-edge with respect to the chord line of the plate is in the range of $\Delta\alpha_s$ = 15° to 19°, except at ϕ = 45°, where the deflection is only $\Delta\alpha_s$ = 1°. At *J* = 0.358, the deflection angle is $\Delta\alpha_s$ = greater than or equal to 10° for all value of ϕ, except at ϕ = 45°, where it has a value of $\Delta\alpha_s$ = 4°. Finally, for *J* = 0.537, the deflection angle of the

streamline from the tip of the trailing-edge has values in the range from 7° to 22°, except at ϕ = 18°, where it has value of $\Delta\alpha_s$ = 1°. Considering all of the foregoing observations, small angle of deflection $\Delta\alpha_s$ of the streamline from the tip of the trailing-edge with respect to the chord line of the wing does not occur for the limiting case J = 0. At finite values of advance ratio J = 0.179, 0.538 and 0.537, a small angle of deflection in the range from $\Delta\alpha_s$ = 1° to 4° occurs only at a single value of rotation angle: ϕ = 45° at J = 0.179; ϕ = 45° at J = 0.358; and ϕ = 18° at J = 0.537. At these values of ϕ, the flow structure has apparently relaxed sufficiently from its transient start up. Well after the onset of wing motion, at larger values of ϕ, the streamline pattern on the leeward side of the wing is highly distorted: ϕ = 270° at J = 0.179 and 0.358; ϕ = 90° and 270° at J = 0.537. These distortions are due to the change in form of the leading-edge vortex, indicated in figure 3.3b. Existence of a Kutta condition at the trailing edge is associated with streamlines approaching the trailing-edge that are parallel to the windward and leeward sides of the plate and zero deflection of the stagnation streamline at the trailing-edge with respect to the chord line of the plate, that is, $\Delta\alpha_s$ = 0° (Basu & Hancock 1978; Ho et al. 1981). These conditions are approximated only for the aforementioned values of $\Delta\alpha_s$ = 1° to 4°.

Finally, at sufficiently large rotation angle phi, a leading-edge vortex is indicated by a focus F, or center, of the swirling streamline pattern in that region. Such foci F are evident for cases where the concentration of vorticity at the leading-edge has a sufficiently large value of circulation (compare figure 3.3b). Downstream of the focus F, the streamline pattern along the leeward surface of the wing indicates an attached flow.

This type of attached flow pattern is, however, not evident at combinations of large rotation angle ϕ and advance ratio *J*, in particular for ϕ = 90°, *J* = 0 .537 and ϕ = 270°, *J* = 0.358 and 0.537. As indicated in the foregoing, departure from attached flow is associated with deflection of the elongated patterns of vorticity away from the leeward surface of the wing, indicated in figure 3.3b.

3.4 THREE DIMENSIONAL FLOW STRUCTURE: EXTREME VALUES OF ADVANCE RATIO

3.4.1 Spanwise Vorticity

Figure 3.6 shows stacked sectional cuts of $\omega_z C/V_{eff}$ for *J* = 0 (Ozen & Rockwell 2012) and 0.537 at ϕ = 36°. The rotating wings with advance ratios of *J* = 0 and 0.537 both have the same effective angle of attack of α_{eff} = 45°, despite different geometric angles of attack of α_{gem} = 45° and 85° respectively. For *J* = 0.537, the free stream velocity is from left to right. The top row of images shows an isometric view of the leeward side of the wing looking from the root to the tip. The second row presents a side view of the root of the wing.

Slices of $\omega_z C/V_{eff}$ along the span of the wing, in the region of the leading-edge, show similar features for both *J* = 0 and 0.537. Namely, the overall structure of the leading-edge vortex is generally conical, and concentrated vorticity remains in the vicinity of the leading-edge, that is, it is not shed. Concentrations of positive vorticity near the tip region, at locations downstream of the leading-edge, occur for both values of advance ratio *J*. They correspond to the tip vortices. The larger cluster of negative (blue) vorticity in the trailing edge region *J* = 0 is associated with the large-scale vortex shed during the startup process. On the other hand, at *J* = 0.537, a single starting vortex is not

evident; rather the pattern of small scale structures suggests existence of a high-frequency (short wavelength) Kelvin Helmholtz instability.

3.4.2 Spanwise Velocity

Figure 3.7 illustrates iso-surfaces of spanwise velocity, w/V_{eff} for $J = 0$ and $J = 0.537$ at a rotation angle of $\phi = 36°$. Positive spanwise velocity is directed from the root to tip. In the absence of mean flow ($J = 0$), distinct patterns of positive w/V_{eff} are present in close proximity to the leading-edge, tip and root of the wing. The concentration at the leading-edge is centered at the midspan of the wing, and an iso-surface of w/V_{eff} occurs along and downstream of the tip. Additionally, at $J = 0$, a concentrated iso-surface exists at the junction of the root and the trailing-edge. This observation is consistent with the root vortical structure indicated by iso-surfaces of *Q*-criterion (Figure 3.8) for $J = 0$.

At $J = 0.537$, an iso-surface concentration of w/V_{eff} extends across a major share of the leading-edge of the wing. In addition, a concentration of w/V_{eff} extends along the tip of the wing, and at the trailing-edge, it increases in width, while extending along the trailing-edge; it has a generally similar form as that at $J = 0$. Moreover, the form of this iso-surface along and downstream of the tip is consistent with the development of the tip vortex. The concentration of w/V_{eff} present at $J = 0$ at the junction of the root and the trailing-edge, however, is not present at $J = 0.537$. This observation suggests that a root vortex is not present at $J = 0.537$, a point that will be addressed in the next section.

3.4.3 Q-Criterion

Surfaces of iso-*Q* correspond to constant values of the second invariant of the velocity gradient tensor as defined in Hunt et al. (1988).

$$Q = \frac{1}{2}\left[\Omega_{ij}\Omega_{ij} - S_{ij}S_{ij}\right] = -\frac{1}{2}\frac{\partial u_i}{\partial x_i}\frac{\partial u_j}{\partial x_i} \qquad (1)$$

The *Q*-criterion indicates the magnitude of rotation relative to the amount of strain, where Ω and *S* are the rotation and stress tensors respectively. When *Q* is positive, rotation dominates the strain, therefore vortical structures can be identified by positive values of *Q*.

In figure 3.8, in absence of the freestream, i.e., at $J = 0$, the leading-edge vortex is well defined over a major share of the span. Near the tip, however, it is partitioned into two structures: a small scale structure that remains along the leading edge; and a large-scale structure located downstream of the leading edge. Regarding the vortical structures in the root, tip, and trailing-edge regions, they are connected to form a continuous loop. At $J = 0.537$, the dual vortex structure observed near the tip at $J = 0$ now extends to a location inboard of the span of the wing. A vortical structure does not exist along the root; rather, in the vicinity of the leading-edge, the iso-*Q* concentration is deflected up and away from the wing root. Moreover, the tip-trailing edge-root loop structure that is prevalent at $J = 0$ does not exist at $J = 0$ .537. Downstream of the trailing-edge, small-scale concentrations of iso-*Q* are evident, apparently due to a Kelvin-Helmholtz instability. Moreover, at $J = 0.537$, the iso-*Q* pattern shows a helical instability about the periphery of the tip vortex; in fact, these small-scale helical strands connect to the small scale concentrations of *Q* that are shed from the trailing-edge. The apparent lack of a large-scale loop structure at $J = 0.537$ in figure 3.8 may be due to one of two

interpretations: it exists, but is swept outside of the field of view by the free stream; or, it does not exist, and the shedding of vorticity from the trailing edge takes the form of a combination of small-scale concentrations of vorticity and distributed vorticity. This issue cannot be completely resolved at this point. The sectional cuts of spanwise vorticity for the start-up of wing motion that are shown in figure 3.3a indicate, however, a pronounced concentration of vorticity shed from the trailing edge at J = 0, and, in contrast, distributed and small-scale concentrations shed at J = 0.537. This type of small scale flow structure in the periphery of the tip vortex connecting to the trailing edge vortices was also observed on the AR = 2 wing in Carr et al. (2013a).

3.5 CONCLUSIONS

The flow structure on a rotating plate at a high angle of attack both with and without an incident mean flow has been characterized for an effective angle of attack α_{eff} = 45^o and angles of rotation ϕ up to 270°, corresponding to 13.6 chords of travel of the wing at the tip. A stable leading-edge vortex persists to large angle of rotation, even in presence of a relatively large inflow (freestream) velocity U of the order of one half the tip velocity V_{tip} of the wing. Furthermore, a number of features of the flow structure are similar over a range of advance ratio $J = U/V_{tip}$ when the effective angle of attack α_{eff} is maintained constant by adjusting the geometric angle of attack α_{gem} of the wing.

During the early and intermediate stages of rotation, ϕ = 9°, 13.5°, 18°, 36°, and 45°, the vorticity concentration of the leading-edge vortex has a remarkably similar form over the range of advance ratio $J = U/V_{tip}$. However at ϕ = 90°, for larger values of J,

the pattern of vorticity at the leading-edge vortex temporarily loses its coherence, prior to becoming stable at large angle of rotation ϕ = 270°.

Patterns of vorticity shed from the trailing-edge are highly dependent on the value of advance ratio $J = U/V_{tip}$. During startup, at J = 0, the shed vorticity takes the form of a highly concentrated vortex from the trailing-edge. As J increases, however, the shed vorticity layer tends to become more distributed. Moreover, at large angle of rotation and sufficiently large values of J, a layer of distributed vorticity from the trailing edge coexists with a distributed layer extending from the leading-edge vortex well into the wake of the rotating plate.

Spanwise velocity w having a magnitude of the order of one half the effective tangential velocity V_{eff} of the wing, persists over the entire range of advance ratio J and rotation angle ϕ. At lower values of ϕ, a cluster of large spanwise velocity w occurs near the leading edge of the wing; it is coincident with the concentration of vorticity of the leading-edge vortex. The cluster of large w tends to move downstream as rotation angle ϕ increases, and extends well into the wake region, especially at ϕ = 90° and 270°. However, even at these larger values of ϕ, a cluster of substantial w can still persist in the leading edge region for values of J greater than zero.

Streamline topology in the wing reference frame shows generic features that extend across the entire range of advance ratio J. The values of rotation angle ϕ over which these features occur, however, depends on the value of J. These features are as follows. (i) A half saddle point, which is equivalent to a stagnation point, exists on the windward side of the wing close to the leading-edge, in fact, within 0.1C from the

leading-edge over the entire range of parameters. (ii) At the trailing-edge of the plate, the patterns of streamlines show varying degrees of distortion and deflection depending upon the value of rotation angle ϕ and advance ratio J. Transient development of the flow structure during start-up of the plate motion, which occurs at low angles rotation, and departures from established, highly coherent flow structure at large angles of rotation, contribute to distortion of the streamline patterns. A Kutta condition at the trailing-edge does not occur for $J = 0$. At finite J, a streamline pattern that represents an approximation to the Kutta condition can be attained, but only for a moderate value of rotation angle. (iii) Along the leeward side of the plate, in the vicinity of the leading-edge, a focus, i.e., center, of spiraling streamlines occurs in accord with the concentration of vorticity in this region. Aft (downstream) of this focus, the pattern of streamlines corresponds to an attached flow along the leeward surface of the wing. Departure from this attached flow pattern occurs, however, for large values of advance ratio J and angle of rotation ϕ.

Three-dimensional representations of the flow structure given in figures 3.6, 3.7 and 3.8, involve slices of spanwise vorticity along the span of the wing, iso-surfaces of spanwise velocity and iso-surfaces of the Q-criterion. These representations show that a stable leading edge vortex along the span of the wing persists for extremes of advance ratio J. A large-scale loop vortex in the wake region, associated with the start-up process, exists at $J = 0$, but not at the largest value of $J = 0.537$. The sectional patterns of spanwise vorticity at the midspan of the wing, shown in figures 3.3a and 3.3b, indicate the evolution of distributed and concentrated vorticity from the trailing-edge of the wing at values of rotation angle extending from 0° to 36°. For the case $J = 0$, at $\phi = 36°$, a concentration of vorticity exists downstream of the trailing-edge at essentially the same

location as the midspan of the iso-surface of Q indicated in figure 3.8. On the other hand, at $J = 0.537$, there is no sectional concentration of vorticity shed from the trailing-edge over the range of rotation angles extending from 0° to 36°; this observation is qualified by the lack of images in the range of rotation angle from $\phi = 0°$ to $\phi = 9°$. Moreover, the structure of the vortex in the root region of the wing, i.e., the root vortex, is fundamentally different for these extreme values of J. In essence, the effect of finite J, corresponding to finite magnitude of the freestream velocity U incident upon the wing, is to either preclude or shift the timing of formation of the large-scale coherent loop vortex in the trailing edge and root regions; for the latter case, it would form and depart from the field of view at a very early time after the onset of wing motion, and thereby would not be visible in the images herein.

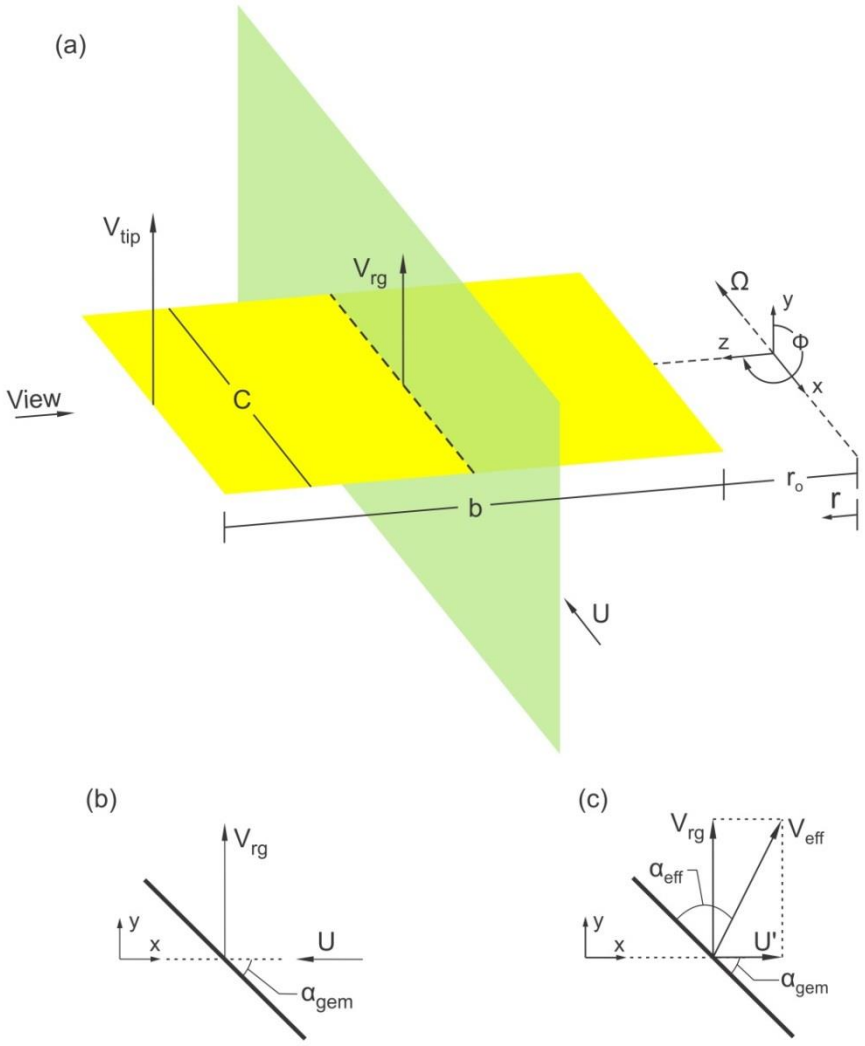

Figure 3.1: (a) Schematic of rotating wing and related parameters as well as orientation of the laser sheet. (b) Side view of wing as viewed during experiment. (c) Laboratory fixed reference frame where $U' = -U$.

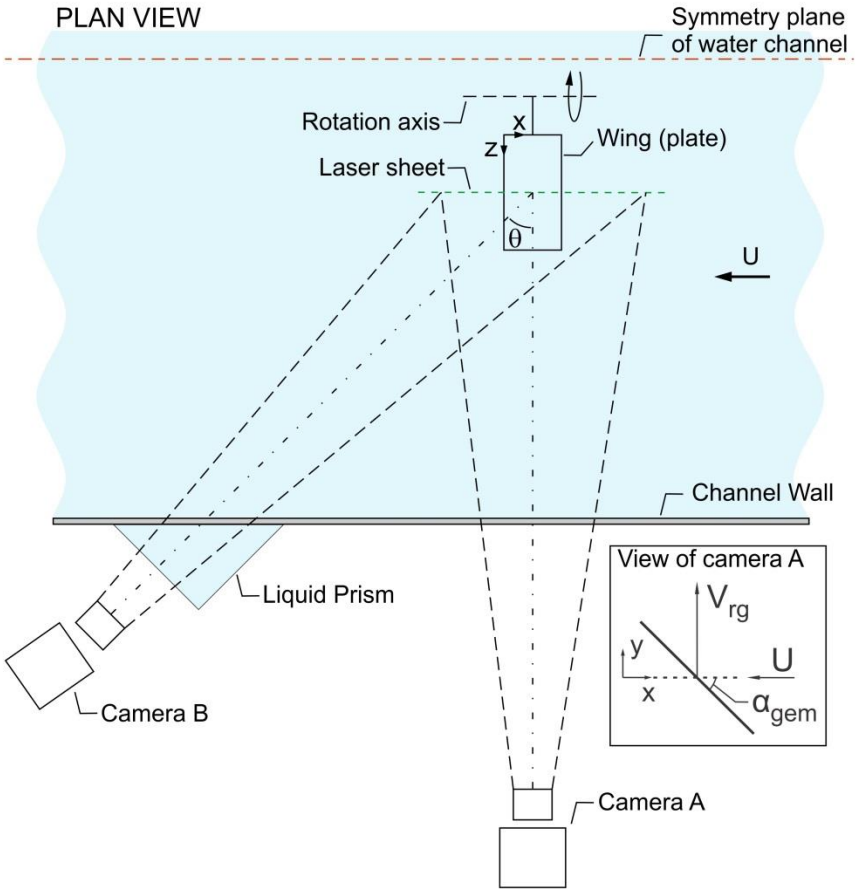

Figure 3.2: Schematic of water channel test section and orientation of stereo PIV. Also indicated is side view of wing as seen by camera A.

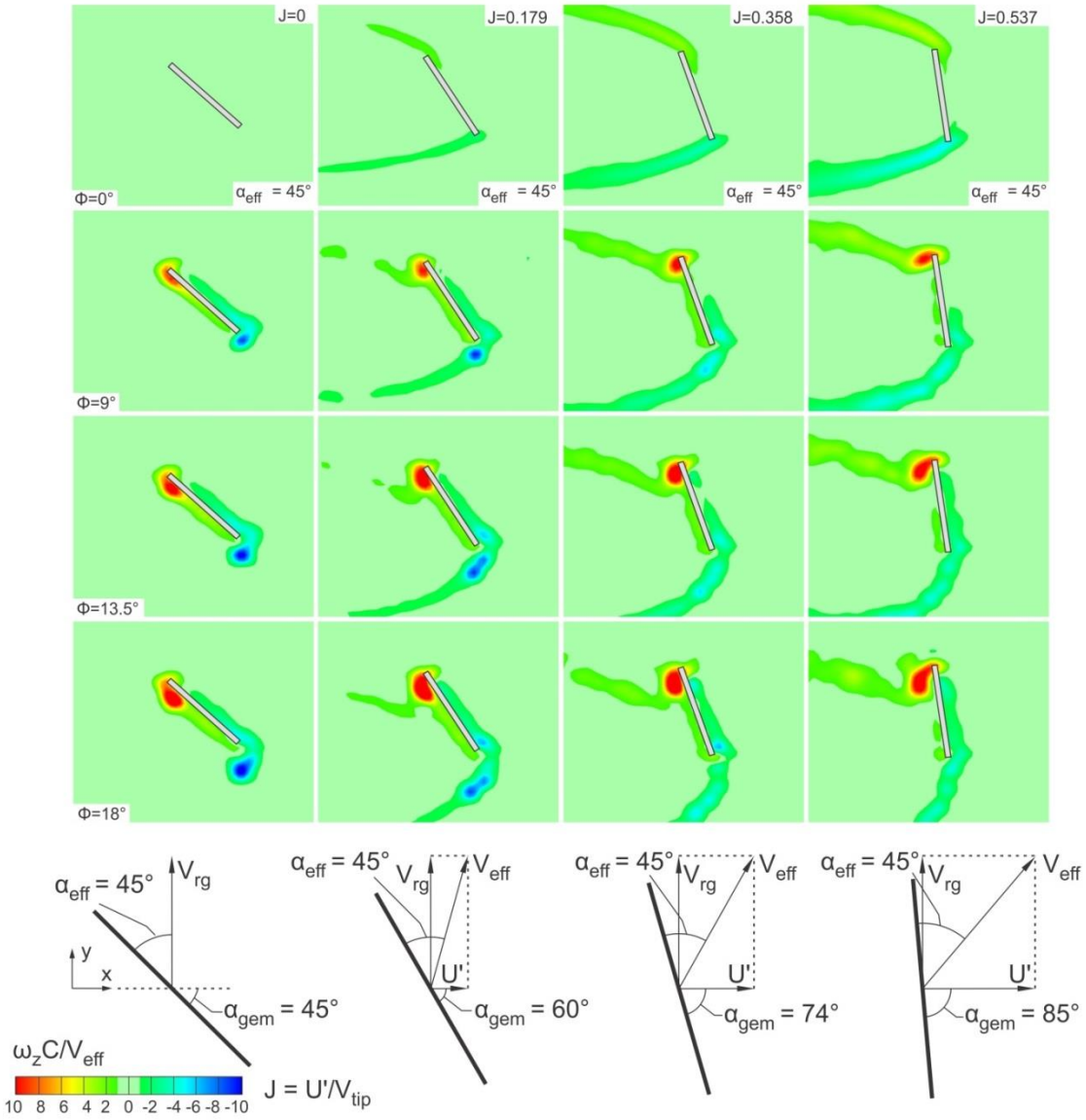

Figure 3.3a: Comparison of patterns of spanwise vorticity $\omega_z C/V_{eff}$ at the midspan of the wing for α_{eff} = 45°. Patterns are shown at four different values of advance ratio *J* as a function of ϕ during the early stages of rotation (ϕ = 0°, 9°, 13.5°, 18°).

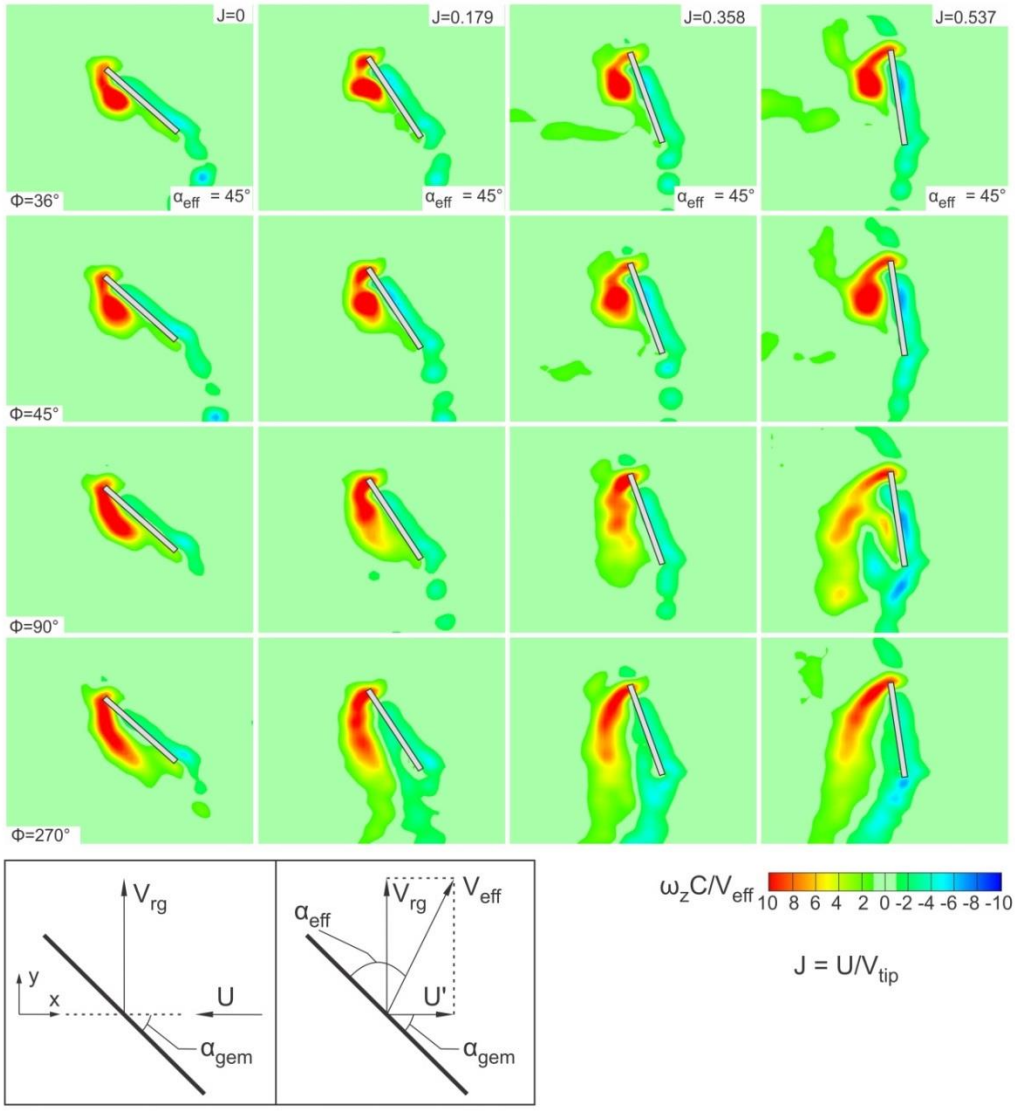

Figure 3.3b: Comparison of patterns of spanwise vorticity $\omega_z C/V_{eff}$ at the midspan of the wing for α_{eff} = 45°. Patterns are shown at four different values of advance ratio *J* as a function of ϕ during the intermediate and final stages of rotation (ϕ = 36°, 45°, 90°, 270°).

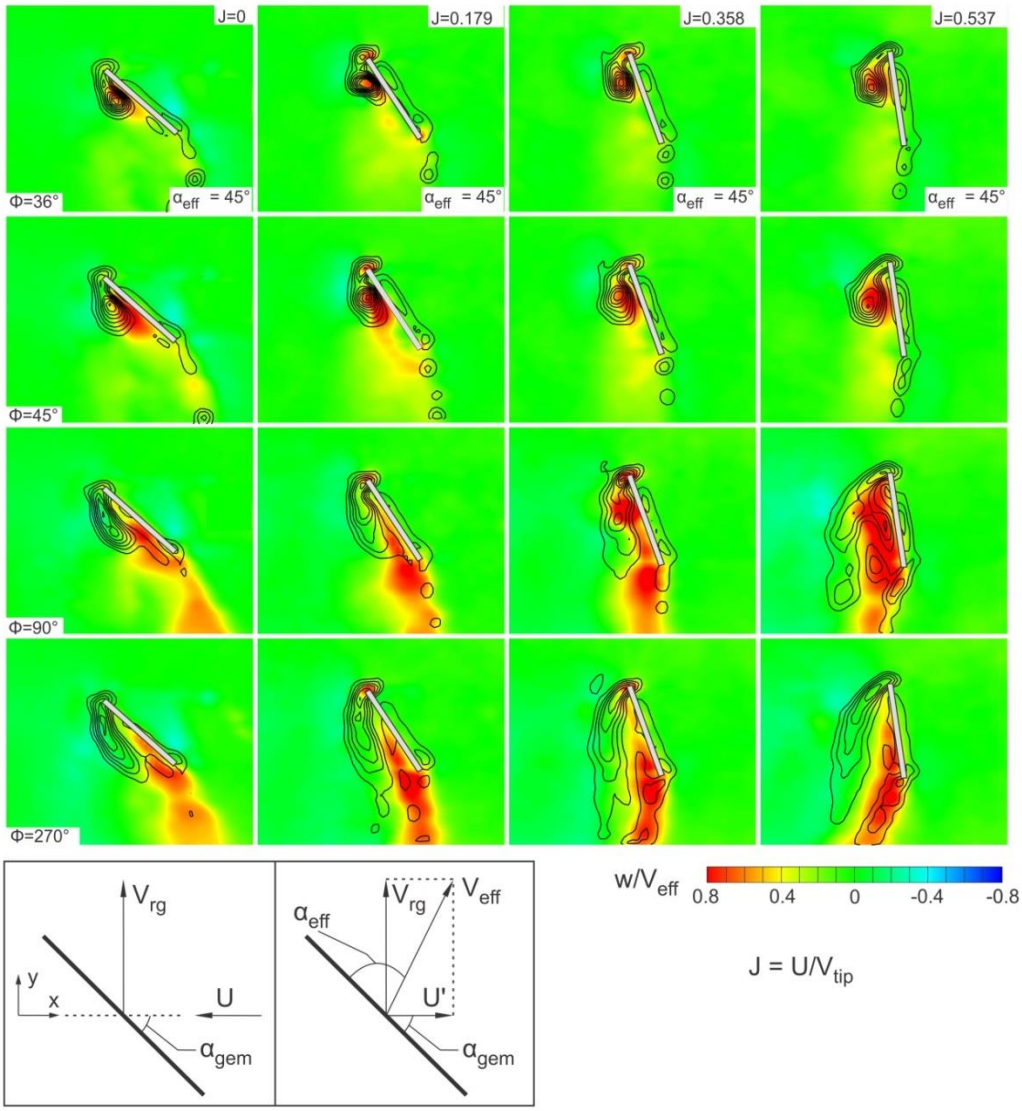

Figure 3.4: Comparison of patterns of spanwise velocity w/V_{eff} at the midspan of the wing for α_{eff} = 45°. Superposed are spanwise vorticity, $\omega_z C/V_{eff}$ contour lines. Patterns are shown at four different values of advance ratio J as a function of ϕ during the intermediate and final stages of rotation (ϕ = 36°, 45°, 90°, 270°).

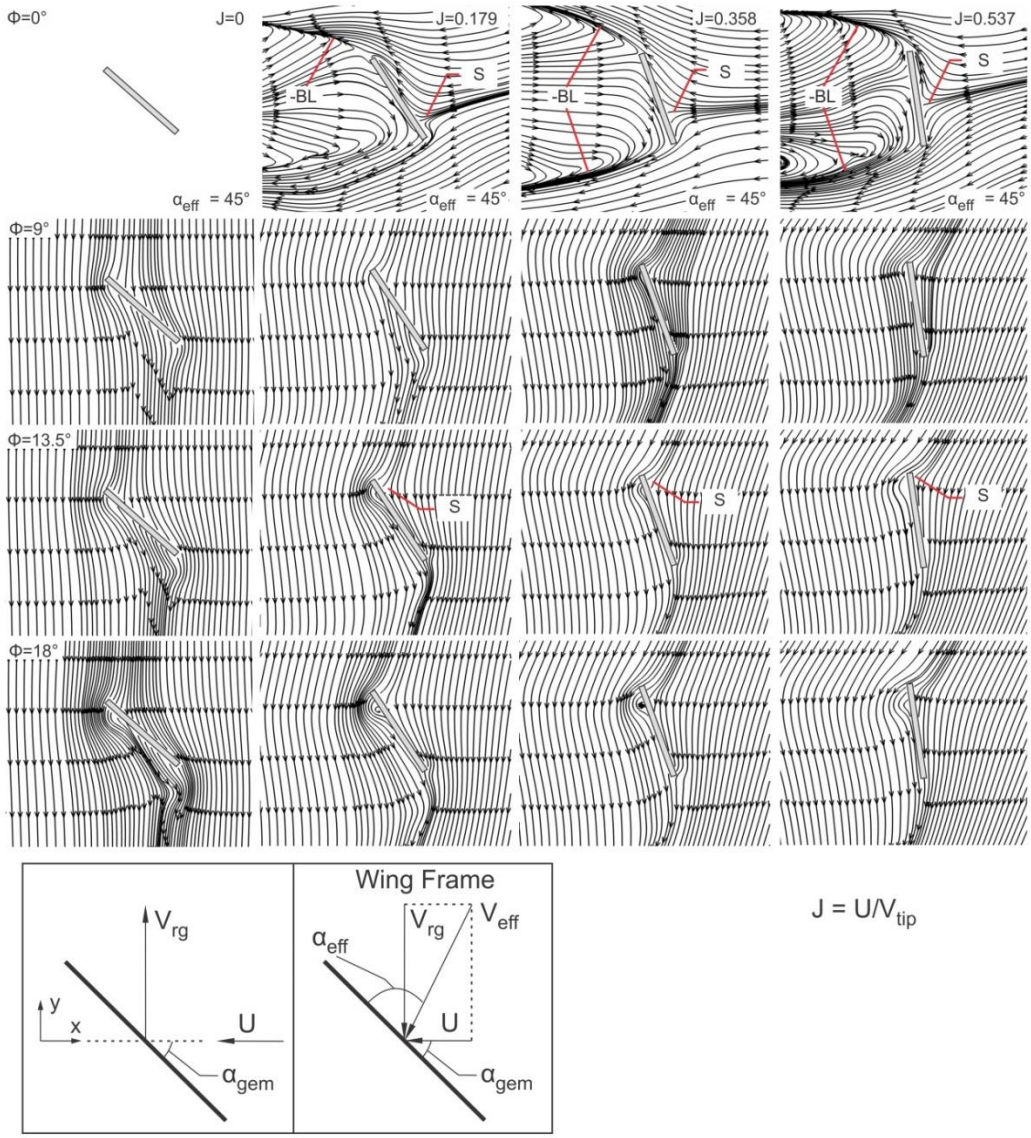

Figure 3.5a: Streamline topology in wing fixed reference frame at the midspan of the wing for α_{eff} = 45°. Patterns are shown at four different values of advance ratio J as a function of ϕ during the early stages of rotation (ϕ = 0° to 18°).

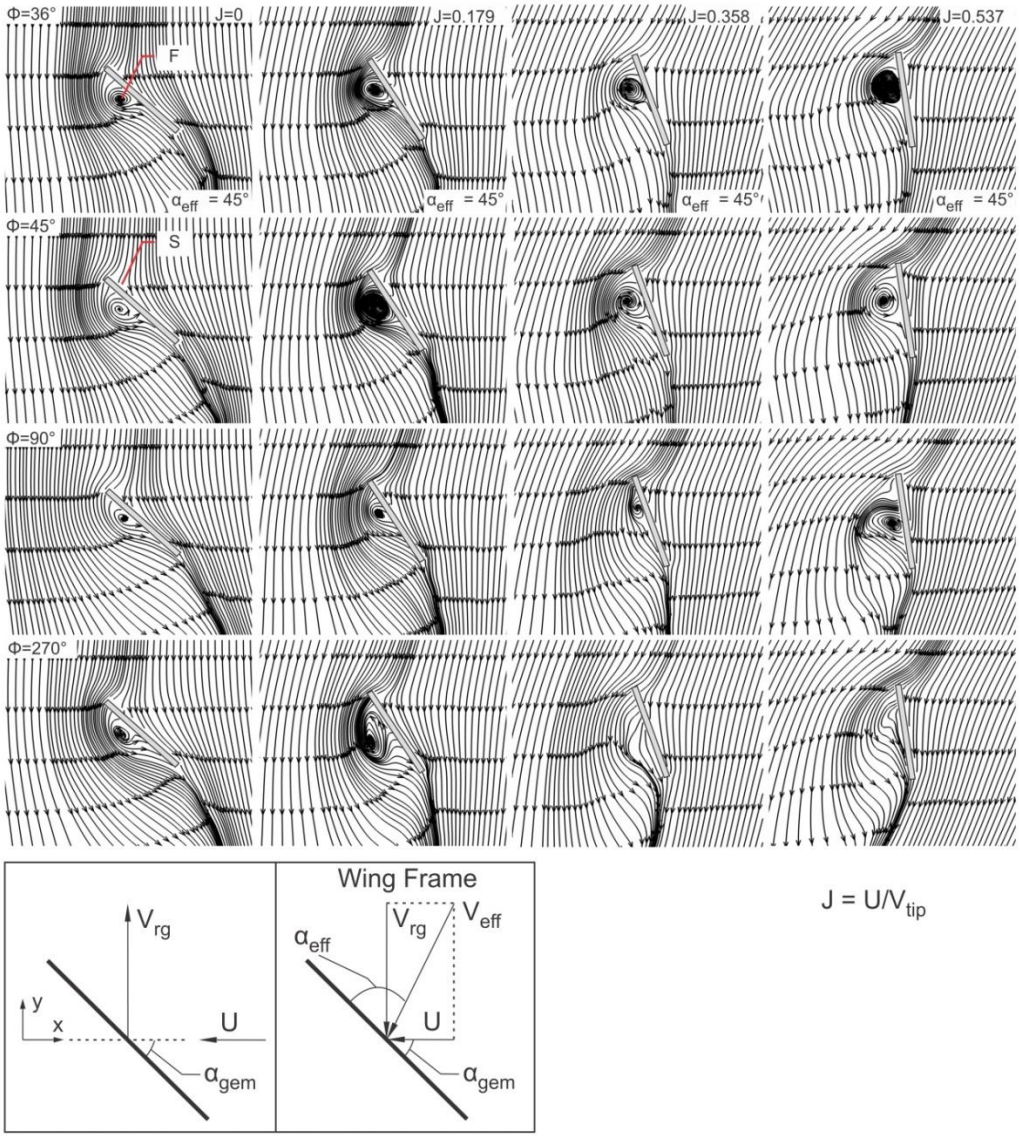

Figure 3.5b: Streamline topology wing fixed reference frame at the midspan of the wing for α_{eff} = 45°. Patterns are shown at four different values of advance ratio *J* as a function of ϕ during the intermediate and final stages of rotation (ϕ = 36° to 270°).

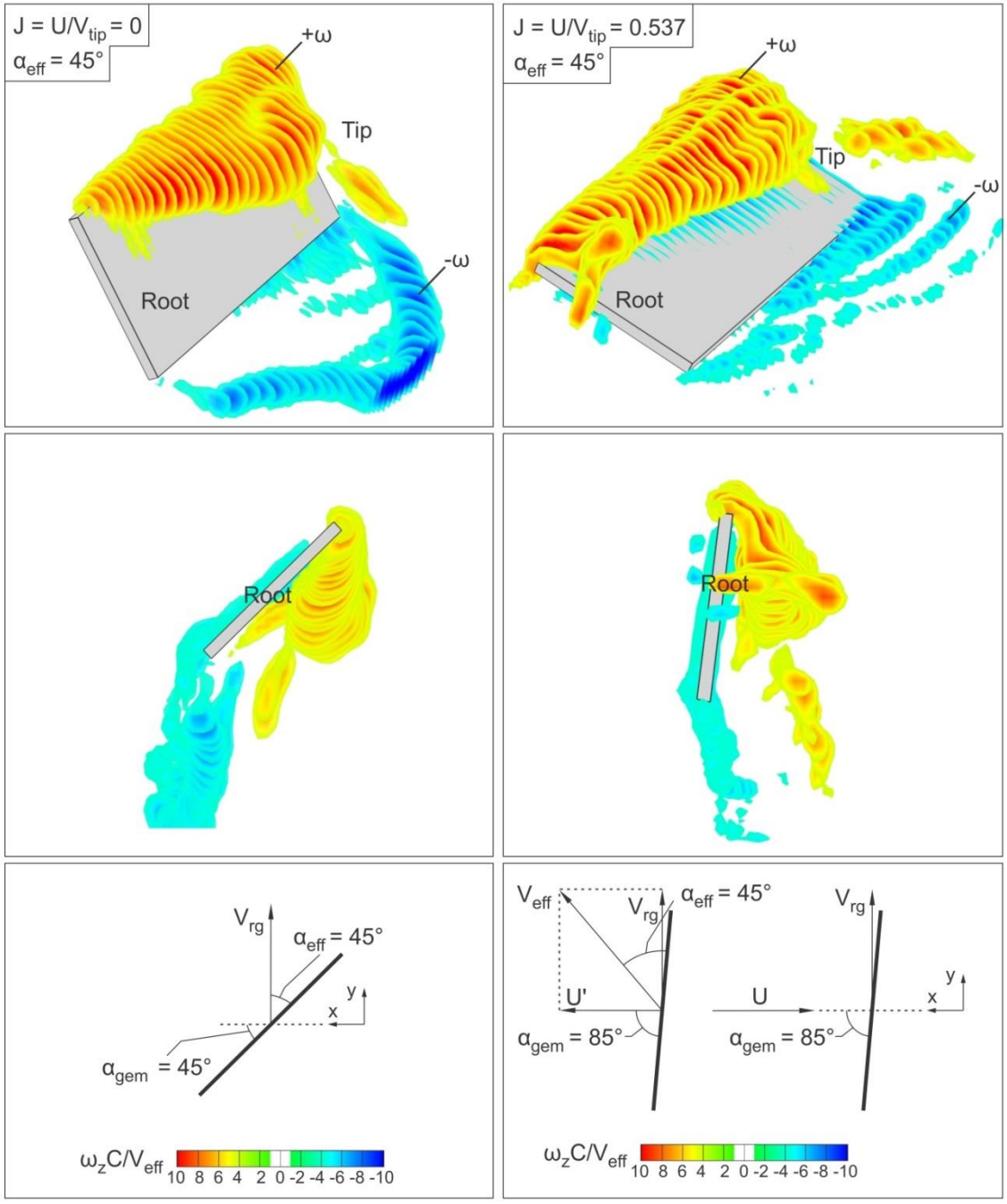

Figure 3.6: Sectional cuts of spanwise vorticity $\omega_z C/V_{eff}$ on chordwise oriented planes for values of advance ratio J = 0 and 0.537 at rotation angle ϕ = 36°.

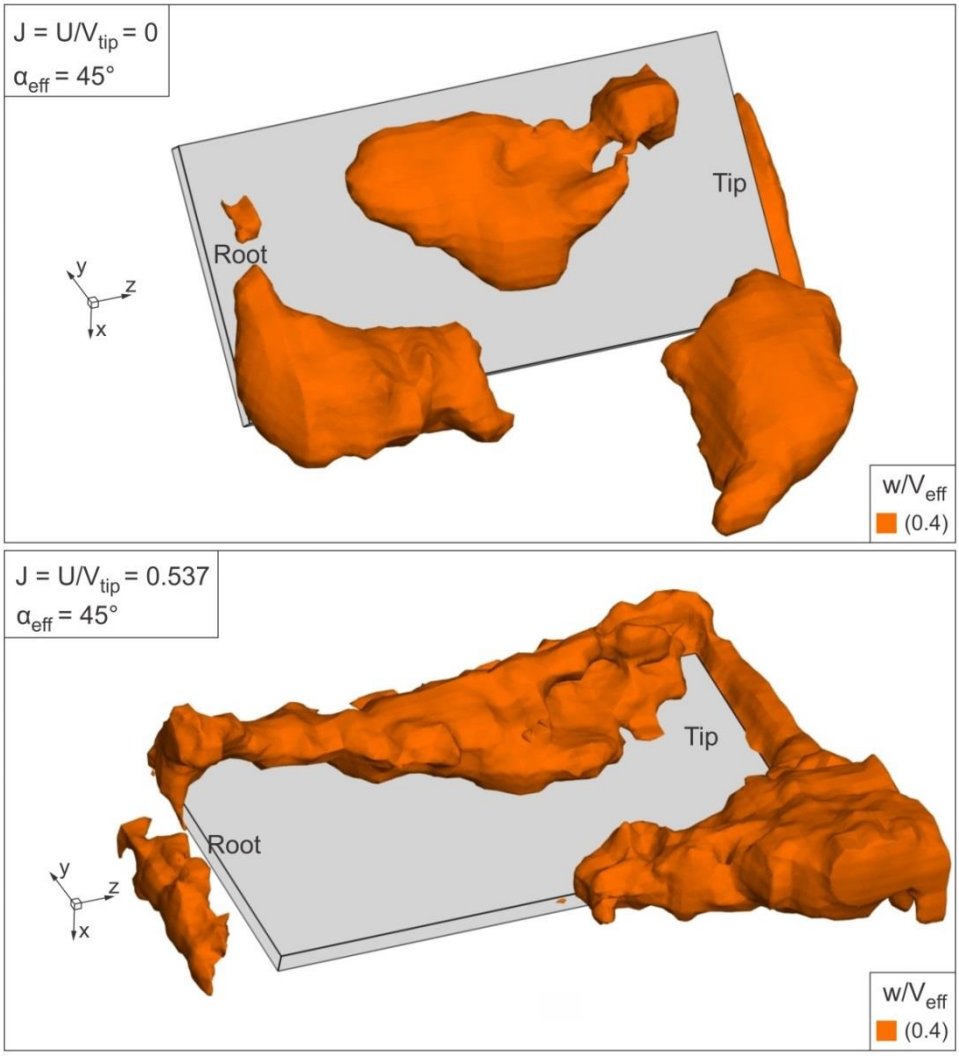

Figure 3.7: Iso-Surface of spanwise velocity for J = 0 and 0.537 at rotation angle ϕ = 36°. For both values of J, iso-surface volumes correspond to levels of w/V_{eff} = 0.4.

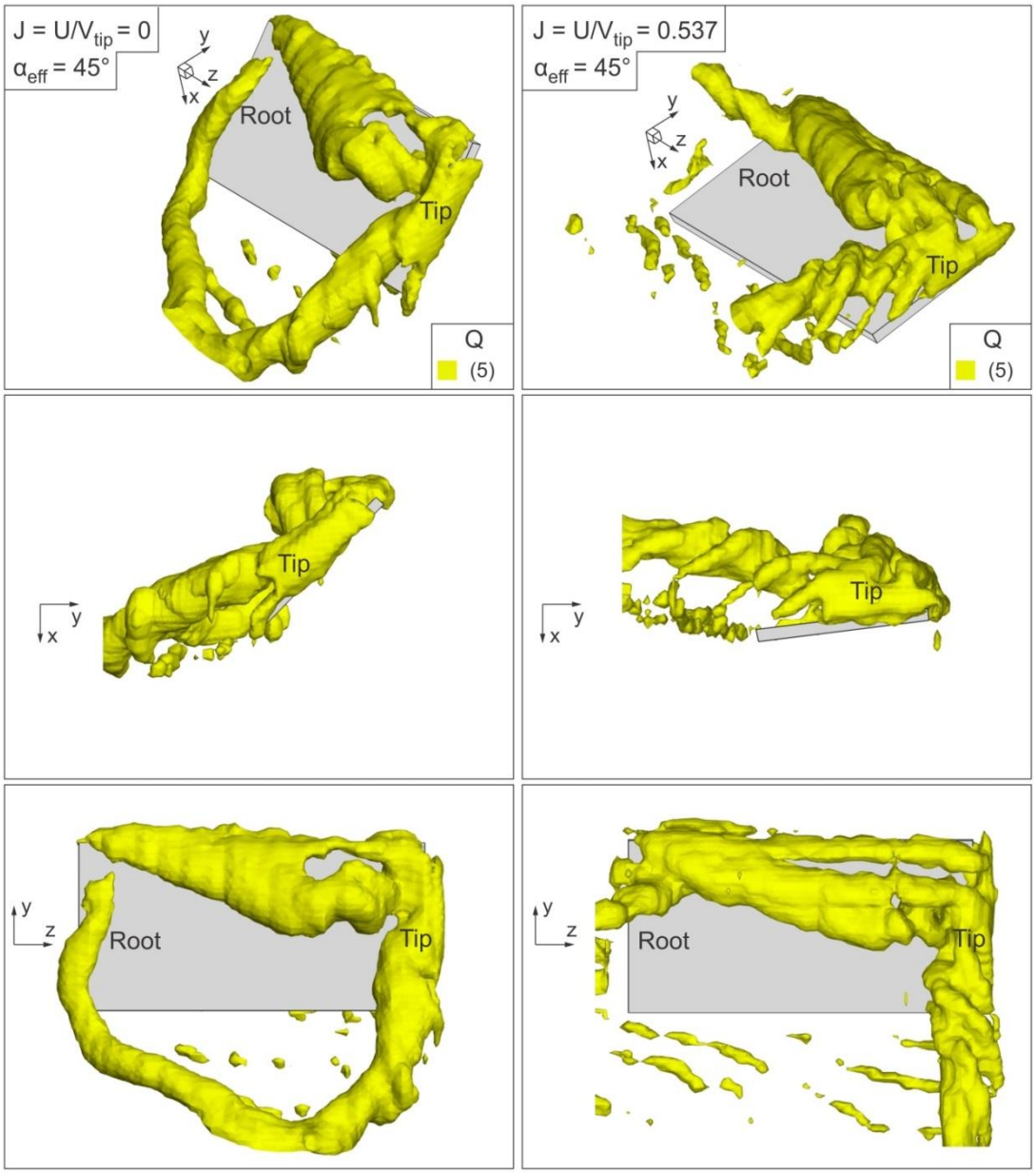

Figure 3.8: Surfaces of iso-Q corresponding to a level of Q = 5, for advance ratios J = 0 and 0.537 at a rotation angle, ϕ = 36°.

CHAPTER 4:

FLOW STRUCTURE ON A SIMULTANEOUSLY PITCHING AND ROTATING WING

4.1 BACKGROUND

Biological flyers that inspire the design of micro air vehicles typically employ a combination of pitching, plunging, and rotational motions in order to optimize the aerodynamic performance. The present investigation, found in this chapter, focuses on the detailed flow structure along a low aspect ratio wing undergoing a prevalent combination of motions, i.e., combined pitch-up and rotation, in comparison with simple pitch-up and pure rotation. These maneuvers were chosen to represent generic unsteady motions, and are broadly applicable to a range of applications, including a rotating helicopter blade or propeller. Within the category of bio-inspired phenomena, the combination of pitch-up and rotation is most akin to a perching type maneuver of a biological flyer. Of particular interest is the effect of rotation on the evolution of the flow structure induced by pitch-up motion. Quantitative imaging is employed to characterize the detailed three-dimensional flow structure.

4.2 EXPERIMENTAL SYSTEM AND TECHNIQUES

Experiments for combined pitch-up-rotation and pure rotation were performed in a free-surface water channel with an overall test section length of 4877 mm, a width of 927 mm, and a depth of 610 mm. Figure 4.1 shows isometric and side views of the rotating and pitching wing system. A flat plate with sharp (rectangular) edges was used as the wing model. The yellow-colored (transparent) wing has an aspect ratio $AR = b/C = 2$, a chord $C = 38.1$ mm, a span $b = 78.1$ mm and a thickness $t = 2.8$ mm. The root of the

wing connects to a rotating centerbody of diameter 31.75 mm with a rod, which had a diameter of 3.17 mm at the wing root. The distance between the surface of the rotating body and the root of the wing was maintained at 19.05 mm while the distance from the center of rotation to the root of the wing was r_0 = 34.93 mm. The green plane represents the laser sheet that intersects the wing; it is oriented in the chordwise direction. The angle of rotation and the pitch angle of the wing are defined respectively as ϕ and α.

These experiments were performed in quiescent fluid. An original rotating and pitching apparatus was designed and constructed for these experiments as shown in Figure 4.2. One stepper motor drove a rotation stage while another stepper motor drove a system of belts and chain linkage, which were located inside the rotating shaft, controlling the pitching motion. The stepper motors were driven by micro stepper drivers controlled through LabView software. Encoders attached to the stepper motors were set to indicate the error of plus or minus 2 steps. Additionally, the mechanical lag in the components was estimated to be 1° and 2° respectively for the pitching and rotation motions.

The wing was rotated about the y-axis at an angular velocity $\dot{\phi}$ = 2.79 rad s^{-1}, corresponding to values of tip velocity V_{tip} = 310 mm s^{-1} and velocity at the radius of gyration V_{rg} = 204 mm s^{-1}. The Reynolds number based on the tip velocity was Re = 11 776. The reduced pitch rate had values of $K = \dot{\alpha}C/(2V_{rg})$ = 0.393, 0.262, and 0.098. Correspondingly, the reduced rotation rate had a value of $\Omega = \dot{\phi}C/(2V_{rg})$ = 0.261. For the experiments involving rotation, the wing reached a constant angular (rotation) velocity $\dot{\phi}$

at ϕ = 25.6° corresponding to τ = 0.86. Similarly, for experiments involving pitch-up motion, the wing reached constant angular (pitching) velocity $\dot{\alpha}$ at α = 9.7°, 14.5°, 19.3°, i.e., τ = 0.83, 0.48 and 0.43, for K = 0.098, 0.262, and 0.393 respectively. Slight smoothing, corresponding to a value of the parameter α = 700 of Eldredge & Wang (2010) was used at the beginning and end of the linear ramp-up motion to avoid possible vibration and transient effects. The side view of the wing in figure 4.1 (bottom schematic) shows the linear velocity in the plane of rotation of the wing V_{rg} at the radius of gyration and the angle of attack α. Also displayed in the side view are the positive directions of the *x*, *y*, and *z* axes.

The flow structure due to pure pitch-up of the wing provides a basis for comparison of the flow patterns arising from: pure rotation; and simultaneous pitch-up and rotation. The quantitative images from the pure pitch-up experiments of Yilmaz (2011), Yilmaz & Rockwell (2012) are employed for this comparison. In their experiments, the Reynolds number based on the velocity is $Re = UC/\nu$ = 10 000, in which U is the freestream velocity incident upon the nominally stationary (non-translating) pitching wing, and C is the wing chord. This value of Re is close to the aforementioned Reynolds number of Re = 11 776; previous experiments of Ozen & Rockwell (2011) indicate insensitivity of the flow structure to variations of Re on a rotating wing over this range of Reynolds number. Moreover, the reduced dimensionless pitch rate for pure pitching is K = 0.098; this value provides a reference pitch rate for the present experiments. Herein, the pitch rate of the wing undergoing simultaneous rotation has values less than, equal to, and greater than the non-dimensional rotation rate, Ω = 0.261. Due to the large amplitude unsteady motion, the very early development of the

flow structure will be dominated by the flow pattern induced by the pitch-up maneuver. The current case of a stationary pitching wing with incident freestream will therefore exhibit flow structure very similar to that of on an impulsively translating pitching wing when a reference frame transformation is employed.

Quantitative imaging via angular displacement stereo particle image velocimetry (SPIV) was used to determine the three-dimensional velocity field. In order to employ SPIV, the water was seeded with 12 μm hollow metallic coated plastic spheres, providing 15-20 particle images in the interrogation window size of 32 x 32 pixels^2. A 1 mm thick laser sheet was produced by a dual-pulsed Nd-YAG operating at 14.29 Hz. Images were acquired with a camera system having a CCD array of 1600 by 1200 pixels^2. Image pairs were acquired at an effective chordwise magnification for combined pitch-up-rotation of 9.088 pixels mm^{-1} and 9.482 pixels mm^{-1} for pure rotation. The acquired images were evaluated using a cross-correlation technique with 50% overlap, yielding 5856 and 6262 vectors in the field of view for the combined pitch-up-rotation and pure rotation respectively.

Image acquisition at the midspan of the wing was repeated ten times and the ten instantaneous images were phase averaged to produce final images. Three-dimensional images of stacked slices of spanwise vorticity $\omega_z C/V_{rg}$ and iso-surfaces of the parameter Q (defined subsequently) involved acquisition of six instantaneous images at each location of the laser sheet along the span of the wing; these images were then phase averaged prior to construction of a three-dimensional image. In order to change the position of the laser sheet along the span of the wing, a traverse system translates the

entire pitching-rotating wing assembly to successive spanwise locations. Image acquisition was performed on 46 planes for combined pitch-up and rotation and on 51 planes for pure rotation, with a spacing of $\Delta r/b$ = 0.024. The spatial separation of the velocity data on the PIV imaging planes for combined pitch-up and rotation is 1.74 mm and for pure rotation it is 1.67 mm, which corresponds to a non-dimensional distance of $\Delta x/b = \Delta y/b = 0.022$ and $\Delta x/b = \Delta y/b$ = 0.021 respectively. The total number of velocity vectors in the volume for combined pitch-up and rotation is 274 988 and for pure rotation 319 362.

An estimation of the in-and out-of-plane uncertainties followed procedures outlined in Adrian & Westerweel (2010), which indicated that the maximum bias error associated with the optical parameters in the experiment herein was approximately 5% of the maximum local velocity (V_{rg}). Additionally the RMS random error estimation of the in-plane instantaneous velocity vectors was between 4-5% of the maximum local velocity. The out-of-plane displacement is often expressed in terms of the error ratio, i.e. the ratio of random RMS error in the z-direction to the random RMS error in x-direction (assuming errors in x and y directions are equivalent). Using the theoretical relationship, $\sigma_{\Delta z}/\sigma_{\Delta x} \cong \tan\theta^{-1}$ Lawson & Wu (1997), where θ is the stereo half angle, the error ratio is equivalent to 2.41. The estimated random RMS in-plane error is $\sigma_{\Delta X}$ = 6.67-6.95 μm, therefore the estimated out-of-plane random RMS error is $\sigma_{\Delta Z}$ = 16.10-16.79 μm. An assessment of the uncertainty in the three-dimensional reconstruction techniques can be found in Yilmaz & Rockwell (2012).

The first group of experiments involves investigation of the flow structure at the midspan of the wing undergoing pure pitch-up, combined pitch-up and rotation, and pure rotation at sequential values of the convective time scale $\tau = tU/C$ or tV_{rg}/C. Imaging was performed from τ = 2 to the cessation of the pitch-up maneuver at τ = 4, corresponding to an angle of attack between α = 22.5° and 45°. Additionally, imaging was performed at τ = 5.6 while the wing remained at fixed angle of attack and continued to rotate. The schematics, shown at the bottom of figure 4.3, clarify the classes of wing motion. In the second group of experiments, three-dimensional volume images are constructed at τ = 4 for pure-pitch-up, combined pitch-up and rotation, and pure rotation. The final set of experiments provides sectional images of flow past a wing undergoing combined pitching and rotating motions at three different pitch rates; these images are compared with those from the corresponding case of pure rotation at fixed angle of attack. In addition, images taken during relaxation of the flow structure after cessation of the pitching motion while the wing continues to rotate provide further insight.

4.3 FLOW STRUCTURE: EVOLUTION OF SECTIONAL SPANWISE VORTICITY

Figure 4.3 shows patterns of normalized spanwise vorticity $\omega_z C/U$ and $\omega_z C/V_{rg}$ on a plane at the midspan of the wing for pure pitch-up, combined pitch-up and rotation and pure rotation. Imaging is performed at selected convective times scales during the pitching and rotation motions. In the case of the pure pitch-up experiments, the wing pitches from zero angle of attack α to α = 45°. For combined pitch-up and rotation, the wing is initially at α = 0°, and begins to pitch at the onset of rotation. Finally, the pure rotation experiments represent a wing rotating at different fixed angles of attack α.

Imaging is performed for each maneuver at values of convective time, τ = 2, 2.4, 3.2, 4, and 5.6. Images for the case of pure pitch-up in this figure, as well as in subsequent figures, are from the image data of Yilmaz & Rockwell (2012) and Yilmaz (2011).

The sectional images in the left column of figure 4.3 indicate that pure pitch-up gives rise to a leading-edge vortex that rapidly lifts away from the surface of the wing. In contrast, as indicated in the middle and right columns of figure 4.3, either combined pitch-up and rotation or pure rotation stabilizes the vorticity layer at the leading-edge of the wing. Of these motions, combined pitch-up and rotation yields a vorticity layer in closest proximity to the surface of the wing for all values of dimensionless time $\tau = tV_{rg}/C$. This observation is valid for imaging at the mid-span location. Three-dimensional imaging described in the foregoing sections reveals differences of the flow structure between combined pitch-up and rotation and pure rotation at the off-midplane locations. However, figure 4.3 demonstrates that the scale and shape of the leading-edge vortex are dominated by effects due to rotation, relative to the effects of pitch-up motion.

4.4 FLOW STRUCTURE: THREE DIMENSIONAL REPRESENTATIONS

4.4.1 Iso-Surfaces of Q-Criterion

Surfaces of iso-*Q* correspond to constant values of the second invariant of the velocity gradient tensor as defined in Hunt *et. al.* (1988).

$$Q = \frac{1}{2}[\Omega_{ij}\Omega_{ij} - S_{ij}S_{ij}] = -\frac{1}{2}\frac{\partial u_i}{\partial x_j}\frac{\partial u_j}{\partial x_i} \tag{1}$$

The *Q*-criterion indicates the magnitude of rotation relative to the amount of strain, where $\boldsymbol{\Omega}$ and $\boldsymbol{S}$ are the rotation and stress tensors respectively. When *Q* is positive,

rotation dominates the strain; therefore, vortical structures can be identified by positive values of *Q*.

Figure 4.4 shows three-dimensional iso-surfaces of the *Q* -criterion for pure pitch-up, combined pitch-up and rotation, and pure rotation. As indicated in the top image, the vortical structure on the purely pitching wing is dominated by a symmetric leading-edge vortex; at the midplane, the iso-surface extends along the chord and arches away from the surface of the wing. This pattern was originally computed by Visbal (2011), Visbal (2012) and described experimentally by Yilmaz & Rockwell (2012). The middle image of figure 4.4 indicates that, in presence of rotation, the three-dimensional vortex structure of the pitching wing is transformed to a conical, stable vortical structure along the leading-edge. Moreover, a stable tip vortex also exists, along with small-scale three-dimensional structures in the wake of the wing, which wind about the tip vortex. In contrast, for the case of the rotating wing, as illustrated in the bottom image of figure 4.4, the tip vortex has degenerated, and the region of the leading-edge vortex in the vicinity of the tip has also lost its coherence. Additionally, the tip vortex structure for the combined pitch-up and rotation is in the form of one consistent structure, in contrast to the pair of structures seen on the purely rotating wing, similar to the results of Poelma et al. (2006).

For the case of combined pitch-up and rotation shown in figure 4.4, the wing motion started at $\tau = tV_{rg}/C = 0$ at $\alpha = 0^{\circ}$ and pitched-up simultaneously during rotation to an angle of attack α = 45°. However, the angle of attack of the purely rotating wing was maintained at α = 45° from the onset of motion at a value of the convective time τ = 0. This difference in history of the wing motion indicates an important point regarding the coherence of the tip vortex. For the kinematics and Reynolds numbers examined here,

coherence is maintained if the angle of attack α is increased gradually during the pitch-up motion. On the other hand, if α is maintained constant from the onset of rotation, substantial degradation of the tip vortical structure occurs.

4.4.2 Three-Dimensional Patterns of Spanwise Vorticity

Figure 4.5 shows stacked sectional cuts of spanwise vorticity $\omega_z C/U$ for pure pitch-up and $\omega_z C/V_{rg}$ for combined pitch-up and rotation, and pure rotation. These sequences of patterns of spanwise vorticity along the span of the wing further indicate the coherence of the vortex structure, or lack thereof. For the case of the wing undergoing pure pitch-up, as well the wing experiencing combined pitch-up and rotation, the structure of the leading-edge vortex is well organized. Moreover, for the case of combined pitch-up and rotation, the structure of both the spanwise oriented (negative) vorticity and small-scale structures in the wake region are highly ordered. The small scale vortices from the trailing-edge suggest existence of a short wavelength Kelvin Helmholtz instability. In contrast, as evident in figure 4.6, for the case of the rotating wing, the leading-edge vortex, as well as the vorticity from the trailing-edge of the wing, show substantial loss of coherence, i.e., relatively strong disorder. This interpretation is based on the surfaces of iso-*Q*, which account for all three components of vorticity. On the other hand, as indicated in figure 4.5, which shows slices of only spanwise vorticity, such degradation of coherence is not evident in the leading-edge, but is indicated in the vortical structures from the trailing-edge of the wing.

4.4.2 Helicity and Three-Dimensional Streamline Patterns

Figure 4.6 displays three-dimensional streamlines and (colored) helical density on iso-*Q* surfaces for a wing undergoing pure pitch-up, combined pitch-up and rotation, and

pure rotation. These images are displayed in the fluid at infinity reference frame (fluid at rest at infinity). The helical density, *h*, or helicity per unit volume, is calculated by taking the scalar product of the three-dimensional velocity field $\boldsymbol{V}$ and the three-dimensional vorticity field $\boldsymbol{\omega}$ Moffatt (1969), i.e. , $h = (\mathbf{V} \cdot \boldsymbol{\omega})$. Helical density indicates to what degree a flow structure is three dimensional and serves as an indicator of vorticity flux on the primary axis of the vortex Carr et al. (2013a), Moffatt (1969), Le et al. (2011).

As shown in the top image of figure 4.6, values of *h* on the purely pitching wing have opposite signs, i.e., positive and negative coloring, on either side of the midplane of the wing, extending to a region ahead of the arch vortex. These contours indicate strong spanwise flow directed outboard from the plane of symmetry on either side of the arch vortex. For the combined pitching and rotating wing, a relatively large extent of positive *h* persists near the root of the leading-edge vortex. For the purely rotating wing, however, the spatial extent is much smaller in the same region of the leading-edge vortex. Correspondingly, the iso-*Q* surface that represents the leading-edge vortex has degenerated into a form involving several finger-like iso-*Q* surfaces along and downstream of the leading-edge. In essence, the larger extent of helicity close to the root of the leading-edge vortex on the wing undergoing simultaneous pitch-up and rotation is correlated with preservation of the integrity of the entire leading-edge vortex. Degradation of the leading-edge vortex for pure rotation is associated with the smaller concentration of positive helicity close to the root of the wing.

Regarding the structure of the tip vortices for the various types of wing motion shown in figure 4.6, consider first the case of pure pitch-up. For both of the tip vortices, high levels of positive and negative helicity *h* occur, indicating upstream flow through the

vortex cores. For simultaneous pitch-up and rotation, shown in the middle image of figure 4.6, the highly coherent tip vortex shows a region of large negative h on the iso-Q surface. Physically, this observation indicates a relatively large magnitude of the vector $\boldsymbol{V}$ oriented in a direction opposite to the primary axis of the vorticity vector $\boldsymbol{\omega}$. The purely rotating wing (bottom image) also has concentrations of negative h in the tip region; however, in this case, the onset of negative h occurs in the region where the tip vortex becomes disorganized or incoherent. Furthermore, the largest value of h extends only over a fraction of the diameter of the incoherent tip vortex.

The corresponding representations of three-dimensional streamlines given in figure 4.6 further characterize the flow structure along the span of the wing for each type of maneuver. For the case of pure pitch-up, streamlines are directed upstream through the cores of the tip vortices; moreover, streamlines are directed outboard from the plane of symmetry through the core of the leading edge vortex. For combined pitch-up and rotation, the streamlines are in accord with the well-organized conical leading-edge vortex and the tip vortex represented by the corresponding patterns of iso-Q and h. For the wing undergoing pure rotation, the corresponding streamlines indicate less organized and distorted leading-edge and tip vortices. For the case of combined pitch-up and rotation, the well-defined swirl of the tip vortex in the wake of the wing contrasts with the case of pure rotation, where the prominent feature is weak swirl, accompanied by flow in the upstream direction towards the leading-edge. This observation is consistent with the different patterns of helical density in the tip vortex of the combined pitching and rotating wing compared to the wing in pure rotation.

Taken together, all of the foregoing representations of patterns of iso-*Q*, helicity, and streamlines indicate the global influence of the simultaneous pitch-up and rotation of the wing, relative to the case of pure rotation. That is, enhanced magnitude and spatial extent of helicity and degree of organization of the streamline patterns extend all the way from the root region of the leading-edge vortex to the trailing region of the tip vortex. In the following, sectional representations of the flow structure are provided.

4.5 FLOW STRUCTURE: SECTIONAL REPRESENTATIONS

4.5.1 Sectional Patterns of Spanwise Vorticity

Figure 4.7 shows selected sectional slices of spanwise vorticity along the span of purely pitching, combined pitching and rotating, and purely rotating wings. The wing geometry in these images is stretched in the z-direction, in order to clearly display the vortex structure of the selected sectional slices. The range of dimensionless vorticity contour levels and incremental values are: for pure pitch-up, $\omega_z C/U$ = -20 to 2.8; with $\Delta(\omega_z C/U)$ = 1.2, and for combined pitch-up and rotation, as well as pure rotation, $\omega_z C/V_{rg}$ = -10 to 21.2 with $\Delta(\omega_z C/V_{rg})$ = 1.2.

For pure pitch-up, as shown in the top image of figure 4.7, the scale of the leading-edge vortex increases from the tips of the wing towards the plane of symmetry. At the plane of symmetry (plane D), the leading-edge vortex arches away from the surface of the wing. In the presence of rotation, i.e. , combined pitch-up and rotation and pure rotation, which is represented by the middle image of figure 4.7, the structure of the leading-edge vortex takes the form of an elongated pattern of vorticity, in comparison with the aforementioned vorticity concentration arising from pure pitch-up motion of the

wing. This elongated pattern increases in scale and begins to lift away from the surface of the wing, with increasing distance along the span, i.e., from the root to the tip. This trend is more severe for the case of pure rotation shown in the bottom image of figure 4.7, relative to the case of combined pitch-up and rotation, i.e., the vorticity layers are deflected away from the surface of the wing to a larger degree at larger spanwise distances from the root. This enhanced outward deflection of the vorticity layers for the case of pure rotation occurs in conjunction with loss of organization, or coherence, of the three-dimensional structure of the leading-edge vortex as the tip is approached, illustrated by the iso-surfaces of figures 4.4 and 4.6. On the other hand, vorticity layers remaining closer to the surface of the wing during combined rotation and pitching is associated with retention of the coherent structure of the leading-edge vortex in figures 4.4 and 4.6.

4.5.2 Sectional Downwash

Figure 4.8 shows sectional contours of the v-component of velocity, which is normal to the linear velocity in the plane of rotation of the wing, as indicated in the schematics. These contours are superposed on the sectional images of spanwise-oriented vorticity along the spans of wings undergoing pure pitch-up, combined pitch-up and rotation, and pure rotation, described in figure 4.7.

For pure pitch-up, as shown in the top image of figure 4.8, the scale of concentrations of positive *v*-velocity, i.e., downwash, diminishes from the tips of the wings towards the plane of symmetry. The edge of large magnitude downwash at each sectional location is coincident with the edge of the vorticity concentration of the leading-edge vortex, despite the increase in scale and proximity to the wing surface of the leading-edge vortex near the plane of symmetry. In presence of rotation, as indicated in

the middle and bottom images of figure 4.8, the change of character of the leading-edge vortex influences the distribution of the v-component along the span. For the combined pitch-up and rotation maneuver (middle image), large-scale positive levels of *v*-component (downwash) persist along the span, and close to the leading edge, of the wing until plane *F*. Starting on plane *D*, the downwash concentration begins to diminish in scale, decreasing successively to a smaller scale on planes *E* and *F*, and eventually is not detectable on plane G, corresponding to the tip of the wing. Moreover, smaller-scale clusters of negative *v*-component (upwash) exist in the region of the trailing edge on planes *E*, *F*, and *G*. They are located adjacent to the slices of concentrated vorticity that represent the tip vortex, which is deflected across the wake, as shown in figure 4.4. In fact, the concentrations of downwash on planes *D*, *E*, and *F* are bounded on one side by the slices of vorticity concentration of the deflected tip vortex (located downstream of the trailing edge) and on the other side by the leading-edge vortex. Additionally, the presence of this large scale concentration of downwash downstream of the leading-edge suggests a relationship between the two components, i.e. the large scale concentrations of downwash are consistent with proximity of the vortex structure to the leading edge of the wing.

For pure rotation, shown in the bottom image of figure 4.8, generally similar patterns of downwash and upwash occur in relation to the slices of spanwise vorticity of the leading-edge vortex and the tip vortex that is deflected across the wake. Slight distinctions do occur, however, relative to the foregoing case of combined pitch-up and rotation. Downwash persists as a large-scale region from the root of the wing to plane *E* to a location slightly beyond the midplane of the wing. Similar to the case of combined pitch-up and rotation, the downwash concentrations on planes *D* and *E* appear to be

bounded by the leading-edge and tip vortices. The sectional pattern of vorticity from the leading-edge is detected well away from the surface of the wing on plane *F*; correspondingly, the concentration of downwash disappears, suggesting that presence of downwash in proximity to the leading-edge vortex is consistent with vortex coherence as in the case of combined pitch-up and rotation. Furthermore, concentrations of upwash are evident in plane *E* and become more pronounced in planes *F* and *G*. Despite the relative loss of coherence, i.e, onset of disorder, of the system of the leading-edge and tip vortices for the case of pure rotation, the sectional representations of downwash are qualitatively similar to the case of combine pitch-up and rotation.

4.5.3 Sectional Spanwise-Oriented Velocity

Figure 4.9 shows sectional contours of the w (spanwise) component of the velocity field superposed on sectional vorticity contours at the indicated locations *A* through *G* along the span of the wing. The top, middle and bottom images correspond respectively to pitch-up, combined pitch-up and rotation, and rotation.

For the case of pure pitch-up (top image of figure 4.9), the spanwise velocity component w is always oriented towards the plane of symmetry of the wing. Correspondingly, concentrations of positive and negative w-component are located on either side of the midplane of the wing. This representation is compatible with the streamline representation in figure 4.6, which shows counter rotating swirl patterns having a component parallel to the surface of the wing.

For the combined pitch-up and rotation case (middle image of figure 4.9), regions of positive spanwise flow are present on all planes extending from *A* to *G*. As the scale of

the sectional pattern of vorticity increases at successive planes *A* through *D* along the span, the sectional concentrations of positive w-component move further downstream and extend well into the wake. On the other hand, on planes *E* through *G*, the concentrations of positive w-component are coincident with the sectional vorticity concentrations of the tip vortex that is deflected across the wake (compare the iso-*Q* image of figure 4.4). As concentrations of positive w-component move downstream of leading-edge in planes *E*, *F*, and *G*, patterns of negative w-component form near the leading edge; they indicate induced flow from the tip vortex in the negative z-direction towards the root of the wing.

For pure rotation (bottom image of figure 4.9), the patterns of spanwise velocity are broadly similar to the foregoing case of pitch-up and rotation, but distinctions are evident. On planes *D* through *G*, only concentrations of negative *w*-component are associated with the sectional patterns of vorticity of the leading-edge vortex, and both the sectional vorticity layers and the negative regions *w*-component are deflected further above the surface of the wing than for the case of pitch-up and rotation shown in the middle image of figure 4.9. As the leading-edge vortex begins to deflect from the surface of the wing, significant negative concentrations of w develop in planes *E*, *F*, and *G*. This enhanced extent of the region of negative *w* is associated with the onset of disorder, i.e., loss of coherence, at the junction of the leading-edge vortex and the tip vortex, as shown by the surface of iso-*Q* in figure 4.4.

4.5.4 Sectional Spanwise-Oriented Vorticity Flux

Figure 4.10 shows sectional contours of spanwise vorticity flux, $\omega_z Cw/(U)^2$ and $\omega_z Cw/(V_{rg})^2$ superposed on sectional contours of spanwise-oriented vorticity along the spans of wings undergoing pure pitch-up, combined pitch-up and rotation, and pure rotation.

For the case of pure pitch-up (top image of figure 4.10), positive and negative regions of spanwise vorticity flux occur at sections where the leading-edge vortex is relatively concentrated and remains close to the surface of the wing, i.e. , planes *B* and *F*. On planes *C* and *E*, negative and positive flux occurs along the trailing portion of the vorticity concentration of the sectional cut of the leading-edge vortex. Moreover, the flux is zero along the plane of symmetry of the wing, i.e., plane *D*.

For the combined pitch-up and rotation maneuver (middle image of figure 4.10), positive concentrations of spanwise vorticity flux exist on planes *A* to *F* where the sectional cut of vorticity is well organized and remains close to the surface of the wing. On these planes, concentrations of positive flux coincide with the core of the leading-edge vortex. This persistence of positive flux across the entire span of the wing, especially in the region extending from the midspan to the tip, is associated with the highly coherent leading-edge and tip vortices in that region, as shown in the iso-*Q* plot of figure 4.4. Representative previous investigations that have pointed out existence of a stable leading-edge vortex in the presence of substantial spanwise velocity along the wing include Ellington et al. (1996), Lentink & Dickinson (2009b), Ozen & Rockwell (2012), and Garmann & Visbal (2014). Garmann & Visbal (2014) interpret the stabilization of the leading-edge vortex in terms of the spanwise pressure gradient and the centripetal

component of acceleration; the Coriolis component of acceleration was found not to exert a significant influence. Concentrations of negative flux associated with outboard flux of negative vorticity, form downstream from the trailing edge on planes *D* through *G* and are associated with deflection of the tip vortex across the wake, evident in the iso-*Q* patterns of figure 4.4.

For the wing undergoing pure rotation (bottom image of figure 4.10), positive concentrations of spanwise vorticity flux are coincident with the leading-edge vortex only in planes *A*, *B*, and *C*. Starting in plane *D*, the sectional cut of the vorticity layer, which represents the leading-edge vortex, elongates, lifts away from the surface of the wing on planes *E*, *F*, and *G*. On planes, *D*, *E*, *F* and *G*, only negative concentrations of flux occur. This existence of only negative flux between the midspan and the tip of the wing is associated with onset of disorder, i.e., loss of coherence, at the junction of the leading-edge vortex and the tip vortex, as shown in the iso-*Q* plot of figure 4.4. Moreover, this negative flux associated with the leading-edge vortex is complemented by negative flux in the region of the trailing-edge, associated with deflection of the tip vortex across the wake.

4.6 FLOW STRUCTURE: EFFECT OF PITCH-RATE

4.6.1 Vortical Structures at Leading-Edge and From Trailing-Edge

Figure 4.11 (left column) shows images for combined pitch-up and rotation, where the rate of pitch-up is greater than, equal to, and less than the rate of rotation. That is, the variation of pitch rate was selected so that the wing completed the pitch-up maneuver at $\alpha = 45^{\circ}$ at values of τ = 1, 1.5, and 4, where $\tau = tV_{rg}/C$; the corresponding

values of reduced pitch rates $K = \dot{\alpha}C/(2V_{rg})$ are K_1 = 0.393, K_2 = 0.262, and K_3 = 0.098. The matching cases of pure rotation at fixed angle of attack α = 45° are given in the right column of figure 4.11. To quantify the strength of the vortical structures present in figure 4.11, the circulation of each vortical structure was calculated by integrating the spanwise vorticity normal to a rectangular box encompassing the desired vortical structure. The location of the rectangular boundary (box) was determined by a vorticity threshold, this threshold being 10% of the maximum positive and negative contour levels. Non-zero vorticity values within the box below the threshold value were not considered for the circulation calculation.

$$\Gamma = \iint \omega_z dxdy \tag{2}$$

In the left column of Figure 4.11, it is evident that the streamwise length of the region of highest positive (red) vorticity $\omega_z C/V_{rg}$ increases with decreasing K. This corresponds to an increase in non-dimensional circulation $\Gamma/V_{rg}C$ of the leading-edge vortex, i.e., $\Gamma/V_{rg}C$ = 0.59, 0.86, and 1.57 for K_1, K_2, and K_3 respectively. Positive circulation values for the leading-edge vortex from Sections 4.6.1 and 4.6.2 are compiled in Table 4.1 for reference. This general trend occurs for the corresponding cases of pure rotation given in the right column of figure 4.11. However, the corresponding cases of pure rotation show a distinctly different development of the structure of the leading-edge vortex, if one compares images at a given value of dimensionless convective time scale τ. For combined pitch-up and rotation, where the motion starts at zero angle of attack, the vorticity layer remains closer to the surface of the wing for all time scales. The wing undergoing pure rotation, where the angle of attack is fixed at 45°, shows a vorticity layer

deflected away from the wing that tends to form a vorticity concentration and has a larger overall scale than the corresponding vorticity concentration due to combined pitch-up and rotation. This observation is confirmed by the relatively larger values of circulation $\Gamma/V_{rg}C$ = 1.31, 1.59, and 1.95 of the leading-edge vortex at ϕ = 30°, 45°, and 125° for pure rotation (see table 4.1).

Formation of concentrations of vorticity from the trailing-edge of the wing is also influenced by the nature of the wing motion. For the case of combined pitch-up and rotation (left column of figure 4.11), a train, or succession of small-scale concentrations of vorticity, apparently due to a Kelvin-Helmholtz instability, is evident in the region downstream of the trailing-edge. Similar representations of *K*-H instabilities on a rotating wing were computed by Wilkins & Knowles (2007) and confirmed experimentally by Ansari et al. (2009) Ansari et al. (2011).

These concentrations are designated by a, b, c, d, and e with subscripts 1, 2, and 3, which correspond to pitch rates K_1, K_2, and K_3. The wavelength between them is in the range $0.29C$ to $0.43C$, where C is the wing chord. For the highest pitch rate K_1, the distinct structures a_1, b_1, c_1, and d_1 remain in close proximity to one another with a low level layer of vorticity forming between each structure. With decreasing pitch rate, and hence increasing convective time of the maneuver, the sequence of vortices becomes more distinct and extends further into the wake of the wing as evidenced by the vortical structures a_2, b_2, c_2, d_2, e_2 and a_3, b_3, c_3, d_3, e_3. As indicated in the bottom left image of figure 4.11, a further type of vortical structure, designated as TV, is present. This structure is not shed from the trailing-edge, rather, it is the cross-section of the tip

vortex that is deflected across the wake, shown by the iso-Q surface in figure 4.3. The circulation of the TV structure in this case has a magnitude close to that of the leading-edge vortex LEV, i.e., $\Gamma/V_{rg}C(TV)$ = -1.62 and $\Gamma/V_{rg}C(LEV)$ = 1.92.

For pure rotation (right column of figure 4.11), such a well-preserved sequence of small-scale vortices does not occur. At $\tau = tV_{rg}/C$ = 1, three small-scale vortices indicated by a, b, and c tend to coalesce immediately downstream of the trailing-edge. At τ = 1.5 concentrations a and b are distinguishable; however, c appears to have rolled up into the TV vortex structure. At τ = 4, small-scale concentrations are not identifiable; only a large tip vortex TV is evident. The circulation of the TV vortex structure grows with increasing rotation angle, having values $\Gamma/V_{rg}C(30^\circ)$ = -0.48, $\Gamma/V_{rg}(45^\circ)$ = -0.70, and $\Gamma/V_{rg}C(125^\circ)$ = -1.41.

ϕ	Pure Rotation	K_1	K_2	K_3
30°	1.31	0.59	–	–
45°	1.59	–	0.86	–
125°	1.95	1.87	1.89	1.57
210°	–	–	–	1.92

Table 4.1: Normalized Positive Circulation of LEV

4.6.2 Relaxation of Vortical Structures

Figure 4.12 illustrates the relaxation of flow after the pitching motion is completed for the combined pitch-up and rotation maneuver for reduced pitch rates K_1, K_2, and K_3. The images in the left column are at the end of the pitch-up motion that terminates at α = 45°. The right column of images represents the vortex structure after

completion of pitching while the wing continues to rotate. The delay between the cessation of the pitch-up motion (left column) and the acquisition of each image (right column) is maintained constant at values in the window of ϕ = 85° to 95°, corresponding to the window of convective time of $\tau = tV_{rg}/C$ = 2.5 to 3.

It is evident that, despite the substantial differences of rate of pitch-up and the corresponding distinctions of the flow structure given in the left column of images of figure 4.12, the relaxation process gives rise to broadly similar, extended regions of vorticity concentrations. Of particular note, after the relaxation process, the sequence of vortical structures from the trailing-edge, denoted by a_1, b_1, c_1, and d_1 in the left column of figure 4.8 appear to have rolled up into the cross-sectional tip vortex *TV*, designated in the right column of figure 4.12.

The circulation of the leading-edge vortex shown in the images in the left column of figure 4.12, compared to the images in the right column, further exemplifies the relaxation process. Namely, the circulation of the leading-edge vortex corresponding to the left column of images increases with decreasing K, i.e. , $\Gamma/V_{rg}C$ = 0.59 at K_1, $\Gamma/V_{rg}C(K_2)$ = 0.86, and $\Gamma/V_{rg}C(K_3)$ = 1.57. After relaxation, however, the strength of the leading-edge vortex in the right column of images is very similar, i.e. , $\Gamma/V_{rg}C(K_1)$ = 1.87, $\Gamma/V_{rg}C(K_2)$ = 1.89, and $\Gamma/V_{rg}C(K_3)$ = 1.92, despite the different initial conditions (see table 4.1 for reference). Similarly, the strength of the negative vortex agglomerations designated by *TV* in the right column are comparable, $\Gamma/V_{rg}C(K_1)$ = -1.62, $\Gamma/V_{rg}C(K_2)$ = -1.32, and $\Gamma/V_{rg}C(K_3)$ = -1.32.

Despite large variation of the pitch-up rate relative to the rotation rate of the wing, the foregoing observations indicate that a common state of the flow structure, both at the leading-edge and from the trailing-edge, is rapidly attained after cessation of the pitch-up motion. This relaxation process occurs within a time scale corresponding to a few chords of wing travel. The onset of the common state is thereby insensitive to the time scale of the pitch up motion of the wing at the beginning of wing motion. Rotational effects, more specifically centripetal acceleration and spanwise pressure gradients, prevail once the pitch-up motion has terminated. For each case of combined pitch-up and rotation, the rotation rate is the same, explaining the similar relaxation process.

4.7 CONCLUSIONS

The flow patterns due to pure pitch-up and pure rotational motions of a wing have been addressed extensively in previous investigations. Very little is understood, however, of the flow structure on a wing subjected to simultaneous pitching and rotation, which is the subject of the present investigation. The new flow physics revealed herein for these simultaneous motions includes: stabilization of the large-scale vortex generated at the leading-edge; preservation of a coherent tip vortex-leading-edge vortex system; generation of a highly ordered vortex system from the trailing-edge of the wing; and rapid relaxation of the flow structure to a common state upon termination of the pitch-up component of the simultaneous pitch-up and rotational motions of the wing. The specifics of these concepts are summarized in the following.

4.7.1 Effects of rotation on the flow structure induced by pitch-up motion of a wing

The pitch-up motion of a wing is a classic maneuver that gives rise to a large-scale leading-edge vortex, which moves away from the wing and in the downstream

direction with increasing time. If the wing has a small aspect ratio, formation of the leading-edge vortex takes the form of an arch vortex, and at the plane of symmetry of the wing, the large-scale vortex rapidly departs from the leading-edge. It is demonstrated herein that the nature of the pitch-induced vortex at the leading-edge is fundamentally altered in presence of wing rotation. That is, the leading-edge vortex remains at, and close to, the surface of the leading-edge of the wing with the addition of rotation.

This observation, which indicates dominance of the effects of wing rotation, is associated with the following features of flow structure. In presence of rotation, the spanwise velocity along the wing has a large magnitude and is unidirectional, except in the tip region; this pattern of spanwise velocity contrasts with the pattern on the purely pitching wing (without rotation), where the sign of the spanwise velocity is opposite on either side of the plane of symmetry of the wing. Moreover, it is possible to attain spanwise flux of vorticity through the leading-edge vortex that is unidirectional along the span of the wing for combined pitching and rotation, in contrast to the oppositely-directed vorticity flux on either side of the plane of symmetry of the purely pitching wing. Finally, in the presence of rotation, patterns of large magnitude downwash on the pitching-rotating wing extend to a region close to the leading-edge, in contrast to the purely pitching wing, where they are displaced to a larger chordwise distance. All of these features contribute to the fundamental difference of the three-dimensional surfaces of iso-Q, which exhibit a conical leading-edge vortex in the presence of rotation, in contrast to the arch leading-edge-vortex for pure pitching.

4.7.2 Effects of rotation on the flow structure induced by pitch-up motion of a wing: relaxation after cessation of pitch-up

A further indicator of the strong influence of rotation is the rapid relaxation of the flow structure upon termination of pitch-up, irrespective of the value of pitch rate. When the rate of rotation is held constant, and the pitch rate takes values less than, equal to, and greater than the rotation rate, the sectional cut of the leading-edge vortex at the midspan of the wing shows different degrees of development at the end of the pitch-up motion. Yet, after only a few convective time scales of the wing rotation, the leading-edge vortex evolves to a form characteristic of pure rotation of the wing over the entire range of the maneuver. That is, it is stable, in an elongated form, and remains close to the surface of the wing. Moreover, the circulation of the leading-edge vortex at the end of this brief relaxation process has nearly the same value for all values of initial pitch rate. Likewise, the sequence of vortices from the trailing-edge of the wing shows different patterns at the end of the pitch-up motion, but collapse to a similar form dominated by the deflected tip vortex at the end of relaxation. In essence, consideration of a large range of values of the pitch-up rate relative to the rotation rate of the wing shows that a common pattern of vortical structures rapidly develops after termination of the pitch-up motion. This common pattern, or state, which involves structures at the leading-edge and downstream of the trailing-edge, is attained within a relatively small convective time scale, corresponding to a few chords of wing travel. The onset of the common state is associated with the dominant effects of centripetal acceleration and spanwise pressure gradient due to equivalent rotation rates for each maneuver.

4.7.3 Effects of rotation on the flow structure induced by pitch-up motion of a wing: comparison with the flow structure arising from pure rotation

From the foregoing, it is evident that the effects of rotation have a strong influence on the flow structure during pitch-up. The distinctions between the flow structure on a wing undergoing combined pitch-up and rotation and a wing in pure rotation have been identified in the present investigation. For pure rotation, it is shown that the coherence of the tip vortex is substantially degraded at sufficiently large rotation angle. This degradation extends into the outboard region of the leading-edge vortex. With simultaneous pitch-up and rotation, however, the coherence of the entire tip-leading-edge vortex system is maintained. These features are evident from comparison of iso-Q surfaces. Superposed surfaces of helical density show regions of large magnitude positive and negative helical density respectively extending across the leading-edge vortex and the tip vortex for simultaneous pitch-up and rotation. Corresponding patterns of streamlines show well defined swirl throughout the leading-edge-tip vortex system; in contrast, for pure rotation, the ordered nature of the swirl streamlines is disrupted and there is upstream flow through the disordered tip vortex.

Sectional representations of the flow structure along the span of the wing indicate that, in the region from the midspan to the tip of the wing, the effect of the combined pitch-up and rotation motion is to retain the sectional patterns of spanwise vorticity close to the surface of the wing and maintain positive vorticity flux through the regions of large spanwise vorticity, in conjunction with large magnitude downwash extending close to the tip of the wing. All of these features are not attained for the case of pure rotation of the wing.

In the region downstream of the trailing edge of the wing, patterns of vortical structures are distinctly different for the cases of simultaneous pitch-up rotation, in

comparison with pure rotation. For the former, a highly ordered series of small-scale vorticity concentrations, with nearly constant wavelength between them, is formed from the trailing-edge. On the other hand, for the case of pure rotation, the structure from the trailing-edge is not so ordered, and the near-wake is dominated by the deflected tip vortex across the wake.

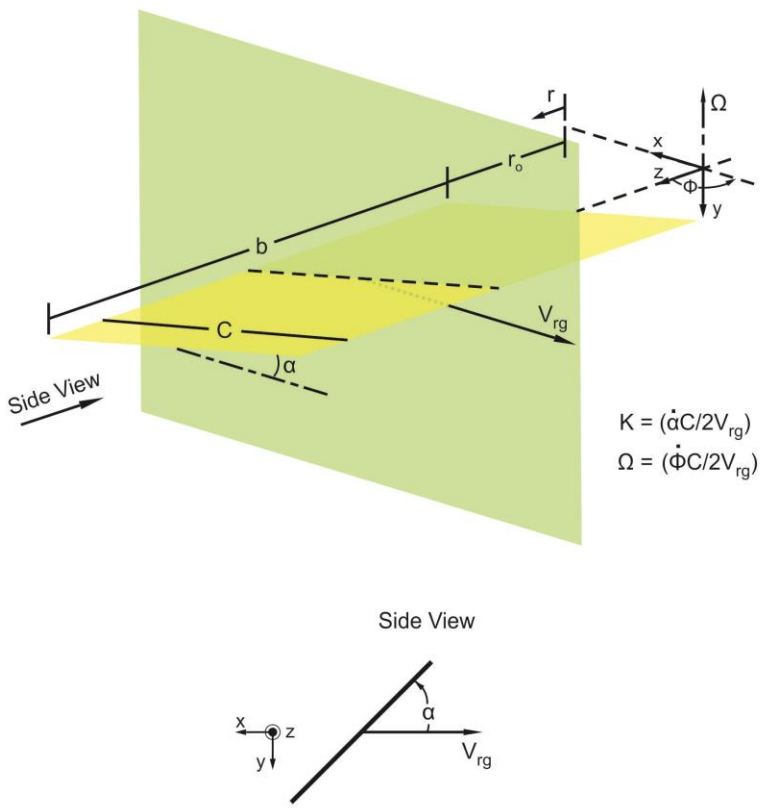

Figure 4.1: Schematic of rotating-pitching wing and related parameters

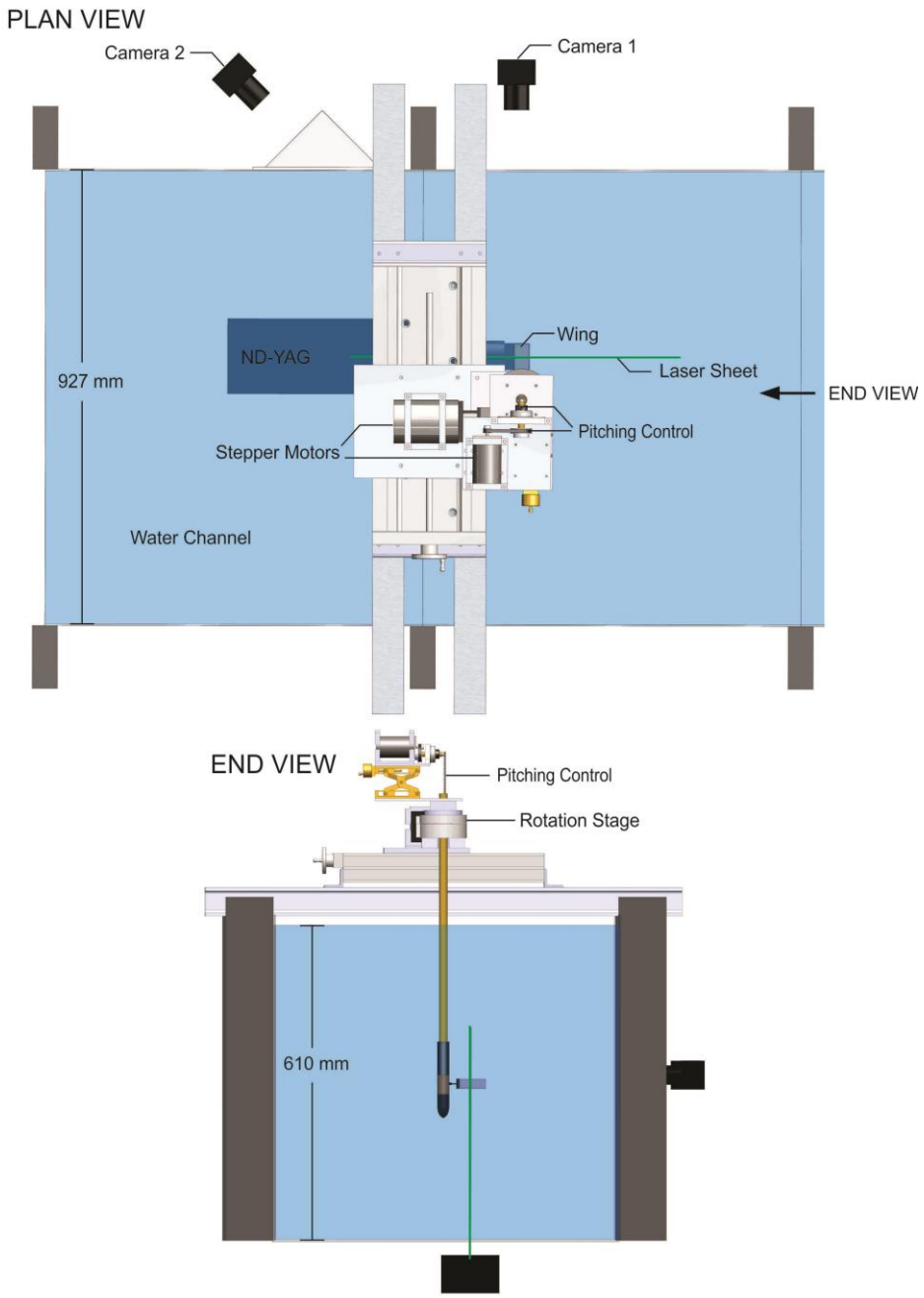

Figure 4.2: Schematic of rotating-pitching wing apparatus and PIV arrangement

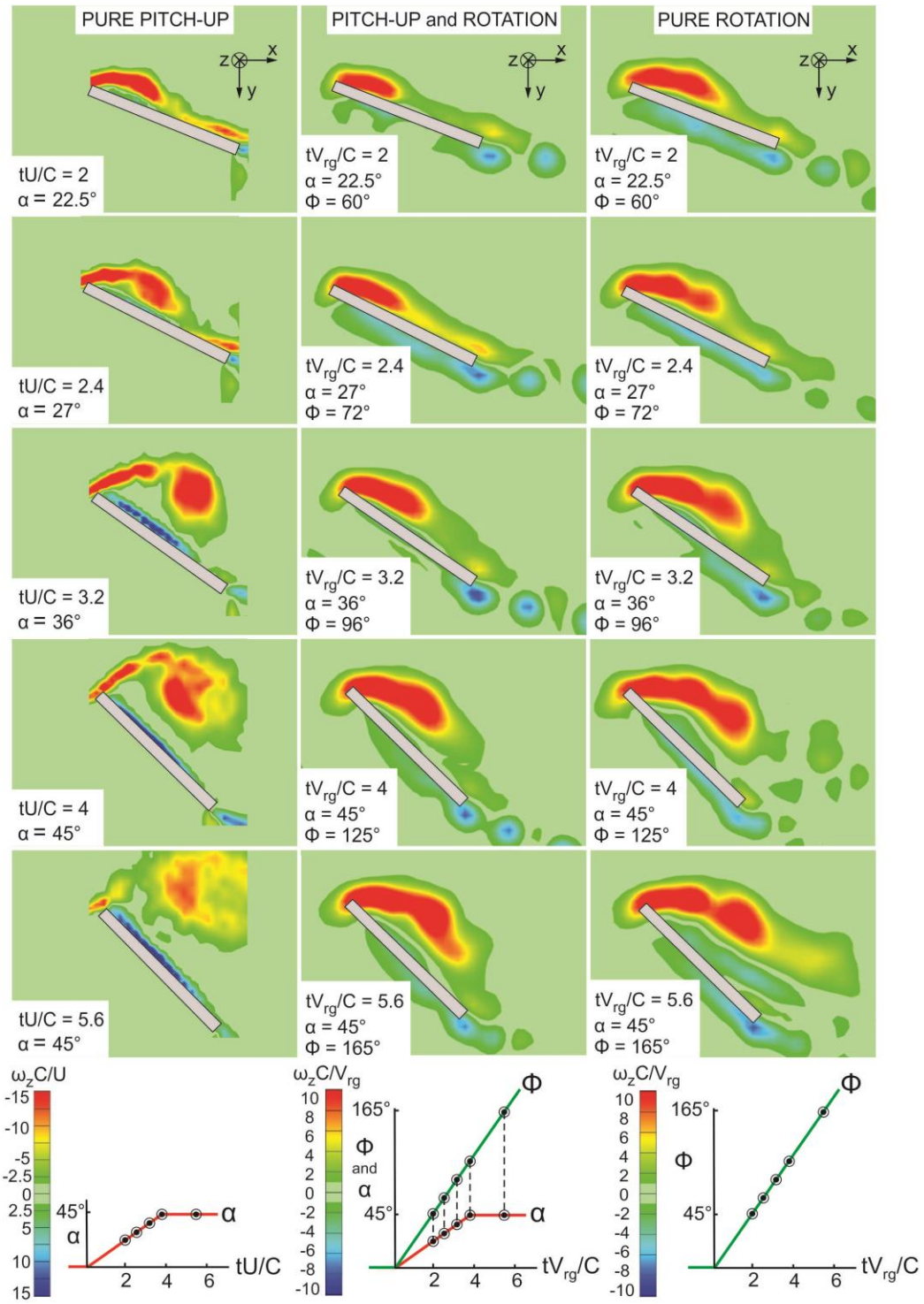

Figure 4.3: Sectional images of spanwise vorticity $\omega_z C/U$ and $\omega_z C/V_{rg}$ at midspan of wing for: pure pitch-up; pitch-up and rotation; and pure rotation at convective times, $\tau = tU/C$ or tV_{rg}/C = 2, 2.4, 3.2, 4, and 5.6. Images for pure pitch-up were determined from data set of Yilmaz (2011).

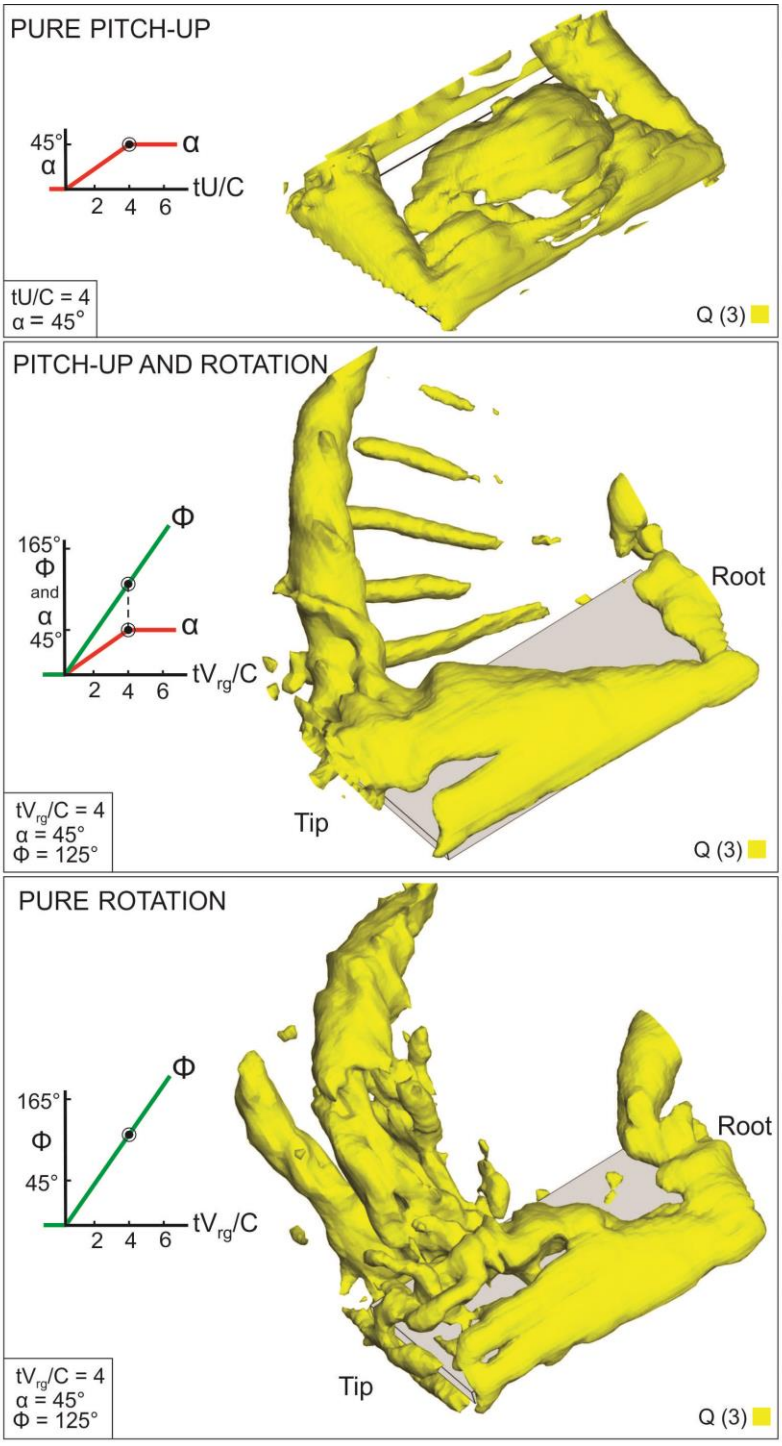

Figure 4.4: Iso-surfaces of Q-criterion for pure pitch-up, pitch-up and rotation, and pure rotation of wing. Image for pure pitch-up was constructed from data set of Yilmaz (2011).

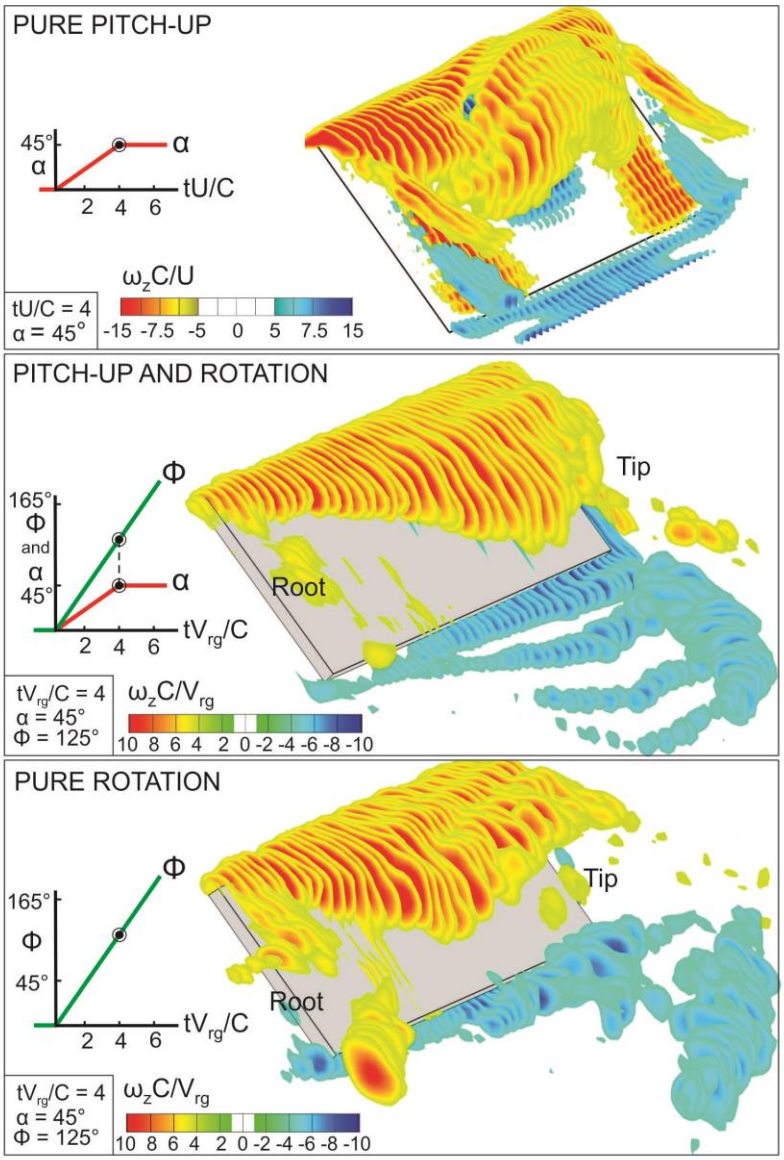

Figure 4.5: Sectional images of spanwise oriented vorticity, $\omega_z C/U$ and $\omega_z C/V_{rg}$ along span of wing undergoing pitch-up, pitch-up and rotation, and rotation. Image for pure pitch-up was constructed from data set of Yilmaz (2011).

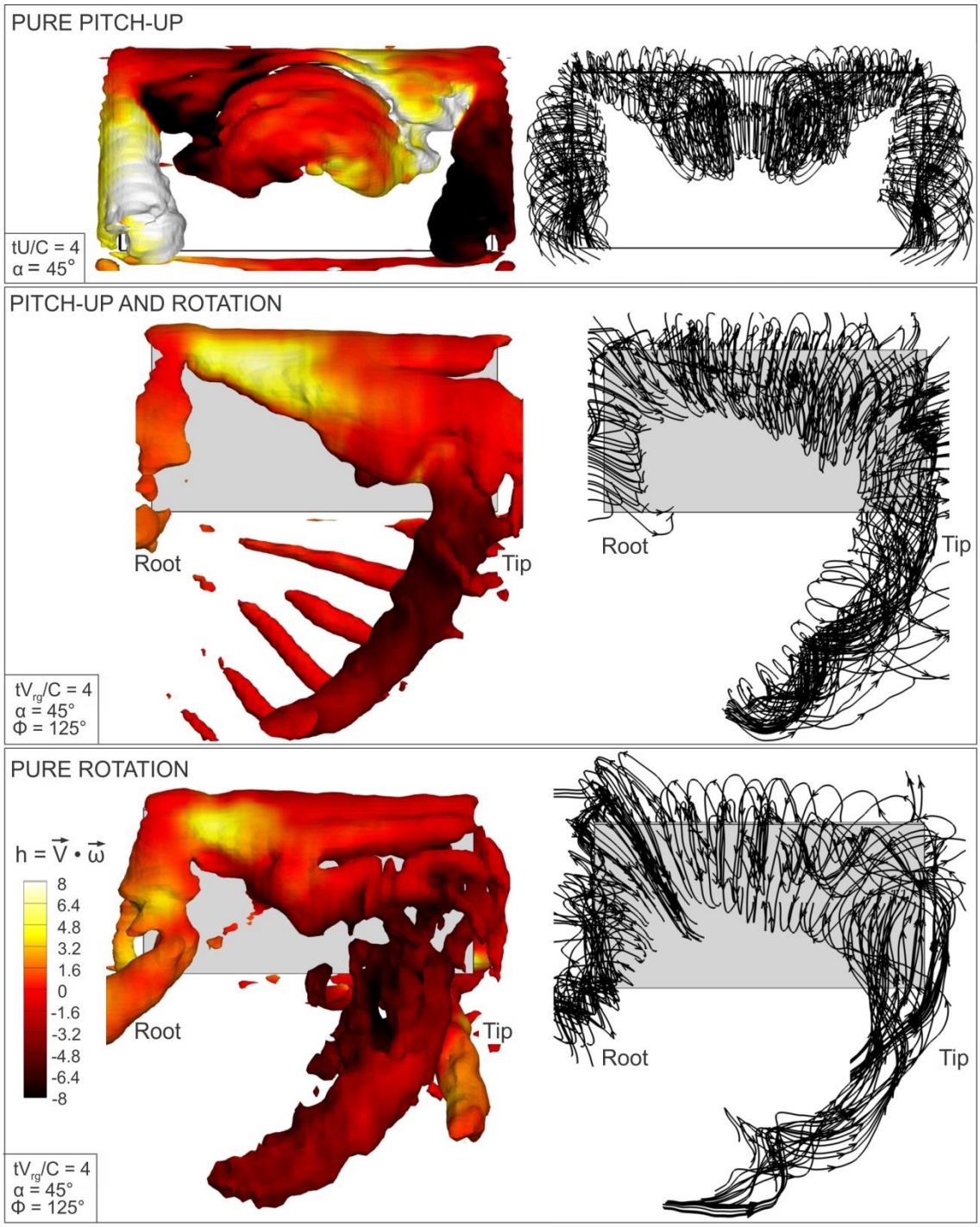

Figure 4.6: Streamlines and colored helical density h on iso-Q surfaces for flat plate undergoing pitch-up, pitch-up and rotation, and rotation. For pure pitch-up, h-Q and streamlines images were constructed from data set of Yilmaz (2011).

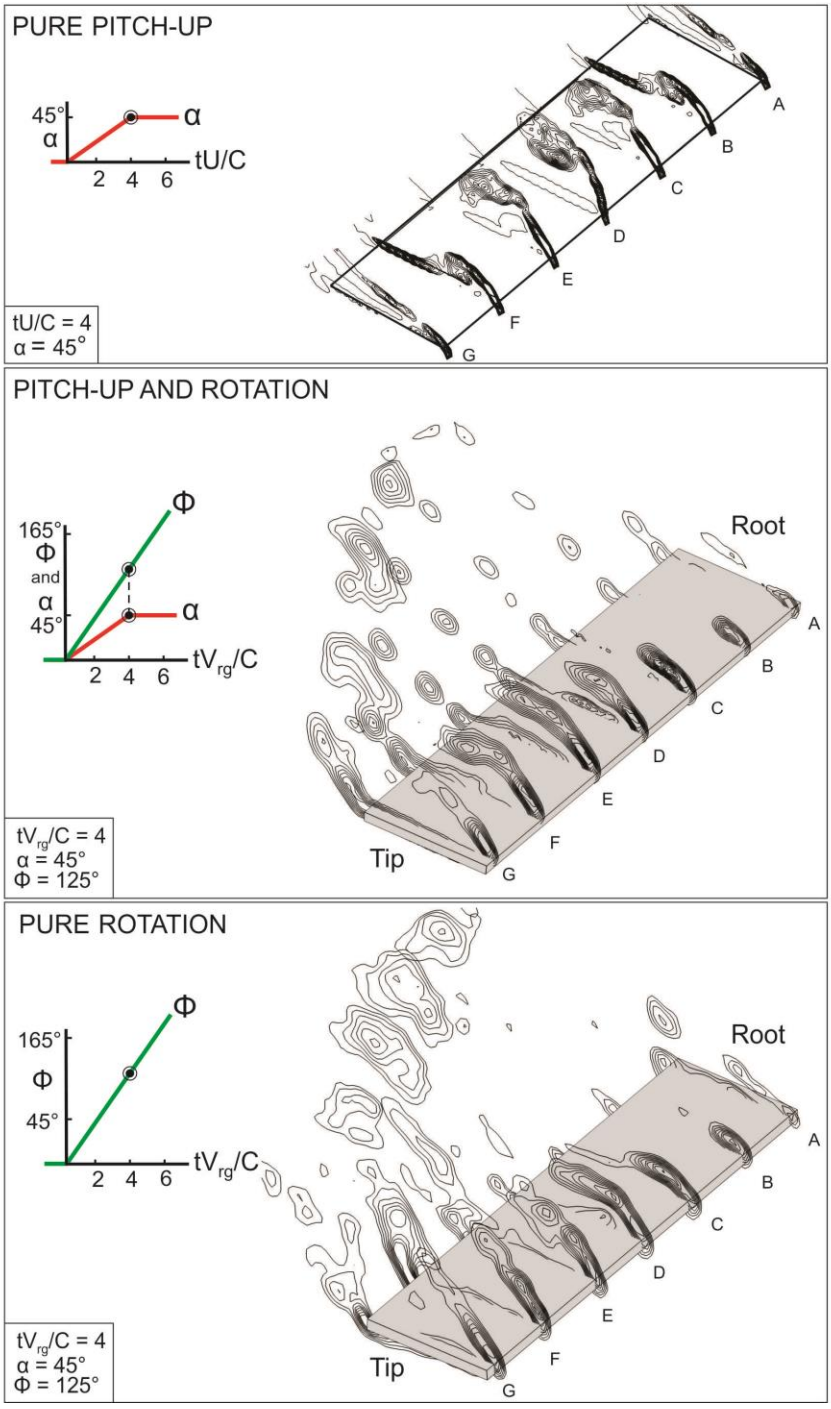

Figure 4.7: Sectional images of spanwise-oriented vorticity, $\omega_z C/U$ and $\omega_z C/V_{rg}$ along span of wing undergoing pitch-up, pitch-up and rotation, and rotation. For pure pitch-up, images in Figures 7-10 were determined from data set of Yilmaz (2011).

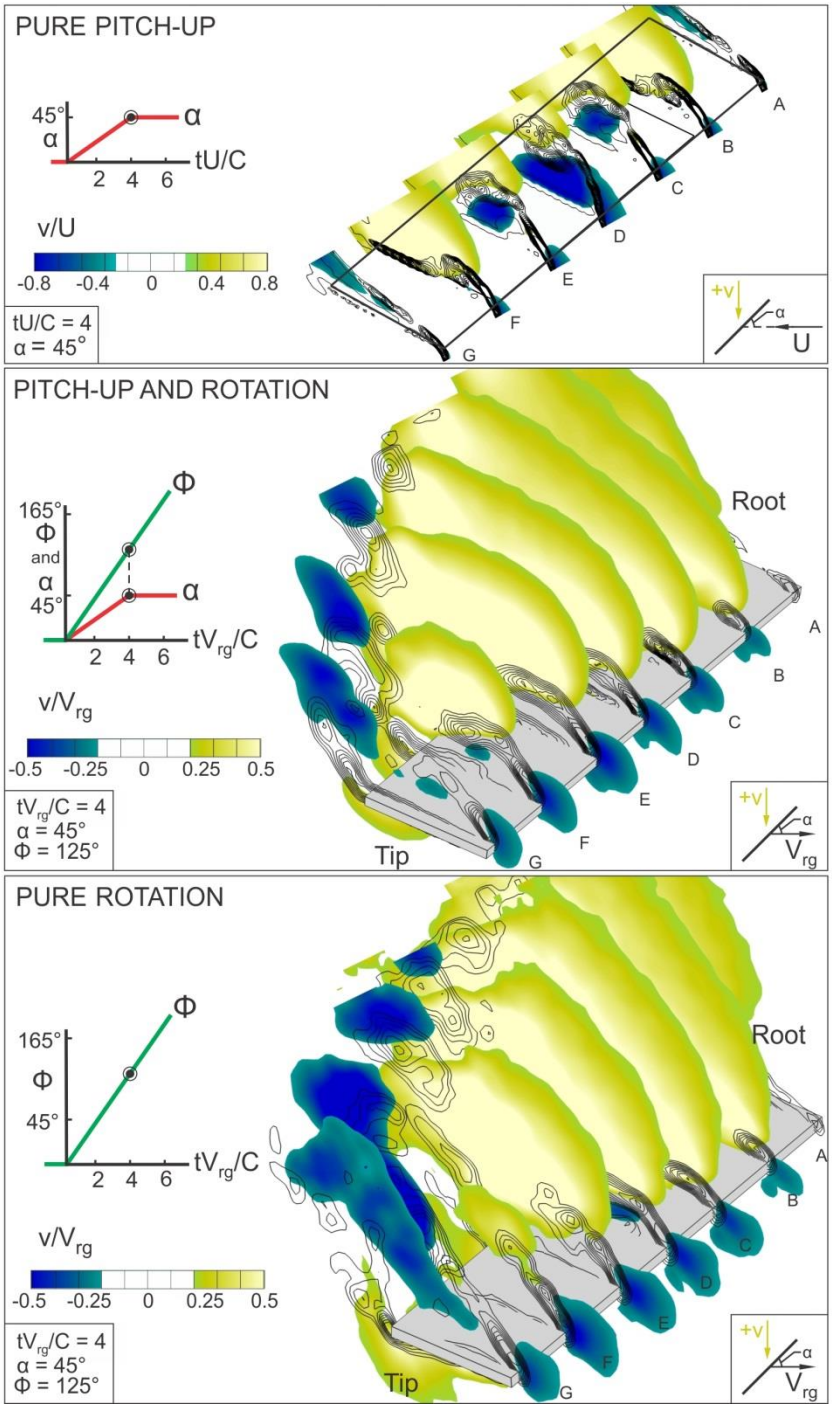

Figure 4.8: Sectional (color) contours of v-component of velocity superposed on sectional (black line) contours of spanwise-oriented vorticity, $\omega_z C/U$ and $\omega_z C/V_{rg}$ along span of wing undergoing pitch-up, pitch-up and rotation, and rotation.

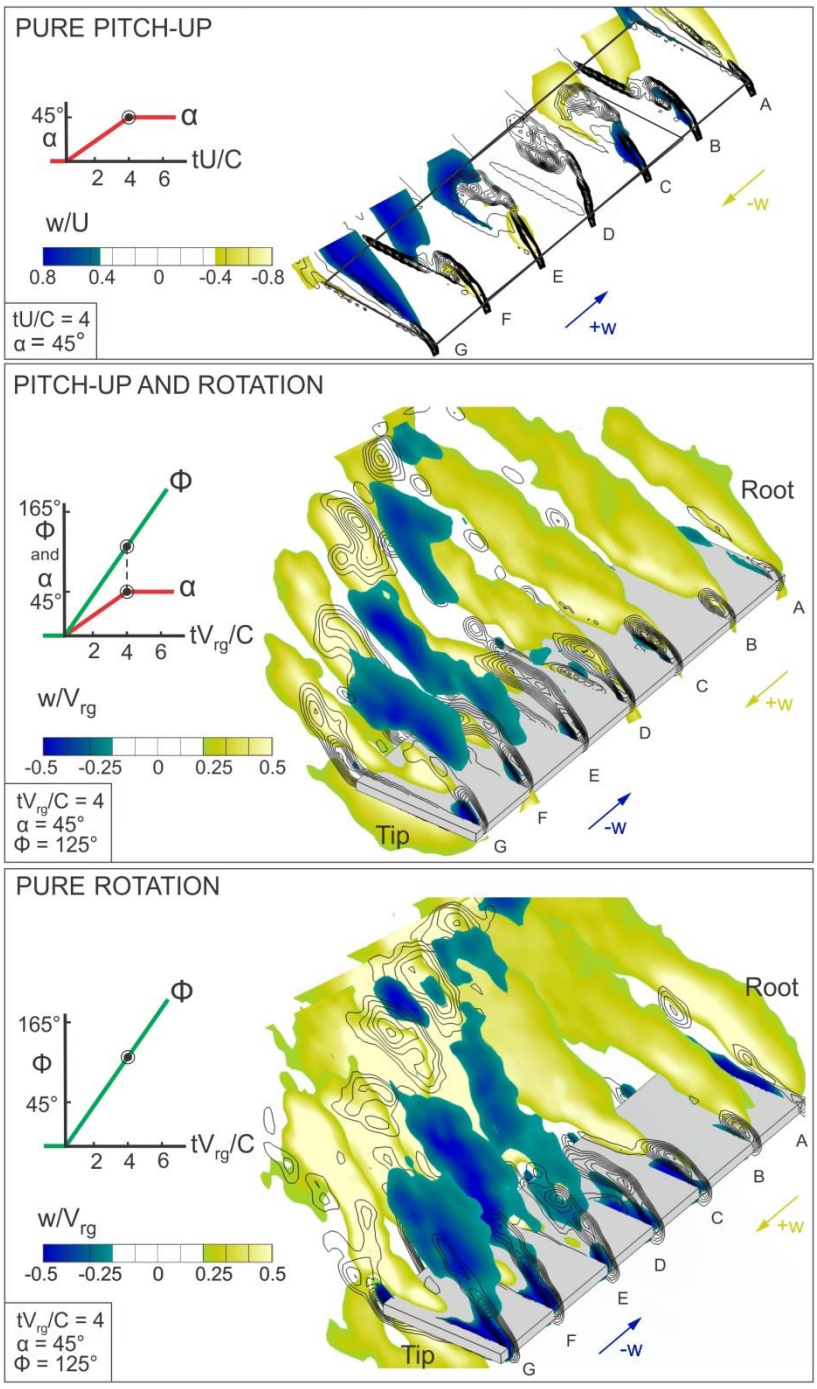

Figure 4.9: Sectional (color) contours of w (spanwise) component of velocity superposed on sectional (black line) contours of spanwise-oriented vorticity, $\omega_z C/U$ and $\omega_z C/V_{rg}$ along span of wing undergoing pitch-up, pitch-up and rotation, and rotation.

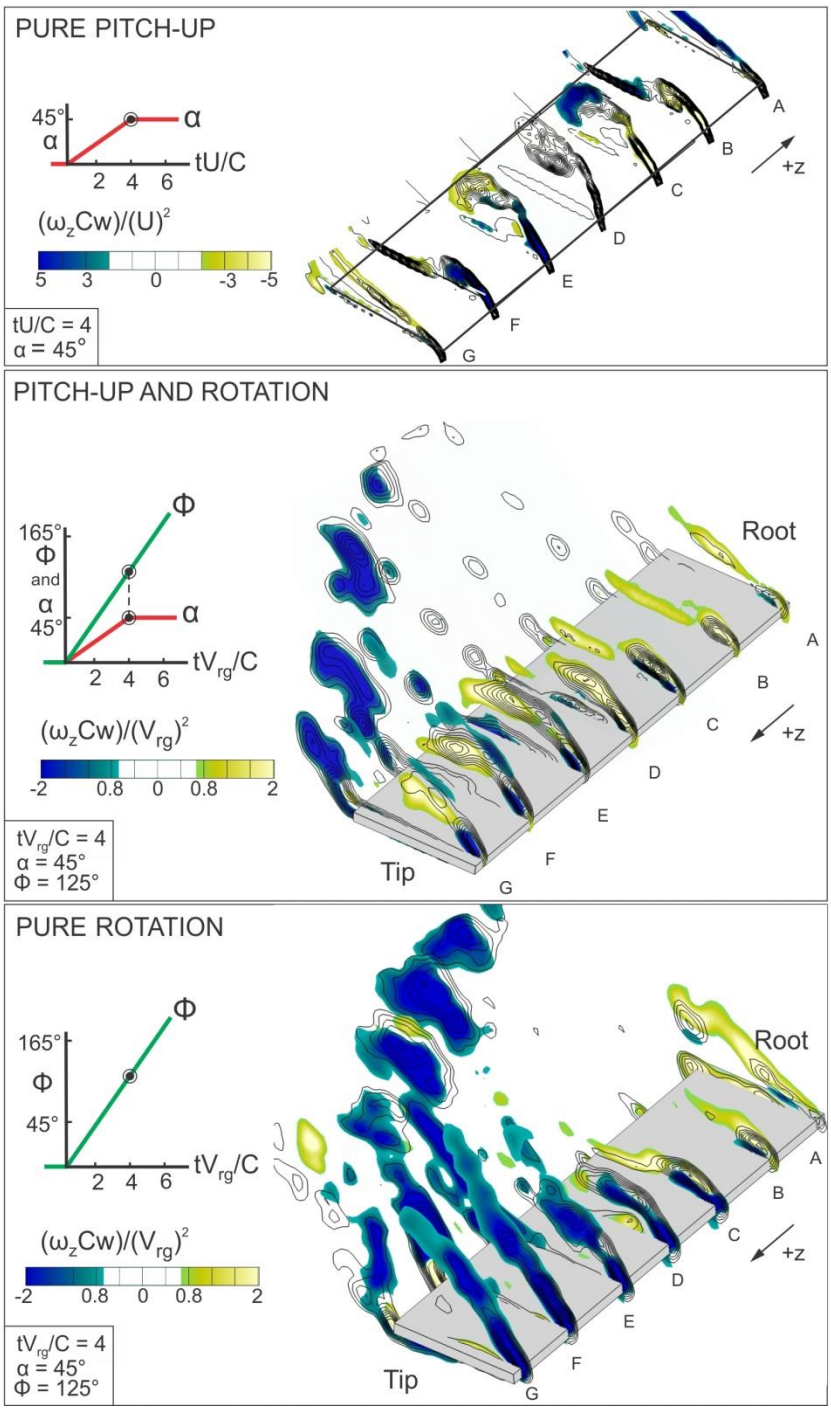

Figure 4.10: Sectional (color) contours of spanwise vorticity flux, $\omega_z Cw/(U)^2$ and $\omega_z Cw/(V_{rg})^2$ superposed on sectional (black line) contours of spanwise-oriented vorticity, $\omega_z C/U$ and $\omega_z C/V_{rg}$ along span of wing undergoing pitch-up, pitch-up and rotation, and rotation.

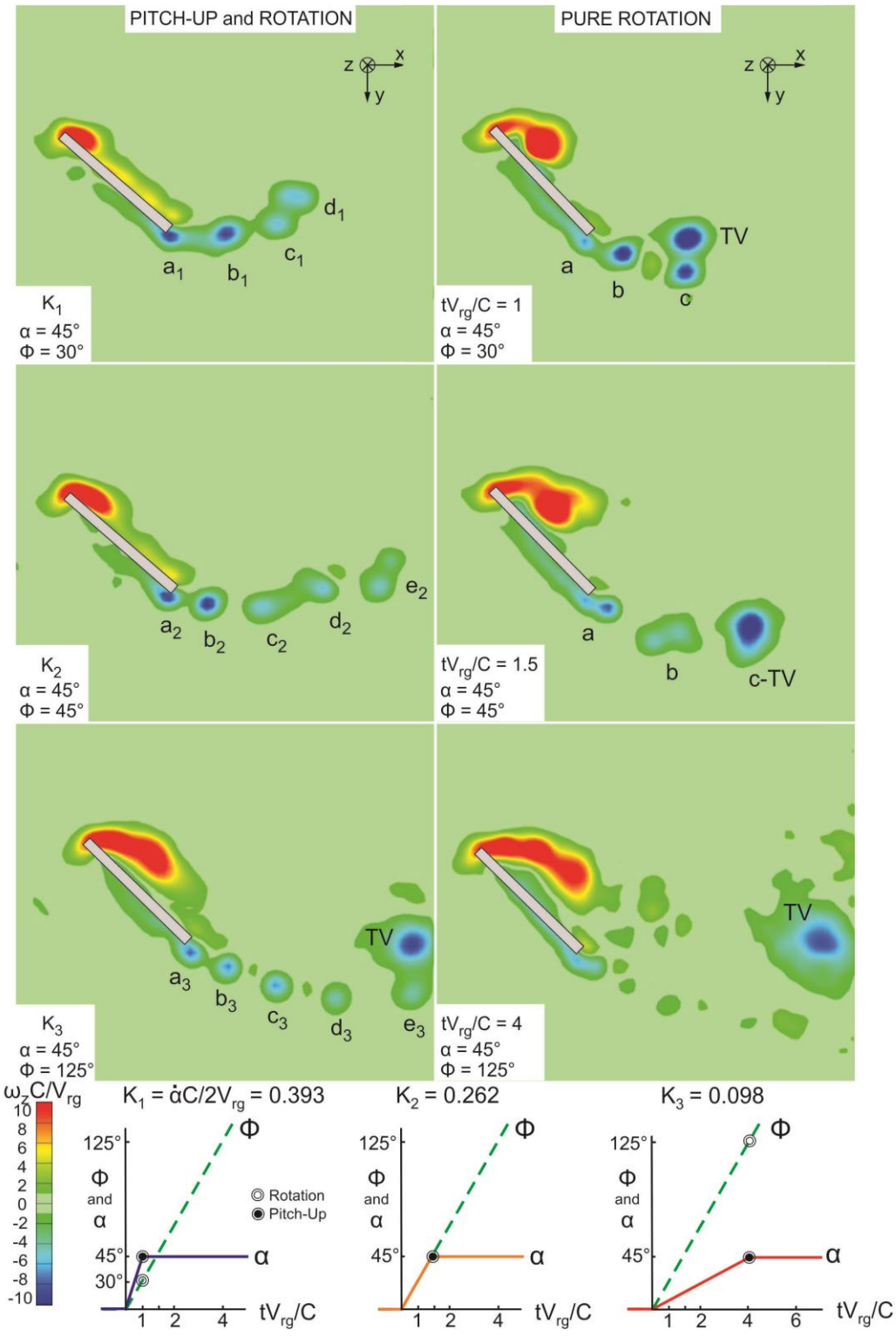

Figure 4.11: Sectional images of spanwise-oriented vorticity $\omega_z C/V_{rg}$ for: simultaneous pitch-up and rotation of wing (left column); and pure rotation of wing (right column) at different pitch rates K.

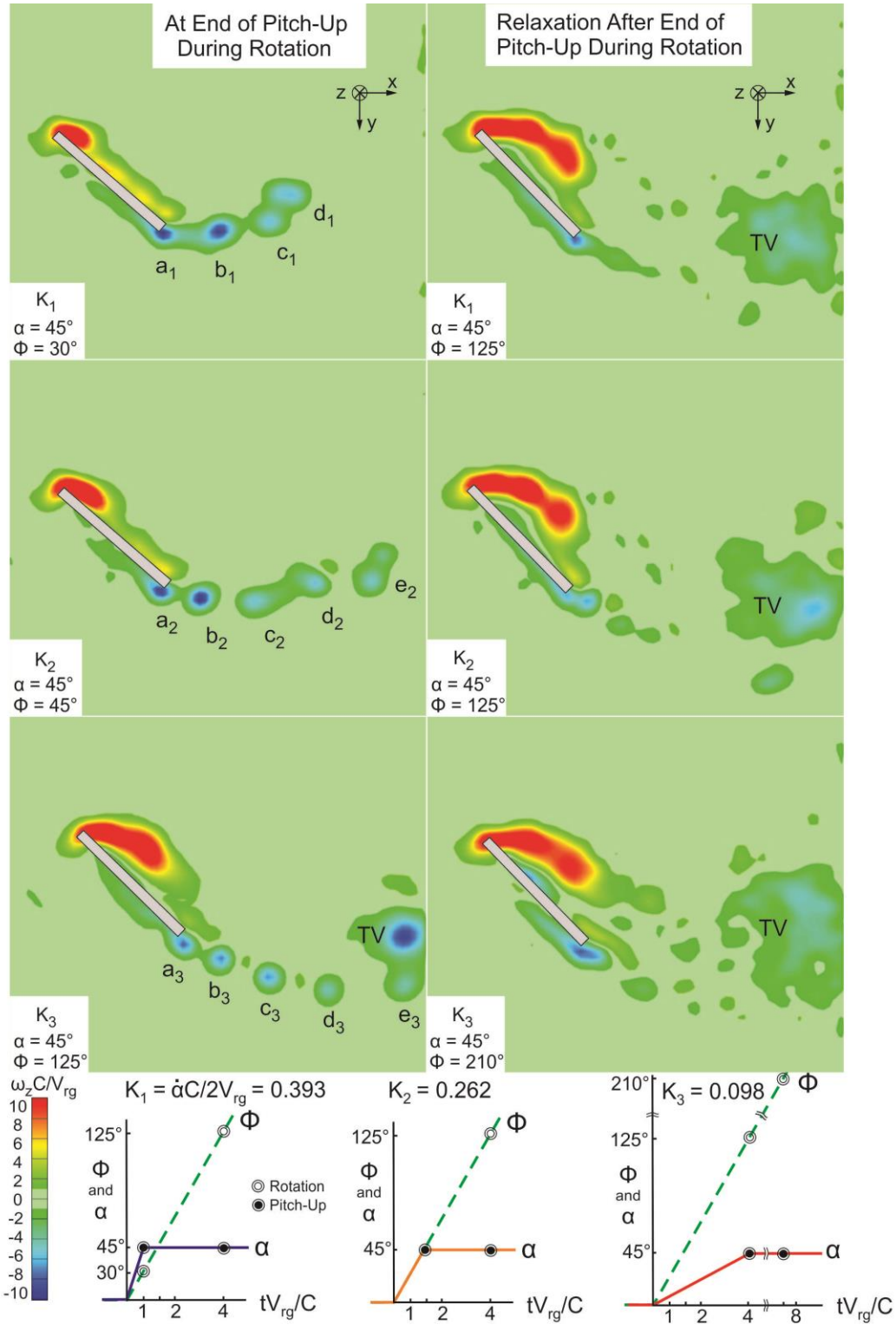

Figure 4.12: Sectional images of spanwise-oriented vorticity, $\omega_z C/V_{rg}$ at midspan of wing for simultaneous pitch-up and rotation: at end of pitch-up motion (left column); and subsequent relaxation after end of pitch-up motion (right column).

CHAPTER 5

THREE-DIMENSIONAL FLOW STRUCTURE ALONG SIMULTANEOUSLY PITCHING AND ROTATING WINGS: EFFECT OF PITCH RATE

5.1 BACKGROUND

Large amplitude unsteady motion of wings has been of great interest in recent years. This type of maneuver, involving rotation, pitch-up, and plunging, is common in biological flyers and is in stark contrast to the generally two-dimensional steady flow over conventional aircraft wings.

Of specific interest herein is the development of flow structure over simultaneously rotating and pitching wings having low aspect ratio. The generic maneuver of pitch-up and rotation is applicable to turbines and rotorcraft and is akin to the perching motion of a bird. This chapter explores the effect of pitch rate relative to rotation rate on the development of the tip, root, and leading-edge components of the three-dimensional vortex system. Quantitative imaging is employed to characterize the detailed three-dimensional flow structure. Imaging is performed for a range of pitch rates, with emphasis on the three-dimensional structure during start-up and relaxation. Surfaces of transparent iso-Q and helicity are employed to interpret the flow physics.

5.2 EXPERIMENTAL SETUP

The experiments in this investigation were performed in a free surface water channel with an overall test section length of 4877 mm, a width of 927 mm, and a depth of 610 mm. Figure 5.1 shows an isometric view of the rotating and pitching wing system. A flat plate with sharp (rectangular) edges was used as the wing model. This rectangular wing had an aspect ratio $AR = b/C = 2$, chord $C = 38.2$ mm, span $b = 76.3$

mm and thickness t = 2.8 mm. It was made from clear acrylic, depicted with yellow shading in figure 5.1. The distance from the center of the rotating body to the root of the wing was r_o = 38.2 mm. The laser sheet, shown in figure 5.1 and depicted in green, intersects the wing at the mid-span location. The angle of rotation, ϕ, and pitch angle, i.e., angle of attack α, are also denoted in figure 5.1. More detailed information on the design and operation of the combined pitching and rotating apparatus can be found in Bross & Rockwell (2014).

The first group of experiments includes imaging of the flow structure due to combined pitch-up and rotation. Images were acquired at the cessation of the pitch-up maneuver and at a later time after the flow structure underwent a relaxation process while the wing continued to rotate at fixed angle of attack. The reduced pitch rate for these experiments had values of $K = \dot{\alpha}C/(2V_{rg}) = 0.1$, 0.2, and 0.4 while the reduced rotation rate remained fixed at $\Omega = \dot{\phi}C/(2V_{rg}) = 0.261$. For these experiments, K was varied by changing the rotation rate $\dot{\phi}$ and hence V_{rg}, while the pitch rate $\dot{\alpha}$ remained constant. The wing was pitched about the z-axis at a constant rate $\dot{\alpha}$ = 1.05 rad s^{-1} while the wing rotated about the y-axis at constant rates $\dot{\phi}$ = 2.79, 1.39, and 0.698 rad s^{-1} corresponding respectively to V_{rg} = 204, 102, and 51 mm s^{-1} for K = 0.1, 0.2, and 0.4. Additionally, the Reynolds number based on the tip velocity was Re_{tip} = 11 822, 5911, and 2955 for K = 0.1, 0.2, and 0.4 respectively. The second group of experiments involved time resolved imaging of the flow structure on a combined rotating and pitching wing at reduced pitch rates K = 0.1, 0.2, and 0.4 and a reduced rotation rate Ω = 0.261. For these experiments, the rotation rate remained fixed while the pitch rate varied in order to change K. The fixed rotation rate was $\dot{\phi}$ = 0.698 rad s^{-1}, corresponding to V_{rg} = 51 mm s^{-1} and Re_{tip} =

2947; the pitch rates had values of $\dot{\alpha}$ = 0.262, 0.524, and 1.05 rad/s for K = 0.1, 0.2, and 0.4 respectively.

Quantitative imaging via angular displacement stereo particle image velocimetry (SPIV) was used to determine the three-dimensional velocity field. The water channel was seeded with 12 μm hollow metallic coated plastic spheres, thereby providing 15-20 particle images in the interrogation window size of 32 x 32 pixels^2. A dual pulsed Nd-YAG laser generated a 1mm thick laser sheet at 14.29 Hz. Images were acquired by a CCD camera system at 1600 by 1200 pixels^2. Image pairs were recorded at effective values of in-plane magnification ranging between 8.563 pixels mm^{-1} and 8.617 pixels mm^{-1}. The acquired images were evaluated using a cross-correlation technique with 50% overlap, yielding 5310 to 5551 in-plane vectors.

Three-dimensional representations of iso-surfaces of the Q-criterion involved acquisition of six instantaneous images on evenly spaced planes along the span of the wing. The instantaneous images were phase averaged before the final three-dimensional reconstruction. The laser position along the span of the wing was varied by translating the entire wing apparatus to successive spanwise positions. Image acquisition was performed for 55 to 57 planes along the span b of the wing. For all experiments, the spatial separation between planes was Δr = 1.905 mm or, in normalized form, $\Delta r/b$ = 0.025. The spatial separation of velocity vectors on the image planes ranged from 1.84 to 1.85 mm corresponding to non-dimensional distances of $\Delta x/b = \Delta y/b$ = 0.0241 to 0.0242. The total number of vectors in the reconstructed volumes ranged from 297 000 to 302 670, depending on the number of planes imaged. Details of the error calculations for the SPIV arrangement are provided in Bross & Rockwell (2014).

This investigation involves quantitative visualization of the flow structure on a combined pitching and rotating wing for values of reduced pitch rate K = 0.1, 0.2, and 0.4. The first group of experiments involved imaging of the three-dimensional flow structure at the cessation of the pitch-up maneuver, i.e., when the wing reached an angle of attack α = 45°, corresponding to values of convective time $\tau = tV_{rg}/C$ = 1, 2, and 4 for K = 0.4, 0.2, and 0.1 respectively. Additional imaging was performed after cessation of the pitch-up maneuver while the wing continued to rotate at fixed α = 45° up to a time of 3τ for each value of K. In the second group of experiments, the development of the three-dimensional flow structure on a wing undergoing combined pitch up and rotation for K = 0.1, 0.2, and 0.4, is characterized; the wing starts from rest. Comparisons of the flow structure at the same angles of attack, α = 15°, 30°, and 45° are made for each value of K. Additionally, representations are provided at the same value of rotation angle ϕ = 10°, 30°, and 50° for each value of K.

5.3 THREE DIMENSIONAL REPRESENTATIONS OF FLOW STRUCTURE: COMBINED ROTATION AND PITCH-UP

5.3.1 Cessation of Pitch-Up Maneuver and Relaxation of the Vortex System

Nested transparent iso-surfaces of the Q-criterion (Hunt et al. 1988) are provided in Figure 5.2. This criterion is defined as follows:

$$Q = \frac{1}{2}\left[\Omega_{ij}\Omega_{ij} - S_{ij}S_{ij}\right] = -\frac{1}{2}\frac{\partial u_i}{\partial x_i}\frac{\partial u_j}{\partial x_i} \qquad (1)$$

The Q-criterion indicates the magnitude of rotation relative to the amount of strain, where Ω and S are the rotation and stress tensors respectively. When Q is positive, rotation dominates the strain, therefore vortical structures can be identified by positive values of

Q. The sets of iso- surfaces shown in figure 5.2 correspond to values of non-dimensional pitch rate K = 0.1, 0.2, and 0.4.

The wing reaches cessation of its pitch-up maneuver at α = 45° for each value of K in the left column of images in figure 5.2. This terminal angle, α = 45°, is attained at dimensionless times τ = 1, 2, and 4. The right column of images represents the flow structure in a relaxed state three convective times τ after cessation of the pitch-up maneuver, corresponding to τ = 4, 5, and 7.

Patterns of the leading-edge, tip, and trailing-edge vortex structures are distinctly different at the cessation of the pitch-up maneuver (left column) for each value of K. At the highest value of pitch rate corresponding to K = 0.4, a stable coherent leading-edge vortex is present. The leading-edge vortex connects to the tip vortex structure, forming a loop in the wake of the wing. High levels of *Q*-criterion persist throughout this three-dimensional vortex system, indicating the organized nature of the leading-edge, tip, root, and wake vortex structures. Considering the flow structure at K = 0.2, the leading-edge vortex has increased in scale compared to K = 0.4. In the region between the midspan and tip of the wing, the leading-edge vortex forms a distinct break, indicating the onset of vortex shedding. The coherence of the tip vortex is evidenced by high levels of iso-*Q* though the extent of the vortex. Furthermore, highly ordered wake structures emanate from the trailing edge of the wing, forming several distinct vortex tubes evenly distributed in the wake. At the slowest pitch rate, K = 0.1, the flow structure is distinctly less organized in comparison to K = 0.2 and 0.4. In this case, the leading-edge vortex exhibits vortex shedding near the tip region, where high levels of iso-*Q* are still observed. Additionally, the tip vortex, which reoriented towards the wake of the wing, has the

largest scale of all three values of *K*. Ordered vortex structures are evident in the wake region, but involve only low levels of iso-*Q* and are less organized when compared to *K* = 0.2 and 0.4. Moreover, the root vortex is reoriented in the spanwise direction towards the center of rotation of the wing. The aforementioned differences of the three-dimensional flow structure at cessation of the pitch-up maneuver are most likely due to the increasingly larger values of rotation angle ϕ associated with decreasing values of reduced pitch rate *K*.

The position of the wing as it continues to rotate at fixed angle of attack ($\alpha = 45°$) after the cessation of the pitch-up maneuver at each value of *K* is indicated in the lower right schematic at the bottom of figure 5.2. The three-dimensional volumes of the flow structure shown in the right column are imaged at a time increment of 3τ after cessation of the pitch-up maneuver, i.e., after the states of the vortex systems shown in the left column. This time increment corresponds to τ = 4, 5, and 7 for *K* = 0.4, 0.2, and 0.1 respectively. In other words, the images in the right column represent the relaxed states of the corresponding images given in the left column of Figure 5.3. Despite the different vortex patterns at the cessation of the pitch up motion the relaxed flow structures are very similar. The leading-edge vortex undergoes vortex shedding in the region extending from the mid-span to the tip of the wing for each value of *K* in the right column of Figure 5.3. Moreover, the tip vortex has a complex, but remarkably similar structure for all values of *K*. In addition, the dual tip vortices can be seen for each case of the relaxed flow structure. The formation of helical structure on the tip vortex was also observed by Poelma et al. (2006), Carr et al. (2013a), Percin et al. (2014). The aforementioned similarities of the vortex structures after the relaxation process (right column of images of

figure 2), despite different initial conditions at the cessation of pitch up (left column), indicate the dominant effects of wing rotation on the development of the flow structure and the resulting three-dimensional vortex system.

5.4 THREE-DIMENSIONAL DEVELOPMENT OF FLOW STRUCTURE

5.4.1 Vortex structure as a function of pitch rate: comparison at given angles of attack.

Nested transparent iso-Q surfaces on wings undergoing combined pitch-up and rotation for reduced pitch rates K = 0.1, 0.2, and 0.4 (columns of images) at instants where the angles of attack are at the same values α = 15°, 30°, and 45° (rows of images) are provided in Figure 5.3a. The levels of the Q-criterion are Q = 2, 8, and 22.

At an angle of attack of α = 15° (first row of images), the flow structure exhibits large variations with K, i.e., the leading-edge, tip, and trailing-edge vortex patterns are less developed with increasing K. For example, at K = 0.1, the leading-edge, tip, and wake vortex structures are evident, compared to K = 0.2 where the leading-edge and wake structures are visible but less developed in scale and coherence. Finally, at K = 0.4, only the starting vortex emanating from the trailing edge is present. This general trend occurs for each value of angle of attack, i.e., the degree of development and scale of the vortical structures increases for increasing α or decreasing K. Furthermore, the number of vortices shed from the trailing edge follows the same trend. The number of shed vortices for each series of increasing α or decreasing K is associated with the increase of rotation angle ϕ. Eventually, in the limit of very large rotation angle ϕ, small pitch rate K, and large angle of attack α, as represented by the bottom left image (K = 0.1, α = 45°), these vortices in the wake region break down and are no longer evident in a coherent

form. The physical trends represented by the foregoing images indicate that rotation angle ϕ is more influential than angle of attack α or pitch rate K in the development of the three-dimensional vortex systems.

5.4.2 Vortex structure and helical density as a function of pitch rate: comparison at given angles of attack.

Nested transparent iso-Q surfaces colored with helical density h on wings undergoing combined pitch-up and rotation are displayed in Figure 5.3b. These images correspond to the same reduced pitch rates K and pitch angles α as shown in figure 5.3a. The helical density h, i.e., helicity per unit volume, is calculated by taking the scalar product of the three-dimensional velocity field $\boldsymbol{V}$ and the three-dimensional vorticity field $\boldsymbol{\omega}$ (Moffatt 1969), i.e., $h = (\boldsymbol{V} \cdot \boldsymbol{\omega})$. It therefore represents the strength of vorticity flux along the axis of a vortical structure. The velocity field $\boldsymbol{V}$ employed for the evaluation of h in figure 5.3b and subsequent images is in the wing fixed reference frame.

Figure 5.3b complements Figure 5.3a and provides further insight into the observation that the development and scale of the flow structure increases for increasing α or decreasing K. The highest levels of positive (red) helicity h exist in the tip region for the cases where the tip vortex is coherent and stable. The tip vortex grows in scale and the extent of positive h increases as α increases, thereby indicating alignment of flow velocity $\boldsymbol{V}$ and vorticity $\boldsymbol{\omega}$, and large values of vorticity flux along the axis of the tip vortex. However, when the vortex system near the tip begins to show signs of disorganization at $K = 0.1$, $\alpha = 45°$, the positive (red) concentration of h, and thereby large vorticity flux, is attenuated.

In addition, the coherence of the leading-edge vortex is conveyed through the color of the helical density. Positive (red-yellow) helicity is observed in the leading-edge region as the leading-edge vortex develops for increasing α or decreasing K, indicating spanwise vorticity flux through the core of the leading-edge vortex. For the limiting case of $K = 0.1$, $\alpha = 45°$, the leading-edge vortex forms a break at the midspan of the wing; at this location a concentration of positive (red) h is observed.

5.4.3 Vortex structure as a function of pitch rate: comparison at given angles of rotation.

Nested transparent surfaces of iso-Q on wings undergoing combined pitch-up and rotation for reduced pitch rates $K = 0.1$, 0.2, and 0.4 (columns) and for values of rotation angle, $\phi = 10°$, 30°, and 50° (rows) are provided in Figure 5.4a.

The three-dimensional vortex systems across each row, i.e., at a given value of ϕ in figure 5.4a have similar patterns despite major differences in the angle of attack α. Namely, the formation of the leading-edge vortex, tip vortex and periodically shed vortices from the trailing edge are consistent for each value of ϕ. However, at a given value of ϕ, the scale of vortical structures increases significantly with increasing K. This trend accompanied by an increase in spatial extent of the high concentration of iso-Q ($Q = 22$). Furthermore, at each value of ϕ, the flow structures in the region downstream of the trailing edge are generally similar. Remarkably, the same number of vortices is shed from the trailing edge of the wing at a given value of ϕ despite the large variation in angle of attack α. This observation is in contrast to comparisons at a given α (see figure 5.3a), where the flow structure varies greatly.

At the largest values of K, a globally connected system of root, leading-edge, and tip vortices becomes evident in the right column of figure 5.4a. In other words, this

connected vortex loop from the root to the tip becomes more prominent for a given ϕ with increasing K. This loop is most pronounced for ϕ = 30° and 50° at K = *0.4*. At a given value of ϕ, when the wing is at lower angle of attack α, the vortex system is less developed in terms of vortex scale and maximum level of iso-Q.

5.4.4 Vortex structure and helical density as a function of pitch rate: comparison at given angles of rotation

Nested iso-Q surfaces colored with helical density h (previously defined in section 5.4.2) on wings undergoing combined pitch-up and rotation for reduced pitch rates K are provided in Figure 5.4b. The parameters in this figure have the same values as in figure 5.4a, i.e., pitch rates K = 0.1, 0.2, and 0.4 at rotation angles ϕ = 10°, 30°, and 50°.

The presence of high level positive (red) helicity in the tip vortices is evident, especially as ϕ increases. The coherence of the tip vortex, which is associated with positive helical density h and thereby large magnitude vorticity flux through the core of the vortex, is evident at larger values of ϕ and K. In addition, positive (red-yellow) helicity in the leading-edge region is evidence of spanwise flow and vorticity flux through the core of the leading-edge vortex. This is observed most notably for: K = 0.2, ϕ = 30°; K = 0.2, ϕ = 50°; K = 0.4, ϕ = 30°; and K = 0.4, ϕ = 50°. Furthermore, at the location where the leading-edge vortex splits at K = 0.4, ϕ = 50°, a high concentration of positive helicity is present; this observation is similar to splitting of the leading-edge vortex in figure 5.4b at K = 0.1, α = 45°.

5.5 TEMPORAL DEVELOPMENT OF INTERIOR STRUCTURE OF THE THREE-DIMENSIONAL VORTEX SYSTEM:

The interior structure of the leading-edge, root, tip, and wake vortices is visible through transparent iso-Q surfaces provided herein. High levels of iso-Q present within a vortex serve as an indication of the degree of coherence of the vortex system. In addition, helical density shading on the iso-Q surfaces provides a measure of the vorticity flux along the axis of a given component of the vortex system. These representations of the vortex structure have been employed in the foregoing sets of images. The image layouts shown in figures 5.5a and 5.5b emphasize the timing of development of the components of the vortex system for the extreme values of pitch rate used in this study, K = 0.1 and 0.4, during the initial stage of wing rotation. This timing is interpreted in terms of surfaces of iso-Q and helical density h within the vortex system. Comparison of Figures 5.5a and 5.5b shows that the manner in which high levels of iso-Q (Q = 8 and 22) appear and propagate through the vortex system is fundamentally different for the values of pitch rate K = 0.1 and 0.4. In essence, at K = 0.1, development of the leading edge vortex precedes other components of the vortex system, whereas at K = 0.4 the vortex shed from the trailing edge precedes other components. More specifically, the evolution of the components of the vortex system is as follows.

At low pitch rate K = 0.1 (figure 5.5a, left column of images), the highest level of Q = 8 first appears in the leading-edge vortex at ϕ = 20°. Subsequently at ϕ = 30° the level of Q = 8 grows in spatial extent in the leading-edge region. At ϕ = 40° the Q = 8 surface extends along the tip towards the trailing edge. In contrast, at the high value of pitch rate K = 0.4 (figure 5.5b left column of images), the high level of Q = 22 first

appears in the vortex shed from the trailing edge at ϕ = 10°, then propagates upstream along the tip (ϕ = 20°), finally extending through the leading-edge vortex at ϕ = 25° and 30°.

The magnitudes of helical density *h* are indicated in the right columns of figures 5.5a and 5b. For the low pitch rate K = 0.1 of figure 5.5a, at rotation angles ϕ = 20° through 40°, moderately positive (yellow-orange) helical density *h* is evident along both the leading edge and the tip of the wing. The fact that the helicity *h* is consistently positive indicates presence of positive vorticity flux along these regions of the wing, which is associated with the high degree of coherence of the leading-edge and tip vortices. For values of ϕ larger than those shown in figures 5.5a and 5.5b, the leading-edge and tip vortices continue to develop with increasing ϕ, and higher levels of positive (red) helical density h are observed (see figures 5.3b and 5.4b).

For the high value of pitch rate K = 0 .4 in figure 5.5b, the development of the large (red) region of helicity *h* within the tip/trailing vortex follows the upstream movement of the region of large Q = 22 for increasing values of rotation angle ϕ. The consistently positive sign of the moderate (yellow-orange) and large (red) helicity in the leading edge and tip regions indicates positive vorticity flux through these vortex components, and is again associated with a highly coherent stable vortex system.

Taking an overview of the foregoing observations of figures 5.5a and 5.5b, is evident that, for the simultaneously pitching and rotating wing, the timing of development of the components of three-dimensional vortex system, i.e., the leading-edge, tip and shed vortices, can be radically different. Despite this distinction, the existence of moderate and high values of helicity having the same sign through the

leading-edge and tip vortex components is associated with a highly coherent vortex system.

5.6 CONCLUDING REMARKS

The three-dimensional vortex system due to a simultaneously pitching and rotating wing is addressed herein. Emphasis is on the effect of dimensionless pitch rate relative to rotation rate of the wing, in particular the consequences for development of the interior structure of components of the vortex system. These components include the vortices formed at the leading-edge and at the tip, and vortices shed from the trailing-edge of the wing. The interiors of these vortex components are represented by transparent iso-Q surfaces and surfaces of helicity. This approach allows characterization of the relative timing of onset and development of each of the components of the vortex system as a function of dimensionless pitch rate relative to rotation rate. Moreover, it is possible to attain detailed interpretation of the relaxation process of the vortex system when pitch-up motion of the wing is terminated, while it continues to rotate. The major findings are discussed in the following categories.

5.6.1 Relaxation of the flow structure during pure rotation after simultaneous rotation and pitch-up motion of wing

The non-dimensional pitch rate K influences the patterns of flow structure at the cessation of the pitch-up maneuver. In other words, the three-dimensional flow structure that occurs at each value of pitch rate K is distinctly different when the wing reaches the terminal angle of attack $\alpha = 45°$. At this instant, the flow structure for decreasing K is less developed, in terms of the scales and magnitudes of the iso-Q surfaces within the leading-edge, trailing, and tip vortices. During the pitch up maneuver, however, the wing

is undergoing rotation; it rotates through a smaller azimuthal angle ϕ for decreasing K. This observation indicates that rotation has an important, if not dominant, role in defining the development of the vortex system on the wing. Moreover, images acquired after cessation of the pitch-up maneuver while the wing continues to rotate, more specifically at a time corresponding to three convective times (3τ) after the termination of pitch-up, show a strong similarity, further indicating the strong influence of rotation on the structure of the vortex system. That is, for each value of pitch rate K, the flow structures at the same time scale τ of relaxation during pure rotation are almost identical, despite the difference in initial conditions corresponding to cessation of the pitch up maneuver.

5.6.2 Flow structure at: given angle of attack for variable angle of rotation; and at given rotation angle for variable angle of attack for wings undergoing combined rotation and pitch-up

Three-dimensional images at the same angle of attack α for different values of non-dimensional pitch rate K were determined and compared. At larger values of α, the development of the flow structure is further delayed for increasing values of K. Furthermore, for this comparison at the same angle of attack, the development of the leading-edge, root, and tip vortices occurs at a slower rate and the number of vortices shed from the trailing edge decreases for increasing K. These observations are attributed to the decrease in wing travel distance as K increases.

In the foregoing, rotational motion of the wing has been discussed as the dominant effect in defining the flow structure on a wing undergoing combined pitch-up and rotation. Exploring this concept further, comparisons of the flow structure at the same rotation angle ϕ of the wing for different values of K reveal the influence of rotation

on the development of the three-dimensional flow structure. In contrast to comparisons at the same angle of attack α, the three-dimensional vortex system has a generally similar form at the same rotation angle ϕ. That is, the formation and subsequent development of the leading-edge vortex, the tip vortex, and the vortices shed into the wake are similar at a given value of ϕ, even though the angle of attack is different at each given value of ϕ. When the angle of attack is larger (at larger K) at a given value of Q, the maximum iso-Q level within the vortex system is larger despite the similarity of the vortex structure (lowest Q level) at all values of K.

6.3 Temporal development of interior structure of vortex system

Visualization of the interior structure of the vortex system using the approaches described in the foregoing defines the sequence of development of the components of the vortex system in relation to the reduced pitch rate K. It is demonstrated that the direction of propagation of high levels of the Q-criterion through the wake, tip, and leading-edge vortices is significantly different for the extreme values of non-dimensional pitch rate K examined herein. High levels of Q form at the leading-edge and propagate through the tip vortex into the wake region for the lowest value of K, in contrast, high levels of Q form initially at the trailing edge for the highest K value, and eventually move in the upstream direction through the tip vortex and into the leading-edge vortex. Despite this fundamental difference in the sequence of development of the vortex components, moderate to high levels of positive helicity h are maintained throughout the leading-edge and tip vortices. Moreover, the development of these regions of positive helicity h is in accord with the propagation of high levels of iso-Q through these vortices. Finally, concentrations of moderate and high levels of positive h indicate strong axial flow within

the leading-edge and tip vortices, and are consistent with existence of a highly coherent vortex system. The stability of the leading-edge vortex in conjunction with strong spanwise flow has been previously established and cited in the introduction for the case of pure rotation of the wing. The present investigation shows that the coherence and stability of the leading-edge vortex is also associated with continuous axial flow passing through the cores of the leading-edge and tip vortices.

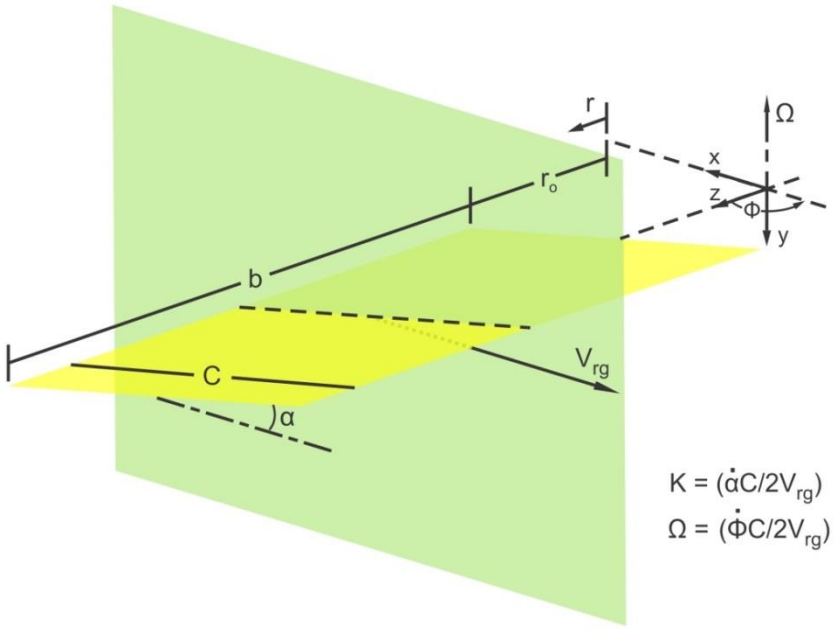

Figure 5.1: Schematic of rotating-pitching wing and corresponding parameters.

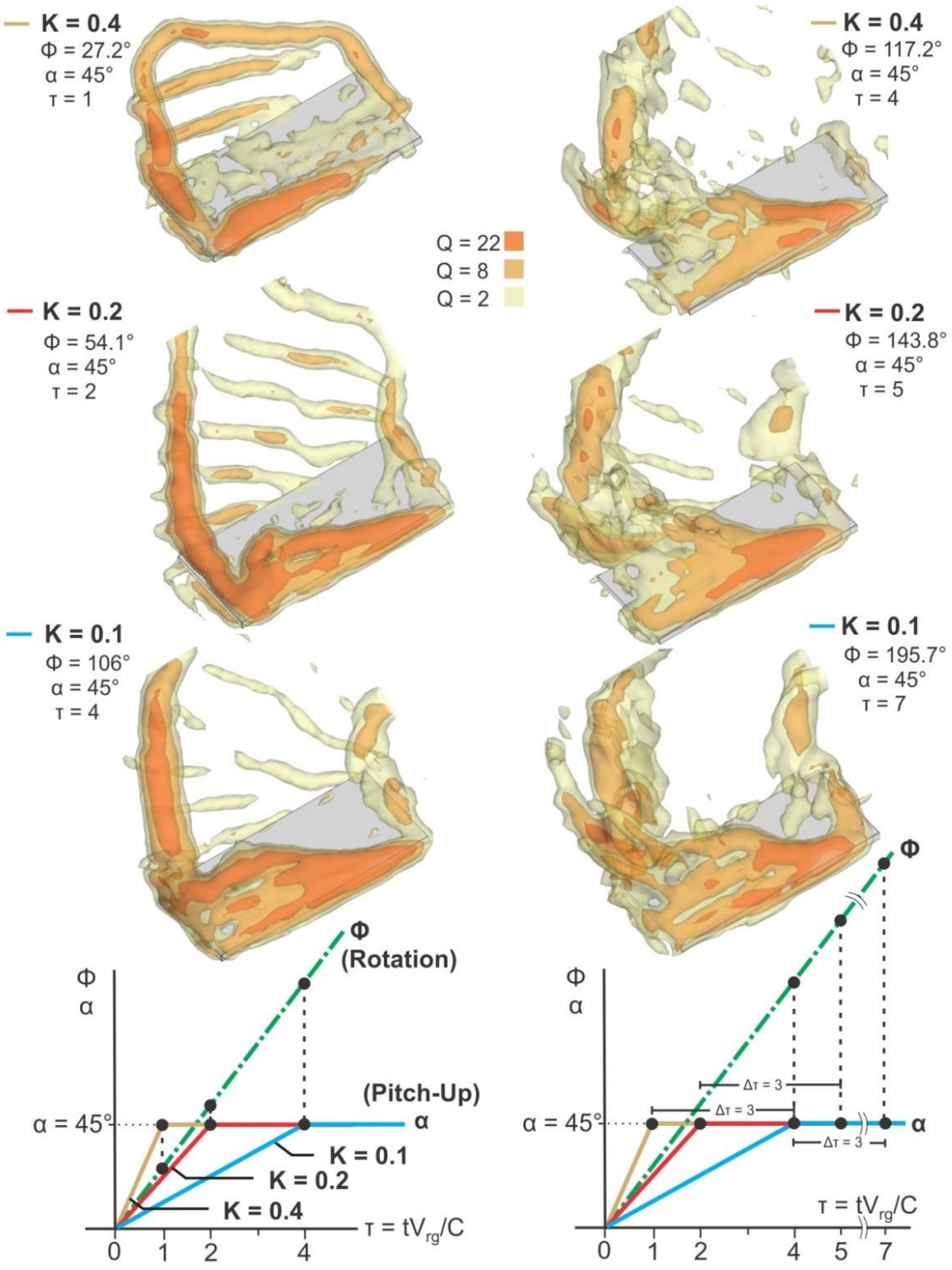

Figure 5.2: Iso-surfaces of *Q*-criterion at cessation of pitch-up maneuver (left column) and relaxation of flow structure after 3τ rotational relaxation for reduced pitch rates K = 0.1, 0.2, and 0.4 (right column).

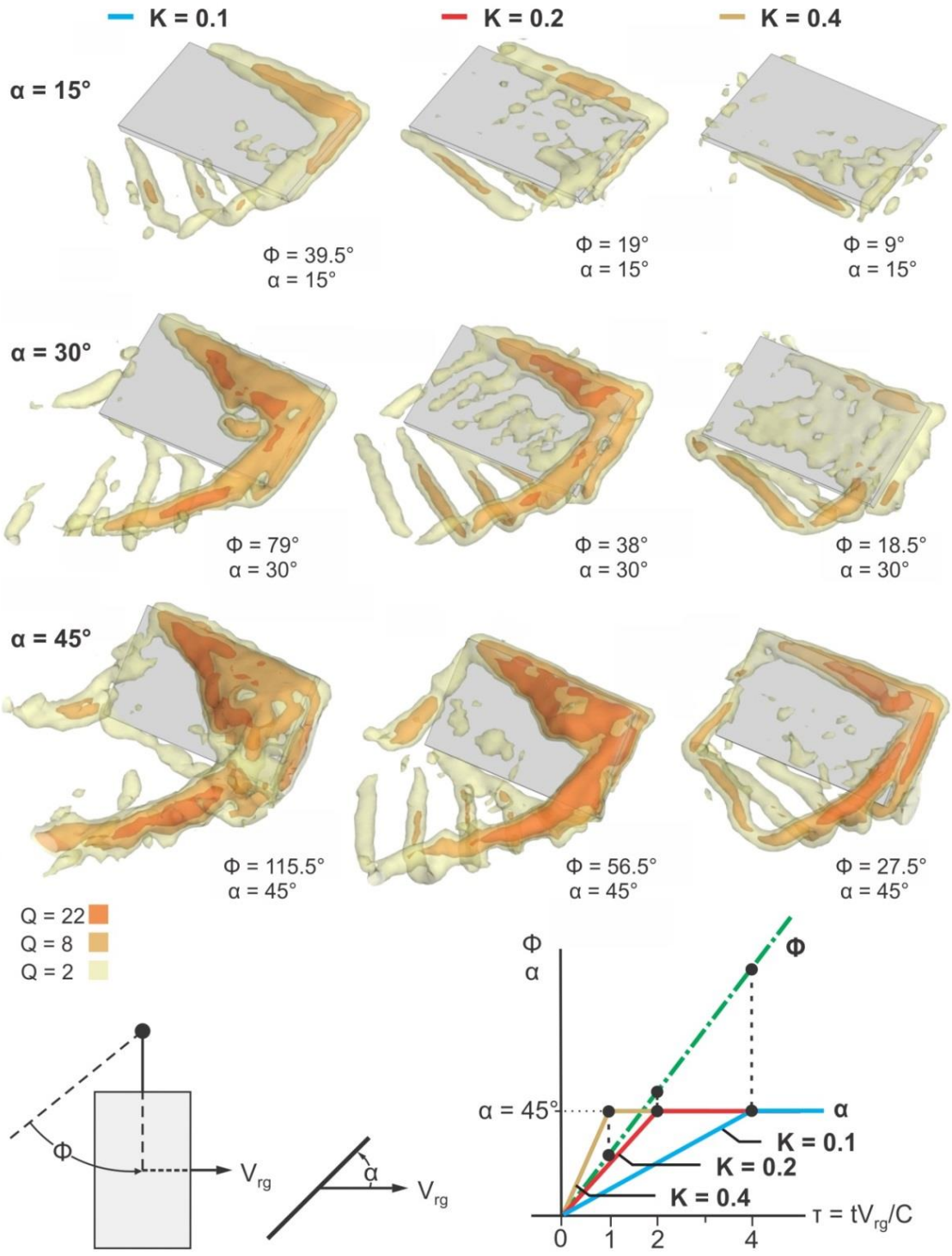

Figure 5.3a: Iso-surfaces of *Q*-criterion for values of reduced pitch rate (columns of images) K = 0.1, 0.2 and 0.4 at angles of attack, α = 15°, 30°, and 45° (rows of images).

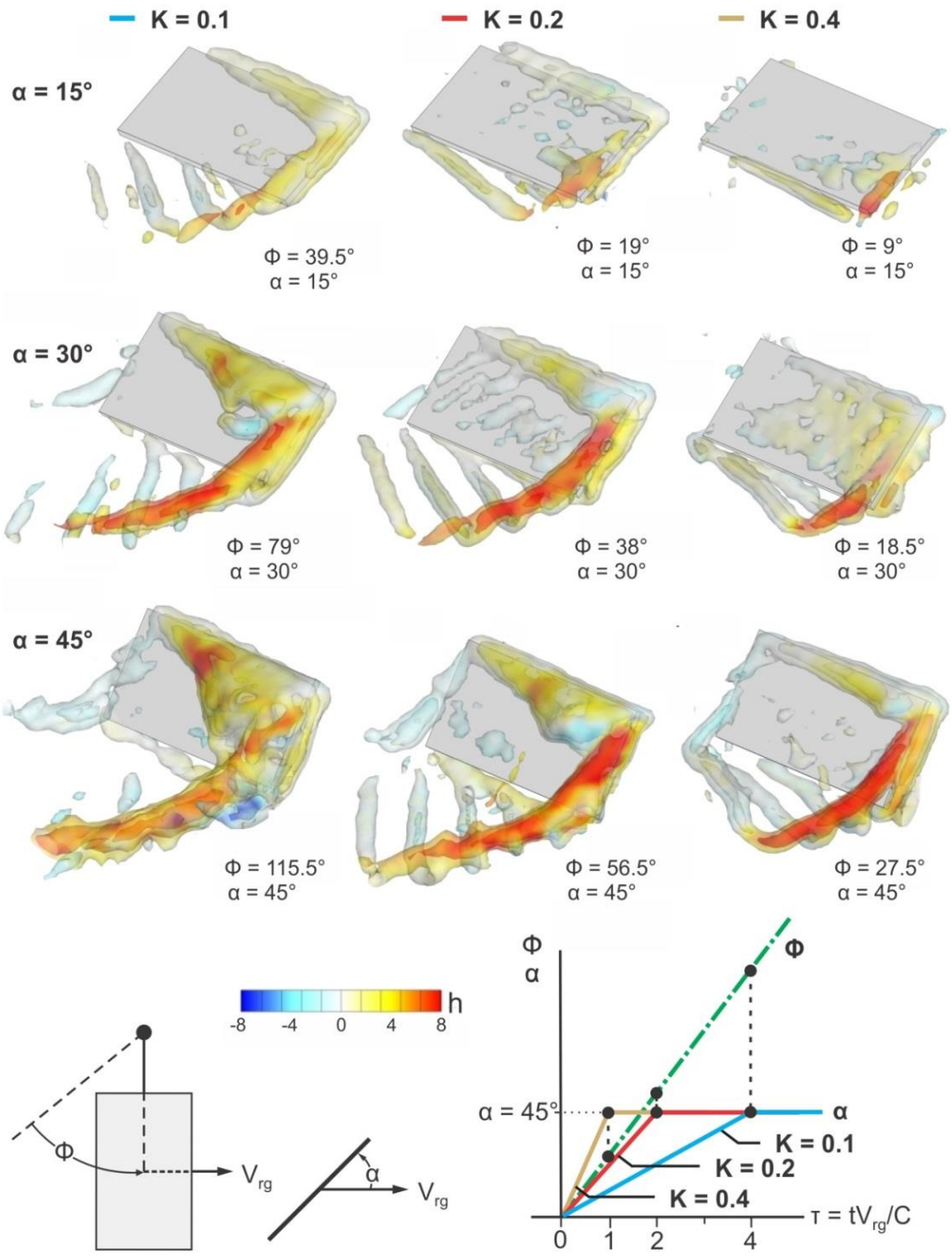

Figure 5.3b: Iso-surfaces of *Q*-criterion (compare Figure 3a) colored with helical density *h* for values of reduced pitch rate (columns of images) K = 0.1, 0.2 and 0.4 at angles of attack, α = 15°, 30°, and 45° (rows of images).

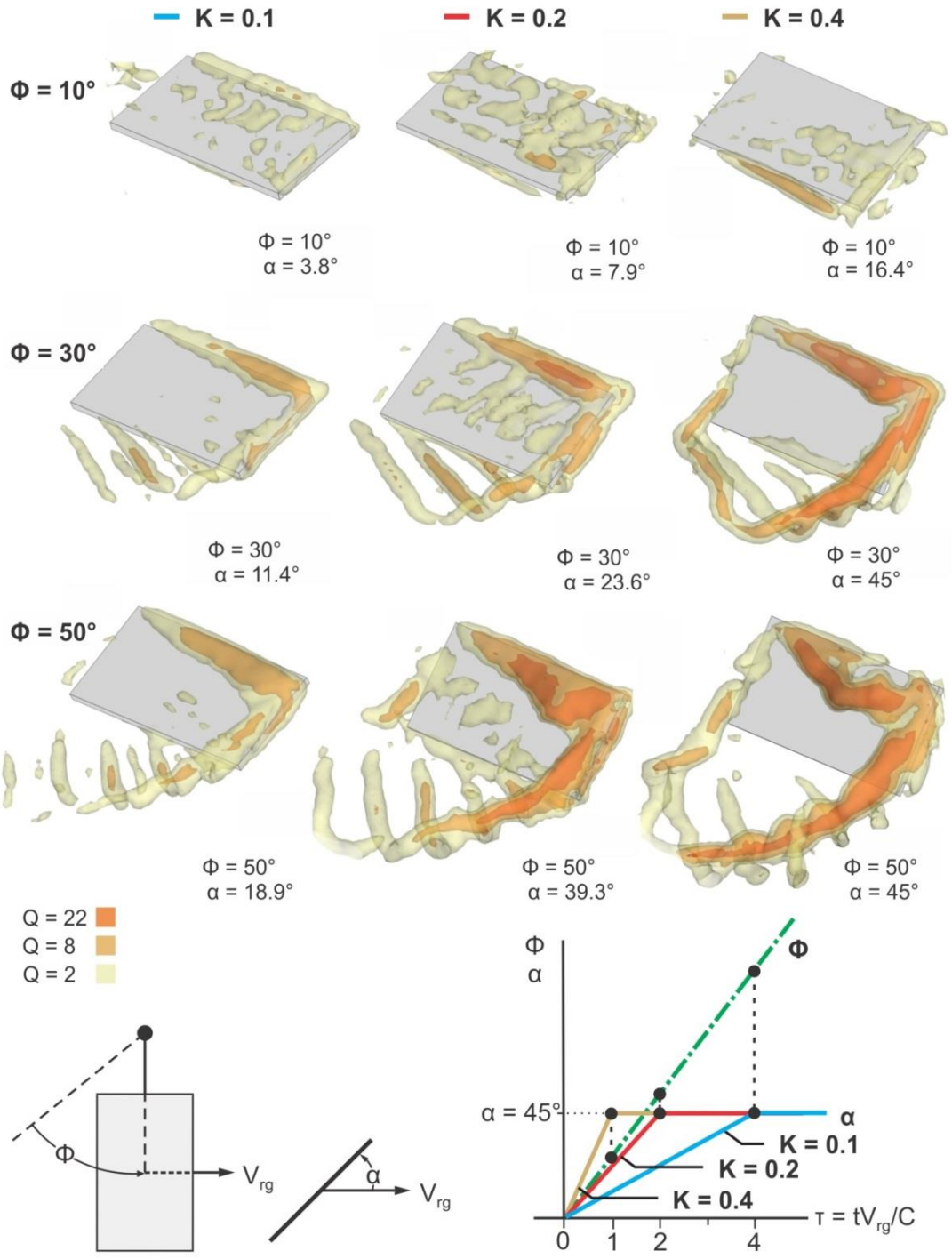

Figure 5.4a: Iso-surfaces of *Q*-criterion for values of reduced pitch rate (columns of images) K = 0.1, 0.2 and 0.4 at angles of rotation, ϕ = 10°, 30°, and 50° (rows of images).

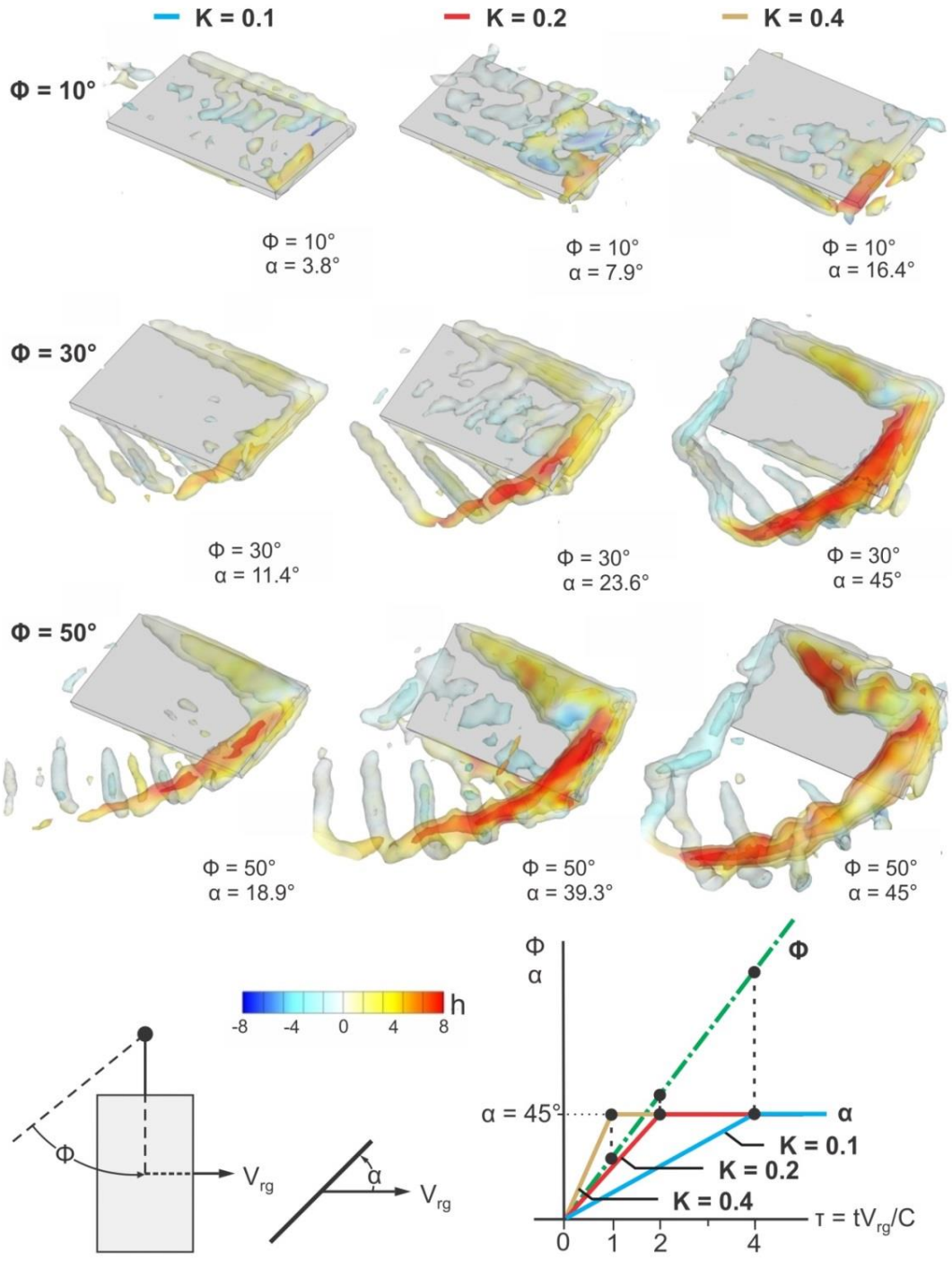

Figure 5.4b: Iso- surfaces of *Q*-criterion (see Figure 4a) colored with helical density *h* for values of reduced pitch rate (columns of images) K = 0.1, 0.2 and 0.4 at angles of rotation, ϕ = 10°, 30°, and 50° (rows of images).

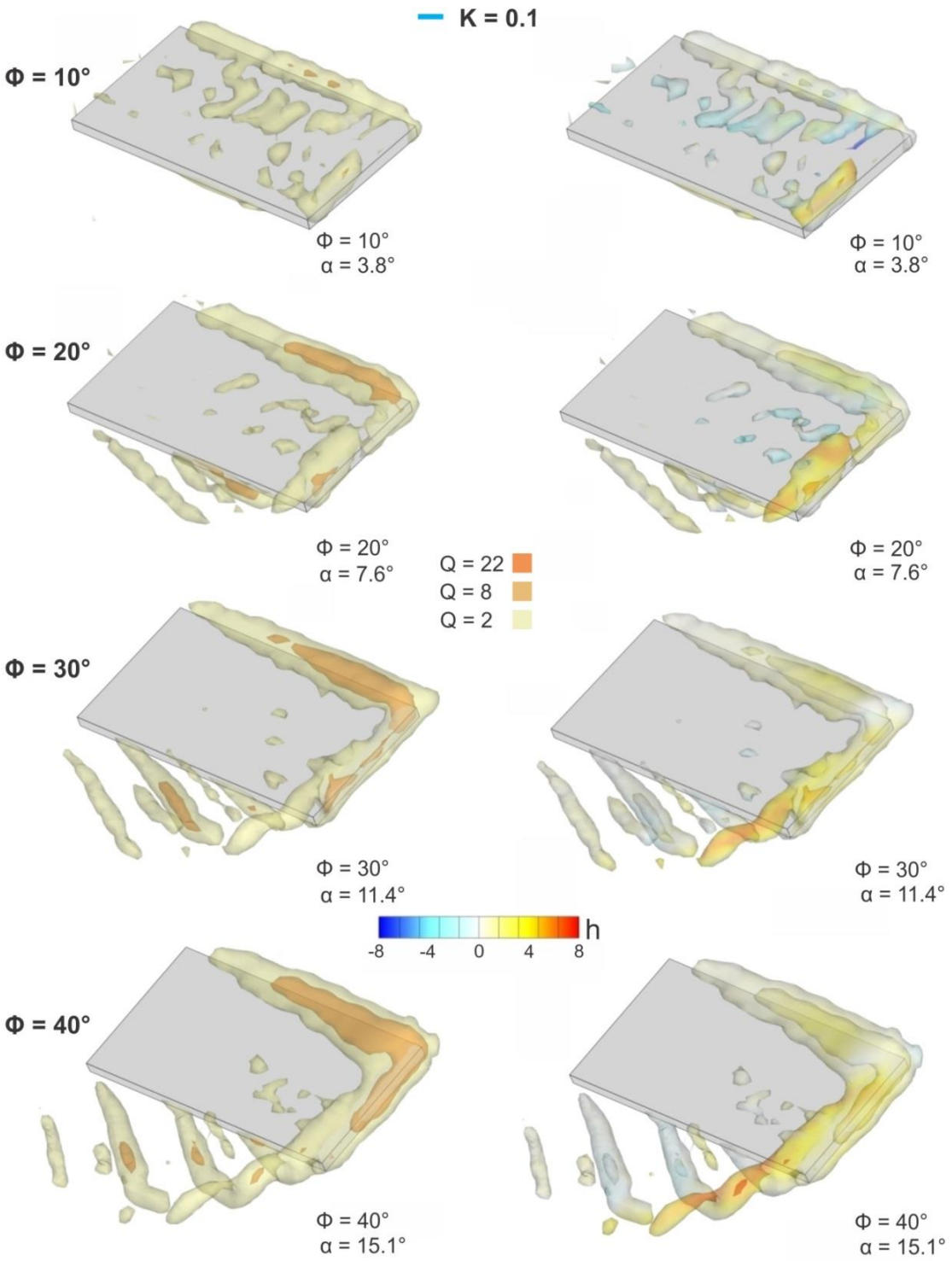

Figure 5.5a: Iso-surfaces of *Q*-criterion (left column) and iso-*Q* colored with *h* (right column), for reduced pitch rate $K = 0.1$ at angles of rotation, $\phi = 10°$, 20°, 30°, and 40° (rows of images).

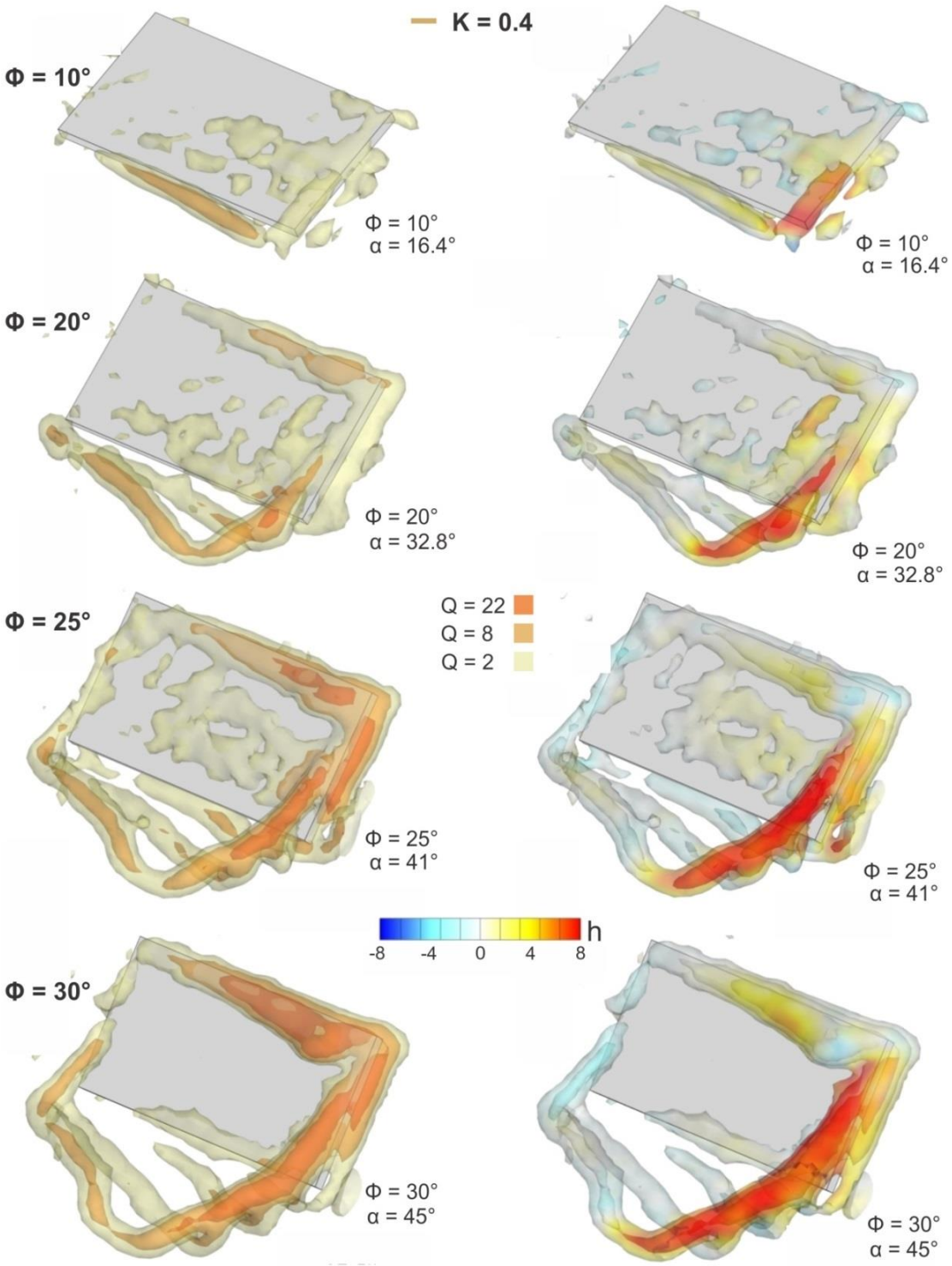

Figure 5.5b: Iso-surfaces of *Q*-criterion (left column) and iso-*Q* colored with *h* (right column), for reduced pitch rate $K = 0.4$ at angles of rotation, $\phi = 10°$, 20°, 25°, and 30° (rows of images).

CHAPTER 6

CONCLUSIONS AND RECOMMENDATIONS

6.1 CONCLUSIONS

This investigation focuses on the three-dimensional flow structure on low aspect ratio wings undergoing bio-inspired unsteady flight maneuvers. An experimental apparatus was designed in order to execute high-amplitude unsteady pitching, rotating, and combined pitch-up and rotation maneuvers of rectangular wings. The flow structures present on wings executing maneuvers of this type include: a stable leading-edge vortex with enhanced spanwise flow; periodic vortex shedding from the trailing edge; and large scale tip vortices extending well into the wake. Quantitative flow visualization techniques via stereo particle image velocimetry were employed in order to determine phase-averaged sectional and volumetric patterns of velocity and vorticity components, streamlines, and *Q*-criterion.

Chapters 3, 4, and 5 describe the three-dimensional flow structure on purely rotating wings with an incident freestream, as well as combined pitching and rotating wings in absence of a free stream. Topics addressed include: formation of a leading-edge vortex; dominance of rotation on the features of the flow structure; and time evolution of three-dimensional root, leading-edge, tip and wake vortices for a combined pitching and rotating wing. Detailed concluding remarks can be found at the end of each of the foregoing chapters. Summaries of the most important results are provided in the following.

6.1.1 Flow structure on a rotating wing: effect of incident flow

The flow structure on a rotating plate at a high angle of attack, both with and without incident mean flow, is representative of forward and hovering flight conditions for a bio-inspired flyer. The results show that a stable leading-edge vortex persists to large angle of rotation, even in the presence of a relatively large inflow (freestream) velocity. Furthermore, a number of features of the flow structure are similar over a range of advance ratios when the effective angle of attack is maintained constant by adjusting the geometric angle of attack of the wing.

Three-dimensional representations of the flow structure show that a stable leading edge vortex persists along the span of the wing for extreme values of advance ratio. A large-scale loop vortex, associated with the start-up process, exists in the wake region for hovering conditions, and is not evident for fast forward flight. However, during fast forward flight, a single starting vortex is not evident; rather a pattern of small scale structures shed from the trailing edge appears. Moreover, the structure of the root vortex is fundamentally different for these extreme values of advance ratio. In essence, the effect of increasing advance ratio, corresponding to an increase in magnitude of the freestream velocity incident upon the wing, is to either preclude or shift the timing of formation of the large-scale coherent loop vortex in the trailing edge and root regions.

6.1.2 Flow structure on combined pitching and rotating wings

Purely pitching and purely rotating wings have been extensively studied in previous investigations. Details of the complex flow structure, generated from generic rotation and pitch-up maneuvers, are presented in this investigation. The new flow physics revealed herein for these simultaneous motions includes: stabilization of the

large-scale vortex generated at the leading-edge; preservation of a coherent tip/leading-edge vortex system; generation of a highly ordered vortex system from the trailing-edge of the wing; and rapid relaxation of the flow structure to a common state upon termination of the pitch-up component of the simultaneous pitch-up and rotational motions of the wing.

From the foregoing, it is evident that the effects of rotation have a strong influence on the flow structure during pitch-up. The flow structure on a purely pitching wing includes a large scale leading-edge vortex, which takes the form of an arch vortex at the plane of symmetry of the wing. It was demonstrated herein that the nature of the pitch-induced vortex at the leading-edge is fundamentally altered in presence of wing rotation. That is, a conical leading-edge vortex forms across the span of the wing with the addition of rotation.

The distinctions between the flow structure on a wing undergoing combined pitch-up and rotation and a wing in pure rotation are also identified in the present investigation. The coherence of the entire tip-leading-edge vortex system is maintained with simultaneous pitch-up and rotation, while the coherence of the tip vortex is substantially degraded at sufficiently large rotation angle for pure rotation. Corresponding patterns of streamlines show well defined swirl throughout the leading-edge-tip vortex system; in contrast, for pure rotation, the ordered nature of the swirl streamlines is disrupted, and there is upstream flow through the disordered tip vortex.

6.1.3 Effect of pitch rate on development of three dimensional flow structure on combined pitching and rotating wings

Variation of the non-dimensional pitch rate for a combined pitching and rotating wing influences the patterns of flow structure, particularly at the cessation of the pitch-up maneuver. In other words, the three-dimensional flow structures that occur at each value of pitch rate investigated herein are distinctly different when the wing reaches the maximum pitch angle. At this instant, the flow structure for decreasing pitch rate appears less developed, in terms of the scales and magnitudes of iso-Q surfaces within the leading-edge, trailing, and tip vortices. In addition, the propagation of high levels of Q-criterion through the wake, tip, and leading-edge vortices is significantly different for the extreme values of non-dimensional pitch. However, volumetric images, acquired after cessation of the pitch-up maneuver while the wing continues to rotate, show strong similarity, thereby indicating the strong influence of rotation on the structure of the vortex system. That is, for each value of pitch rate, the flow structures at the same time scale of relaxation during pure rotation are almost identical, despite the difference in initial conditions at the cessation of the pitch up maneuver. Stabilization of the leading-edge vortex exists when significant levels of axial vorticity flux persist through the leading-edge and tip vortices.

6.2 RECOMMENDATIONS

The design of micro-air or unmanned-air vehicles involves unsteady large amplitude flight maneuvers often used by biological flyers, i.e. rotation, pitching, and plunging. The present investigations provide a basis for understanding the flow structure associated with bio-inspired flight.

The flow structure arising from generic kinematics, such as pure rotation and combined pitching and rotation, has been determined. However, bio-inspired flyers often

use a complex combination of rotation, pitching, and plunging for a variety of maneuvers. Future investigations should focus on more complicated kinematics involving the combination of basic classes of motion, rotation, pitching, and plunging, in order to expand our understanding of the complex flow structures associated with bio-inspired flight.

The three-dimensional flow structures arising from unsteady maneuvering wings are provided in this investigation. However, a link between the aerodynamic forces and the structures on combined pitching and rotating wing is not addressed. Simultaneous force measurements and flow visualization for a range of prescribed unsteady kinematics will provide further meaningful information to designers of micro-air vehicles.

Rigid wings having rectangular planform designs were used in this investigation. However, flyers found in nature use more complex elliptically-shaped wings that often have some degree of flexibility. Due to the vast range of wing geometries used by insects and birds, selection of wing design parameters becomes a complex decision. Therefore, it may be most productive to explore rigid wings that are elliptical in shape and compare the flow structure to that of a rectangular wing undergoing combined pitch-up and rotation. The flow structure and loading on a rectangular wing, with uniform flexibility in either the chordwise or spanwise direction, in comparison with similar rigid wings, would be productive first step.

WORKS CITED

Adrian, R. J. & Westerweel, J. (2010) *Particle Image Velocimetry.* Cambridge University Press.

Ansari, S. a., Phillips, N., Stabler, G., Wilkins, P.C., Żbikowski, R. & Knowles, K. (2009). Experimental investigation of some aspects of insect-like flapping flight aerodynamics for application to micro air vehicles. *Exp. Fluids* **46**, 777–798.

Ansari, S. a., Phillips, N., Stabler, G., Wilkins, P.C., Żbikowski, R. & Knowles, K. (2011). Erratum to: Experimental investigation of some aspects of insect-like flapping flight aerodynamics for application to micro air vehicles. *Exp. Fluids* **51**, 571–572.

Basu, B. C. & Hancock, G. J. (2009) The unsteady motion of a two-dimensional aerofoil in incompressible inviscid flow. *J. Fluid Mech.* **87**, 159.

Bross, M., Ozen, C. a. & Rockwell, D. (2013). Flow structure on a rotating wing: Effect of steady incident flow. *Phys. Fluids* **25**, 081901.

Carr, Z.R., Chen, C. & Ringuette, M.J. (2013a). Finite-span rotating wings: three-dimensional vortex formation and variations with aspect ratio. *Exp. Fluids* **54**, 1444.

Carr, Z.R., DeVoria, A.C. & Ringuette, M.J. (2013b). Aspect Ratio Effects on the Leading-Edge Circulation and Forces of Rotating Flat-Plate Wings. In *AIAA Paper 2013-0675*.

Cheng, B., Sane, S.P., Barbera, G., Troolin, D.R., Strand, T. & Deng, X. (2013). Three-dimensional flow visualization and vorticity dynamics in revolving wings. *Exp. Fluids* **54**, 1423.

Dickinson, M.H. & Gotze, K.G. (1993). Unsteady aerodynamic performance of model wings at low Reynolds numbers. *J. Exp. Bio.* ***174***, 45–65.

Dickinson, M.H., Lehmann, F.O. & Sane, S.P. (1999). Wing Rotation and the Aerodynamic Basis of Insect Flight. *Science.* **284**, 1954–1960.

Dickson, W.B. & Dickinson, M.H. (2004). The effect of advance ratio on the aerodynamics of revolving wings. *J. Exp. Biol.* **207**, 4269–81.

Ekaterinaris, J. a. & Platzer, M.F. (1998). COMPUTATIONAL PREDICTION OF AIRFOIL DYNAMIC STALL. *Prog. Aerosp. Sci.* **33**, 759–846.

Eldredge, J.D. & Wang, C. (2010). High-Fidelity Simulations and Low-Ordering Modeling of a rapidly Pitching Plate. In *AIAA Paper 2010-4281*.

Eldredge, J.D., Wang, C. & Ol, M. (2009). A Computational Study of a Canonical Pitch-up, Pitch-down Wing maneuver. In *AIAA Paper 2009-3687*.

Ellington, C.P. & Berg, C. van den. (1997). The three-dimensional leading-edge vortex of a ’ hovering ' model hawkmoth. *R. Soc.* **352**, 329–340.

Garmann, D.J. & Visbal, M.R. (2011). Numerical investigation of transitional flow over a rapidly pitching plate. *Phys. Fluids* **23**, 094106.

Garmann, D.J. & Visbal, M.R. (2013). A numerical study of hovering wings undergoing revolving or translating motions. In *AIAA Paper 2013-3052*. Reston, Virginia: American Institute of Aeronautics and Astronautics.

Garmann, D.J. & Visbal, M.R. (2014). Dynamics of revolving wings for various aspect ratios. *J. Fluid Mech.* **748**, 932–956.

Garmann, D.J., Visbal, M.R. & Orkwis, P.D. (2013). Three-dimensional flow structure and aerodynamic loading on a revolving wing. *Phys. Fluids* **25**, 034101.

Gopalakrishnan, P. & Tafti, D. K. (2010) Effect of wing flexibility on lift and thrust production in flapping flight. *AIAA J.* **48**, 865–877.

Granlund, K., Ol, M. & Bernal, L.P. (2011). Experiments on Pitching Plates : Force and Flowfield Measurements at Low Reynolds Numbers. In *AIAA Paper 2011-872*.

Harbig, R.R., Sheridan, J. & Thompson, M.C. (2013). Reynolds number and aspect ratio effects on the leading-edge vortex for rotating insect wing planforms. *J. Fluid Mech.* **717**, 166–192.

Harbig, R.R., Sheridan, J. & Thompson, M.C. (2014). The role of advance ratio and aspect ratio in determining leading-edge vortex stability for flapping flight. *J. Fluid Mech.* **751**, 71–105.

Hartloper, C., Kinzel, M. & Rival, D.E. (2012). On the competition between leading-edge and tip-vortex growth for a pitching plate. *Exp. Fluids* **54**, 1447.

Ho, C. M. & Chen, S. H. (1981) Unsteady Kutta condition of a plunging airfoil. *Unsteady Turbulent Shear Flow (IUTAM Symposium)*, Toulouse, France.

Hunt, J.C.R., Wray, A.A. & Moin, P. (1988) Eddies, Streams, and Convergence Zones in Turbulent Flows. In *Studying Turbulance Using Numerical Simulation databases, vol 2*: 193–208.

Kim, D. & Gharib, M. (2010). Experimental study of three-dimensional vortex structures in translating and rotating plates. *Exp. Fluids* 329–339.

Lawson, N.J. & Wu, J. (1997). Three-dimensional particle image velocimetry : error analysis of stereoscopic techniques. *Meas. Sci. Technol.* **8**, 897–900.

Lehmann, F.O. & Dickinson, M.H. (1998). THE CONTROL OF WING KINEMATICS AND FLIGHT FORCES IN FRUIT FLIES. *J. Exp. Biol.* **401**, 385–401.

Lentink, D. & Dickinson, M.H. (2009a). Rotational accelerations stabilize leading edge vortices on revolving fly wings. *J. Exp. Biol.* 2705–2719.

Lentink, D. & Dickinson, M.H. (2009b). Biofluiddynamic scaling of flapping, spinning and translating fins and wings. *J. Exp. Biol.* 2691–2704.

McCroskey, W.J. (1982). Unsteady Airfoils. *Annu. Rev. Fluid Mech.* **14**, 285–311.

Nagai, H., Isogai, K., Fujimoto, T. & Hayase, T. (2009) Experimental and numerical study of forward flight aerodynamics of insect flapping wing. *AIAA J.* **47**, 730–742.

Ozen, C. a. & Rockwell, D. (2011). Flow structure on a rotating plate. *Exp. Fluids* **52**, 207–223.

Ozen, C. a. & Rockwell, D. (2012). Three–dimensional vortex structure on a rotating wing. *J. Fluid Mech.* **707**, 1–10.

Ozen, C. A. (2012) Unsteady flow structures on rotating and flapping wings. PhD thesis, Lehigh University.

Percin, M., van Oudheusden, B.W., Eisma, H.E. & Remes, B.D.W. (2014). Three-dimensional vortex wake structure of a flapping-wing micro aerial vehicle in forward flight configuration. *Exp. Fluids* **55**, 1806.

Poelma, C., Dickson, W.B. & Dickinson, M.H. (2006). Time-resolved reconstruction of the full velocity field around a dynamically-scaled flapping wing. *Exp. Fluids* **41**, 213–225.

Prasad, A.K., Adrian, R.J., Landreth, C.C. & Offutt, P.W. (1992) Effect of resolution on the speed and accuracy of particle image velocimetry interrogation. *Exp. Fluids* **116**, 105–116.

Prasad, a K. & Jensen, K. (1995). Scheimpflug stereocamera for particle image velocimetry in liquid flows. *Appl. Opt.* **34**, 7092–9.

Sane, S.P. (2003). The aerodynamics of insect flight. *J. Exp. Biol.* **206**, 4191–4208.

Shih, C., Lourenco, L., Dommelen, L. Van & Krothapallij, A. (1992). Unsteady Flow Past an Airfoil Pitching at a Constant Rate. *AIAA J.* **30**, 1153–1161.

Shyy, W., Aono, H., Chimakurthi, S.K., Trizila, P., Kang, C.-K.C.K., Cesnik, C.E.S. & Liu, H. (2010). Recent progress in flapping wing aerodynamics and aeroelasticity. *Prog. Aerosp. Sci.* **46**, 284–327.

Visbal, M.R. (1989). Dynamic Stall of a Constant-Rate Pitching Airfoil. *J. Aircr.* **27**, 400.

Visbal, M.R. (2011). Three-Dimensional Flow Structure on a Heaving Low-Aspect-Ratio Wing. In *AIAA Paper 2011-219*.

Visbal, M.R. (2012) Flow Structure and Unsteady Loading Over a Pitching and Perching Low-Aspect-Ratio Wing. In *AIAA Paper 2012-3279*: 1–30.

Wojcik, C.J. & Buchholz, J.H.J. (2014). Vorticity transport in the leading-edge vortex on a rotating blade. *J. Fluid Mech.* **743**, 249–261.

Wolfinger, M. & Rockwell, D. (2014). Flow structure on a rotating wing: effect of radius of gyration. *J. Fluid Mech.* **755**, 83–110.

Yilmaz, T.O., Ol, M. & Rockwell, D. (2010). Scaling of flow separation on a pitching low aspect ratio plate. *J. Fluids Struct.* **26**, 1034–1041.

Yilmaz, T. O. (2011) Investigation of three-dimensional flow structure on maneuvering finite-span wings. PhD thesis, Lehigh University.

Yilmaz, T.O. & Rockwell, D. (2012). Flow structure on finite-span wings due to pitch-up motion. *J. Fluid Mech.* **691**, 518–545.

Zhang, X. & Schlüter, J.U. (2012). Numerical study of the influence of the Reynolds-number on the lift created by a leading edge vortex. *Phys. Fluids* **24**, 065102.

APPENDIX A

SUPPLEMENT TO CHAPTER 2: ERROR ANALYSIS

PHASE AVERAGING EFFECT ON FLOW STRUCTURE

The error of velocity displacements present in PIV measurements was previously discussed in section 2.4. In addition, analysis of error reduction associated with phase averaging was discussed in section 2.4.4. Figures A.1 and A.2 provide additional representations of the effect of phase averaging on the velocity and vorticity components.

Sectional representations of spanwise vorticity contours at the midplane are provided in figure A.1 for an instantaneous image, as well as phase-averaged images constructed from three, six, and two hundred instantaneous images. These images reveal that the patterns of vorticity quickly converge, as indicated by the similarity of the vorticity patterns for averages of three and two hundred images. Three locations, i.e., points in the flow field, were selected to analyze the convergence of velocity and vorticity components. These points are located one chord to left of wing (Point 1), inside the leading-edge vortex (Point 2), and one chord to the right of the wing (Point 3). At Points 1 and 3 the convergence of velocity components is displayed, while at point 2 spanwise vorticity is displayed. At each location, the velocity or vorticity components converge (less than 1% variation) after approximately twenty averages for velocity at points 1 and 3, and approximately fifty averages of vorticity at Point 2. However, at points 1 and 3 the velocity levels after six averages are within 5-6% of the asymptotic value reached at higher averages. Furthermore, the vorticity at six averages at Point 2 is approximately 5% of the asymptotic value reached at higher averages. Some of the

variation of spanwise vorticity within the leading-edge vortex can be attributed to a slight lack of repeatability of the flow structure for sequential experiments.

The variation of flow patterns for different groups of six phase-averaged images is provided in figure A.2. This figure was constructed because the majority of volume reconstructions presented in this dissertation used six phase averaged velocity fields. Images in the left column of figure A.2 show contour lines of spanwise vorticity for vorticity levels of +6 and -5 for three different sets of six phase averaged images. These contour lines approximately represent the edges of the leading-edge and tip vortices, respectively. In addition, the superposition of all thirty-four groups of six averages is displayed in the bottom row of figure A.2. Based on this plot one can conclude that the shapes of the leading-edge and tip vortices do not vary significantly between groups of six averages. Furthermore, the variation of velocity and vorticity at three points (same as figure A.1), indicate that variation in velocity and vorticity are on the order of a few percent between groups of six averages.

RANDOM AND BIAS ERROR EFFECT ON VOLUME RECONSTRUCTION

In the research conducted in this investigation, the bias and random errors of the velocity fields were both approximately 5% of V_{rg}, as indicated in section 2.4. The manifestation of velocity errors of this order in the volumetric flow patterns is explored in this section. A random perturbation, on the order of 5% of V_{rg}, was applied to the instantaneous velocity field in Figure A.3. This random error is essentially minimized after six averages, as indicated by relatively smooth surface of the *Q*-criterion shown in the bottom image of figure A.3.

Bias error, however, will not be reduced with phase averaging. To approximate the effect of bias error, a random perturbation, on the order of 5% of $V_{rg,}$ was applied to each image of the instantaneous velocity field. After these instantaneous images are phase averaged, another random perturbation, on the order of 5% of V_{rg}, was applied to each phase averaged velocity field. Volumetric reconstructions illustrating the effect of bias error on instantaneous, three, and six phase averaged flow fields are provided in Figure A.4. The surfaces of the *Q*-criterion indicate that this small magnitude bias error has little effect on the coherence and formation of the phase averaged images.

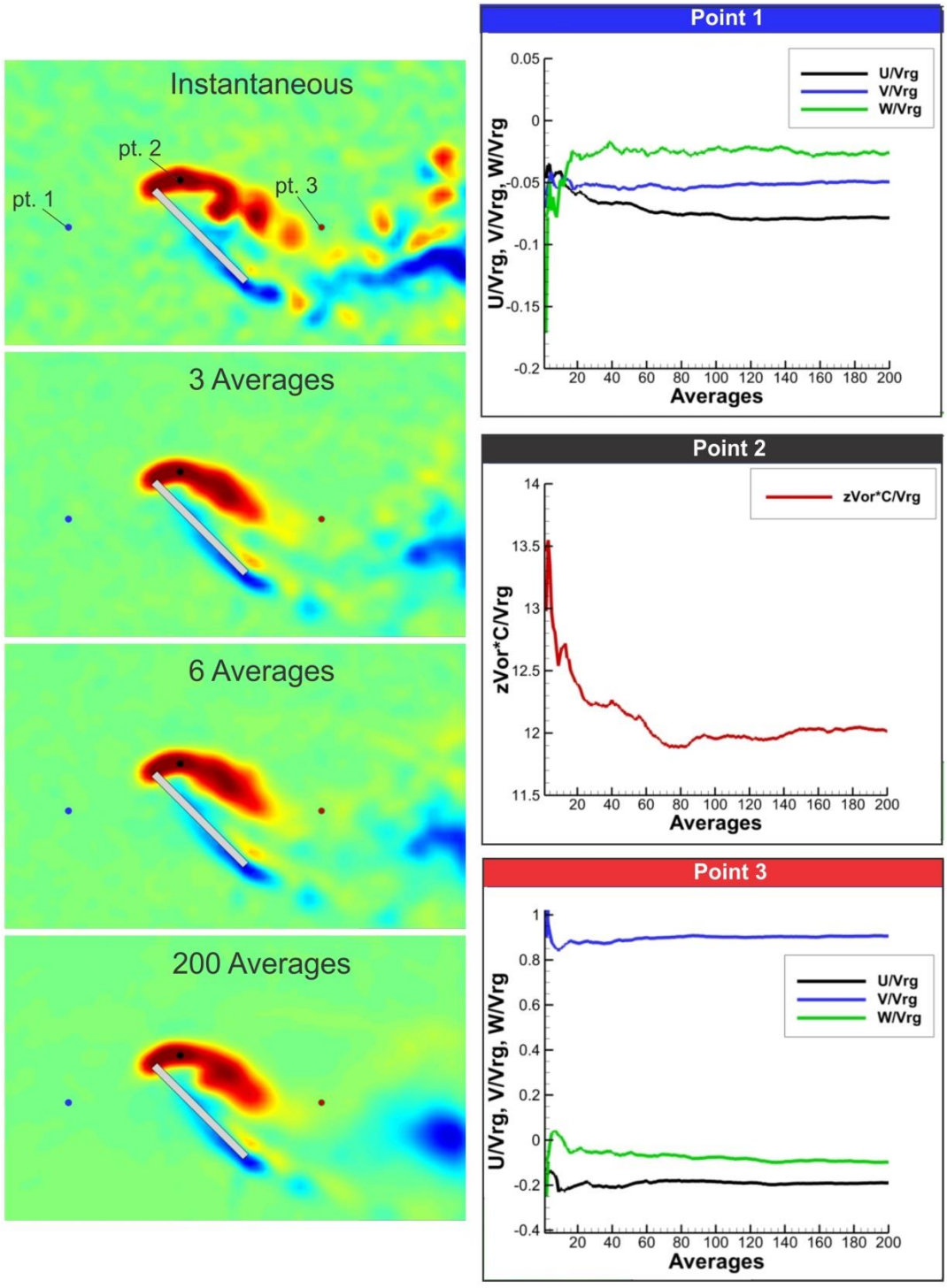

Figure A.1: Effect of phase averaging on spanwise vorticity contours at the midplane. An instantaneous image and phase averaged images constructed from 3, 6, and 200 instantaneous images are shown. The convergence of 3 components of velocity and vorticity is shown at 3 locations indicated on the images: 1 chord to the left of the wing (pt. 1), within the leading edge vortex (pt. 2), and 1 chord to the right of the wing (pt. 3).

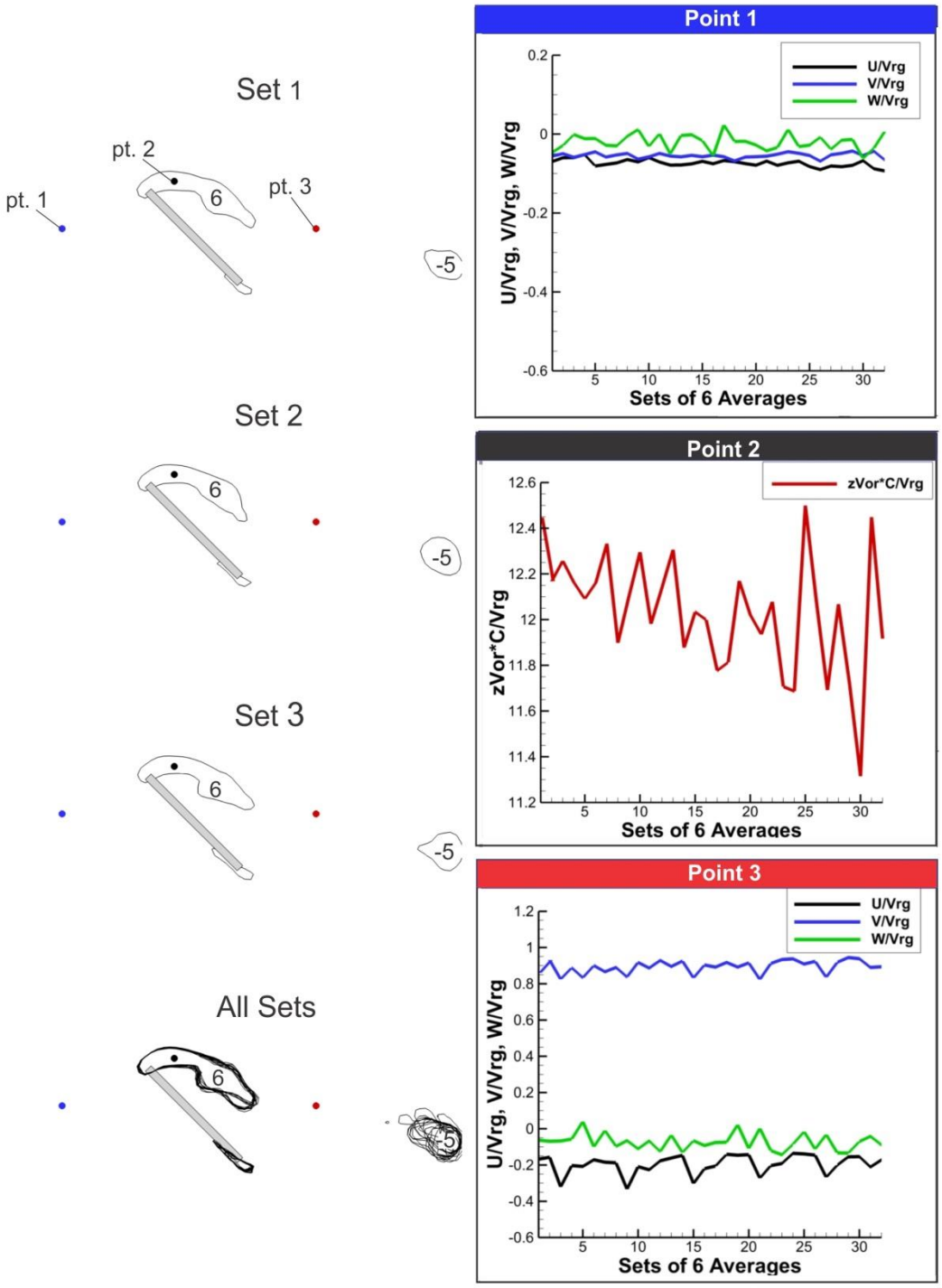

Figure A.2: Effect of phase averaging on spanwise vorticity contour lines at the midplane. Sets of six averages are compared, superposition of all sets (36 total) are proved. Variation of 3 components of velocity and vorticity shown at 3 locations, 1 chord to the left of the wing (pt. 1), within the leading edge vortex (pt. 2), and 1 chord to the right of the wing (pt. 3).

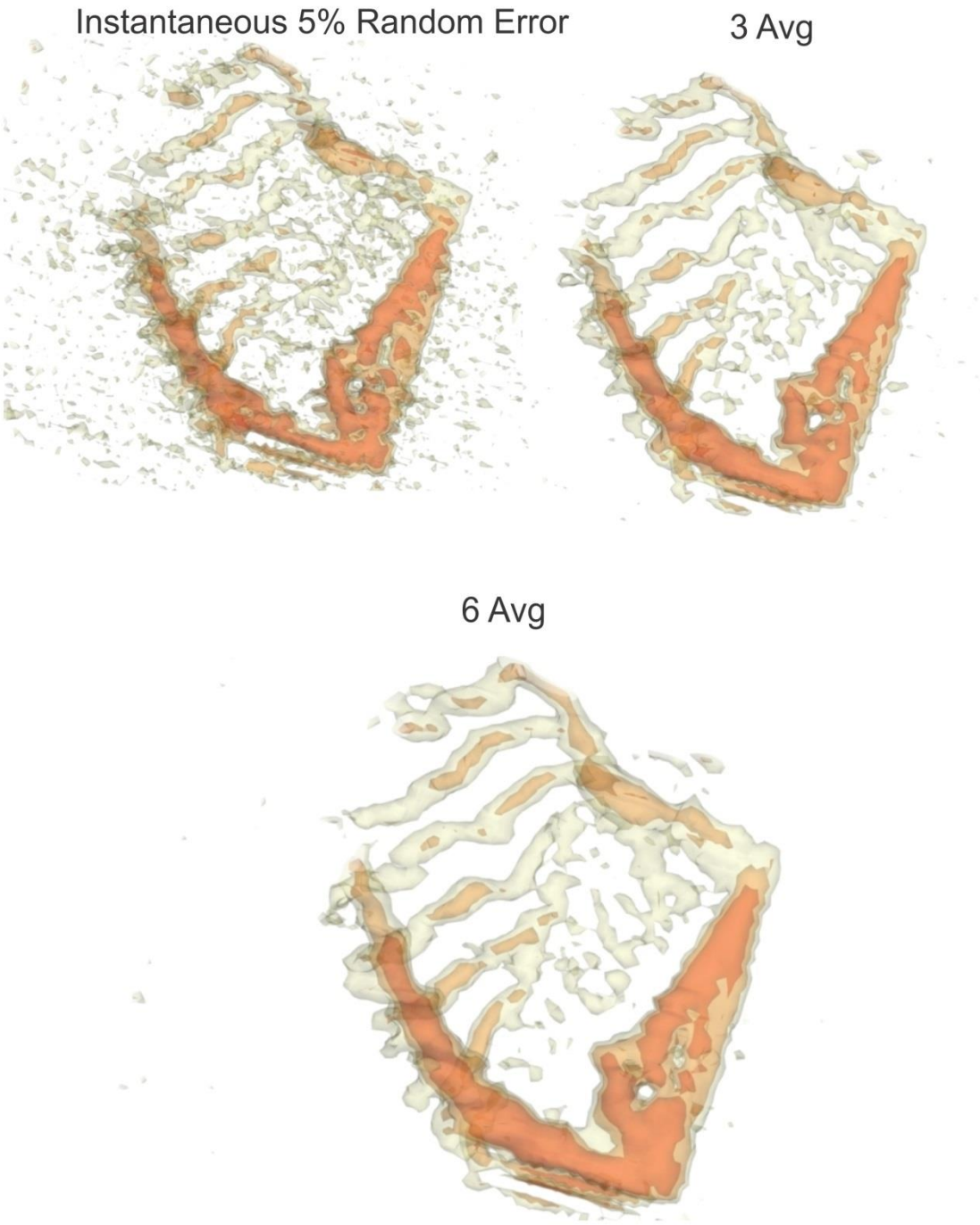

Figure A.3: Effect of random perturbation of the order of 5% of V_{rg} to all velocity components on reconstructed volume image. Attenuation of random error with phase averaging is shown.

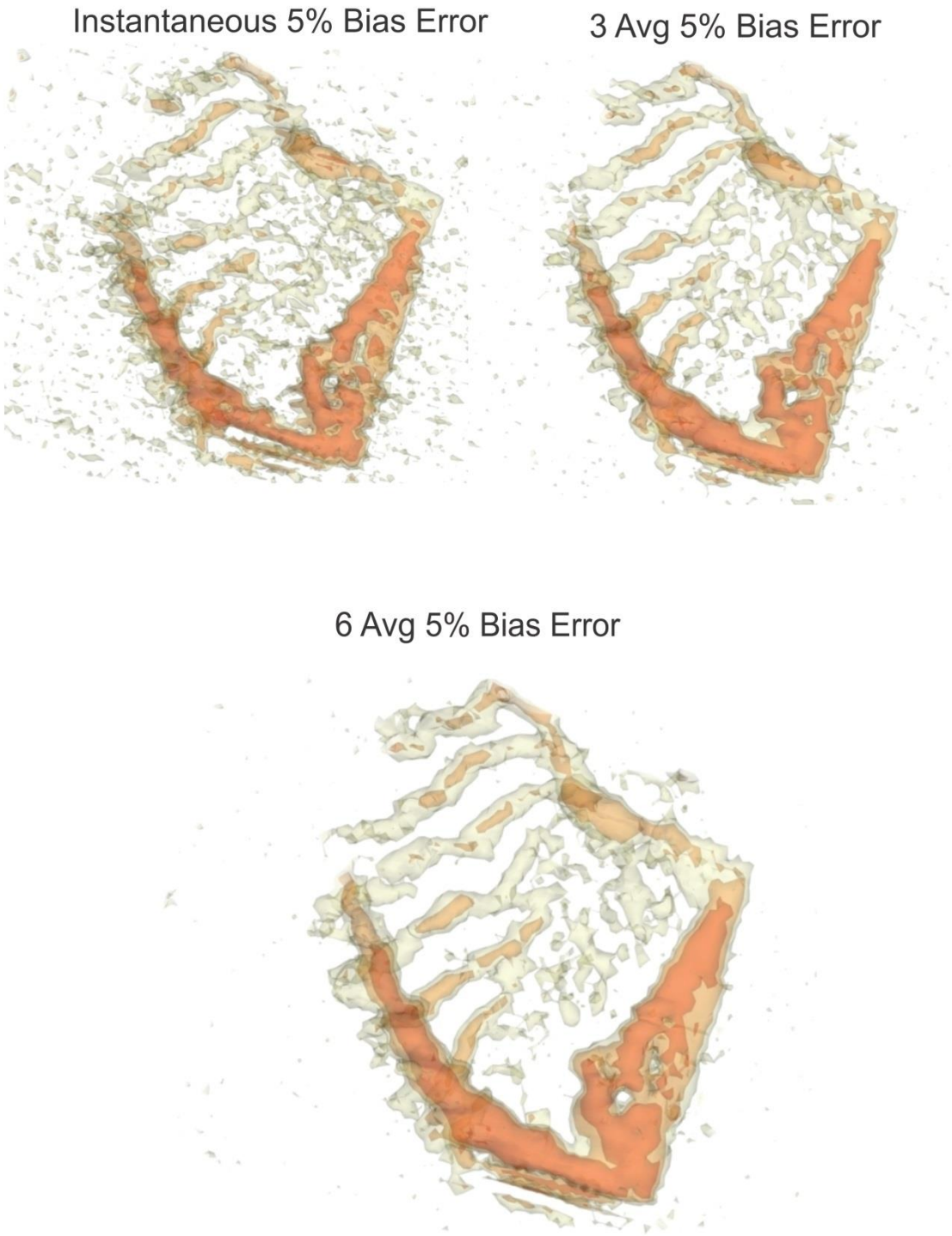

Figure A.4: Effect of bias perturbation of the order of 5% of V_{rg} to all velocity components on reconstructed volume image for each phase average.

APPENDIX B

SUPPLEMENT TO CHAPTER 3: FLOW STRUCTURE ON A ROTATING WING: EFFECT OF STEADY INCIDENT FLOW

RECOVERY FROM THREE-DIMENSIONAL STALL ON ROTATING WING

Three dimensional flow structures on rotating wings with an incident freestream are addressed in Chapter 3. However, volumetric images at ϕ = 0° (stationary) when the flow is fully stalled prior to the onset of wing motion and at ϕ = 270° where the flow structure is fully evolved is not provided. Figure B.1 contains sectional cuts of spanwise vorticity $\omega_z C/V_{eff}$ on chordwise oriented planes for values of advance ratio $J = \infty$ at ϕ = 0° and J = 0.537 at rotation angles ϕ = 36°and 270°.

When the wing is at rest and high angle of attack, as in the case ϕ = 0°, the flow is fully stalled and would not produce any lift. However, after the wing begins to rotate, this stalled flow quickly evolves into a stable leading-edge vortex with periodic shedding occurring in its wake at ϕ = 36°. This is a pure example of how conventional fixed wing aircraft flight differs from bio-inspired flight. The rotational accelerations stabilize the flow structure, yielding the lift generating leading-edge vortex (*LEV*) seen at ϕ = 36°. Further development of the flow structure is shown in the bottom image at ϕ = 270°. At this large value of rotation angle, the positive vorticity near the tip region appears to be unsteady and disordered. Furthermore, the vorticity across the entire span and in the wake region is less coherent than at lower angles of rotation.

VARIATION OF EFFECTIVE ANGLE OF ATTACK

The effective angle used in the experiments presented in Chapter 3 was α_{eff} = 45°. Sectional slices at the midplane on wings with 30° and 60° effective angles of attack are

compared to the case of α_{eff} = 45° in Figures B.3 and B.4. In this comparison, the advance ratio was J = 0.171, where the freestream velocity U_∞ = 105 mm s^{-1} and V_{rg} = 395 mm s^{-1} corresponding to a value of Reynolds number based on tip velocity of Re_{tip} = 23 595. The effective angle of attack was varied by changing the geometric angle of attack values α_{gem} = 75°, 60°, and 45° to give α_{eff} = 30°, 45°, and 60° respectively.

During the early stage of development, the leading-edge vortex is evident for all values of α_{eff} at ϕ = 9°, following the fully stalled flow state at ϕ = 0°. However, with increasing α_{eff}, the scale of maximum positive vorticity concentration within core of the *LEV* increases. Furthermore, this same trend is observed at ϕ = 18°, where vorticity concentration and scale of the *LEV* increases with increasing α_{eff}. In addition, a distinct concentration of negative vorticity forms at the trailing edge for α_{eff} = 60° at ϕ = 9° ; it starts to shed at ϕ = 18°. On the other hand, for α_{eff} = 30° and 45° the vorticity at the trailing edge forms a distributed layer; it is most likely due to the remnant of the separated shear layer formed at ϕ = 0°.

Figure B.4 shows the continued development of the flow structure at values of rotation angle ϕ = 36°, 90°, and 270°. In general, the strength (maximum vorticity level) and the scale of the *LEV* grow with increasing α_{eff} at each value of ϕ. The *LEV* vortex begins to exhibit signs of vortex shedding at ϕ = 90° for all values of $\alpha_{eff.}$ However, the shedding is more significant at α_{eff} = 60°. Eventually at ϕ = 270°, the *LEV* vortex at each value of α_{eff} is more distributed, however, at α_{eff} = 30° the distributed *LEV* remains in closer proximity to the wing surface than at α_{eff} = 60°.

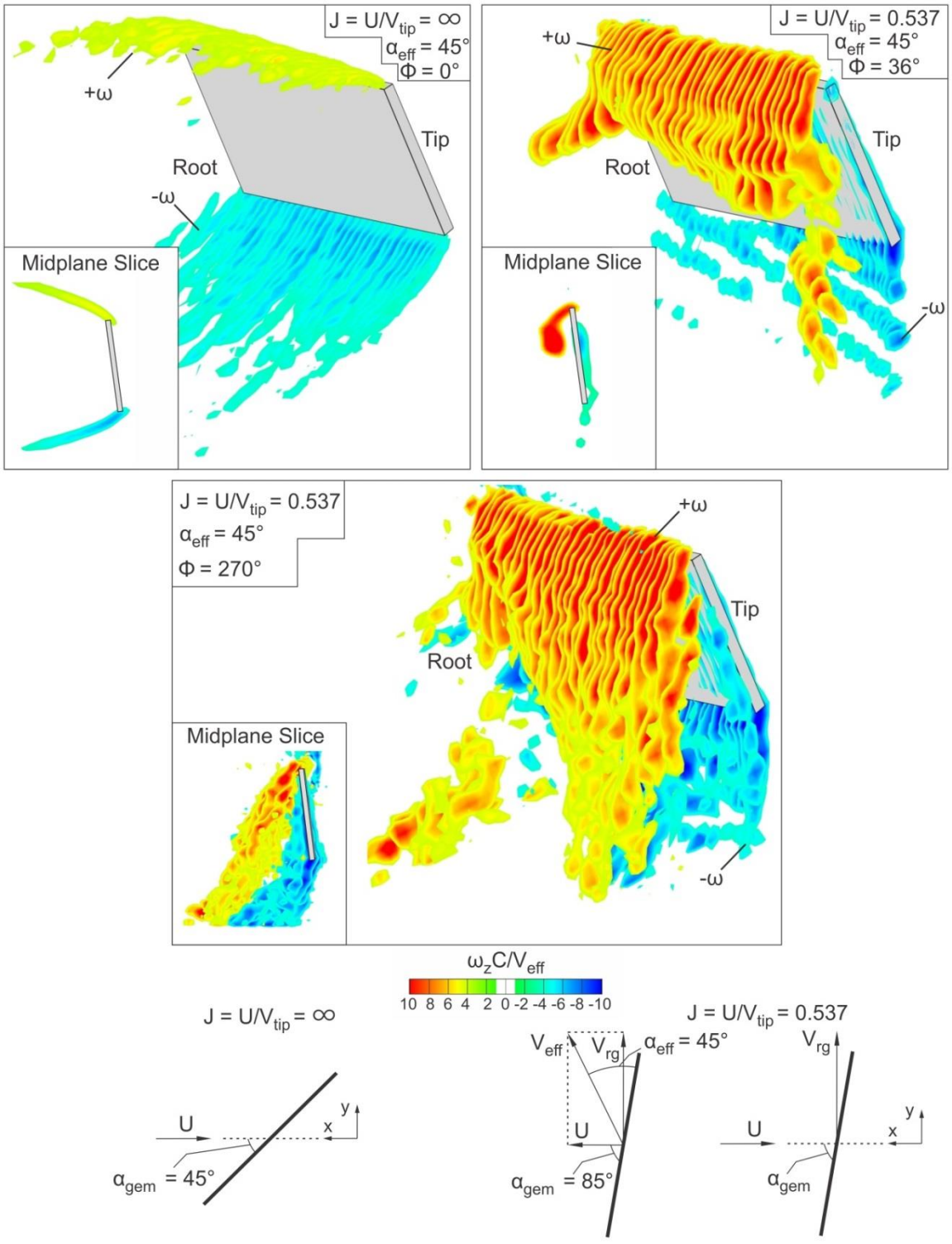

Figure B.1: Sectional cuts of spanwise vorticity $\omega_z C/V_{eff}$ on chordwise-oriented planes for values of advance ratio $J = \infty$ at $\phi = 0°$ and $J = 0.537$ at rotation angles $\phi = 36°$and 270°.

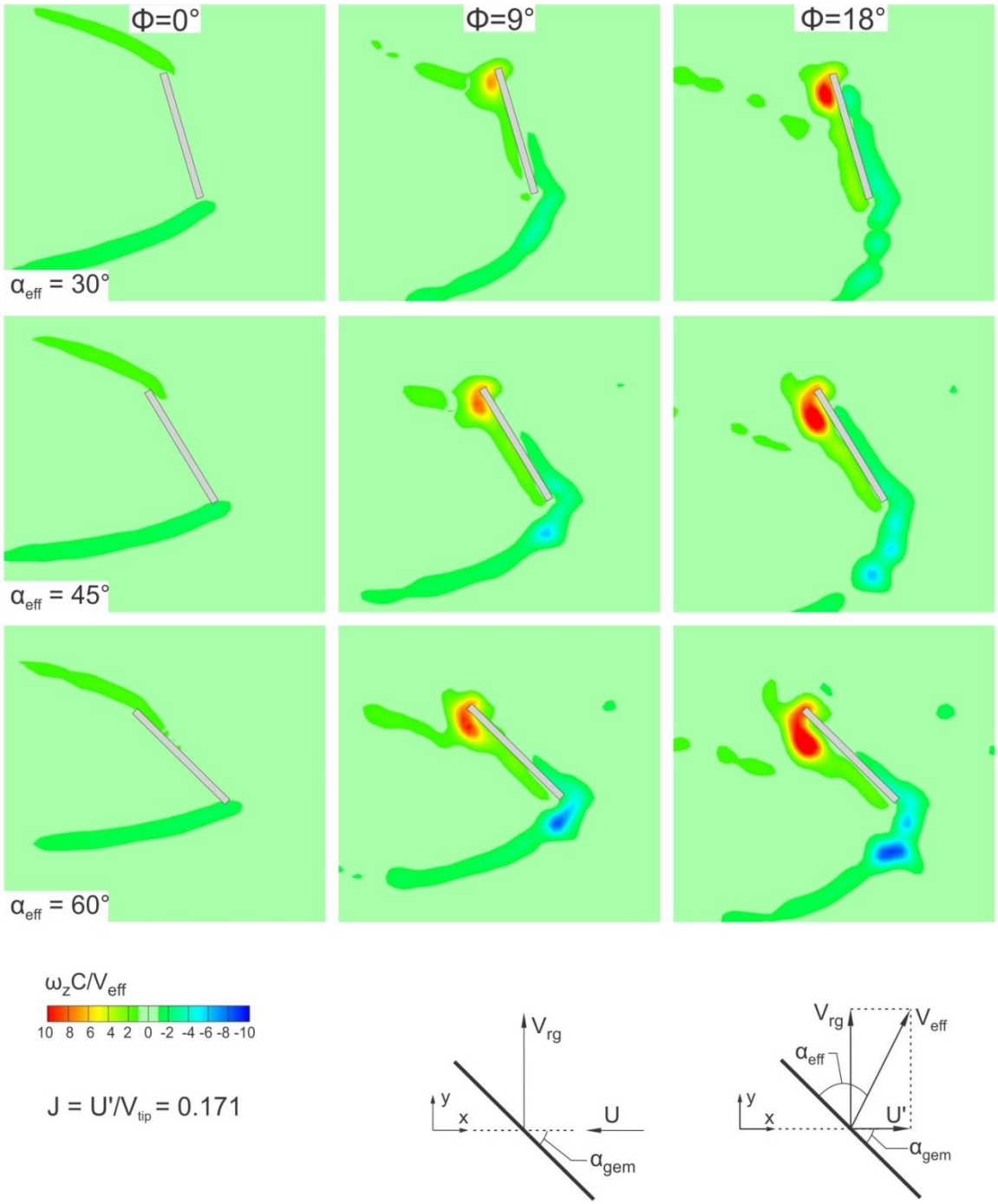

Figure B.2: Sectional cut of spanwise vorticity $\omega_z C/V_{eff}$ at the midplane location for α_{eff} = 30°, 45°, and 60° at rotation angles ϕ = 0°, 9°, and 18°. Advance ratio J = 0.171 for all cases.

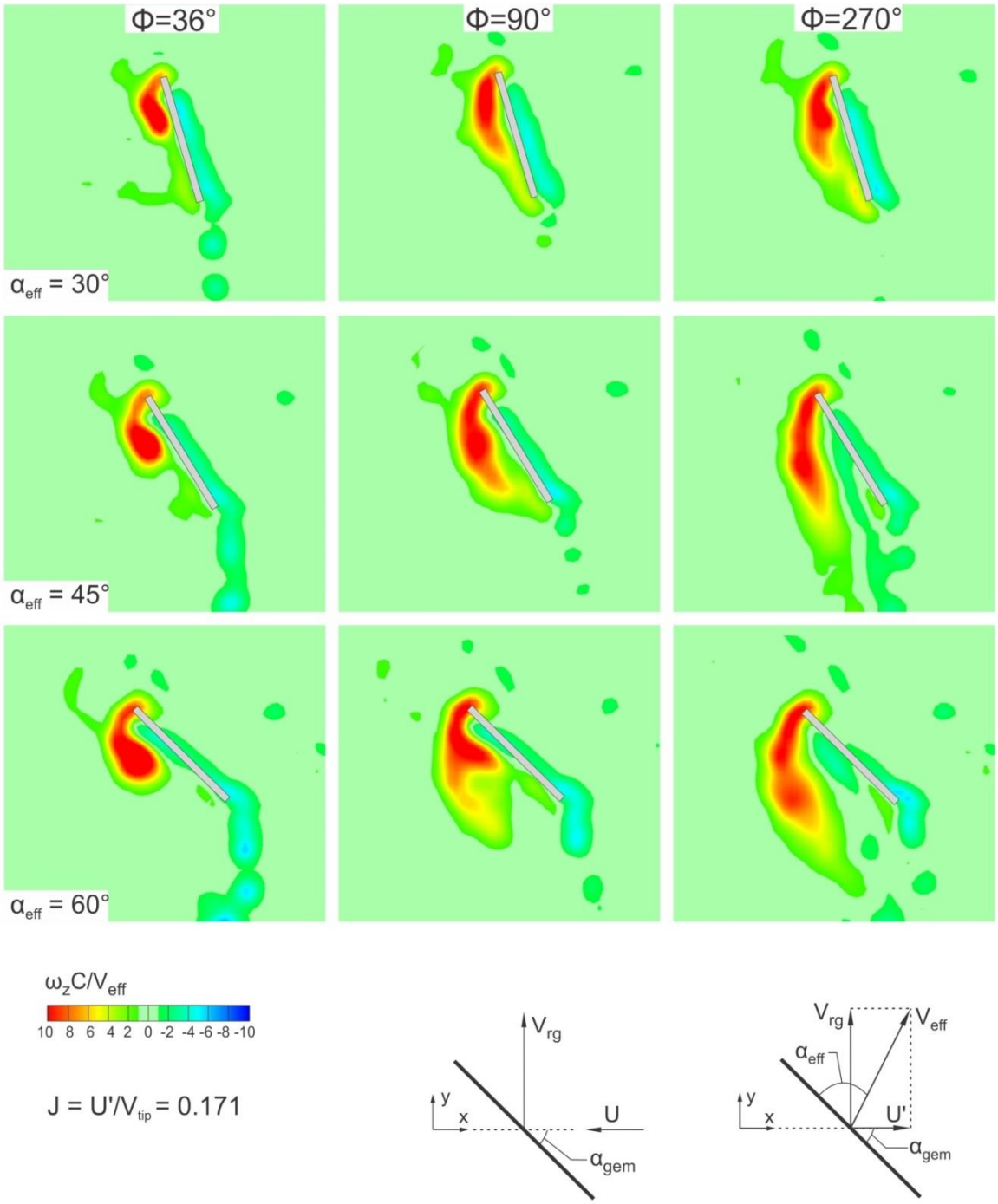

Figure B.3: Sectional cut of spanwise vorticity $\omega_z C/V_{eff}$ at the midplane location for α_{eff} = 30°, 45°, and 60° at rotation angles ϕ = 36°, 90°, and 270°; advance ratio J = 0.171 for all cases.

APPENDIX C

SUPPLEMENT TO CHAPTERS 4 AND 5: THREE-DIMENSIONAL FLOW STRUCTURE ALONG SIMULTANEOUSLY PITCHING AND ROTATING WINGS

MULTIPLE REVOLUTIONS PRIOR TO PITCH-UP

The experiments presented in Chapters 4 and 5 involved simultaneous rotation and pitch-up motions. This section explores the effect of multiple revolutions at zero angle of attack before the start of pitch-up motion. The flow structure on an $AR = 2$ wing that rotates at zero angle of attack for five revolutions before the start of pitch-up and the flow structure due to simultaneous pitch-up and rotation is provided in Figure C.1. Sectional slices at the midplane location for $K = \dot{\alpha}C/(2V_{rg}) = 0.1$, 0.2 and 0.4 indicate that the flow structures are essentially identical including the number of shed vortices from the wake region.

Figure C.2 extends this concept to three dimensions. Nested transparent iso-Q surfaces for a simultaneous pitching and rotating wing (left image) at $K = 0.2$ and a pitching and rotating wing are shown for the case where the pitch-up starts after five revolutions (right image). Similar to the sectional slices in figure C.1, the three-dimensional flow structures are essentially identical. In particular, the distribution of high levels of the Q-criterion within the vortex system is consistent for both cases and the number of shed vortices from the trailing edge is the same.

DELAYED OR ADVANCED ROTATION BEFORE PITCH-UP MOTION

Figures C.3 and C.4 show sectional slices for spanwise vorticity imaged at the midplane for a range of delayed rotation with respect to the start of pitch-up (C.3) and

delayed pitch-up with respect to the start of rotation (C.4). Schematics detailing the cases of motion delay for each value of *K* are provided at the bottom of each figure.

In figure C.3, the appearance of the trailing-edge vortex patterns varies with the magnitude of the delayed rotation. In general, the trailing edge vortex forms distinct, periodically shed structures (*g*-*i*) to single concentrations that form and remain near the trailing edge (e-g). The nature of the negative vortex patterns also changes with non-dimensional pitch-rate *K*. For example, as *K* increases, the trailing-edge vortex patterns appear more concentrated at each value of delay (columns *e*-*i*). Furthermore, the leading-edge vortex structure appears distributed across the surface of the wing at $K = 0.4$ (columns *a*-*i*). In contrast, for the reduced frequencies $K = 0.1$ and 0.2, the leading-edge vortex remains concentrated and in close proximity to the leading-edge.

When the pitching motion is delayed relative to the rotational maneuver (figure C.4), the flow structure does not change significantly for increasing delay (*j*-*m*) when compared to the simultaneous start (*i*). Namely, the size and scale of the leading-edge vortex and the nature of the shed trailing edge vortices are comparable for each value of *K* with increasing delay. However, the characteristics of the leading-edge and trailing-edge vortices are influenced by non-dimensional pitch rate *K*. Distributed positive vorticity is evident along the surface of the wing across the entire chord at $K = 0.393$. Furthermore, as seen in figure C.3, with increasing *K* at each delay value (*j*-*m*), the trailing-edge structures are more concentrated and the frequency at which these vortices are shed decreases.

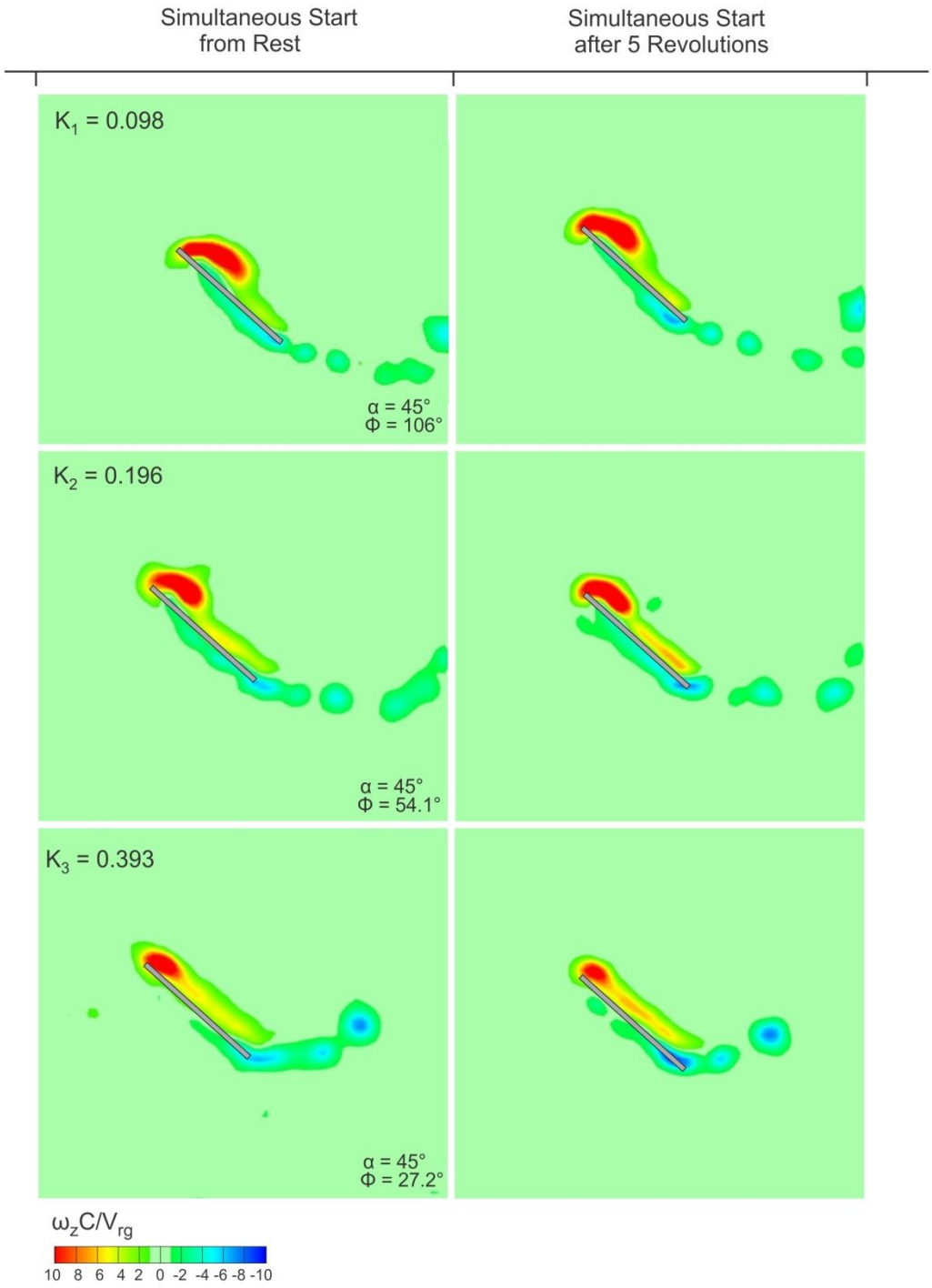

Figure C.1: Sectional slices at the midplane for simultaneous pitch-up and rotation of a wing (left image) and simultaneous pitch-up and rotation of a wing where the pitching motion starts after 5 full revolutions at zero angle of attack for pitch rates K = 0.1, 0.2 and 0.4.

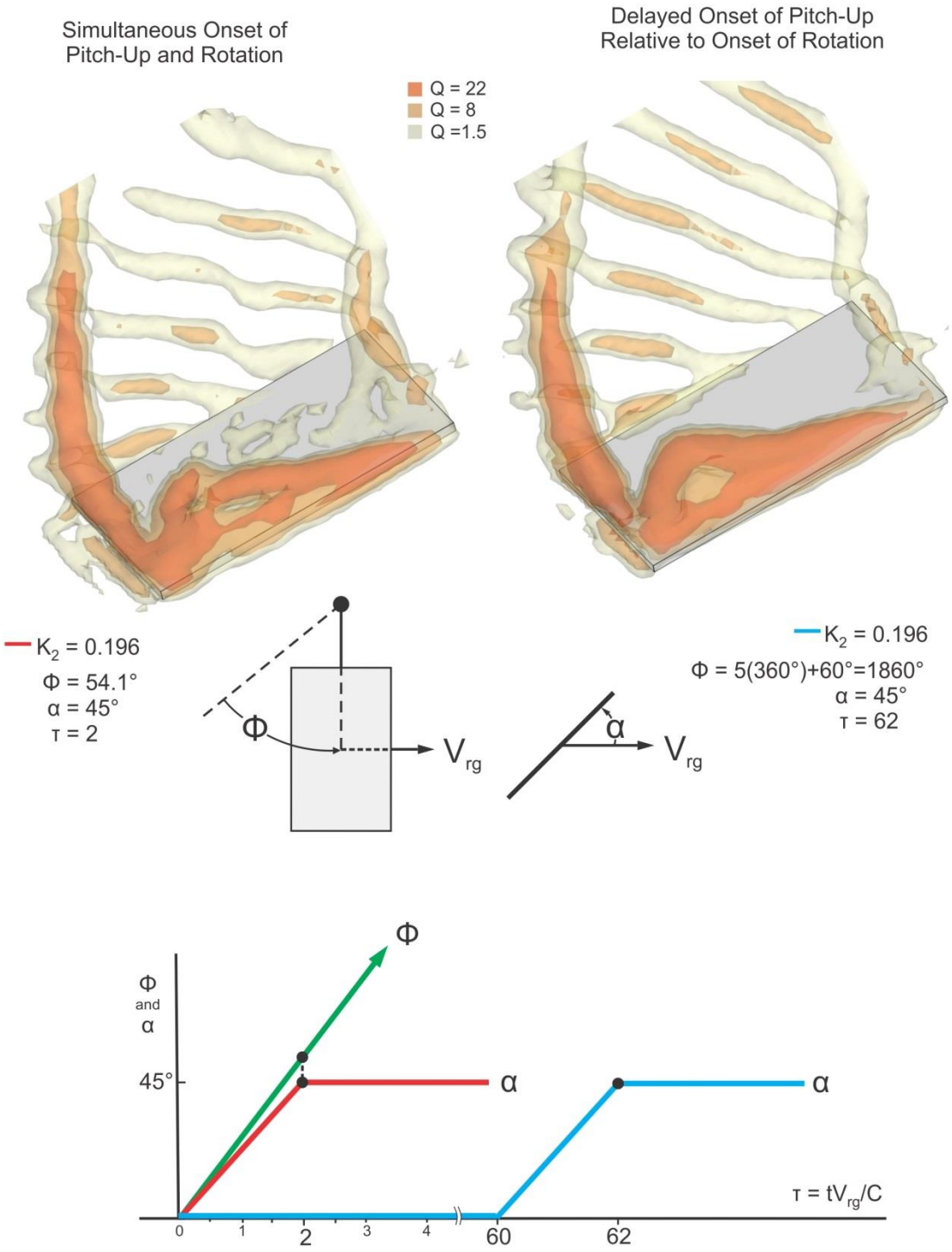

Figure C.2: Three dimensional iso-*Q* surfaces of pitch-up and rotation of a wing (left image) and simultaneous pitch-up and rotation where the pitching motion starts after 5 full revolutions at zero angle of attack.

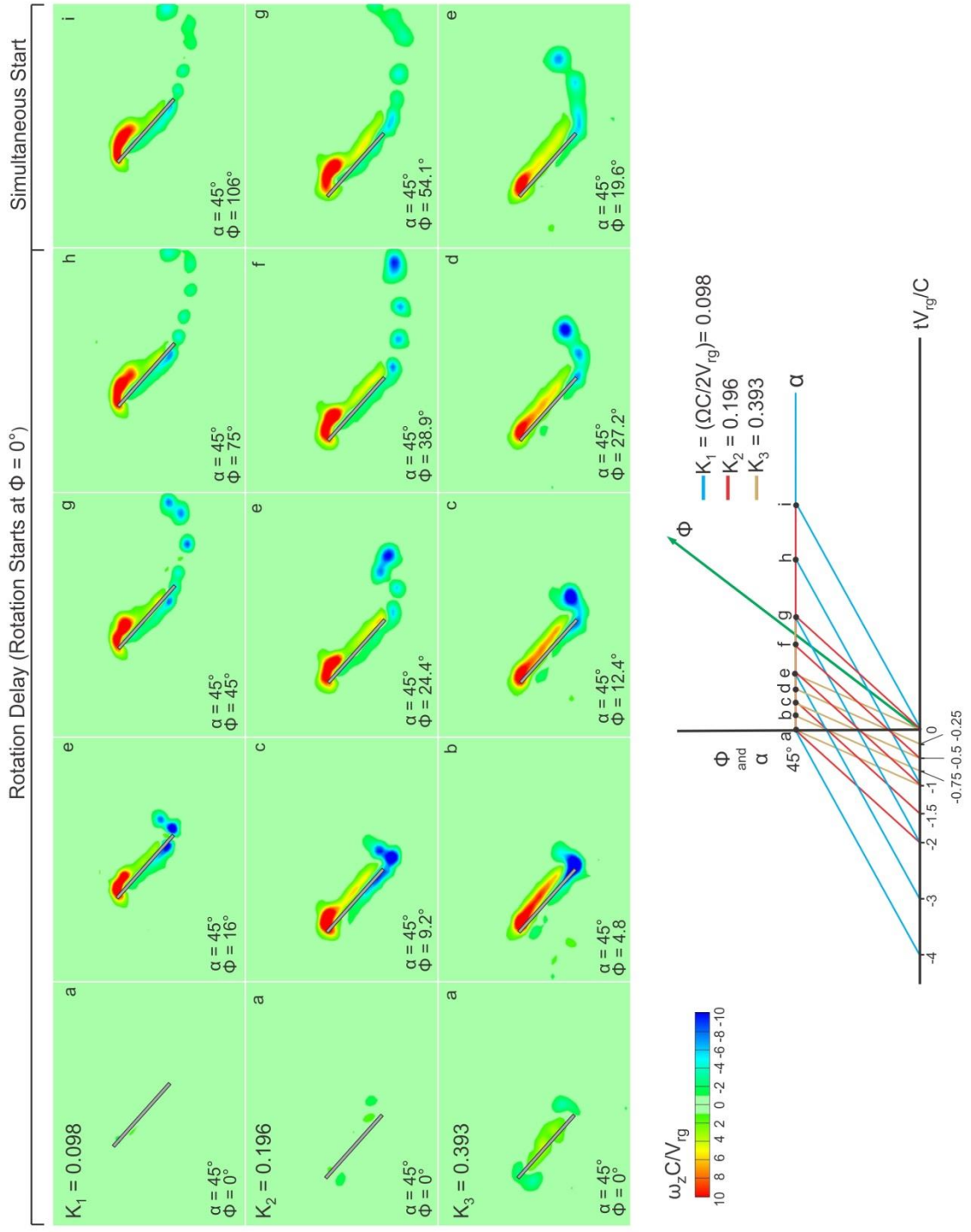

Figure C.3: Sectional slices taken at the midplane for simultaneous pitch-up and rotation of a wing for pitch rates K = 0.1, 0.2 and 0.4. Columns (*a*-*h*) represent the wing starting pitch-up at various times before the rotation starts. Column (*i*) represents the simultaneous starts of rotation and pitch-up motions.

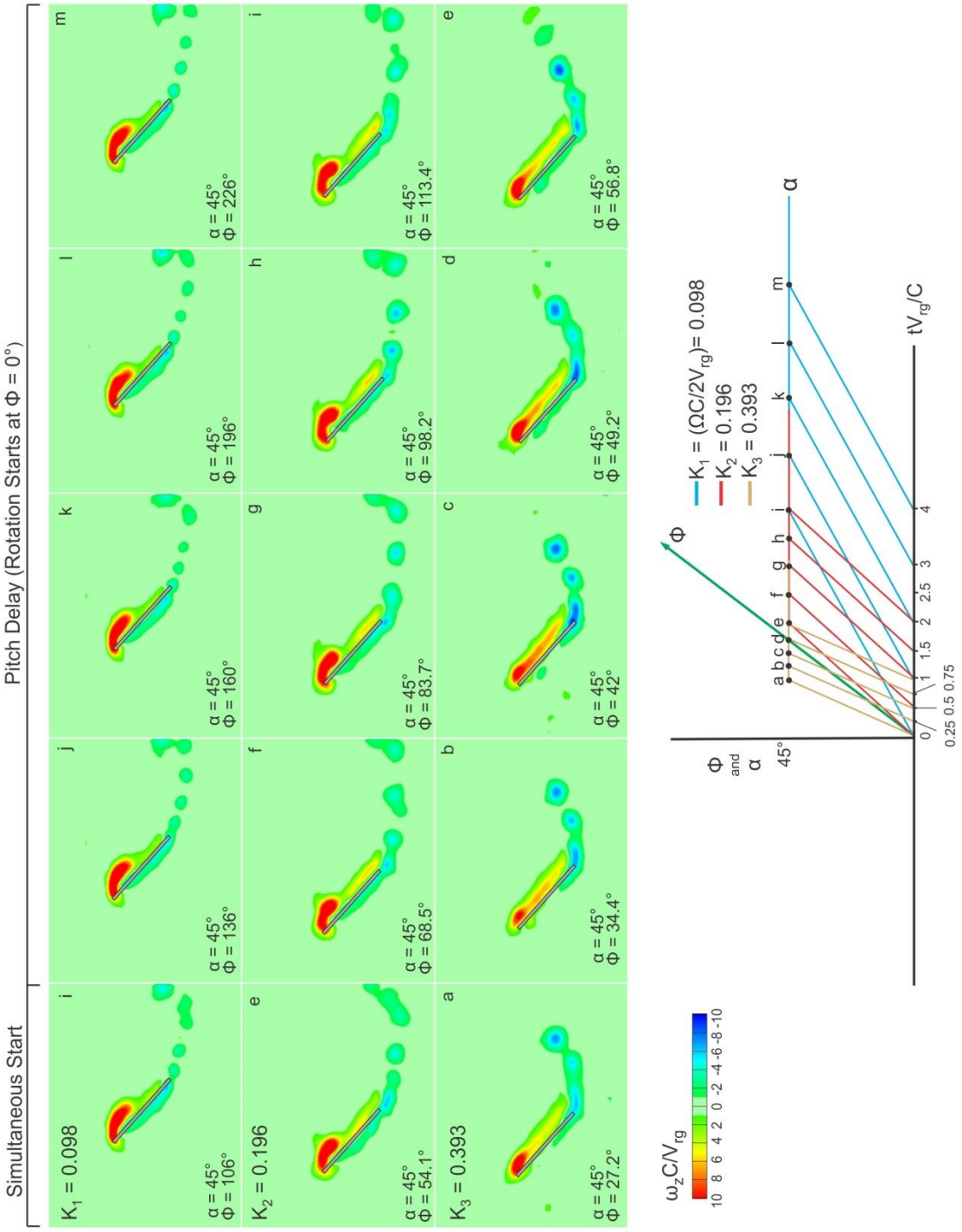

Figure C.4: Sectional slices taken at the midplane for simultaneous pitch-up and rotation of a wing for pitch rates K = 0.1, 0.2 and 0.4. Columns (*j*-*m*) represent the wing rotating at various times before the pitching begins. Column (*i*) represents the simultaneous starts of rotation and pitch-up motions.

VITA

The author was born to Thomas and Debbie Bross in Bethlehem, Pennsylvania on March 19th, 1988. He received his Bachelor of Science with Honors in Physics from Moravian College in May 2010. Promptly after his undergraduate studies he joined the Mechanical Engineering and Mechanics Department in the P.C. Rossin College of Engineering at Lehigh University where he was awarded a RCEAS Fellowship for the Fall 2010 semester. He completed the requirements for a Masters of Engineering in January 2013. Currently, he is enrolled in a doctoral program in Mechanical Engineering under the supervision of Dr. Donald Rockwell. He was honored as a Rossin Doctoral Fellow at Lehigh University in 2013. As a result of the research conducted during the doctoral program, the author has published the following articles,

Bross, M., Ozen, C. a. & Rockwell, D. 2013 Flow structure on a rotating wing: Effect of steady incident flow. *Phys. Fluids* **25**.

Bross, M. & Rockwell, D. 2014 Flow structure on a simultaneously pitching and rotating wing. *J. Fluid Mech.* **756**, 354–383.

Bross, M. & Rockwell, D. 2015 Three-dimensional flow structure along simultaneously pitching and rotating wings: effect of pitch rate. *Exp.in Fluids:* Under Review